



**CONSTRUCTION OF MULTIFUNCTIONAL  
LANTHANIDE COORDINATION POLYMERS WITH  
HYDRAZIDE LIGAND**

**BY**

**CHATPHORN THEPPITAK**

**A DISSERTATION SUBMITTED IN PARTIAL  
FULFILLMENT OF THE REQUIREMENTS FOR THE DEGREE  
OF DOCTOR OF PHILOSOPHY (CHEMISTRY)  
DEPARTMENT OF CHEMISTRY  
FACULTY OF SCIENCE AND TECHNOLOGY  
THAMMASAT UNIVERSITY  
ACADEMIC YEAR 2022**

**CONSTRUCTION OF MULTIFUNCTIONAL  
LANTHANIDE COORDINATION POLYMERS WITH  
HYDRAZIDE LIGAND**

**BY**

**CHATPHORN THEPPITAK**

**A DISSERTATION SUBMITTED IN PARTIAL  
FULFILLMENT OF THE REQUIREMENTS FOR THE DEGREE  
OF DOCTOR OF PHILOSOPHY (CHEMISTRY)  
DEPARTMENT OF CHEMISTRY  
FACULTY OF SCIENCE AND TECHNOLOGY  
THAMMASAT UNIVERSITY  
ACADEMIC YEAR 2022**

THAMMASAT UNIVERSITY  
FACULTY OF SCIENCE AND TECHNOLOGY

DISSERTATION

BY

CHATPHORN THEPPITAK

ENTITLED

CONSTRUCTION OF MULTIFUNCTIONAL LANTHANIDE COORDINATION  
POLYMERS WITH HYDRAZIDE LIGAND

was approved as partial fulfillment of the requirements for  
the degree of Doctor of Philosophy (Chemistry)

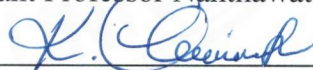
on May 15, 2023

Chairman



(Assistant Professor Nanthawat Wannarit, Ph.D.)

Member and Advisor



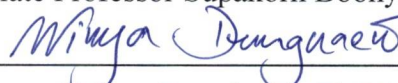
(Associate Professor Kittipong Chainok, Ph.D.)

Member and Co-advisor



(Associate Professor Supakorn Boonyuen, Ph.D.)

Member and Co-advisor



(Winya Dungkaew, Ph.D.)

Member



(Assistant Professor Filip Kielar, Ph.D.)

Dean



(Associate Professor Supet Jirakajohnkool, Ph.D.)

Dissertation Title	CONSTRUCTION OF MULTIFUNCTIONAL LANTHANIDE COORDINATION POLYMERS WITH HYDRAZIDE LIGAND
Author	Chatphorn Theppitak
Degree	Doctor of Philosophy (Chemistry)
Department/Faculty/University	Department of Chemistry Faculty of Science and Technology Thammasat University
Dissertation Advisor	Associate Professor Kittipong Chainok, Ph.D.
Dissertation Co-Advisor	Associate Professor Supakorn Boonyuen, Ph.D.
Dissertation Co-Advisor	Winya Dungkaew, Ph.D.
Academic Years	2022

## ABSTRACT

In this research, a range of lanthanide complexes incorporating hydrazide ligands have been synthesized and their photoluminescent sensing, magnetic, and CO<sub>2</sub> adsorption properties were investigated.

Three series of lanthanide (III) coordination complexes with hydrazide ligands have been synthesized and structurally characterized. The first series, [Ln(bzz)(NO<sub>3</sub>)(NO<sub>3</sub>)<sub>2</sub>] (**1**<sub>Ln</sub>; **Ln** = **1**<sub>Sm</sub>, **2**<sub>Eu</sub>, **3**<sub>Gd</sub>, **4**<sub>Tb</sub>, **5**<sub>Dy</sub>), were obtained by slow evaporation methods at room temperature and feature a discrete structure. The complex molecules are assembled into a 3D supramolecular structure via intermolecular N–H...O hydrogen bonds. The complexes in second series, [Ln(bzz)(ben)<sub>3</sub>(H<sub>2</sub>O)]·H<sub>2</sub>O (**2**<sub>Ln</sub>; **Ln** = **6**<sub>Pr</sub>, **7**<sub>Nd</sub>, **8**<sub>Sm</sub>, **9**<sub>Eu</sub>, **10**<sub>Gd</sub>, **11**<sub>Tb</sub>, **12**<sub>Dy</sub>, **13**<sub>Er</sub>), were synthesized by hydrothermal methods at 110 °C. The bzz ligands occurred *in situ* generated to benzoate (ben) ligands and both bzz and ben ligands are bridged the central Ln<sup>3+</sup> ions to form a one-dimensional (1D) polymeric chain. The third series of the complexes, [Ln<sub>3</sub>(ben)<sub>3</sub>] (**3**<sub>Ln</sub>; **Ln** = **14**<sub>Eu</sub>, **15**<sub>Gd</sub>, **16**<sub>Tb</sub>, **17**<sub>Dy</sub>, **18**<sub>Er</sub>, **19**<sub>Tm</sub>, **20**<sub>Yb</sub>, **21**<sub>Lu</sub>), were also formed at 145 °C by using hydrothermal method. The bzz ligand was found to be completely hydrolyzed to generate the ben ligand under hydrothermal conditions. The coordination assemblies feature a 1D zigzag chain built up by a low coordination



number of the 6- and 7-fold of  $\text{Ln}^{3+}$  centers. It is interesting that **2<sub>Ln</sub>** can be transformed into the **3<sub>Ln</sub>** structure upon heating at 400 °C. Moreover, the Eu- and Tb-containing complexes have shown red and green luminescence emissions in the solid state at room temperature under UV radiation. They could be used as fluorescent probes for the selective detections of acetone and  $\text{Co}^{2+}$  ions. Concurrently, the Gd (**10<sub>Gd</sub>**, **15<sub>Gd</sub>**) and Dy (**12<sub>Dy</sub>**, **17<sub>Dy</sub>**) based complexes exhibit weak antiferromagnetic interactions between the central  $\text{Ln}^{3+}$  ions.

Furthermore, two novel lanthanide complexes bearing the bzz and ben ligands,  $[\text{Sm}_2(\text{bzz})(\text{ben})_6(\text{H}_2\text{O})_3] \cdot 0.5\text{H}_2\text{O}$  (**22<sub>Sm</sub>**) and  $[\text{Eu}(\text{bbz})(\text{ben})_3]$  (**23<sub>Eu</sub>**), were synthesized through in situ ligand formation under hydrothermal conditions. Complex **22<sub>Sm</sub>** displays a 1D double-chain structure, while complex **23<sub>Eu</sub>** exhibits a 3D channel with a 4-connected ( $6^6$ ) dia topology. High-pressure  $\text{CO}_2$  sorption of **22<sub>Sm</sub>** at 298 K was found to be  $376.7 \text{ cm}^3 \text{ g}^{-1}$  (42.5 wt%) under a pressure of 50 bar. Whereas, **23<sub>Eu</sub>** exhibits red emission in a solid state at room temperature.

**Keywords:** Coordination polymers, lanthanide, hydrazide, photoluminescence, magnetism,  $\text{CO}_2$  adsorption

## ACKNOWLEDGEMENTS

I would first like to express my gratitude to everyone who advised and assisted with this research while at Thammasat University. Your time, opinions, and efforts are greatly appreciated.

To Associate Professor Dr. Kittipong Chainok, my advisor. Thank you for allowing me to work in your lab as well as for your guidance and support. Many years ago, ideas, discussions, and research have been by far one of the greatest learning experiences. I will ever know. I appreciate his clear vision of scientific content in a tremendous manner and for offering several precious opportunities to attend and make presentations at national and international academic conferences. How can I ever thank you enough. Teachers like you are not easy to find. Thank you very much and I value and respect your opinion.

I would like to thank all my co-advisors and the committee's Associate Professor Dr. Supakorn Boonyeun, Assistant Professor Dr. Nanthawat Wannarit, and Assistant Professor Dr. Fillip Kielar at Naresuan University. Thank you again for your very fruitful collaborations, all your assistance, and for sharing your experience with my research. To Dr. Winya Dungkeaw at Mahasarakham University who cheers and says that life is never giving up. They have been a consultant source of information and insight. Many thanks.

I gratefully acknowledge Professor Dr. Mongkol Sukwattanasinitt at Chulalongkorn University, Dr. Laongdao Kangkaew and Dr. Somboon Sahasithiwat at MTEC, Dr. Sakchai Laksee at TINT, Dr. Hikaru Zenno and Professor Dr. Shinya Hayami at Kumamoto University, The Department of Chemistry Faculty of Science and Technology at Thammasat University and Dr. Somchintana Puttamat. Thank you for your support. Spacial thanks to Prof. Dr. Kenneth Haller for provide me with the correct information. I'm glad you noticed.

This research is supported by the Graduate Development Scholarship 2020, National Research Council of Thailand (Contact No. 15/2563), and Science, Technology Engineering, and Mathematics (STEM) for the research and developed part of industrial (SCA-CO-2561-6014-TH).

To my fellow group members in KC'Zoo, alumni and TU-McMa (Songwuit Chanthee, Sujirat Boonlue, Natthakorn Phadungsak, Suwadee Jiajaroen, Kenika Khotchasanthong, Nutchana Ponchan, Siripak Jittirattanakul, Kodchakorn Samakun, Nucharee Chongboriboon, Chanida Puttichaem, Chana Panyanon, Kunlanit Jeanjan, Kanthida Kummooon, Patcharapon Jiaranaiwiwat, Jannarong Ngoensri, Dr.Raul Diaz Torres, Kulwadee Ponanunrirk, Wanassanan Chaisuriya, and Chanikarn Kummuang). Thank you for your advice, patience, and camaraderie. My time spent at TU, whether in the lab or otherwise, would never have been what it was without you each keeping me focused, honest, and smiling. You all have amazing futures to look forward to.

Thank you to my beloved parents (Mongkut Theppitak, Kimhuay Saelor, Tanat Theppitak), and Noikor family (Kornbunya, Anan, Ramin, Anek, Prapaporn, Urassayaporn, Aumnaj, Wandee, and Wannakorn) for all your support, and my best friends (Preeyanut Wongsricha and Bhornlada Pundee) for putting up with my nonsense this whole time. All animals everywhere, thank you for existing. Finally, all the unnamed relationships, thank you for believing in me again. Always remember, someone's effort reflects their interest in you.

Chatphorn Theppitak

## TABLE OF CONTENTS

	Page
ABSTRACT	(1)
ACKNOWLEDGEMENTS	(3)
LIST OF TABLES	(9)
LIST OF FIGURES	(10)
LIST OF ABBREVIATIONS	(16)
CHAPTER 1 INTRODUCTION	1
1.1 General introduction	1
1.2 Research objectives	3
1.3 Scope and limitation	3
1.4 Expected benefits	5
1.5 Research procedure	5
CHAPTER 2 REVIEW OF LITERATURE	7
2.1 Supramolecular chemistry and crystal engineering	7
2.1.1 Supramolecular chemistry	7
2.1.2 Crystal engineering	11
2.2 Polymeric networks	14
2.2.1 Coordination polymers (CPs)	14
2.2.2 Metal-organic frameworks (MOFs)	16
2.3 Basic principles of lanthanide and their applications	19

## TABLE OF CONTENTS (CONT.)

	Page
2.3.1 Electronic structure and spectra term	19
2.3.2 f-f absorption spectra	20
2.3.3 Emission spectra, energy transfer, and antenna effect	21
2.3.4 Photoluminescent sensing properties of LnCPs	25
2.3.5 Magnetic properties of LnCPs	28
2.3.6 Gas adsorption properties of LnCPs	33
2.4 References	35
 CHAPTER 3 MATERIALS AND METHODS	 41
3.1 Materials	41
3.2 Instrumentations	42
3.2.1 Single crystal X-ray diffractometer (SCXRD)	42
3.2.2 Powder X-ray diffractometer (PXRD)	43
3.2.3 Fourier transform infrared spectrometer (FTIR)	43
3.2.4 CHN analyzer (CHN)	43
3.2.5 Thermogravimetric analyzer (TGA)	43
3.2.6 Photoluminescence spectrometer (PL)	43
3.2.7 Superconducting quantum interference device (SQUID)	43
3.2.8 X-Ray fluorescence spectrometer (XRF)	44
3.2.9 Gas adsorption	44
3.3 References	44
 CHAPTER 4 THE COORDINATION POLYMERS OF BENZHYDRAZIDE WITH LANTHANIDE(III) IONS	 45
4.1 Introduction	45
4.2 Experimental section	47

## TABLE OF CONTENTS (CONT.)

	Page
4.2.1 Materials and methods	47
4.2.2 Synthesis of $[\text{Ln}(\text{bzz})(\text{NO}_3)](\text{NO}_3)_2$ ( <b>1<sub>Ln</sub></b> ; <b>Ln</b> = <b>1<sub>Sm</sub></b> , <b>2<sub>Eu</sub></b> , <b>3<sub>Gd</sub></b> , <b>4<sub>Tb</sub></b> , <b>5<sub>Dy</sub></b> )	48
4.2.3 Synthesis of $[\text{Ln}(\text{bzz})(\text{ben})_3(\text{H}_2\text{O})] \cdot \text{H}_2\text{O}$ ( <b>2<sub>Ln</sub></b> ; <b>Ln</b> = <b>6<sub>Pr</sub></b> , <b>7<sub>Nd</sub></b> , <b>8<sub>Sm</sub></b> , <b>9<sub>Eu</sub></b> , <b>10<sub>Gd</sub></b> , <b>11<sub>Tb</sub></b> , <b>12<sub>Dy</sub></b> , <b>13<sub>Er</sub></b> )	49
4.2.4 Synthesis of $[\text{Ln}_3(\text{ben})_3]$ ( <b>3<sub>Ln</sub></b> ; <b>Ln</b> = <b>14<sub>Eu</sub></b> , <b>15<sub>Gd</sub></b> , <b>16<sub>Tb</sub></b> , <b>17<sub>Dy</sub></b> , <b>18<sub>Er</sub></b> , <b>19<sub>Tm</sub></b> , <b>20<sub>Yb</sub></b> , <b>21<sub>Lu</sub></b> )	50
4.2.5 X-ray crystallography	52
4.3 Results and discussion	56
4.3.1 Synthesis	56
4.3.2 Structural description	57
4.3.3 Infrared spectra	68
4.3.4 Powder X-ray diffraction	69
4.3.5 Thermogravimetric analysis	74
4.3.6 Solid-state photoluminescence properties	76
4.3.7 Photoluminescent sensing properties	80
4.3.8 Magnetic properties	90
4.4 Conclusion	91
4.5 References	92
 CHAPTER 5 SELF-ASSEMBLY OF LANTHANIDE COORDINATION POLYMERS VIA IN SITU-GENERATED BENZHYDRAZIDE LIGANDS	 101
5.1 Introduction	101
5.2 Experimental section	102
5.2.1 Materials and methods	102
5.2.2 Synthesis of $[\text{Sm}_2(\text{bzz})(\text{ben})_6(\text{H}_2\text{O})_3] \cdot 0.5\text{H}_2\text{O}$ ( <b>22<sub>Sm</sub></b> )	103

## TABLE OF CONTENTS (CONT.)

	Page
5.2.3 Synthesis of [Eu(bzz)(ben) <sub>3</sub> ] ( <b>23<sub>Eu</sub></b> )	103
5.2.4 X-ray crystallography	103
5.3 Results and discussion	106
5.3.1 Synthesis	106
5.3.2 Structural description	106
5.3.3 Infrared spectra	114
5.3.4 Powder X-ray diffraction	115
5.3.5 Thermogravimetric analysis	117
5.3.6 High pressure CO <sub>2</sub> adsorption	118
5.3.7 Solid-state photoluminescence properties	120
5.4 Conclusion	122
5.5 References	122
 CHAPTER 6 CONCLUSIONS AND RECOMMENDATIONS	 127
 APPENDIX	 129
 BIOGRAPHY	 134

## LIST OF TABLES

Tables	Page
2.1 Summary of supramolecular interactions	11
2.2 The relationship between the quantum numbers of electrons	20
2.3 Selection rules for f-f transitions	21
2.4 The typical emission bands of the lanthanide ions $\text{Eu}^{3+}$ , $\text{Tb}^{3+}$ , $\text{Nd}^{3+}$ , $\text{Er}^{3+}$ , and $\text{Yb}^{3+}$ in solution	22
2.5 A summary of types of magnetic behavior	30
2.6 Some ionic properties and magnetic moment of the lanthanides	31
3.1 The chemicals used in the present study	41
3.2 The organic solvents used in the present study	42
4.1 Crystal data and structural refinements for <b>1<sub>Sm</sub>-5<sub>Dy</sub></b>	53
4.2 Crystal data and structural refinements for <b>6<sub>Pr</sub>-13<sub>Er</sub></b>	54
4.3 Crystal data and structural refinements for <b>14<sub>Eu</sub>-21<sub>Lu</sub></b>	55
4.4 Selected bond lengths (Å) and bond angles (°) for <b>1<sub>Sm</sub>-5<sub>Dy</sub></b>	58
4.5 Selected bond lengths (Å) and bond angles (°) for <b>6<sub>Pr</sub>-13<sub>Er</sub></b>	61
4.6 Selected bond lengths (Å) and bond angles (°) for <b>14<sub>Eu</sub>-21<sub>Lu</sub></b>	66
4.7 Emission bands, luminescent lifetimes ( $\tau$ ), and CIE color coordinates of the Eu- and Tb-based CPs	79
5.1 Crystal data and structure refinement for <b>22<sub>Sm</sub></b> and <b>23<sub>Eu</sub></b>	105
5.2 Selected bond lengths (Å) and bond angles (°) for <b>22<sub>Sm</sub></b>	109
5.3 Hydrogen-bond geometry (Å, °) for <b>22<sub>Sm</sub></b>	110
5.4 Selected bond lengths (Å) and bond angles (°) for <b>23<sub>Eu</sub></b>	113
5.5 C–H $\cdots\pi$ interactions (Å, °) for <b>23<sub>Eu</sub></b>	114



## LIST OF FIGURES

Figures	Page
1.1 The hydrazide-based ligands in lanthanide coordination polymers supported	4
1.2 Schematic representation for the research procedure	6
2.1 From molecular to supramolecular chemistry	7
2.2 Molecular recognition of molecules to give supermolecule and periodic arrangement of supermolecules in a crystal lattice	8
2.3 The inner component $\text{Cl}@Q5\cdot(\text{OH}_2)_2$ of the gyroscale inside Q10	9
2.4 (a) Self-assembly of the circular helicate $[(\text{Fe}_5\text{L}_5)\text{Cl}]^{9+}$ from five tris-bpy ligands and five equivalents of $\text{FeCl}_2$ (b) side view	10
2.5 The unit cells of naphthalene and anthracene estimate the size of a benzene ring is a preferred technique for creating useful organic and metal-organic compounds	12
2.6 The hydrogen-bonded sheets of trimesic acid view along [001]	13
2.7 The hydrogen bonding carboxylate of trimesic acid molecular (top) and coordination polymer (bottom)	14
2.8 Schematic illustrating the formation of coordination polymers from their building blocks	15
2.9 Some simple coordination polymer nets	15
2.10 Thermodynamic and kinetic crystallization of products	16
2.11 The $\text{Zn}_4\text{O}(\text{BDC})_3$ framework (left) and the $\text{N}_2$ adsorption isotherm at 78 K for MOF-5 (right)	18
2.12 The structure of $[\text{Cu}(\text{BTC})_2(\text{H}_2\text{O})_3]_n$ viewed paddle-wheel SBUs	18
2.13 A diagram of electronic energy level for $\text{Ln}^{3+}$	19
2.14 Emission processes of (a) organic or transition-metal compounds (large Stokes' shifts) and (b) lanthanide complexes (small Stokes' shifts)	23

## LIST OF FIGURES (CONT.)

Figures	Page
2.15 The antenna effect for $\text{Ln}^{3+}$ sensitization, illustrated using the chromophore chelate (right) and pendant chromophore (left) ligand designs	23
2.16 Simplified diagram showing the main energy flow paths during energy transfer of lanthanide luminescence via its surrounding (ligands)	25
2.17 Crystal structure of compound Eu (left) and Comparison of the luminescence intensity of compound Eu incorporating different metal ions, activated in 10 mm DMF solutions of $\text{M}(\text{NO}_3)_x$	26
2.18 (a) Coordination environment of Tb-MOF (b) Perspective 3D framework of Tb-MOF along the b axis. (c) Simplified topological graph of Tb-MOF	27
2.19 Luminescent intensity of Tb-MOF in an aqueous solution	27
2.20 Synthesis of $[\text{Ln}_4(\text{L})_4(\mu^2\text{-}\eta^1\eta^1\text{Piv})_4] \cdot x\text{H}_2\text{O} \cdot y\text{CH}_3\text{OH}$	33
2.21 (left) Temperature dependence of the $\chi_{\text{MT}}$ for compounds Gd (1–3). The solid line represents the best fit of the experimental data. (right) 2J coupling scheme for Gd compound	33
2.22 The IUPAC classification of adsorption isotherms	34
2.23 (a) The coordination environment of different lanthanide ions with L. At the extreme right is shown the likely structural character of the frameworks before and after evacuation. (b and c) The adsorption of $\text{CO}_2$ , $\text{C}_2\text{H}_4$ , and $\text{C}_2\text{H}_6$ uptake in La-framework at 273 K	35
4.1 Synthetic routes for $\mathbf{1}_{\text{Ln}}$ , $\mathbf{2}_{\text{Ln}}$ , and $\mathbf{3}_{\text{Ln}}$	56
4.2 (a) Coordination environment of the $\text{Eu}^{3+}$ ion and (b) perspective view of the crystal packing in $\mathbf{2}_{\text{Eu}}$ along the c axis	57
4.3 Partial packing diagram of $\mathbf{2}_{\text{Eu}}$ , showing (a) $\text{N-H}\cdots\text{O}$ hydrogen bonds and (b) $\pi\text{-}\pi$ interactions	59

## LIST OF FIGURES (CONT.)

Figures	Page
4.4 (a) Coordination environment of $\text{Eu}^{3+}$ ion, (b) the 1D chain along the $a$ axis, and (c) perspective view of the packing in $\mathbf{9}_{\text{Eu}}$ along the $c$ axis	62
4.5 Partial packing diagram of $\mathbf{9}_{\text{Eu}}$ , (a) showing $\text{O}-\text{H}\cdots\text{O}$ and $\text{N}-\text{H}\cdots\text{O}$ hydrogen bonds and (b) $\text{C}-\text{H}\cdots\pi$ interactions	62
4.6 (a) Coordination environment of $\text{Eu}^{3+}$ ion, (b) the 1D chain, and (c) perspective view of the packing of $\mathbf{14}_{\text{Eu}}$ along the $a$ axis	64
4.7 Partial packing diagram of $\mathbf{14}_{\text{Eu}}$ , showing (a) $\text{C}-\text{H}\cdots\pi$ and (b) $\pi-\pi$ interactions	65
4.8 IR spectra of each series (a) $\mathbf{1}_{\text{Ln}}$ ( $\mathbf{1}_{\text{Sm}}-\mathbf{5}_{\text{Dy}}$ ), (b) $\mathbf{2}_{\text{Ln}}$ ( $\mathbf{6}_{\text{Pr}}-\mathbf{13}_{\text{Er}}$ ), and (c) $\mathbf{3}_{\text{Ln}}$ ( $\mathbf{14}_{\text{Eu}}-\mathbf{21}_{\text{Lu}}$ )	68
4.9 Comparison of the simulated and experimental PXRD patterns of the as-synthesized complexes $\mathbf{6}_{\text{Pr}}-\mathbf{13}_{\text{Er}}$ (a) and $\mathbf{14}_{\text{Eu}}-\mathbf{21}_{\text{Lu}}$ (b)	70
4.10 Comparison of the experimental PXRD patterns of the representative complexes $\mathbf{9}_{\text{Eu}}$ (series $\mathbf{2}_{\text{Ln}}$ ) and $\mathbf{14}_{\text{Eu}}$ (series $\mathbf{3}_{\text{Ln}}$ ) after exposure to air for ten months with the simulated diffraction patterns based on the single crystal X-ray structure determinations	71
4.11 The PXRD patterns of the representative example $\mathbf{9}_{\text{Eu}}$ and $\mathbf{11}_{\text{Tb}}$ (a, b) and $\mathbf{14}_{\text{Eu}}$ and $\mathbf{16}_{\text{Tb}}$ (c, d) after immersing in various organic solvents for 24 h	72
4.12 (a) TGA curves (left) and PXRD patterns (right) at 400 °C for $\mathbf{9}_{\text{Eu}}$ and $\mathbf{14}_{\text{Eu}}$ . VT-PXRD (30–800 °C) patterns for (b) $\mathbf{9}_{\text{Eu}}$ and (c) $\mathbf{14}_{\text{Eu}}$	75
4.13 IR spectra of $\mathbf{9}_{\text{Eu}}$ at room temperature and 400 °C	76
4.14 (left) Optical microscopy images and (right) irradiated under UV light of complexes $\mathbf{2}_{\text{Eu}}$ , $\mathbf{9}_{\text{Eu}}$ , $\mathbf{14}_{\text{Eu}}$ , $\mathbf{4}_{\text{Tb}}$ , $\mathbf{11}_{\text{Tb}}$ , and $\mathbf{16}_{\text{Tb}}$	77

## LIST OF FIGURES (CONT.)

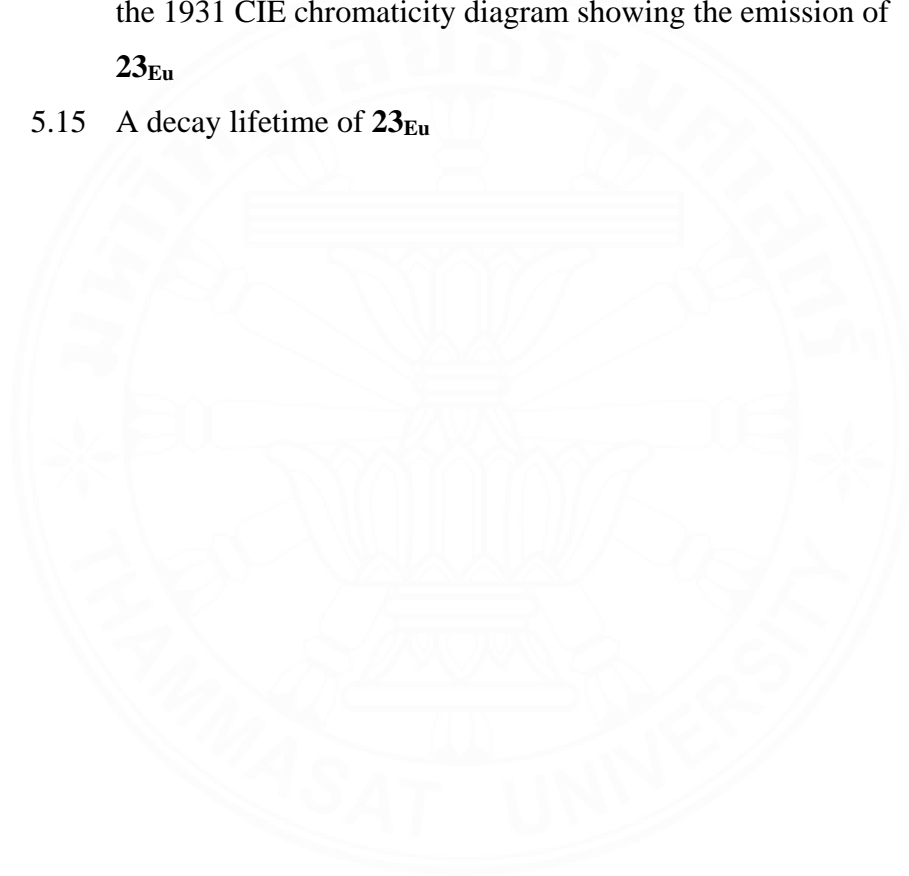
Figures	Page
4.15 The solid-state PL emission spectra of the free ligands (a) bzz and (b) ben when excited at 290 nm	78
4.16 Emission spectra and colorimetric coordinates (insert) of (a) <b>2<sub>Eu</sub></b> , (b) <b>4<sub>Tb</sub></b> , (c) <b>9<sub>Eu</sub></b> , (d) <b>11<sub>Tb</sub></b> , (e) <b>14<sub>Eu</sub></b> , and (f) <b>16<sub>Tb</sub></b>	78
4.17 Luminescence decay ( $\tau$ ) curves for <b>2<sub>Eu</sub></b> , <b>9<sub>Eu</sub></b> , <b>14<sub>Eu</sub></b> , <b>4<sub>Tb</sub></b> , <b>11<sub>Tb</sub></b> , and <b>16<sub>Tb</sub></b>	79
4.18 Emission intensities in different organic solvents for (a) <b>9<sub>Eu</sub></b> , (b) <b>11<sub>Tb</sub></b> , (c) <b>14<sub>Eu</sub></b> , and (d) <b>16<sub>Tb</sub></b>	80
4.19 UV-Vis spectra of acetone and excitation spectra of <b>2<sub>Eu</sub></b> , <b>4<sub>Tb</sub></b> , <b>9<sub>Eu</sub></b> , <b>11<sub>Tb</sub></b> , <b>14<sub>Eu</sub></b> , and <b>16<sub>Tb</sub></b>	81
4.20 PXRD patterns of <b>9<sub>Eu</sub></b> , <b>11<sub>Tb</sub></b> , <b>14<sub>Eu</sub></b> , and <b>16<sub>Tb</sub></b> : simulated and after sensing of acetone	81
4.21 Emission intensities for (a) <b>9<sub>Eu</sub></b> , (b) <b>11<sub>Tb</sub></b> , (c) <b>14<sub>Eu</sub></b> , and (d) <b>16<sub>Tb</sub></b> in MeCN solutions of different metal ions	82
4.22 Relative luminescence intensities of (a) <b>9<sub>Eu</sub></b> , (b) <b>11<sub>Tb</sub></b> , (c) <b>14<sub>Eu</sub></b> , and (d) <b>16<sub>Tb</sub></b> dispersed in the solutions of individual metal ions and the quenched luminescence intensities after the addition of solutions of $\text{Co}^{2+}$ in acetonitrile	83
4.23 Plots of $I_0/I$ versus the concentration of $\text{Co}^{2+}$ ions plotted according to the Stern–Volmer equation as well as the linear fitting results for (a) <b>9<sub>Eu</sub></b> , (b) <b>11<sub>Tb</sub></b> , (c) <b>14<sub>Eu</sub></b> , and (d) <b>16<sub>Tb</sub></b>	84
4.24 PXRD patterns of <b>9<sub>Eu</sub></b> , <b>11<sub>Tb</sub></b> , <b>14<sub>Eu</sub></b> , and <b>16<sub>Tb</sub></b> : simulated and after sensing of $\text{Co}^{2+}$ ions	85
4.25 (a) UV-Vis absorption spectra for metal ions in acetonitrile solutions. (b) UV-Vis spectra of $\text{Co}^{2+}$ and excitation spectra of <b>2<sub>Eu</sub></b> , <b>4<sub>Tb</sub></b> , <b>9<sub>Eu</sub></b> , <b>11<sub>Tb</sub></b> , <b>14<sub>Eu</sub></b> , and <b>16<sub>Tb</sub></b> . (c) UV-Vis spectra of $\text{Mn}^{2+}$ and $\text{Ni}^{2+}$ and excitation spectra of <b>2<sub>Eu</sub></b> , <b>4<sub>Tb</sub></b> , <b>9<sub>Eu</sub></b> , <b>11<sub>Tb</sub></b> , <b>14<sub>Eu</sub></b> , and <b>16<sub>Tb</sub></b>	86

## LIST OF FIGURES (CONT.)

Figures	Page
4.26 Emission intensities of the representative complexes (a) <b>9<sub>Eu</sub></b> and (b) <b>11<sub>Tb</sub></b> in acetonitrile solutions containing potassium salts at the concentration of $5.0 \times 10^{-4}$ M	87
4.27 The quenching and recyclability test of (a) <b>9<sub>Eu</sub></b> , (b) <b>11<sub>Tb</sub></b> , (c) <b>14<sub>Eu</sub></b> , and (d) <b>16<sub>Tb</sub></b> , the upper dots represent the initial luminescence intensity and the lower dots represent the intensity upon addition of $5 \times 10^{-4}$ M of the acetonitrile solution of $\text{Co}^{2+}$	88
4.28 PXRD patterns of (a) <b>9<sub>Eu</sub></b> , (b) <b>11<sub>Tb</sub></b> , (c) <b>14<sub>Eu</sub></b> , and (d) <b>16<sub>Tb</sub></b> , before and after three cycles of sensing tests	89
4.29 XRF spectra of (a) <b>9<sub>Eu</sub></b> , (b) <b>11<sub>Tb</sub></b> , (c) <b>14<sub>Eu</sub></b> , and (d) <b>16<sub>Tb</sub></b> after sensing tests	90
4.30 Plots of $\chi_{\text{MT}}$ as a function of temperature for the <b>10<sub>Gd</sub></b> , <b>15<sub>Gd</sub></b> and <b>12<sub>Dy</sub></b> , <b>17<sub>Dy</sub></b> containing complexes under a 5000 Oe field	91
5.1 Synthetic routes for compounds <b>22<sub>Sm</sub></b> and <b>23<sub>Eu</sub></b>	104
5.2 (a) Coordination environment of the $\text{Sm}^{3+}$ ion in <b>22<sub>Sm</sub></b> . (b) 1D chain of <b>22<sub>Sm</sub></b> . (c) 3D packing of <b>22<sub>Sm</sub></b> and yellow colored space is the void space	107
5.3 Coordination environment of <b>23<sub>Eu</sub></b>	111
5.4 Views of (a) SBU of $[\text{Eu}_2(\text{ben})_6]$ (b) the packing of SBUs (c) the simplified 4-connected node of the SBUs and 2-connected of the ligand, and (d) the 4-connected ( $6^6$ ) dia of <b>23<sub>Eu</sub></b>	112
5.5 C–H $\cdots\pi$ interactions for compound <b>23<sub>Eu</sub></b>	114
5.6 FTIR spectra for compounds <b>22<sub>Sm</sub></b> and <b>23<sub>Eu</sub></b>	115
5.7 PXRD pattern for compounds <b>22<sub>Sm</sub></b> and <b>23<sub>Eu</sub></b>	116
5.8 Variable temperature PXRD patterns of <b>23<sub>Eu</sub></b>	117
5.9 TGA curves for compounds <b>22<sub>Sm</sub></b> and <b>23<sub>Eu</sub></b>	118
5.10 Single crystal of <b>22<sub>Sm</sub></b> , (left) as-synthesized (right) after measuring $\text{CO}_2$ adsorption	119

**LIST OF FIGURES (CONT.)**

Figures	Page
5.11 The high pressure CO <sub>2</sub> adsorption for <b>22<sub>Sm</sub></b>	119
5.12 PXRD pattern before and after the CO <sub>2</sub> adsorption for <b>22<sub>Sm</sub></b>	120
5.13 Solid state excitation of <b>23<sub>Eu</sub></b> at $\lambda_{em} = 615$ nm	121
5.14 Solid state emission spectrum of <b>23<sub>Eu</sub></b> at $\lambda_{ex} = 297$ nm. Insert: the 1931 CIE chromaticity diagram showing the emission of <b>23<sub>Eu</sub></b>	121
5.15 A decay lifetime of <b>23<sub>Eu</sub></b>	122



## LIST OF ABBREVIATIONS

Symbols/Abbreviations	Terms
Abs	absorbance
A	acceptor atom
Å	angstrom
$C_g$	aromatic centroid
BDC	1,4-benzenedicarboxylate
BTC	1,3,5-benzenetricarboxylate
ben	benzoate
bzz	benzohydrazide
Calc.	calculated
CSD	Cambridge Structural Database
CO <sub>2</sub>	carbon dioxide gas
Oe	Centimeter-gram-second electromagnetic unit of magnetic intensity
$R_1$	conventional crystallographic discrepancy index
C	Curie constant
°	degree in bond angle
°C	degree Celsius
$d$	distance
D	donor atom
$\mu_{\text{eff}}$	effective magnetic moment
ET	energy transfer
$\rho$	electron density
Exc	excitation
Ems	emission
FTIR	Fourier transform infrared spectrometer

**Symbols/Abbreviations****Terms**

GOF	good of fitness
HP	high pressure
CIE	International Commission on Illumination
IUPAC	International union of pure and applied chemistry
ISC	intersystem crossing
K	kelvin
kJ	kilojoules
Ln	lanthanide
LOD	limit of detection
$\tau$	luminescence decay
$I_0, I$	luminescence intensities of sample
SHELXL	least squares structure refinement program
SHELXT	least squares structure solution program
M	magnetization
$\chi_m$	magnetic susceptibility
H	magnetizing field
B	magnetic flux density
MOFs	metal-organic frameworks
m	medium
NIR	near-infrared
Z	number of formula units in the unit cell
1D	one-dimensional
$\mu$	permeability
PL	photoluminescence
PCPs	porous coordination polymers
PXRD	powder X-ray diffraction



**Symbols/Abbreviations****Terms**

$\phi$	quantum yield
$K_{sv}$	quenching constant
S	singlet
SCXRD	single crystal X-ray diffraction
k	slope
$\sigma$	standard error
s	strong
SQUID	superconducting quantum interference device
2D	two-dimensional
3D	three-dimensional
TGA	thermogravimetric analysis
T	triplet
T	temperature
$a, b, c$	unit cell dimensions
$\alpha, \beta, \gamma$	unit cell angles
$\text{cm}^{-1}$	unit per centimeter
VT-PXRD	Variable-temperature powder X-ray diffraction
$\nu$	wave number
$\theta$	Weiss constant
$wR_2$	weighted crystallographic discrepancy index
XRF	X-ray fluorescence spectrometry

## CHAPTER 1

### INTRODUCTION

#### 1.1 General introduction

One of the modern goals of chemistry is the design and construct of new compounds with expected structural topology and desired properties. Crystal engineering is the classical approach for design and construction of solid crystals which provide the current capabilities and essential properties. In the past decade, this principle was widely applied in the fields of coordination chemistry and supramolecular chemistry for the synthetic design of the structure of new functional materials, organized through the self-assembly process in the solid-state. Crystalline porous coordination polymers (PCPs) or metal-organic frameworks (MOFs) are a new class of porous materials, and have been intensively studied of the structure-property relationship in scientific and technological research over the past three decades. This is due to the fact that they have potential applications in the fields of gas storage and separation, catalysis, magnetism, luminescence, chemical sensing, proton-conducting, biomedical imaging, and drug delivery. Traditional porous materials such as activated carbon, activated alumina, and silica gels are all amorphous, and have limitations of pore size, pore size distribution, and surface area. MOF materials are constructed by coordination bonds through self-assembly between inorganic metal units and organic linkers to form crystalline porous hybrids, in which the pore sizes and shapes can be tuned by the adjustment of the geometry, length, ratio, and functional group of the organic linkers. Owing to their high surface area, wide opportunities for functionalization and tunable pore sizes/shapes, MOFs are preferable compared with those traditional porous materials.

In recent years, much effort has been contributed to the development of porous lanthanide based MOFs (Ln-MOFs) by incorporating  $\text{Ln}^{3+}$  metal ions and organic linkers into a framework. High coordination number ( $\text{CN} = 6\text{-}13$ ) and more flexible coordination environment of  $\text{Ln}^{3+}$  ions compared with transition metal ions can lead to the formation of condensed microporous frameworks with permanent porosity.

This result offers a distinct advantage in gas and small molecule capture/separation applications. Moreover, one of the most significant features of  $\text{Ln}^{3+}$  ions is their photoluminescence properties (high color purity, high quantum yields, narrow bandwidths, relatively long lifetimes, and large Stokes' shifts), arising from triplet excited states of f-f transitions. As is well-known,  $\text{Ln}^{3+}$  ions have a high affinity in relatively hard oxygen-containing linkers over other functional groups. On the other hand, organic linkers can strongly influence light absorption by transferring energy to  $\text{Ln}^{3+}$  ions to enhance their fluorescence intensity. Hence, the utilization of suitable organic antenna chromophores is one of the efficient methods to construct and to develop new functional luminescent Ln-MOFs for chemical sensing, displaying, and optical devices. The electron-rich  $\pi$  system of an aromatic dicarboxylic acid, for instance, terephthalic acid, is known to provide an efficient energy transfer to support strong  $\text{Ln}^{3+}$  centered luminescent emission (*via* the antenna effect). Also, small rigid planar species with versatile coordination oxygen donor sites such as oxalate anions are a very important class of organic linkers for the construction of multidimensional Ln-MOFs with short intermetallic distances, aiding the energy transfer process between chromophore antenna ligands and  $\text{Ln}^{3+}$  ions. Lastly, isostructural Ln-MOFs have been used for their emissive color tuning and white-light emission properties, which have potential applications as the phosphor coating in white-light-emitting diodes. Generally, color-tunable and white-light emissions can be achieved through changing the relative amount of different light emitters, encapsulation of organic fluorescent dyes with different contents within the pores of Ln-MOFs, or co-doping of various concentrations of multiple  $\text{Ln}^{3+}$  ions into isostructural frameworks. The study of Ln-MOFs is still a burgeoning field. New intriguing varieties of topologies with permanent porosities and excellent photoluminescence sensing materials, showing a fast and highly selective response to molecules or ions, are expected to be developed. These materials will eventually be implemented in practical industrial applications in gas storage/separation and chemical sensors in the near future.

This research is interested in the use of principles of crystal engineering and supramolecular chemistry to construct new coordination polymers to promote the investigation of the structure-property relationship. In continuation of this theme, the focus is on the use of a simple system of  $\text{Ln}^{3+}$  ions and the hydrazide-based ligands,

Figure 1.1, using hydro/solvothermal conditions to explore the formation of new Ln-MOFs from the *in-situ* synthesis of new bifunctional ligands. Analysis of the effect of hydrogen bonds and other supramolecular interactions for extending architecture dimensionality, and photoluminescence or adsorption properties. This research involves aspects of crystal growth, chemical crystallography, adsorption, and photoluminescence. The proposed aims of the present research are very important because this could allow the discovery of a new class of polymeric materials with desirable adsorption and luminescence properties.

## 1.2 Research objectives

1) To construct novel lanthanide based coordination polymers (LnCPs) and metal-organic frameworks (Ln-MOFs) by using the *in-situ* transformation of hydrazide ligands into new ligands through hydro/solvothermal methods.

2) To study their synthesis-structure-property relationships and applications including the structural and topological effects of (i) luminescence sensor for metal ions and small organic molecules, (ii) CO<sub>2</sub> gas adsorption, and (iii) magnetic properties.

3) To study the effect of hydrogen bonds and other supramolecular interactions for extending architectural dimensionality and photoluminescence or adsorption properties.

## 1.3 Scope and limitation

The intention of the present work is the development of new areas of modern structural chemistry, namely, the design and synthesis of new crystalline LnCPs and LnMOFs with desirable gas adsorptions, magnetism, and luminescence properties. The lanthanides used for the preparation of the present complexes are cerium (Ce), praseodymium (Pr), neodymium (Nd), promethium (Pm), samarium (Sm), europium (Eu), gadolinium (Gd), terbium (Tb), dysprosium (Dy), erbium (Er), thulium (Tm), ytterbium (Yb) and lutetium (Lu). The solid-state structures of lanthanide complexes are mainly determined by single-crystal X-ray diffraction (SC-XRD).

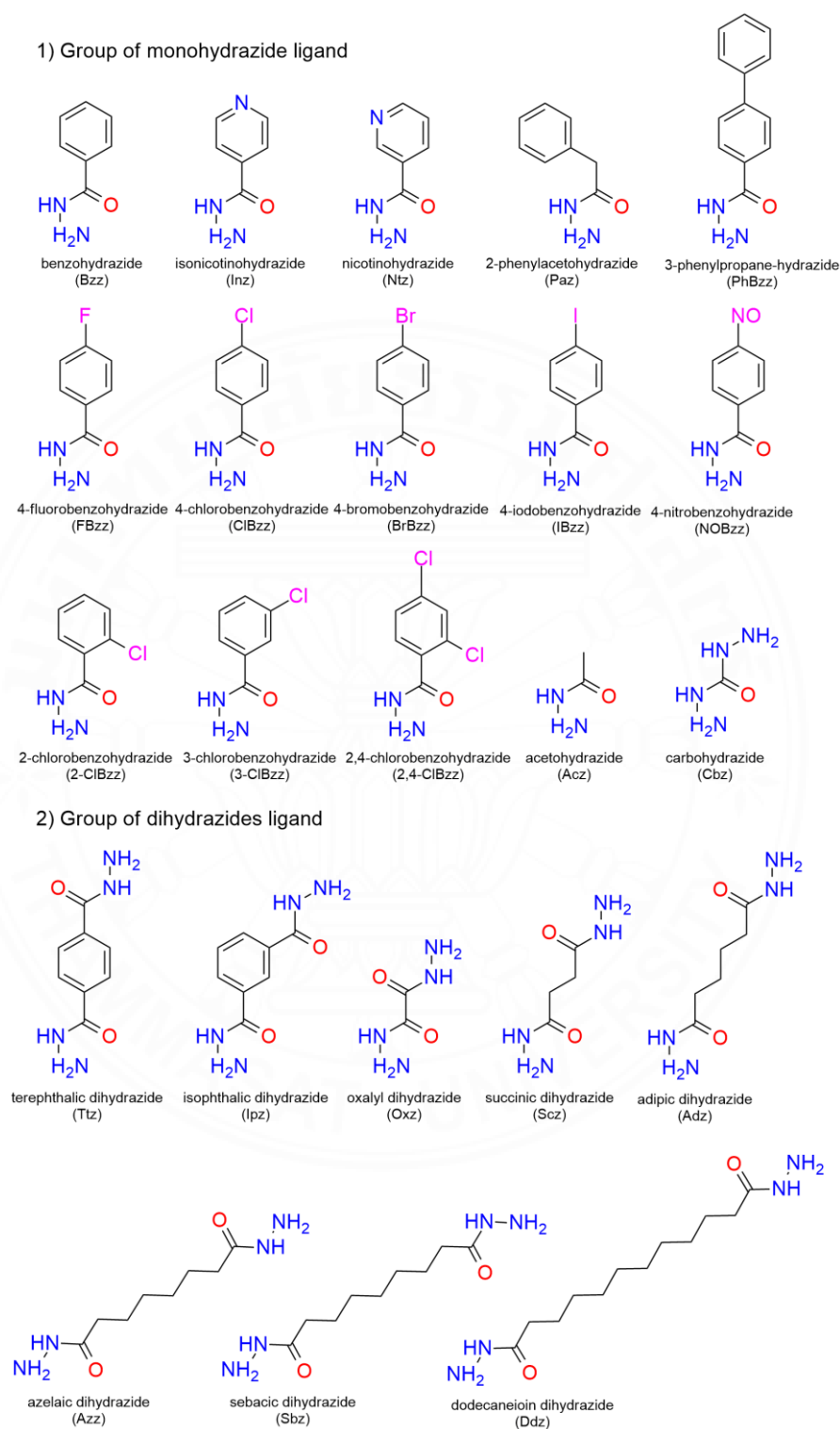


Figure 1.1 The hydrazide-based ligands in lanthanide coordination polymers supported.

#### 1.4 Expected benefits

1) Develop a new class of lanthanide metal-organic frameworks (Ln-MOFs) with hydrazide ligand from the solid-state that exhibit unique and significant properties.

2) These materials have certain an impact and a bright future for practical applications in chemical and gas sensors.

#### 1.5 Research procedure

Schematic representation for the research procedure as well as the sample's determination of the present research is depicted in Figure 1.2.

1) Search the crystallography literature to avoid repeating previous work and obtaining supporting knowledge for the rational design of new lanthanide coordination polymers with hydrazide based ligands.

2) Single crystal growth of lanthanide metals containing hydrazide ligands by using hydro/solvothermal methods.

3) Preliminary examination of samples with an optical microscope (OM). If the solid product of lanthanide coordination polymers is homogeneous go to the next step. If the solid product is heterogeneous it can often be separated by selecting using color, size, or shape of crystalline products, or by utilizing varying solubility of individual components.

4) Characterize the organic components by C H N elemental analysis; inorganic components by energy dispersive X-ray spectroscopy (EDX); functional groups by FTIR.

5) Determine structure by single-crystal X-ray crystallographic methods. Further exploration supramolecular interactions such as hydrogen bonding, dipole-dipole interactions,  $\pi$ - $\pi$  stacking, and so on.

6) Perform a phase purity analysis of the bulk materials using the X-ray powder diffraction technique (PXRD) and comparison of simulated XRD pattern from SC-XRD with the experimental pattern from PXRD.

7) Determine the function or properties of new lanthanide coordination polymer complexes (*i.e.*, thermal stability, luminescence, adsorption).

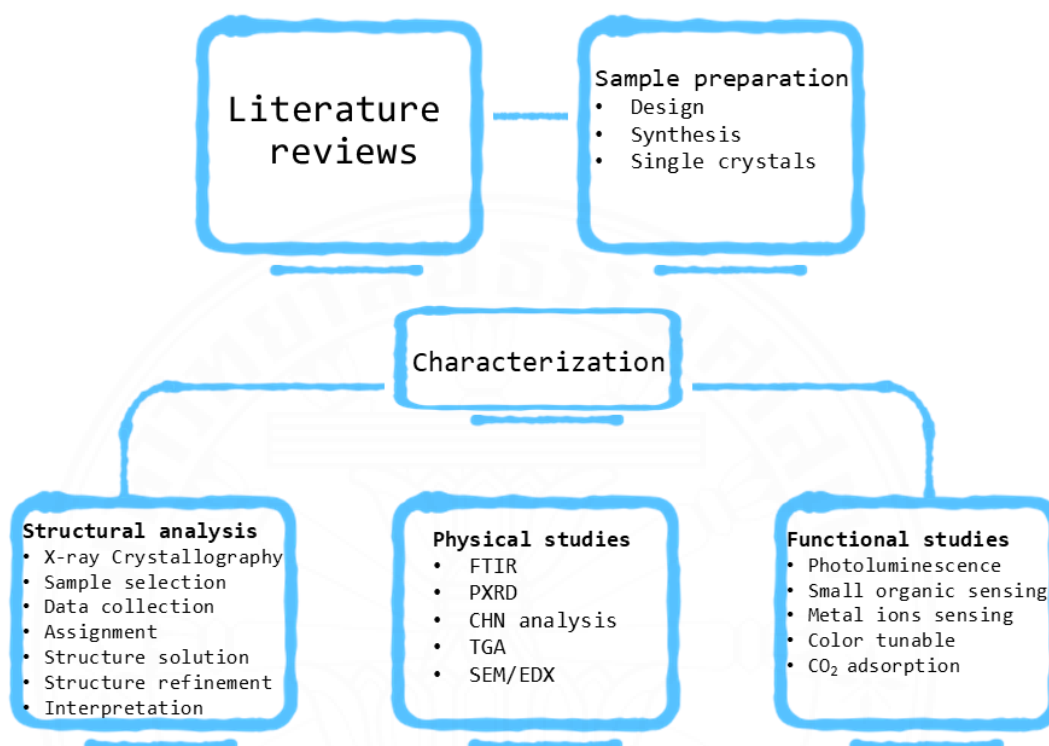


Figure 1.2 Schematic representation of the research procedure.

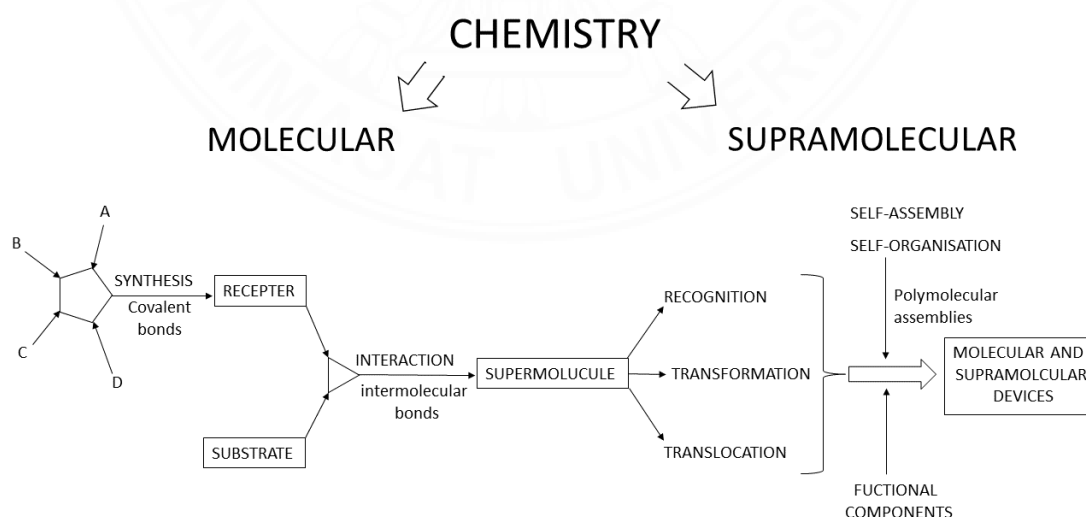
## CHAPTER 2

### REVIEW OF LITERATURE

#### 2.1 Supramolecular chemistry and crystal engineering

##### 2.1.1 Supramolecular chemistry

Supramolecular chemistry is “*Chemistry beyond the molecule*” or “*the chemistry of the noncovalent bond*” as defined by Lehn in 1978 from Latin *supra* “above, beyond”. In the same manner, traditional chemistry utilizes covalent bonds to construct an infinite number of molecules from a limited number of elements, whereas supramolecular chemistry uses non-covalent interactions to create various oligomeric and polymeric molecular ensembles. The development and generalization of supramolecular chemistry were defined as words, “*Just as there is a field of molecular chemistry based on the covalent bond, there is a field of supramolecular chemistry, the chemistry of molecular assemblies and the intermolecular bond*”, as well as in graphical representation aesthetic in Figure 2.1. (Lehn, 1995; Soldatov & Terekhova, 2005). At the end, supramolecular chemistry focuses on the development of functional complex architectures through non-covalent interactions.

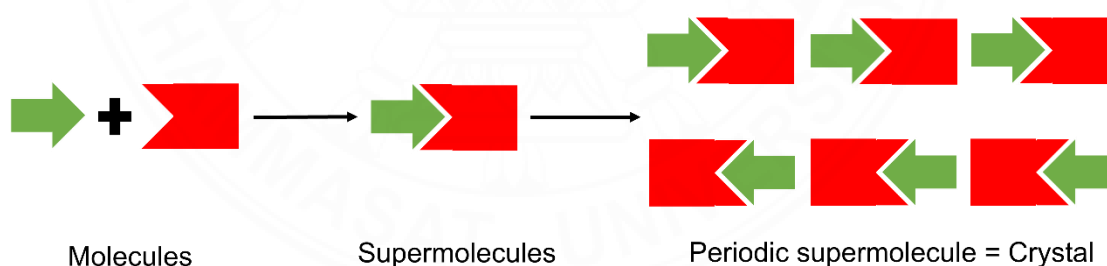


*Figure 2.1* From molecular to supramolecular chemistry: molecules, supermolecules, molecular, and molecular devices. Redrawn from ref. Lehn, 1995.



Although the fundamental recognition processes of regulate supramolecular aggregation are governed by the same principles and forces. Supramolecular chemistry can be split into two parts covering the areas: molecular recognition and self-assembly in solid-state crystal engineering.

**Molecular recognition (host-guest chemistry)** studies specific interactions between two or more molecules. The concept of molecular recognition and interactions via non-covalent bonding is encompassed by host-guest chemistry. Molecular recognition is the precise binding of a guest molecule to a complementary host molecule, resulting in the formation of a host-guest complex known as key and lock as depicted in Figure 2.2. This is important for molecular biology (Steed *et al.*, 2022). Besides, an example of host-guest complex is illustrated using the cucurbit<sub>[n]</sub>urils in Figure 2.3, where a smaller macrocycle, Q5, is located inside a larger macrocycle, Q10, with facile rotation of one relative to the other in solution (Day *et al.*, 2002). Another example is provided by Freeman describing a cyclic hexameric dimethanoglycoluril with potential catalytic activity (Freeman, 1984). The crystal structure contains the p-xylylenediammonium ion as a guest inside the cucurbituril cage by host-guest interactions.



*Figure 2.2* Molecular recognition of molecules to give supermolecule and periodic arrangement of supermolecules in a crystal lattice. Note the complementary shape and bonding feature of interacting molecules. Redrawn from ref. Nangia, 2010.

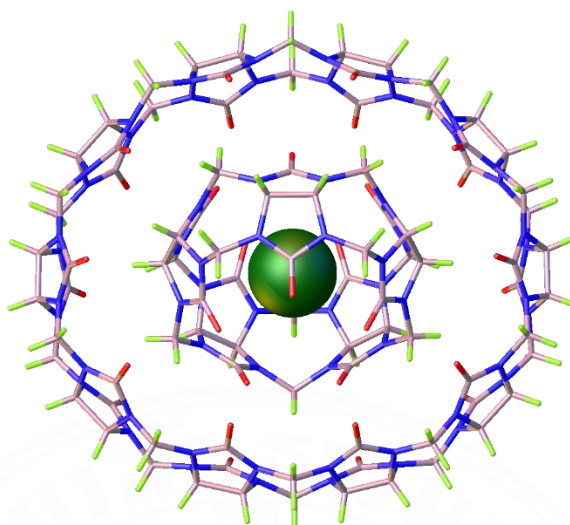
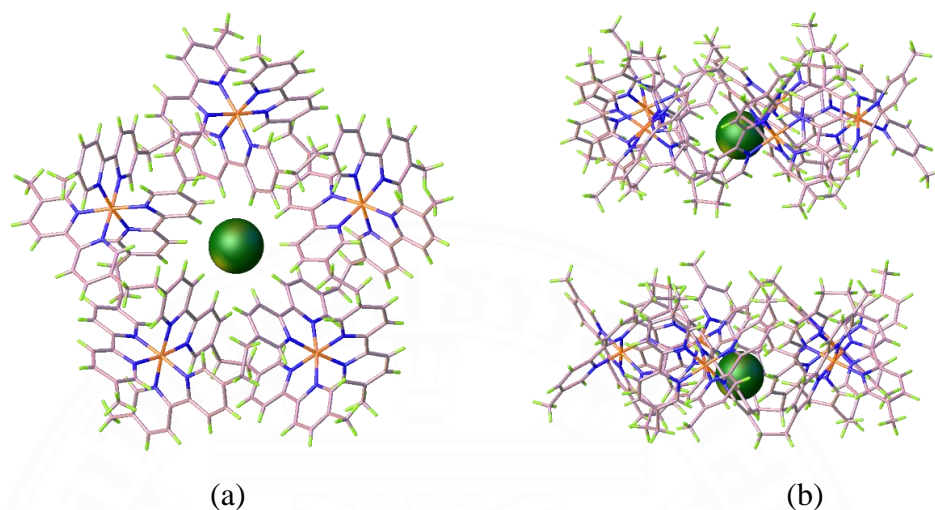


Figure 2.3 The inner component Cl@Q5·(OH<sub>2</sub>)<sub>2</sub> of the gyroscane inside Q10 (Day *et al.*, 2002).

**Self-assembly** in the molecules is constructed without external guidance or management. Non-covalent interactions are used to direct the molecule's assembly. Self-assembly is classified into two types: intramolecular and intermolecular. Intermolecular self-assembly is widely referred to as molecular self-assembly, whereas intramolecular self-assembly is more generally referred to as folding. Molecular self-assembly also allows for the creation of larger structures such as micelles, membranes, vesicles, and liquid crystals. Molecular self-assembly organized in the solid state is known as crystal engineering (Ariga *et al.*, 2008). For example, the coordination polymer of iron(II) chloride and tris-bpy ligand forms spontaneously and quantitatively a circular double helicate by self-assembly as Figure 2.4 viz a double helicate closed into a ring (Hasenknopf *et al.*, 1996). In addition, the series of rigid-rack inorganic complexes with Cu(I) ion were synthesized and characterized. There is a construction strategy for applying a new class of rigid-rack multimetallic complexes by self-assembly (Sleiman *et al.*, 1997) and creating supramolecular complexes with ordered arrays of metal ions, such as helicates (Lehn *et al.*, 1988), racks (Hanan *et al.*, 1995), ladders (Peedikakkal *et al.*, 2010), cages (Baxter *et al.*, 1993), and grid-type complexes (Baxter *et al.*, 1994). Recently, Vittal *et al.* synthesized nickel metallamacrocyclic

complex,  $[\text{Ni}_{15}(\text{EVan})_{10}(\text{H}_2\text{O})_{20}]$ . The complex has a Ni-O-Ni-O-Ni-O configuration and is composed of five discrete trinuclear units (Thio *et al.*, 2014).



*Figure 2.4* (a) Self-assembly of the circular helicate  $[(\text{Fe}_5\text{L}_5)\text{Cl}^{9+}]$  from five tris-bpy ligands and five equivalents of  $\text{FeCl}_2$  (b) side view.

Currently, supramolecular chemistry and self-assembly processes are major, interdisciplinary branches of science dealing with chemical, physical, biological, and technological sciences in the development of new materials.

**Supramolecular interaction (non-covalent interaction)** These forces mediate interactions between molecules. Through various molecular interactions, a molecule recognizes its partner. Individual non-covalent interactions are weak, but many of them produce stable structures with self-healing capabilities. Supramolecular interactions include hydrogen bonding, hydrophobic forces, van der Waals forces, pi-pi interactions, and electrostatic effects. The supramolecular interactions are summarized in Table 2.1.

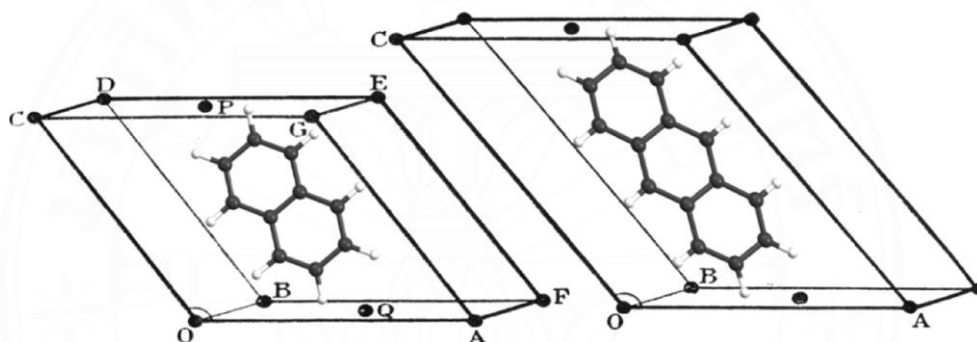
**Table 2.1***Summary of supramolecular interactions*

Interaction	Strength (kJ/mol)	Example
Ion-ion	200-300	Tetrabutylammonium chloride
Ion-dipole	50-200	Sodium crown-5
Dipole-dipole	5-50	Acetone
Hydrogen bonding	4-120	(See Table 2.2)
Cation- $\pi$	5-80	K <sup>+</sup> in benzene
$\pi$ - $\pi$	0-50	Benzene and graphite
Van der Waals	<5 kJ/mol but depending on surface area	Argon: packing in molecular crystals
Hydrophobic	Related to solvent-solvent interaction energy	Cyclodextrin inclusion compounds

### 2.1.2 Crystal engineering

Crystal engineering is an area in the field of supramolecular chemistry that aim to comprehend intermolecular interactions in the context of crystal packing and to apply this knowledge in the design and synthesis of new solid-state functional structures with desired physical and chemical properties (Desiraju & Parshall, 1989). Over the past six decades, crystal engineering has developed as a natural result of crystallography and chemical engineering into a major activity within structural chemistry (Desiraju, 2013). If chemistry works with molecules, crystallography would work with crystals. Thus, the engagement between chemistry and crystallography is the interaction as well as the structure and properties of molecules on the one hand and those of extended assemblies of molecules on the other. Crystal engineering depends on intermolecular interactions to obtain the solid-state organization of molecules and ions. At the heart of crystal engineering is molecular self-assembly, which typically involves an interaction between complementary hydrogen bonding faces or a metal and a ligand. These can be understood using key concepts like supramolecular synthon and secondary building unit.

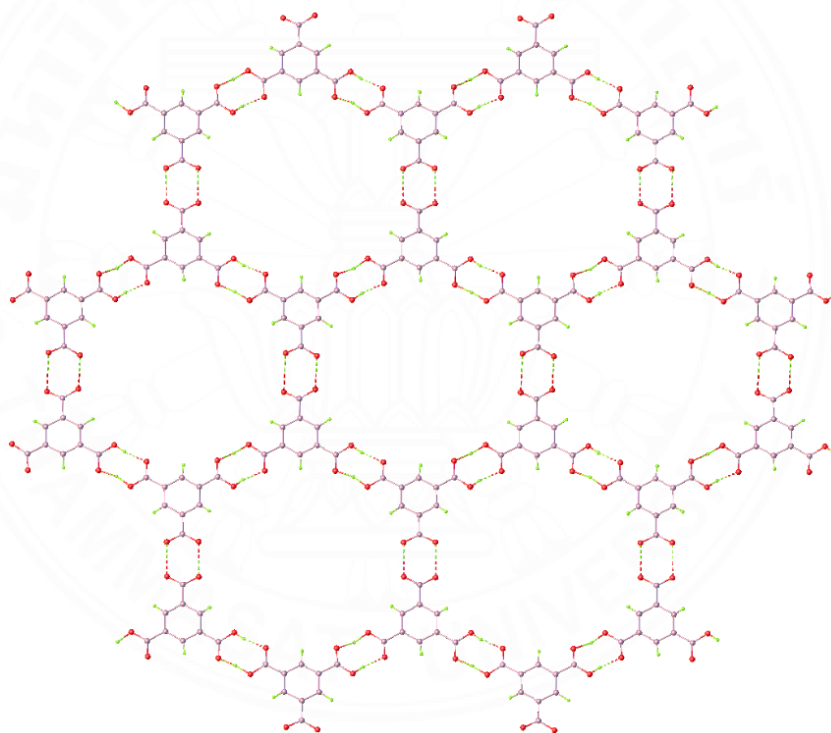
In 1921, W. H. Bragg found the first inter-relationship between molecules and crystals that contain a benzene ring and possess a fixed size and shape. The structure can be transferred from one crystal structure to another with little change as Figure 2.5 (Bragg, 1921). The author tried to compare the unit cell parameters of naphthalene and anthracene and found that they were related. J. D. Bernal (a former student of Bragg's) was able to correct formulas for steroids and bile acids, whilst also studying the unit cell parameters of several aromatic hydrocarbons related to phenanthrene decades ago (Bernal, 1935). This is a good example of using a crystal to study a molecular structure.



*Figure 2.5* The unit cells of naphthalene and anthracene estimate the size of a benzene ring is a preferred technique for creating useful organic and metal-organic compounds. Reproduced from ref. Desiraju, 2013.

Crystal engineering or crystal synthesis is summarized in the question “*Given the molecular structure of a compound, what is its crystal structure?*”. J. M. Robertson (a former student of Bragg's) first attempted to respond to this question in the specific situation of a limited group of polynuclear aromatic hydrocarbon compounds. Because of their effort in designing a crystal structure using molecules as building blocks and success in obtaining crystal properties from a molecular crystal that demonstrates how crystal structure differs from molecular structure (Robertson, 1945). In 1955, R. Pepinsky used the term crystal engineering for the first literature in a meeting abstract of the American Physical Society. G. M. J. Schmidt (a student of Dorothy Crowfoot Hodgkin, herself a student of Bernal) studies the solid-state

reactivity of a majority of photodimerizable compounds, especially the crystal structures of trans-cinnamic acids using the topochemical principle. In the past decade, the topic of developing crystal engineering was discussed. There are several terms such as polymorph, pseudo polymorph, cocrystal, coordination polymer, metal–organic framework, hydrogen bond, and halogen bond. Although the scientist utilizes terms that are both broadly applicable and scientifically accurate, these two characteristics occasionally clash. For instance, Desiraju and a co-worker reported the molecule of trimesic acid (benzene-1,3,5-tricarboxylic acid) tends to form hexagonal sheets. The molecules are connected by classical hydrogen bonds, as shown in Figure 2.6.



*Figure 2.6* The hydrogen-bonded sheets of trimesic acid viewed along [001]; C: grey, H: green, O: red from ref. Desiraju, G. R., & Parshall, G. W., 1989.

Intermolecular interaction is straightforwardly packed arrangements, such as the hydrogen bonding carboxylate motif, which is considered in supramolecular synthons. The coordination bond is referred to as a *synthon* in coordination polymers.

The building blocks of molecular structures are known as *tectons* which are metal ions and ligands in coordination polymers in Figure 2.7.

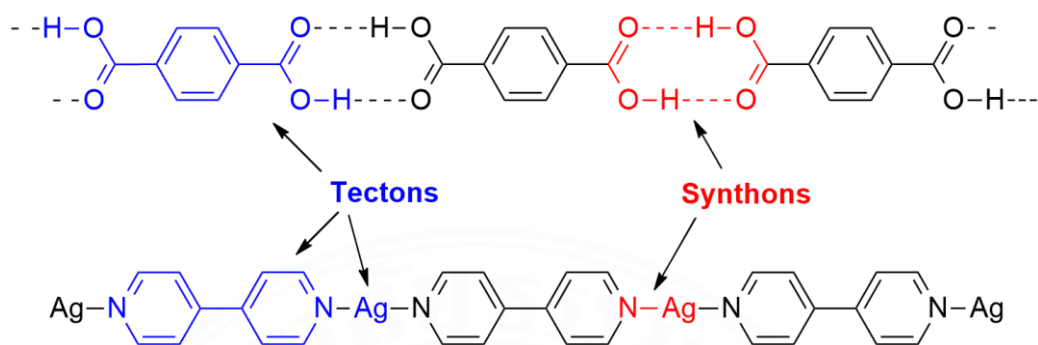


Figure 2.7 The hydrogen bonding carboxylate of trimesic acid molecular (top) and coordination polymer (bottom): tectons and synthons. Redrawn from ref. Batten *et al*, 2008.

## 2.2 Polymeric networks

### 2.2.1 Coordination polymers (CPs)

A coordination polymer definition is “A coordination compound with repeating coordination entities extending in 1, 2, or 3 dimensions”. Coordination polymers have metal ions (or metal clusters) and organic ligands for which metal ions are nodes and organic ligands as the linkers, as a subset of crystal engineering and a direction of structure are linked by coordination bonds into an infinite array as illustrated in Figure 2.8. In case a 3D structure was explained in the sense of the topology that is important for understanding the 3D network structure. In addition, topology has described the design of a novel coordination polymer. Many types of nets have been typical and simple nets such as zigzag or helical, ladder, railway chains for 1D nets, square or rectangular, honeycomb and brick-wall structures for 2D nets, diamondoid, and cubic for 3D nets, as illustrated in Figure 2.9 (Batten *et al*, 2008).

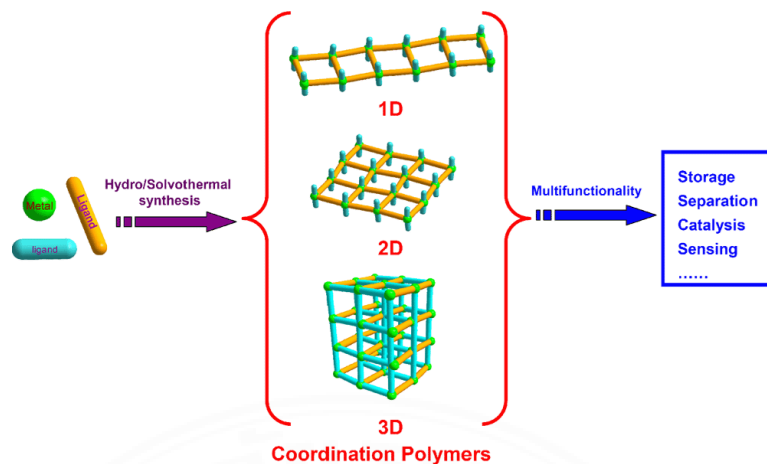


Figure 2.8 Schematic illustrating the formation of coordination polymers from their building blocks. Reproduced from ref. Zhao *et al*, 2010.

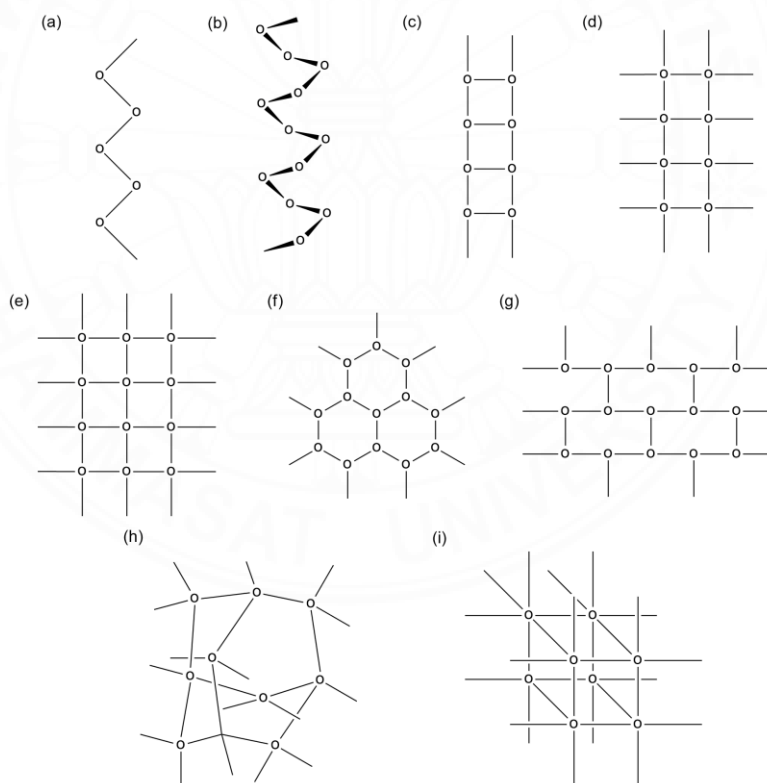


Figure 2.9 Some simple coordination polymer nets. (a) A zigzag chain, (b) a helical chain, (c) a ladder chain, (d) a railway chain, (e) a square net, (f) a honeycomb net, (g) a brick-wall net, (h) diamondoid net, and (i) a cubic net. Redrawn from ref. Chen, 2011 and Batten, 2008.



The reaction parameters can be very significant in the creation of a coordination net such as molar ratio, the reaction/crystallization temperature, pH, solvent, counterions, and time. Consequently, molecular design is difficult to predict as the result of a self-assembly system based on the choice of metal ions, metal clusters, and ligand structure. The different structural diversity is perhaps favored either kinetically or thermodynamically. The free energy for a thermodynamically favored product is generally higher than that of a kinetically favored product in the reaction generated by product crystallization, as illustrated in Figure 2.10. Generally, high concentration and low temperature gives the preferred kinetic product. In contrast, low concentration and high temperature gives the preferred thermodynamic product. However, the different product may be determined by other reaction parameters above.

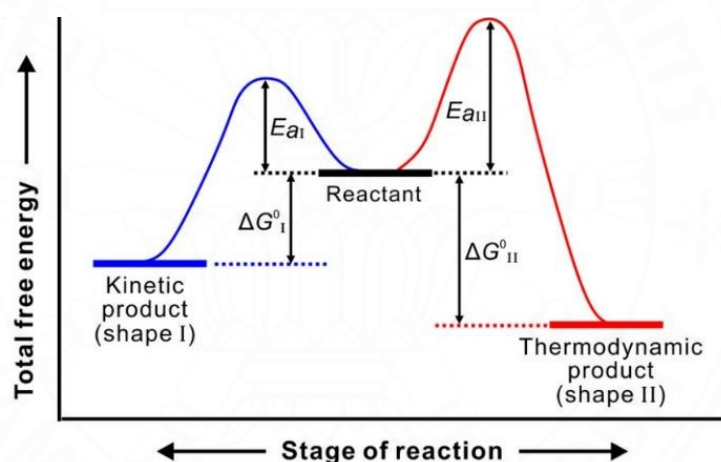


Figure 2.10 Thermodynamic and kinetic crystallization of products. Reproduced from ref. Xia *et al*, 2015.

### 2.2.2 Metal-organic frameworks (MOFs)

Metal-organic frameworks (MOFs) or porous coordination polymers (PCPs) are a class of hybrid materials consisting of metal ions or metal clusters and organic linkers that the frameworks structures contain potential voids (Batten *et al*, 2013). Batten (Batten, 2005) and Yaghi (O’Keeffe *et al*, 2012) reviewed the theory of MOF crystallography in detail, providing information on unpredictability and predictability within the crystallographic domain. The most important characteristics of MOFs are their

high crystallinity, highly ordered framework of pores, and the largest surface areas. In this regard, one gram of MOF materials can have a surface area comparable to a FIFA soccer field, *ca.* 7000 m<sup>2</sup>/g (Furukawa *et al*, 2010). The large surface area provides more space for chemical reactions and the adsorption of molecules. These materials can be able to take up, hold and release small molecules through their pores, which are unique abilities for advanced materials. Notably, unique structural characteristics can be achieved by tuning the basic materials to their specified application. Applications of MOFs in a wide variety of functionalities are thus possible including gas and liquid adsorption, gas storage, gas treatment, conductivity, food, catalysis, textile upgrading, drug delivery, sensing, and detection (Jang *et al*, 2020). Robson and co-workers (Hoskins, 1990; Robson, 2000) illustrated the feature of principles of coordination polymers to infinite metal-organic frameworks. Afterward, Zaworotko (Zaworotko, 1994; 2001), Fujita (Fujita *et al*, 1994), Kitagawa (Kitaura *et al*, 2002), Férey (Livage *et al*, 2001; Serre *et al*, 2002), and others made significant contributions to the development of net-based structures. Over the past four decades, some excellent MOF materials have been achieved and their properties are comparable or even better than those of traditional porous materials such as activated carbon and zeolite.

Indeed, the first example of MOF was discovered in 1999, Yaghi and coworkers synthesized microporous MOF-5  $\text{Zn}_4(\text{O})(\text{BDC})_3$  (BDC = 1,4-benzenedicarboxylate) by using slow vapor diffusion method. As can be seen in Figure 2.11, the structure shows an extended network based on Zn-O-C cluster as a secondary building unit and displays the open framework with large 3D pores (Li *et al*, 1999). This material would be ideal for constructing the desired extended three-dimensional framework which displayed high volumetric N<sub>2</sub> uptake capacities which are higher than those of zeolites.

Later on, Williams and co-workers reported microporous copper(II) tricarboxylate  $[\text{Cu}(\text{BTC})_2(\text{H}_2\text{O})_3]_n$  or **HKUST-1** (BTC = 1,3,5-benzenetricarboxylate) (Chui *et al*, 1999). The structure contains a paddle-wheel secondary building units (SBUs), and exhibits 3D square-shaped pores (9×9 Å) as shown in Figure 2.12. of particular note is that HKUST-1 contains open metal sites, resulting in an enhanced adsorption amount of gases. Given by the discovery this new class of porous materials in the 1990s, large number of MOF materials with different topological nets and properties have been prepared.

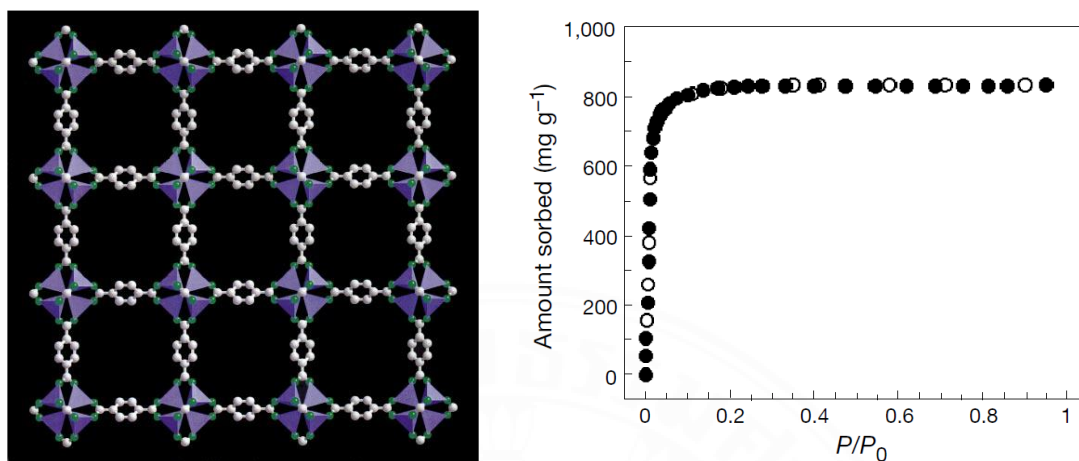


Figure 2.11 The  $\text{Zn}_4\text{O}(\text{BDC})_3$  framework (left) and the  $\text{N}_2$  adsorption isotherm at 78 K for MOF-5 (right). Reproduced from ref. Li *et al*, 1999.

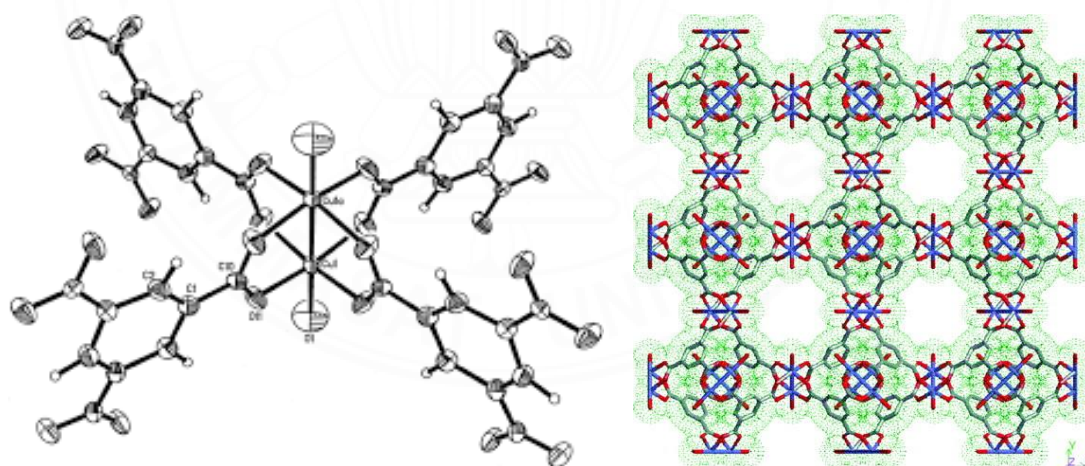


Figure 2.12 The structure of  $[\text{Cu}(\text{BTC})_2(\text{H}_2\text{O})_3]_n$  viewed paddle-wheel SBUs (left) and down the  $a$ -axis without  $\text{H}_2\text{O}$  molecules in the pore (right). Reproduced from ref. Chui *et al*, 1999.

## 2.3 Basic principles of lanthanides and their applications

### 2.3.1 Electronic structure and spectral term

Lanthanide ions ( $\text{Ln}^{3+}$ ) have atomic numbers in the range 57-71 with electronic configurations of  $[\text{Xe}]4f^n$  ( $n = 0-14$ ). Owing to the Ln are distinguished by a gradual filling of the 4f orbitals, ranging from  $4f^0$  (for  $\text{La}^{3+}$ ) to  $4f^{14}$  (for  $\text{Lu}^{3+}$ ), which generates a variety of electronic energy levels as depicted in Figure 2.13.

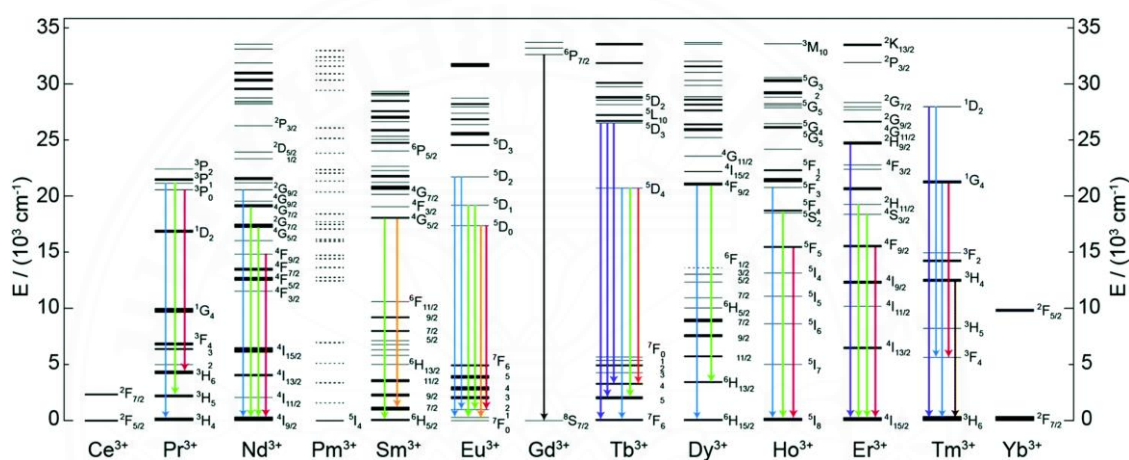


Figure 2.13 A diagram of electronic energy level for  $\text{Ln}^{3+}$ . Reproduced from ref.

Wang *et al*, 2018.

Lanthanide's 4f shells are unfilled, so the various arrangements of 4f electrons produce different energy levels. The energy levels are specified by four quantum numbers. A multielectronic ion gives an electron association with the 4f wave functions that are called a micro state. Resulting from a set of micro states explained by the spectral term. Then, the spectral term is a symbol, and is split into a series of spectroscopic levels. Accordingly, the various arrangements of 4f electrons produce different energy levels or micro states, which corresponded to distinct spectroscopic levels. The 4f electron transitions between various energy levels, resulting in a wide range of absorption and emission spectra. The 4f electrons of free Ln ions are influenced by nuclear attraction. To determine the free ion ground multiplet  $^{2S+1}L_J$  the following scheme in Table 2.2 is helpful ( $N$ : no. of 4f electrons):

1. The term with maximum  $S$  lies lowest in energy ( $\sum m_{s,i} = M_S \rightarrow S$ ).
2. For a given spin multiplicity, the term with the highest  $L$  lies lowest in energy ( $\sum m_{l,i} = M_L \rightarrow L$ ).
3. For less than half-filled subshells, the level with the lowest value of  $J$  lies lowest ( $J = |L - S|$ ), while the highest  $J$  lies lowest when a subshell is more than half full ( $J = L + S$ ).

Examples:  $\text{Pr}^{3+} [4f^2]: S = 1, L = 5, J = 4; (^3\text{H}_4)$

$\text{Dy}^{3+} [4f^9]: S = 5/2, L = 5, J = 15/2; (^6\text{H}_{15/2})$

**Table 2.2**

*The relationship between the quantum numbers of electrons.*

$\text{Ln}^{3+}$	Ce	Pr	Nd	Pm	Sm	Eu	Gd	Tb	Dy	Ho	Er	Tm	Yb	Lu
$N$	1	2	3	4	5	6	7	8	9	10	11	12	13	14
$m_s$	+1/2	+1/2	+1/2	+1/2	+1/2	+1/2	+1/2	-1/2	-1/2	-1/2	-1/2	-1/2	-1/2	-1/2
$m_l$	+3	+2	+1	0	-1	-2	-3	+3	+2	+1	0	-1	-2	-3

Note: Total spin quantum number ( $M_s = \sum m_s$ ), Total orbital quantum number ( $L = \sum l_i$ ), Total magnetic quantum number ( $M_L = \sum m_l$ ), Total angular momentum quantum number ( $J$ ), Total magnetic angular quantum number ( $M_J$ ).

### 2.3.2 f-f absorption spectra

Due to a photon being absorbed, the energy is transferred to an electron which may be pushed into the orbital with higher energy. Lanthanide ions exhibit three different types of electronic transitions: (i) sharp intraconfigurational 4f-4f transitions, (ii) broader 4f-5d transitions, and (iii) broader charge-transfer transitions (metal-to-ligand, MLCT or ligand-to-metal, LMCT). Later, the main type of transition is rather narrow and does not depend on the chemical environment of the central atom. The f-f transitions are separated by operators that are linked to the nature of light into electric dipole transitions (ED), magnetic dipole transitions (MD), and electric quadrupole transitions (EQ). Not all transitions are allowed, and the ones that are represented by selection rules. The first *Laporte's parity selection rule* indicates that the states with the same parity cannot be connected by electric dipole transitions as a

result of the f-f transition being forbidden by the ED mechanism. Whereas, the MD is allowed for parity but the intensity is the same magnitude as ED. In part of EQ transitions are difficult to distinguish due to their lower intensity than MD and ED transitions, though they are also allowed for parity. Furthermore, Table 2.3 shows the list of the other selection rules by  $S$ ,  $L$ , and  $J$  quantum numbers for f-f transitions between spectroscopic states. Some induced ED transitions are *hypersensitive* to minute changes in the  $\text{Ln}^{3+}$  ion environment; a typical example is  $\text{Eu}^{3+}$  ( $^5\text{D}_0 \rightarrow ^7\text{F}_2$ ). The selection rules are derived from several hypotheses that are not always totally fulfilled in reality. A forbidden transition has a low probability of occurring, whereas, an allowed transition has a high probability of occurring. Lanthanide ions absorption spectra are line-like due to the shielding effect of the external  $5p^65s^2$  subshells, but with low absorption efficiency, while the absorption ability of organic ligands has a strong influence on the absorption spectra of lanthanide complexes.

**Table 2.3**

*Selection rules for f-f transitions between spectroscopic levels.*

Operator	$\Delta S$	$\Delta L$	$\Delta J^a$
ED	0	$\leq 6$	$\leq 6$ (2,4,6 if $J$ or $J' = 0$ )
MD	0	0	0, $\pm 1$
EQ	0	0, $\pm 1$ , $\pm 2$	0, $\pm 1$ , $\pm 2$

<sup>a</sup> $J = 0$  to  $J' = 0$  transitions are always forbidden

### 2.3.3 Emission spectra, energy transfer, and antenna effect

Lanthanide ions with organic ligands are a class of luminescent materials as consequences of the f-f intraconfigurational transitions. The absorption spectra are sharply line-like and characteristic of optical bands, since they are insensitivity to the ligand environment. All  $\text{Ln}^{3+}$  ions exhibit emission lines except  $\text{La}^{3+}(4f^0)$  and  $\text{Lu}^{3+}(4f^{14})$ . Their f-f emission lines cover the total spectrum, from UV ( $\text{Gd}^{3+}$ ) to visible ( $\text{Pr}^{3+}$ ,  $\text{Sm}^{3+}$ ,  $\text{Eu}^{3+}$ ,  $\text{Tb}^{3+}$ ,  $\text{Dy}^{3+}$ ,  $\text{Tm}^{3+}$ ) and near-infrared (NIR,  $\text{Pr}^{3+}$ ,  $\text{Nd}^{3+}$ ,  $\text{Sm}^{3+}$ ,  $\text{Dy}^{3+}$ ,  $\text{Ho}^{3+}$ ,  $\text{Er}^{3+}$ ,  $\text{Tm}^{3+}$ , and  $\text{Yb}^{3+}$ ) ranges. Hence, some  $\text{Ln}^{3+}$  ions can be

measured by single visible or NIR emission, a few can emit both visible and NIR light. Some of the emission bands of  $\text{Ln}^{3+}$  ions is provide in Table 2.4.

**Table 2.4**

*The typical emission bands of the lanthanide ions  $\text{Eu}^{3+}$ ,  $\text{Tb}^{3+}$ ,  $\text{Nd}^{3+}$ ,  $\text{Er}^{3+}$ , and  $\text{Yb}^{3+}$  in solution.*

Ion	Transition	Emission (nm)	Ion	Transition	Emission (nm)
$\text{Eu}^{3+}$	$^2\text{D}_0 \rightarrow ^7\text{F}_0$	580	$\text{Nd}^{3+}$	$^4\text{F}_{3/2} \rightarrow ^4\text{F}_{9/2}$	880
	$^2\text{D}_0 \rightarrow ^7\text{F}_1$	590		$^4\text{F}_{3/2} \rightarrow ^4\text{F}_{11/2}$	1060
	$^2\text{D}_0 \rightarrow ^7\text{F}_2$	613		$^4\text{F}_{3/2} \rightarrow ^4\text{F}_{13/2}$	1330
	$^2\text{D}_0 \rightarrow ^7\text{F}_3$	650	$\text{Er}^{3+}$	$^4\text{I}_{13/2} \rightarrow ^4\text{I}_{15/2}$	1550
	$^2\text{D}_0 \rightarrow ^7\text{F}_4$	690	$\text{Yb}^{3+}$	$^2\text{F}_{5/2} \rightarrow ^2\text{F}_{7/2}$	980
	$^2\text{D}_0 \rightarrow ^7\text{F}_5$	710			
$\text{Tb}^{3+}$	$^5\text{D}_4 \rightarrow ^7\text{F}_6$	490			
	$^5\text{D}_4 \rightarrow ^7\text{F}_5$	545			
	$^5\text{D}_4 \rightarrow ^7\text{F}_4$	590			
	$^5\text{D}_4 \rightarrow ^7\text{F}_3$	620			
	$^5\text{D}_4 \rightarrow ^7\text{F}_2$	650			

The configurational coordinate diagram is shown in Figure 2.14. These levels appear as parallel parabolas (a) the emission transitions display broad bands, which can be found in organic or transition compounds. Because excitation leads frequently to a length of the chemical bonds, resulting in large Stokes' shifts case: fwhm  $>50$  nm wherewith the coupling with vibrations is strong in broad emission. On the contrary, (b) the f-f emission lines are sharp by the reason of the rearrangement following the promotion of an electron into 4f orbital of higher energy, which does not significantly perturb the binding pattern in the molecules. As a result, the internuclear distances remain nearly constant in the exited state, which generates narrow bands and very small Stokes' shifts (full-widths at half-maximum, fwhm  $<10$  nm) in different spectra of lanthanide complexes.



If  $\text{Ln}^{3+}$  ions have absorption and emission bands that relate to Laporte-forbidden f-f transitions, the absorptions have very low molar absorptivity, making direct excitation of  $\text{Ln}^{3+}$  ions difficult. This problem is solved by using a highly absorbing chromophore to sensitize  $\text{Ln}^{3+}$  emission in a process called the *antenna effect* or *sensitization* in luminescent lanthanide organic compounds as shown in Figure 2.15.

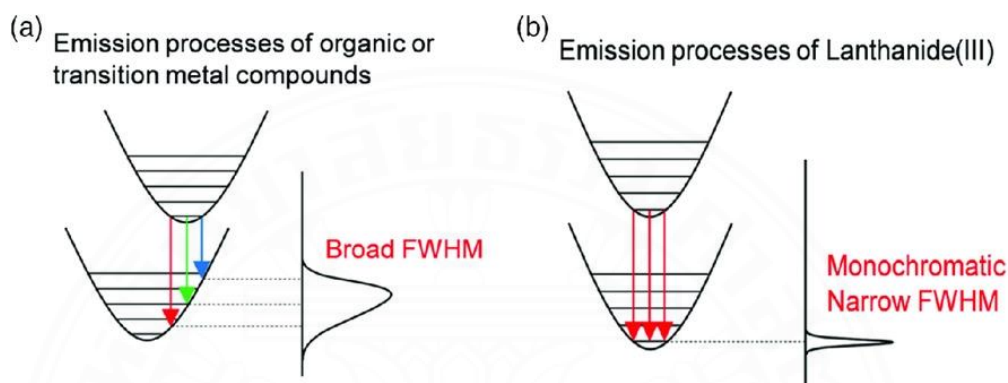


Figure 2.14 Emission processes of (a) organic or transition-metal compounds (large Stokes' shifts) and (b) lanthanide complexes (small Stokes' shifts). Reproduced from ref. Hasegawa *et al*, 2019.

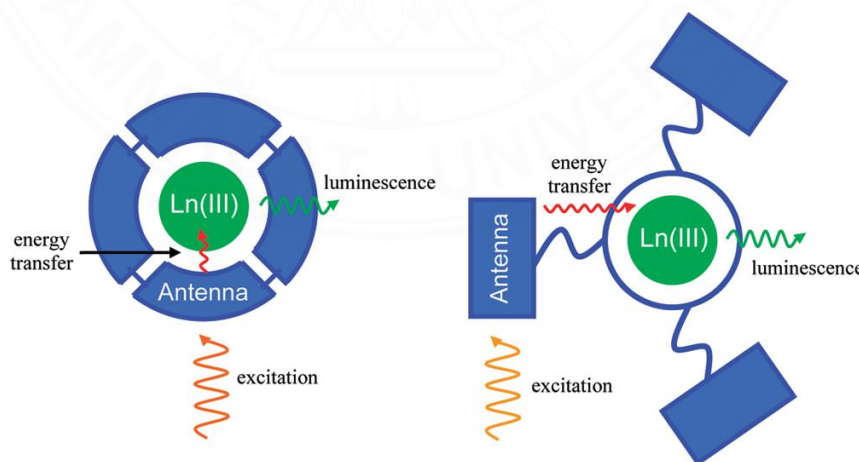
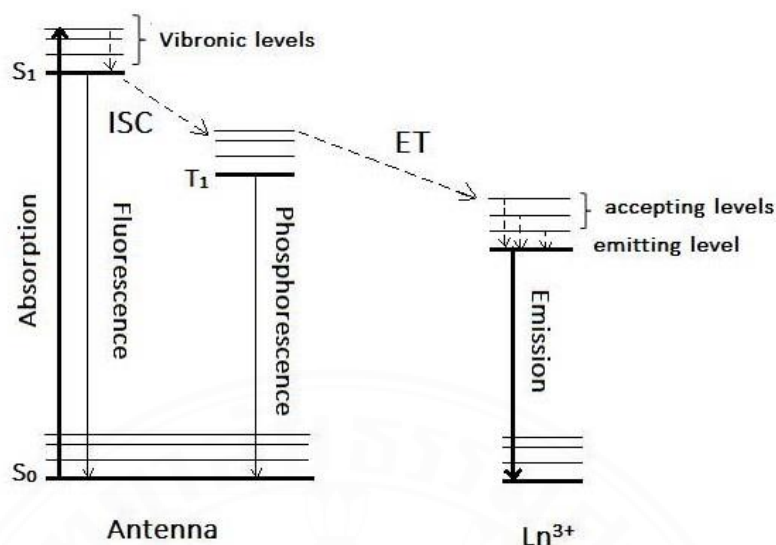


Figure 2.15 The antenna effect for  $\text{Ln}^{3+}$  sensitization, illustrated using the chromophore chelate (right) and pendant chromophore (left) ligand designs. Reproduced from ref. Moore *et al*, 2009.



In 1942, Weissman first reported that the  $\text{Eu}^{3+}$  metal-centered luminescence can be excited via light absorption by organic ligands and after energy transfer in Eu-based  $\beta$ -diketonate, phenolate, or salicylate complexes (Leach *et al*, 2017). Afterward, Crosby and Whan present an idea for studying the mechanism of energy transfer from organic ligands to  $\text{Ln}^{3+}$  ions (Amirkhanov *et al*, 2023).

In a nutshell, the photosensitized energy transfer process is explained by using Jablonski's diagram as illustrated in Figure 2.16, a graphical depiction of energy absorption, migration, emission, and processes in MOFs. Abbreviations: S is singlet; ISC is intersystem crossing; T is a triplet; ET is energy transfer; Ln is lanthanide. The energy transfer process is divided into four steps: (i) the exciting step is adept due to the Laporte- and spin-allowed ligand-centered absorption upon UV light illumination; (ii) the energy of the S1 excited state is transferred to the ligand triplet excited state  $T_1$  through use of nonradiative intersystem crossing (ISC); (iii) the intramolecular energy transfer from  $T_1$  to  $\text{Ln}^{3+}$  ions, which is associated with the excited 4f states; and (iv) the radiative process goes through its typical line emission. Similar to absorption spectra, light emission is due to two main types of transitions, MD and ED. The lifetime of the excited state and the quantum yield ( $\phi$ ) are two important parameters that characterize the light emission from a given  $\text{Ln}^{3+}$  ion. The luminescence spectra are defined as phosphorescence intensity as a function of a wavelength. The quantum yield describes the efficiency of the phosphorescence process, and is defined as the ratio of the number of emitted photons released in the process to the number of photons absorbed. The lifetime refers to the average time the molecule stays in its excited state before emitting a photon. Nonetheless, the maximum wavelength and lifetime in solid MOFs are frequently different from those of molecules. Because the organic linkers are stabilized within MOFs, controlled intramolecular/intermolecular interactions play a crucial role in a MOFs luminescence properties for a specific application.



*Figure 2.16* Simplified diagram showing the main energy flow paths during energy transfer of lanthanide luminescence via its surrounding (ligands). Reproduced from ref. Business Bliss Consultants FZE (November 2018).

### 2.3.4 Photoluminescent sensing properties of LnCPs

LnCP are a class of luminescent materials distinct from inorganic materials. The organic ligand contains an organic chromophore, which absorbs light and transfers energy to the lanthanide ion to increase the effective absorption cross-section. Recently, luminescent LnCPs have been received attention for sensing applications because their structural and chemical tunability show good selectivity via the pore size or host framework-guest interactions. For example, Muller illustrated the perspective for the design of luminescent chiral lanthanide (III) complexes and focused on the optical aspect (Muller, 2009). In particular, Eu<sup>3+</sup> and Tb<sup>3+</sup> are the most emissive lanthanide ions. Cui and coworkers have provided a review with a detailed description of the various types of luminescent MOFs such as the appealing properties of the MOF surrounding to creating luminescent materials, the origin of MOF luminescence, a survey of various luminescent MOF types, and applications (Cui *et al*, 2012). It should be mentioned that Eu- and Tb- based MOFs have given their intense, long-lived, and line-like emission in the visible region. Whereas, Er-, Nd-, and Yb-based luminescent MOFs were studied in the near-infrared (NIR) region.

Daiguebonne and co-workers reported LnMOFs of the formula  $[\text{Ln}_2(1,4\text{-BDC})_3(\text{H}_2\text{O})_4]$ . The isomorphous compounds can be dehydrated for obtain the anhydrous phases. The Eu-, Tb-, and Dy-based MOFs emit red, green, and yellow luminescence at 617, 546, and 575 nm, respectively. The hydrated and anhydrous Tb(III) containing compounds have the highest quantum yields, with the latter reaching 43% (Daiguebonne *et al*, 2008).

For the development of LnCPs based sensor, Chen and co-workers have been prepared a luminescent Eu-MOF,  $[\text{Eu}(\text{PDC})_{1.5}(\text{DMF})] \cdot (\text{DMF})_{0.5}(\text{H}_2\text{O})_{0.5}$ , where PDC = pyridine-3,5-dicarboxylate under solvothermal conditions (Chen *et al*, 2009). The structure features a 3D open framework built up by the central Eu ions bridged by PDC linkers, Figure 2.17. The framework contains 1D channels of dimensions  $6.3 \times 8.5 \text{ \AA}^2$ . It is fascinating that this compound shows unique selectivity for detection of  $\text{Cu}^{2+}$  through fluorescence quenching mechanism with the calculated  $K_{sv}$  value of  $89.4 \text{ M}^{-1}$ .

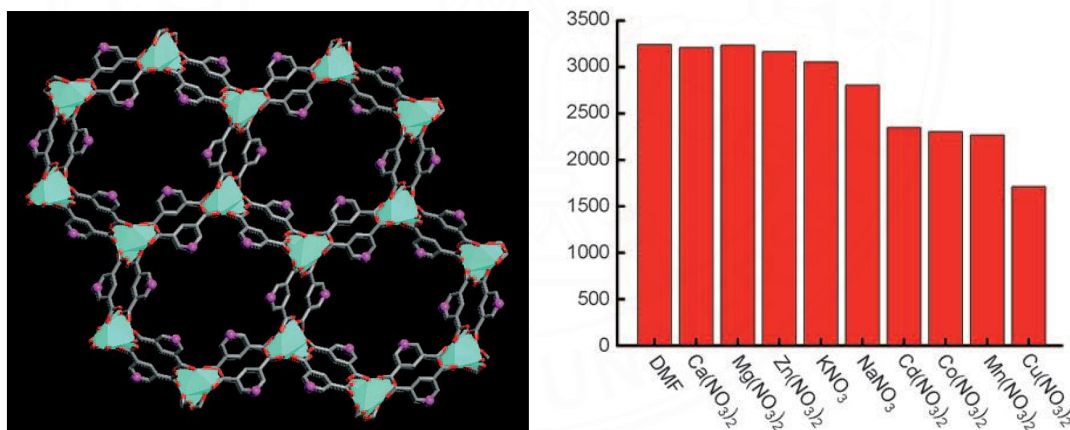


Figure 2.17 Crystal structure of compound Eu (left) and comparison of the luminescence intensity of compound Eu in various metal ions in DMF solutions of  $\text{M}(\text{NO}_3)_x$ . Reproduced from ref. Chen *et al*, 2009.

In another example, Luo and co-workers have synthesized a 3D luminescent Tb(III) MOF containing triazole-dicarboxylate ligand,  $\{[\text{Tb}(\text{L})(\text{CH}_3\text{COO})(\text{H}_2\text{O})] \cdot 0.5\text{DMF}\}_n$  for the development of new sensing materials. The

SCXRD studies reveal the 3D framework with 1D channels of  $13.1 \text{ \AA} \times 3.6 \text{ \AA}$  dimensions, Figure 2.18. This material has excellent solvent and acid/base stability, and has the ability to detect creatinine in an aqueous solution with LOD of  $1.7 \times 10^{-6} \mu\text{M}$ , which is found to be lower than the infective concentration in a real environment. (Luo *et al*, 2022). Interestingly, this sensor can observe the change in creatinine concentration in diluted serum solutions, and can be regenerated at least five times as shown in Figure 2.19.

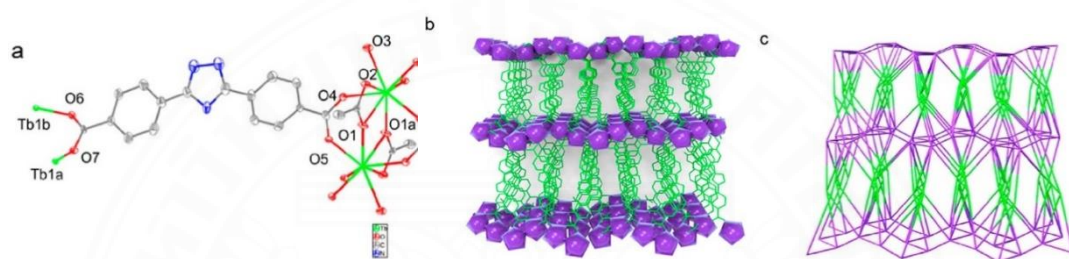


Figure 2.18 (a) Coordination environment of Tb-MOF (b) Perspective 3D channel of Tb-MOF along the b axis. (c) Simplified topological graph of Tb-MOF. Reproduced from ref. Luo *et al*, 2022.

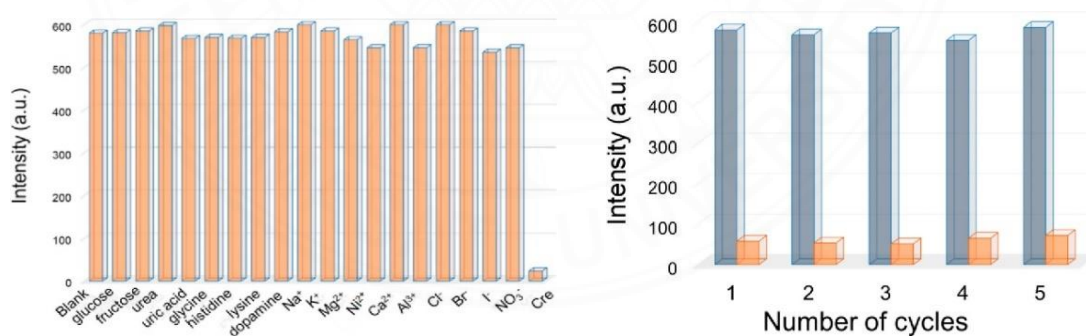


Figure 2.19 Luminescent intensity of Tb-MOF in an aqueous solution ( $\lambda_{\text{ex}} = 250 \text{ nm}$  and  $\lambda_{\text{em}} = 380 \text{ nm}$ ) (left). Circulation efficiency of Tb-MOF for fluorescence detection of creatinine (right). Reproduced from ref. Luo *et al*, 2022.

### 2.3.5 Magnetic properties of lanthanide coordination polymers

The magnetic property of the compound contains the movement of electrical charge that generates the magnetic field in a material. The coupled spin and orbital magnetic moments associated with the motion of electrons are induced by the magnetic field. The spin magnetic moment is caused by electron precession relative to their axes, while the orbital magnetic moment is caused by electron motion around the nucleus. Thus, the observed magnetic properties are the result of the combination of the spin and orbital magnetic moments of the constituent atoms of a material. Compounds containing all paired electrons are diamagnetic while those containing unpaired electrons are paramagnetic. The magnitude of paramagnetism is measured in terms of an effective magnetic moment,  $\mu_{\text{eff}}$ . For first-row transition metals, spin-orbit coupling causes  $\mu_{\text{eff}}$  to deviate from the spin-only formula. Conversely, the spin-orbit coupling cannot be ignored in the heavier transition metals, lanthanides, and actinides. Exchange interaction can emerge in clusters and infinite lattices, a way that results in ferromagnetism, antiferromagnetism, or ferrimagnetism based on the relative orientations of the independent spins. The magnetic behavior of materials can be classified into the following five major groups: diamagnetic, paramagnetic, ferromagnetic, antiferromagnetic, and ferrimagnetic as in Table 2.5.

The magnetic properties of lanthanide complexes are significantly different from those of transition elements. Electromagnetics contain two different kinds of magnetic fields that are the magnetizing field (H) and the magnetic flux density (B). The concept of permeability ( $\mu$ ) arises because there is a simple relationship between H and B at any location or time in many materials (and in a vacuum), in which the two fields are exactly directly proportionate to each other:

$$B = \mu H$$

The permeability of vacuum is  $\mu_0$ ;  $\mu_0 = 4\pi \times 10^{-7}$  ( $1.257 \times 10^{-6}$ ) H/m. The magnetic response of a linear material affiliated with the magnetization (M) that are in:

$$B = \mu_0 H + \mu_0 M$$

Relative permeability is represented by the symbol  $\mu_r$ .

$$\mu_r = \mu / \mu_0$$

**Magnetic susceptibility**  $\chi_m$  in terms of its relative permeability, is the primary unit of measurement in magnetochemistry.

$$\chi_m = \mu_r - 1$$

$$\chi_m = M/H$$

When the temperature is affected in Kelvin, the total susceptibility can be calculated using The Curie-Weiss law.

$$\chi = C/T - \Theta$$

where  $\Theta$  can be positive, negative, or zero.

**The magnetic moment of lanthanide ( $\text{Ln}^{3+}$ ) ions** is generally well-described from the coupling of spin and orbital angular momenta ~ Russell-Saunders Coupling.

Hund's formula eq.

$$\mu = g_J [J(J+1)]^{1/2} \mu_B \quad (\text{except } 4f^4, 4f^5, 4f^6 \text{ systems})$$

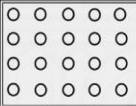
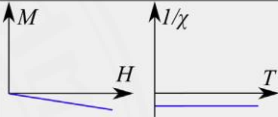

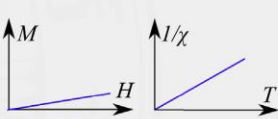

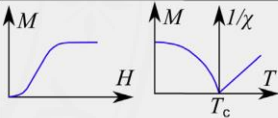
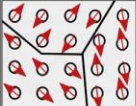
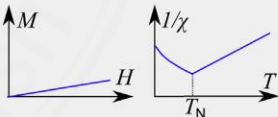

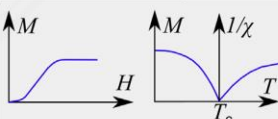
where  $\mu$  is the effective number of Bohr magnetons.  $J$  is the total angular momentum of the ground multiplet and  $g_J$  is the Landé factor.

$$g_J = 1 + [J(J+1) + S(S+1) - L(L+1)] / 2J(J+1)$$

$S$ ,  $L$ , and  $J$  correspond to the total spin angular momentum, the total orbital angular momentum, and the total angular momentum, respectively, of the ground multiplet. As can be seen in Table 2.6, the effective magnetic moments are similar to the experimental values obtained at high temperatures. Note that the empirical number  $\mu_{eff}$  has no connection with the permanent moment  $\mu$  except when Curie's law is obeyed.

**Table 2.5**

*A summary of types of magnetic behavior. Reprinted with permission from Palagummi & Yuan, 2016.*

Magnetism	Examples	Magnetic behaviour		
Diamagnetism	Bi, Si, Cu, inert gases  Susceptibility small and negative ( $-10^{-6}$ to $-10^{-5}$ )	 H = 0	Atoms have no magnetic moments.	
Paramagnetism	Al, O <sub>2</sub> , MnBi  Susceptibility small and positive ( $10^{-5}$ to $10^{-3}$ )	 H = 0	Atoms have randomly oriented magnetic moments.	
Ferromagnetism	Fe, Ni, Co, Gd  Susceptibility large (generally $> 100$ )	 H = 0	Atoms are organized in domains which have parallel aligned magnetic moments.	
Antiferromagnetism	Cr, MnO, FeO  Susceptibility small and positive ( $10^{-5}$ to $10^{-3}$ )	 H = 0	Atoms are organized in domains which have antiparallel aligned moments.	
Ferrimagnetism	Fe <sub>3</sub> O <sub>4</sub> , MnFe <sub>2</sub> O <sub>4</sub> , NiFe <sub>2</sub> O <sub>4</sub>  Susceptibility large (generally $> 100$ )	 H = 0	Atoms are organized in domains which have a mixture of unequal antiparallel aligned moments.	



**Table 2.6**

*Some ionic properties and magnetic moment of the lanthanides.*

$\text{Ln}^{3+}$	Ground state ( $2S+1L_J$ )	No. of unpaired $e^-$	S	L	J	$g_J$	$g_J[J(J+1)]^{1/2}$	Observed $\mu_{\text{eff}}^{\text{exp}}/\mu_B$	$\chi_m T$
$\text{La}^{3+}$	$^1S_0$	0	0	0	0	0	0	0	0
$\text{Ce}^{3+}$	$^2F_{5/2}$	1	1/2	3	5/2	6/7	2.54	2.3–2.5	0.80
$\text{Pr}^{3+}$	$^3H_4$	2	1	5	4	4/5	3.58	3.4–3.6	1.60
$\text{Nd}^{3+}$	$^4I_{9/2}$	3	3/2	6	9/2	8/11	3.62	3.4–3.5	1.64
$\text{Pm}^{3+}$	$^5I_4$	4	2	6	4	3/5	2.68	2.9	0.90
$\text{Sm}^{3+}$	$^6H_{5/2}$	5	5/2	5	5/2	2/7	0.85	1.6	0.09
$\text{Eu}^{3+}$	$^7F_0$	6	3	3	0	0	0	3.5	0
$\text{Gd}^{3+}$	$^8S_{7/2}$	7	7/2	0	7/2	2	7.94	7.8–7.9	7.87
$\text{Tb}^{3+}$	$^7F_6$	6	3	3	6	3/2	9.72	9.7–9.8	11.82
$\text{Dy}^{3+}$	$^6H_{15/2}$	5	5/2	5	15/2	4/3	10.65	10.2–10.6	14.17
$\text{Ho}^{3+}$	$^5I_8$	4	2	6	8	5/4	10.6	10.3–10.5	14.07
$\text{Er}^{3+}$	$^4I_{15/2}$	3	3/2	6	15/2	6/5	9.58	9.4–9.5	11.48
$\text{Tm}^{3+}$	$^3H_6$	2	1	5	6	7/6	7.56	7.5	7.15
$\text{Yb}^{3+}$	$^2F_{7/2}$	1	1/2	3	7/2	8/7	4.54	4.5	2.57
$\text{Lu}^{3+}$	$^1S_0$	0	0	0	0	0	0	0	0



For instance, Das and coworkers reported a discrete tetranuclear Gd(III) complex synthesized through the self-assembly reaction between hydrated chloride salts of Gd(III) metal and a newly synthesized Schiff-base ligand, (E)-2-((6-(hydroxymethyl)pyridin-2-yl)methyleneamino)phenol (LH<sub>2</sub>), Figure 2.20. Magnetic studies showed that the  $\chi_{\text{MT}}$  value for the Gd compound is found to be  $32.42 \text{ cm}^3 \text{ mol}^{-1} \text{ K}$  at room temperature, which is similar to that expected for four noninteracting Gd(III) ions ( $31.5 \text{ cm}^3 \text{ mol}^{-1} \text{ K}$ , with  $S = 7/2$  and  $g = 2$ ). This behavior is also most usually related to intramolecular antiferromagnetic interactions between the Gd(III) ions as shown in Figure 2.21. (Das *et al*, 2014)

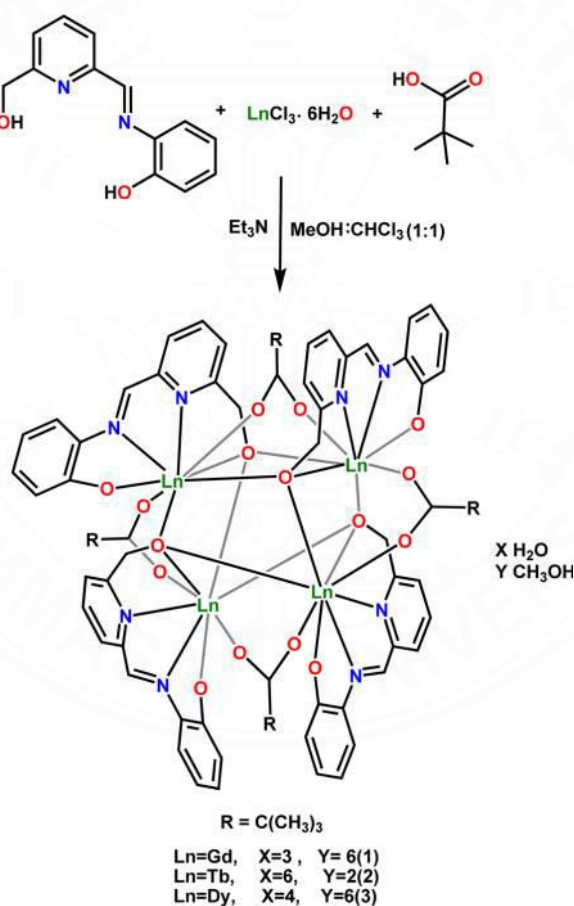


Figure 2.20 Synthesis of  $[\text{Ln}_4(\text{L})_4(\mu^2\text{-}\eta^1\eta^1\text{Piv})_4] \cdot x\text{H}_2\text{O} \cdot y\text{CH}_3\text{OH}$  (**1**, Ln = Gd(III),  $x = 3$ ,  $y = 6$ ; **2**, Ln = Tb(III),  $x = 6$ ,  $y = 2$ ; **3**, Ln = Dy(III),  $x = 4$ ,  $y = 6$ ). Reproduced from ref. Das *et al*, 2014.

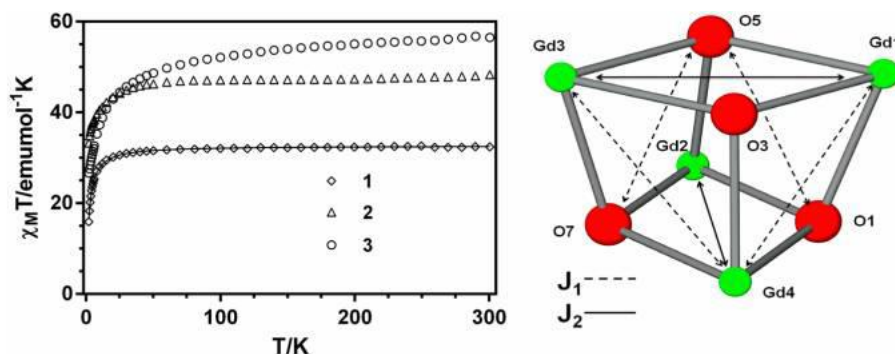


Figure 2.21 (left) Temperature dependence of the  $\chi_M T$  for compounds Gd (**1–3**). The solid line represents the best fit of the experimental data. (right) 2J coupling scheme for Gd compound. Reproduced from ref. Das *et al*, 2014.

### 2.3.6 Gas adsorption properties of lanthanide coordination polymers

An adsorption process consists of adsorptive, adsorbate, and adsorbent. Adsorptive is adsorbate before being adsorbed on the surface. Adsorbate is the gas adsorbed on the surface of solid materials. The adsorbent is solid where adsorption takes place. The gas adsorption technique is the physical adsorption of gas molecules on the surface. Porous and nonporous materials display gas adsorption phenomena where various types of isotherms depend on the surface area, pore diameter, and gas molecule. An isotherm is a measure of the volume of gas adsorbed at a constant temperature as a function of gas pressure.

The IUPAC classifies six types of adsorption isotherms as shown in Figure 2.22. The type I is exhibited by microporous (< 2 nm) and concave to the Y-axis. The type II is exhibited by nonporous or microporous (> 50 nm) and unrestricted monolayer-multilayer adsorption. The type III is exhibited as nonporous or microporous with weak interaction and convex to the Y-axis. The type IV is exhibited by mesoporous, the formation of two surface layers on the plane surface or on the wall of a pore much wider than the sorbate's molecular diameter. The type V is exhibited by mesoporous with weak interaction and is highly uncommon when intermolecular attraction effects are large, and adsorption takes place in pores and capillaries. The type VI is exhibited by layer-by-layer adsorption. Traditional nanoporous materials are typically classified as having a type I adsorption isotherm.

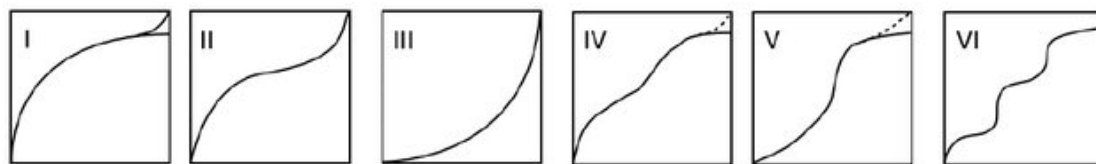


Figure 2.22 The IUPAC classification of adsorption isotherms: the X-axis represents relative pressure, and the Y-axis represents adsorption amount. Reproduced from ref. Kajiro *et al*, 2010.

LnCPs have become a significant area of study for  $H_2$ ,  $CH_4$ , and  $CO_2$  adsorptions. Kitagawa and co-workers reported a series of Ln-MOFs based on an acylamide modified ligand ( $H_3L = 4,4',4''$ -(benzenetricarbonyltris-(azanediyl))tribenzoic acid) and  $Ln(NO_3)_3 \cdot xH_2O$  ( $Ln^{III} = Y, La, Ce, Nd, Eu, Tb, Dy, Ho, \text{ and } Tm$ ) for effective separation of  $CO_2$  gas from  $CO_2/C_2H_4$  and  $CO_2/C_2H_6$  systems (Duan *et al.*, 2013). The flexible nature of the lanthanum framework allowed for the specific capture of  $CO_2$  over  $C_2H_4$  and  $C_2H_6$  at room temperature and pressure. As can be seen in Figure 2.23, the representative example of series, the Y-framework has a rectangular channel with a single wall, whereas the La-framework has a double-walled channel with acylamide groups arranged side by side. Adsorption experiments at 195 K revealed that the La-framework was highly selective for  $CO_2$ , with an uptake capacity of  $115 \text{ cm}^3/\text{g}$ , but almost no uptake for  $C_2H_4$  and  $C_2H_6$ . This result demonstrated that the La-framework material can be used to separate  $CO_2$  from natural gas mixtures. At 150 kPa, further  $CO_2$  adsorption studies at 273 K revealed type-I  $CO_2$  uptake ( $34 \text{ mL/g}$ ). Surprisingly, there was no adsorption of  $C_2H_4$  and  $C_2H_6$  prior to this pressure. This framework sufficient practical applicability stems from its ability to separate  $CO_2$  from natural gas mixtures at 273 K and pressure (0.1-1 bar), as well as selectively adsorb  $CO_2$  from gas mixtures.

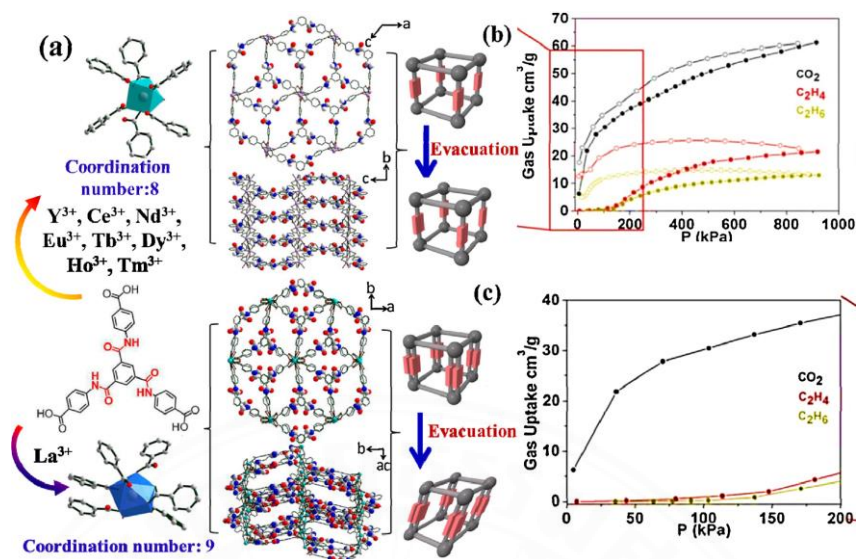


Figure 2.23 (a) The coordination environment of different lanthanide ions with L. At the extreme right is shown the likely structural character of the frameworks before and after evacuation. (b and c) The adsorption of CO<sub>2</sub>, C<sub>2</sub>H<sub>4</sub>, and C<sub>2</sub>H<sub>6</sub> uptake in La-framework at 273 K. Reprinted with permission from ref. Kitagawa *et al.*, 2013. Copyright 2013 RSC.

## 2.4 References

- Amirkhanov, V. M., Kariaka, N. S., Lipa, A., Carneiro Neto, A. N., Malta, O. L., & Gawryszewska, P. (2023). Eu<sup>3+</sup> and Tb<sup>3+</sup> coordination compounds with phenyl-containing carbacylamidophosphates; comparison with selected Ln<sup>3+</sup>  $\beta$ -diketonates. *Frontiers in Chemistry*, 11, 303.
- Ariga, K., Hill, J. P., Lee, M. V., Vinu, A., Charvet, R., & Acharya, S. (2008). Challenges and breakthroughs in recent research on self-assembly. *Science and technology of advanced materials*.
- Batten, S. R. (2005). Glorious uncertainty—challenges for network design. *Journal of Solid State Chemistry*, 178(8), 2475-2479.
- Batten, S. R., Champness, N. R., Chen, X. M., Garcia-Martinez, J., Kitagawa, S., Öhrström, L., ... & Reedijk, J. (2013). Terminology of metal–organic

- frameworks and coordination polymers (IUPAC Recommendations 2013). *Pure and Applied Chemistry*, 85(8), 1715-1724.
- Batten, S. R., Neville, S. M., & Turner, D. R. (2008). *Coordination polymers: design, analysis, and application*. Royal Society of Chemistry.
- Baxter, P., Lehn, J. M., DeCian, A., & Fischer, J. (1993). Multicomponent Self-Assembly: Spontaneous Formation of a Cylindrical Complex from Five Ligands and Six Metal Ions. *Angewandte Chemie International Edition in English*, 32(1), 69-72.
- Baxter, P. N., Lehn, J. M., Fischer, J., & Youinou, M. T. (1994). Self-Assembly and Structure of a  $3 \times 3$  Inorganic Grid from Nine Silver Ions and Six Ligand Components. *Angewandte Chemie International Edition in English*, 33(22), 2284-2287.
- Bernal, J. D., & Crowfoot, D. (1935). 21. The structure of some hydrocarbons related to the sterols. *Journal of the Chemical Society (Resumed)*, 93-100.
- Bragg, W. H. (1921). The structure of organic crystals. *Proceedings of the Physical Society of London (1874-1925)*, 34(1), 33.
- Business Bliss Consultants FZE. (November 2018). Fluorescent Emission of Lanthanide Ions for Their Use in Biomedical Diagnosis. Retrieved from <https://ukdiss.com/examples/fluorescent-emission-lanthanide-ions-biomedical-diagnosis.php?vref=1>.
- Chen, B., Wang, L., Xiao, Y., Fronczek, F. R., Xue, M., Cui, Y., & Qian, G. (2009). A luminescent metal–organic framework with Lewis basic pyridyl sites for the sensing of metal ions. *Angewandte Chemie*, 121(3), 508-511.
- Chen, Y. C., Liu, J. L., Ungur, L., Liu, J., Li, Q. W., Wang, L. F., ... & Tong, M. L. (2016). Symmetry-supported magnetic blocking at 20 K in pentagonal bipyramidal Dy (III) single-ion magnets. *Journal of the American Chemical Society*, 138(8), 2829-2837.
- Chui, S. S. Y., Lo, S. M. F., Charmant, J. P., Orpen, A. G., & Williams, I. D. (1999). A chemically functionalizable nanoporous material  $[\text{Cu}_3(\text{TMA})_2(\text{H}_2\text{O})_3]_n$ . *Science*, 283(5405), 1148-1150.
- Cui, Y., Yue, Y., Qian, G., & Chen, B. (2012). Luminescent functional metal–organic frameworks. *Chemical reviews*, 112(2), 1126-1162.

- Daiguebonne, C., Kerbellec, N., Guillou, O., Bünzli, J. C., Gumy, F., Catala, L., ... & Calvez, G. (2008). Structural and luminescent properties of micro-and nanosized particles of lanthanide terephthalate coordination polymers. *Inorganic chemistry*, 47(9), 3700-3708.
- Das, S., Dey, A., Biswas, S., Colacio, E., & Chandrasekhar, V. (2014). Hydroxide-free cubane-shaped tetranuclear [Ln<sub>4</sub>] complexes. *Inorganic Chemistry*, 53(7), 3417-3426.
- Day, A. I., Blanch, R. J., Arnold, A. P., Lorenzo, S., Lewis, G. R., & Dance, I. (2002). A cucurbituril-based gyroscane: a new supramolecular form. *Angewandte Chemie*, 114(2), 285-287.
- Desiraju, G. R., & Parshall, G. W. (1989). Crystal engineering: the design of organic solids. *Materials science monographs*, 54.
- Desiraju, G. R. (2013). Crystal engineering: from molecule to crystal. *Journal of the American Chemical Society*, 135(27), 9952-9967.
- Duan, J., Higuchi, M., Foo, M. L., Horike, S., Rao, K. P., & Kitagawa, S. (2013). A family of rare earth porous coordination polymers with different flexibility for CO<sub>2</sub>/C<sub>2</sub>H<sub>4</sub> and CO<sub>2</sub>/C<sub>2</sub>H<sub>6</sub> separation. *Inorganic Chemistry*, 52(14), 8244-8249.
- Feng, S. H., & Li, G. H. (2017). Hydrothermal and solvothermal syntheses. In *Modern inorganic synthetic chemistry* (pp. 73-104). Elsevier.
- Freeman, W. A. (1984). Structures of the p-xylylenediammonium chloride and calcium hydrogensulfate adducts of the cavitand 'cucurbituril', C<sub>36</sub>H<sub>36</sub>N<sub>24</sub>O<sub>12</sub>. *Acta Crystallographica Section B: Structural Science*, 40(4), 382-387.
- Fujita, M., Kwon, Y. J., Washizu, S., & Ogura, K. (1994). Preparation, clathration ability, and catalysis of a two-dimensional square network material composed of cadmium (II) and 4, 4'-bipyridine. *Journal of the American Chemical Society*, 116(3), 1151-1152.
- Furukawa, H., Ko, N., Go, Y. B., Aratani, N., Choi, S. B., Choi, E., ... & Yaghi, O. M. (2010). Ultrahigh porosity in metal-organic frameworks. *Science*, 329(5990), 424-428.
- Hanan, G. S., Arana, C. R., Lehn, J. M., & Fenske, D. (1995). Synthesis, Structure, and Properties of Dinuclear and Trinuclear Rack-Type RuII Complexes. *Angewandte Chemie International Edition in English*, 34(10), 1122-1124.



- Hasegawa, Y., & Kitagawa, Y. (2019). Thermo-sensitive luminescence of lanthanide complexes, clusters, coordination polymers and metal–organic frameworks with organic photosensitizers. *Journal of Materials Chemistry C*, 7(25), 7494-7511.
- Hasenknopf, B., Lehn, J. M., Kneisel, B. O., Baum, G., & Fenske, D. (1996). Self-assembly of a circular double helicate. *Angewandte Chemie International Edition in English*, 35(16), 1838-1840.
- Hoskins, B. F., & Robson, R. (1990). Design and construction of a new class of scaffolding-like materials comprising infinite polymeric frameworks of 3D-linked molecular rods. A reappraisal of the zinc cyanide and cadmium cyanide structures and the synthesis and structure of the diamond-related frameworks  $[\text{N}(\text{CH}_3)_4][\text{CuIZnII}(\text{CN})_4]$  and  $\text{CuI}[4,4',4'',4'''\text{-tetracyanotetraphenylmethane}] \text{BF}_4 \cdot x\text{C}_6\text{H}_5\text{NO}_2$ . *Journal of the American Chemical Society*, 112(4), 1546-1554.
- Jang, S., Song, S., Lim, J. H., Kim, H. S., Phan, B. T., Ha, K. T., ... & Park, K. H. (2020). Application of various metal-organic frameworks (MOFs) as catalysts for air and water pollution environmental remediation. *Catalysts*, 10(2), 195.
- Kajiro, H., Kondo, A., Kaneko, K., & Kanoh, H. (2010). Flexible two-dimensional square-grid coordination polymers: Structures and functions. *International Journal of Molecular Sciences*, 11(10), 3803-3845.
- Kitaura, R., Kitagawa, S., Kubota, Y., Kobayashi, T. C., Kindo, K., Mita, Y., ... & Takata, M. (2002). Formation of a one-dimensional array of oxygen in a microporous metal-organic solid. *Science*, 298(5602), 2358-2361.
- Leach, E. G., Shady, J. R., Boyden, A. C., Emig, A. L., Henry, A. T., Connor, E. K., ... & Biros, S. M. (2017). X-ray crystallographic, luminescence and NMR studies of phenacyldiphenylphosphine oxide with the Ln (iii) ions Sm, Eu, Gd, Tb and Dy. *Dalton Transactions*, 46(44), 15458-15469.
- Lehn, J. M. (1988). Supramolecular chemistry- scope and perspectives: molecules - supermolecules-molecular devices. *Journal of inclusion phenomena*, 6(4), 351–396.
- Lehn, J. M., & Rigault, A. (1988). Helicates: tetra-and pentanuclear double helix complexes of  $\text{CuI}$  and poly (bipyridine) strands. *Angewandte Chemie International Edition in English*, 27(8), 1095-1097.

- Lehn, J. M. (1995). *Supramolecular Chemistry: Concepts and Perspectives*. VCH Verlagsgesellschaft, Weinheim.
- Li, H., Eddaoudi, M., O'Keeffe, M., & Yaghi, O. M. (1999). Design and synthesis of an exceptionally stable and highly porous metal-organic framework. *nature*, 402(6759), 276-279.
- Livage, C., Guillou, N., Marrot, J., & Férey, G. (2001). Construction of two-and three-dimensional coordination polymers from cobalt trimesate. *Chemistry of materials*, 13(11), 4387-4392.
- Luo, L., Xie, Y., Hou, S. L., Ma, Y., & Zhao, B. (2022). Recyclable Luminescent Sensor for Detecting Creatinine Based on a Lanthanide–Organic Framework. *Inorganic Chemistry*, 61(26), 9990-9996.
- Moore, E. G., Samuel, A. P., & Raymond, K. N. (2009). From antenna to assay: lessons learned in lanthanide luminescence. *Accounts of chemical research*, 42(4), 542-552.
- Muller, G. (2009). Luminescent chiral lanthanide (III) complexes as potential molecular probes. *Dalton Transactions*, (44), 9692-9707.
- Nangia, A. (2010). Supramolecular chemistry and crystal engineering. *Journal of chemical sciences*, 122(3), 295-310.
- O'Keeffe, M., & Yaghi, O. M. (2012). Deconstructing the crystal structures of metal–organic frameworks and related materials into their underlying nets. *Chemical reviews*, 112(2), 675-702.
- Palagummi, S., & Yuan, F. G. (2016). Magnetic levitation and its application for low frequency vibration energy harvesting. In *Structural Health Monitoring (SHM) in Aerospace Structures* (pp. 213-251). Woodhead Publishing.
- Peedikakkal, A. M. P., & Vittal, J. J. (2010). Solid-state photochemical behavior of a triple-stranded ladder coordination polymer. *Inorganic chemistry*, 49(1), 10-12.
- Robertson, J. M., & White, J. G. (1945). 164. The crystal structure of coronene: a quantitative X-ray investigation. *Journal of the Chemical Society (Resumed)*, 607-617.
- Robson, R. (2000). A net-based approach to coordination polymers. *Journal of the Chemical Society, Dalton Transactions*, (21), 3735-3744.



- Serre, C., & Férey, G. (2002). Hydrothermal synthesis, thermal behaviour and structure determination from powder data of a porous three-dimensional europium trimesate:  $\text{Eu}_3(\text{H}_2\text{O})(\text{OH})_6[\text{C}_6\text{H}_3(\text{CO}_2)_3] \cdot 3\text{H}_2\text{O}$  or MIL-63. *Journal of Materials Chemistry*, 12(10), 3053-3057.
- Sleiman, H., Baxter, P. N., Lehn, J. M., Airola, K., & Rissanen, K. (1997). Multicomponent self-assembly: Generation of rigid-rack multimetallic pseudorotaxanes. *Inorganic chemistry*, 36(21), 4734-4742.
- Soldatov, D. V., & Terekhova, I. S. (2005). Supramolecular chemistry and crystal engineering. *Journal of Structural Chemistry*, 46(1), S1-S8.
- Steed, J. W., & Atwood, J. L. (2022). *Supramolecular chemistry*. John Wiley & Sons.
- Thio, Y., Toh, S. W., Xue, F., & Vittal, J. J. (2014). Self-assembly of a 15-nickel metallamacrocyclic complex derived from the L-glutamic acid Schiff base ligand. *Dalton Transactions*, 43(16), 5998-6001.
- Wang, Y., Zheng, K., Song, S., Fan, D., Zhang, H., & Liu, X. (2018). Remote manipulation of upconversion luminescence. *Chemical Society Reviews*, 47(17), 6473-6485.
- Xia, Y., Xia, X., & Peng, H. C. (2015). Shape-controlled synthesis of colloidal metal nanocrystals: thermodynamic versus kinetic products. *Journal of the American Chemical Society*, 137(25), 7947-7966.
- Zaworotko, M. J. (1994). Crystal engineering of diamondoid networks. *Chemical Society Reviews*, 23(4), 283-288.
- Zaworotko, M. J. (2001). Superstructural diversity in two dimensions: crystal engineering of laminated solids. *Chemical Communications*, (1), 1-9.
- Zhao, Y., Li, K., & Li, J. (2010). Solvothermal synthesis of multifunctional coordination polymers. *Zeitschrift für Naturforschung B*, 65(8), 976-998.

## CHAPTER 3

### MATERIALS AND METHODS

#### 3.1 Material

All chemicals and solvents listed in Tables 3.1 and 3.2 were reagent-grade reliability and acquired without further purification from commercial sources.

**Table 3.1**

*The chemicals used in the present study*

Chemicals	Formula	MW (g/mol)	% Purity	Company
Praseodymium(III) nitrate hexahydrate	$\text{Pr}(\text{NO}_3)_3 \cdot 6\text{H}_2\text{O}$	435.01	99.9%	Sigma-Aldrich, USA
Neodymium(III) nitrate hexahydrate	$\text{Nd}(\text{NO}_3)_3 \cdot 6\text{H}_2\text{O}$	438.24	99.9%	Sigma-Aldrich, USA
Samarium(III) nitrate hexahydrate	$\text{Sm}(\text{NO}_3)_3 \cdot 6\text{H}_2\text{O}$	444.37	99.9%	Acros organics, USA
Europium(III) nitrate hexahydrate	$\text{Eu}(\text{NO}_3)_3 \cdot 6\text{H}_2\text{O}$	446.38	99.9%	Sigma-Aldrich, USA
Gadolinium(III) nitrate hexahydrate	$\text{Gd}(\text{NO}_3)_3 \cdot 6\text{H}_2\text{O}$	451.36	99.9%	Acros organics, USA
Terbium(III) nitrate hexahydrate	$\text{Tb}(\text{NO}_3)_3 \cdot 6\text{H}_2\text{O}$	453.03	99.9%	Sigma-Aldrich, USA
Dysprosium(III) nitrate hexahydrate	$\text{Dy}(\text{NO}_3)_3 \cdot 6\text{H}_2\text{O}$	456.60	99.9%	Sigma-Aldrich, USA
Erbium(III) nitrate hexahydrate	$\text{Er}(\text{NO}_3)_3 \cdot 6\text{H}_2\text{O}$	461.20	99.9%	Acros organics, USA
Thulium(III) nitrate hexahydrate	$\text{Tm}(\text{NO}_3)_3 \cdot 6\text{H}_2\text{O}$	463.04	99.9%	Sigma-Aldrich, USA
Ytterbium(III) nitrate hexahydrate	$\text{Yb}(\text{NO}_3)_3 \cdot 6\text{H}_2\text{O}$	467.16	99.9%	Sigma-Aldrich, USA
Lutetium(III) nitrate hexahydrate	$\text{Lu}(\text{NO}_3)_3 \cdot 6\text{H}_2\text{O}$	469.07	99.9%	Sigma-Aldrich, USA
Benzhydrazide	$\text{C}_6\text{H}_5\text{CONHNH}_2$	136.15	98%	Sigma-Aldrich, USA

**Table 3.2***The organic solvents used in the present study*

Reagents	Formula	MW (g/mol)	% Purity	Company
Acetone	C <sub>3</sub> H <sub>6</sub> O	58.08	98%	TCI Japan
Acetonitrile	C <sub>2</sub> H <sub>3</sub> N	41.05	98%	TCI Japan
Benzene	C <sub>6</sub> H <sub>6</sub>	78.11	98%	TCI Japan
Dioxane	C <sub>4</sub> H <sub>8</sub> O <sub>2</sub>	88.11	98%	TCI Japan
Chloroform	CHCl <sub>3</sub>	119.38	98%	TCI Japan
Dichloromethane	CH <sub>2</sub> Cl <sub>2</sub>	84.93	98%	TCI Japan
<i>N,N</i> -Dimethyl formamide	C <sub>3</sub> H <sub>7</sub> NO	73.09	98%	TCI Japan
Dimethyl sulfoxide	(CH <sub>3</sub> ) <sub>2</sub> SO	78.13	98%	TCI Japan
Toluene	C <sub>7</sub> H <sub>8</sub>	92.14	98%	TCI Japan
Tetrahydrofuran	C <sub>4</sub> H <sub>8</sub> O	72.11	98%	TCI Japan
Methanol	CH <sub>4</sub> O	32.04	98%	TCI Japan
Ethanol	C <sub>2</sub> H <sub>6</sub> O	46.07	98%	TCI Japan
Isopropanol	C <sub>3</sub> H <sub>7</sub> O	60.09	98%	TCI Japan
Ethyl acetate	C <sub>4</sub> H <sub>8</sub> O <sub>2</sub>	88.11	98%	TCI Japan
Distilled water	H <sub>2</sub> O	18.00		

### 3.2 Instrumentation

#### 3.2.1 Single crystal X-ray diffractometer (SCXRD)

The crystallographic data were collected on a Bruker D8 QUEST CMOS X-ray diffractometer using Mo-K $\alpha$  X-radiation ( $\lambda = 0.71073 \text{ \AA}$ ) and a PHOTON II detector with CPAD technology. The computing details were data collection: APEX3 (Bruker, 2016); cell refinement: SAINT (Bruker, 2016); data reduction: SAINT (Bruker, 2016); program(s) used to solve structure: SHELXT (Sheldrick, 2015a); program(s) used to refine structure: SHELXL (Sheldrick, 2015b); molecular graphics: OLEX2 (Dolomanov et al., 2009); software used to prepare material for publication: OLEX2 (Dolomanov et al., 2009).

### 3.2.2 Powder X-ray diffractometer (PXRD)

The samples was packed into the sample holder and prepared sample by a smooth surface. Variable-temperature powder X-ray diffraction (VT-PXRD) was measured on a Bruker D8 ADVANCE X-ray powder diffractometer using Cu-K $\alpha$  ( $\lambda = 1.5418 \text{ \AA}$ ) in the temperature region 30-800 °C. The room temperature PXRD was carried out on a Bruker D2 Phaser X-ray powder Diffractometer Cu-K $\alpha$  ( $\lambda = 1.5418 \text{ \AA}$ ) at 30 kV and 10 mA in the 2-Theta range 5-60°.

### 3.2.3 Fourier transform infrared spectrometer (ATR-FTIR)

The samples was put into the sample holder. IR spectra were collected on a Perkin-Elmer model Spectrum 100 spectrometer using ATR mode in the range of 650-4000 cm<sup>-1</sup>.

### 3.2.4 CHN analyzer

A LECO CHNS 932 element analyzer was used to determine element (C H N) analysis. The sample was weighed and placed into a tin capsule. During the analysis, the sample is dropped into a furnace held at 1000 °C. The sample was combusted forming gases. The instrument detects the weight percentage of C H N by infrared detection of CO<sub>2</sub>, H<sub>2</sub>O, and by the thermal conductivity of N<sub>2</sub>.

### 3.2.5 Thermogravimetric analyzer (TGA)

TGA thermograms were carried out in N<sub>2</sub> atmosphere on a TGA 55 TA instrument. The measurement was carried out from room temperature to 650 °C at a heating rate of 10 °C min<sup>-1</sup>.

### 3.2.6 Photoluminescence spectrometer (PL)

The samples was packed into the sample holder and prepared sample by a smooth surface. Solutions can be performed using standard 10 mm path length cuvettes (3 mL). The luminescence spectra and emission decay curves were determined at room temperature with a Horiba Scientific model FluoroMax-4 spectrofluorometer.

### 3.2.7 Superconducting quantum interference device (SQUID)

Magnetic susceptibility measurements were taken with a Quantum Design SQUID magnetometer that was calibrated against a standard palladium sample. The data was collected between 2 and 300 K, with the temperature scan rate set to 2.0 K min<sup>-1</sup>. Continuous measurements were taken with a field of 5000 Oe applied.

### **3.2.8 X-Ray fluorescence spectrometer (XRF)**

The sample was packed into the sample holder and prepared sample by a smooth surface. The XRF experiment was collected utilizing a Bruker S6 JAGUAR WDXRF spectrometer with a 400W 17 mA X-ray source equipped under helium.

### **3.2.9 Gas adsorption**

The sample was packed into the sample holder and activated sample. A Quantachrome iSorb HP1 analyzer was used to measure high-pressure CO<sub>2</sub> adsorption isotherms in the pressure range of 0.1-50 bar at 298 K. The adsorption measurements were performed using ultrapure (99.995%) CO<sub>2</sub> gas.

## **3.3 References**

- Bruker (2016). APEX3, SAINT, and SADABS. Bruker AXS Inc., Madison, Wisconsin, USA.
- Dolomanov, O.V., Bourhis, L.J., Gildea, R.J, Howard, J.A.K. & Puschmann, H. (2009), J. Appl. Cryst. 42, 339–341.
- Sheldrick, G.M. (2015a). Acta Cryst. A71, 3–8.
- Sheldrick, G.M. (2015b). Acta Cryst. C71, 3–8.

## CHAPTER 4

### THE COORDINATION POLYMERS OF LANTHANIDE(III) IONS WITH BENZHYDRAZIDE

#### 4.1 Introduction

Lanthanide coordination chemistry has received a lot of attention in the last two decades because of the extremely interesting structures and practical benefits in luminescence, magnetism, catalysis, and gas adsorption (Feng *et al*, 2020; Bernot *et al*, 2010) of lanthanide coordination complexes. These materials can be synthesized using simple solvothermal methods from a wide range of organic ligands and lanthanide metal ions, and their structures were described using laboratory X-ray crystallography. Designing and synthesizing controllable lanthanide complexes is more challenging than the synthesis of complexes of transition metal ions because the extremely hard lanthanide ions have more coordination numbers and higher adaptable coordination geometries than transition metal ions. (Chen *et al*, 2010; Eliseeva *et al*, 2010; da Rosa *et al*, 2020). The nature of organic ligands may influence lanthanide assemblies' final structure and coordination number to some extent. (i.e. conformation, binding modes or configurations, and ability to form intermolecular interactions) and synthetic parameters (i.e. metal-ligand ratio, solvent, temperature, time, and pH). (Kumar *et al*, 2020; Liu *et al*, 2020; Zheng *et al*, 2020). There have been numerous reports of lanthanide coordination complexes with extraordinary structures and intriguing properties. Nevertheless, constructing a structure and property relationship in sample is critical in materials science and is still a tough challenge in crystal engineering.

Despite the fact that lanthanides have high affinity for hard donor atoms, many revealed lanthanide CPs are built with organic ligands comprising oxygen-donor atoms. Polycarboxylic acids are commonly utilized in the synthesis of different lanthanide complexes, particularly in optical, magnetic, and energy materials research. (Xu *et al*, 2016; Cui *et al*, 2018; Feng *et al*, 2019; Muldoon *et al*, 2020; Zheng *et al*, 2015). In the meantime, luminescent lanthanide-based porous coordination polymers have been developed using ligands bearing both *N* and *O* donors, such as pyridine

dicarboxylic acid and nicotinic acid (Sairenji *et al*, 2016; Fan *et al*, 2018). Because of the irregular distribution of nitrogen atoms in the framework structures, it has seemed that some complexes with this type of ligand may be extremely specific in its recognition of chemical analytes as well as selective gas adsorption (Chen *et al*, 2009; Jiang *et al*, 2018).

Even though, hydrothermal *in situ* ligand formation is an efficient crystallization process approach in the isolation of pure phases of new coordination structures, especially ones that are inaccessible via conventional conditions (Chen *et al*, 2007). This strategic approach involves molecular bond-breaking and bond-reforming steps that allow more stable thermodynamic substances result with the advancement of this technique, a diversity of new coordination assemblies with *in situ*-generated ligands have been discovered, specially tetrazole, and triazine-based complexes, have been successfully synthesized (Debatin *et al*, 2010; Liu *et al*, 2010; Zhu *et al*, 2011).

We have focused on developing new crystalline coordination materials (Chainok *et al*, 2018; Phadungsak *et al*, 2019; Ponjan *et al*, 2020) with the desire to gain a better understanding of their structure-property relationships, which aids in rationalizing the structures and achieving desired functionalities. As part of this effort, we choose benzhydrazide (bzz) as the linker for the inclusion complexes with lanthanide(III) ions as a result of our ongoing investigation into this subject. This ligand was selected because it is made up of N-hydrazide and O-carbonyl, that also assist to saturate lanthanide coordination sites. Moreover, the bzz ligand shows chelating ability and possibilities for the establishment of strong hydrogen bonds. There have been only a few reported lanthanide coordination complexes with this type of ligand, and these structures are indeed discrete mononuclear structures (Zinner *et al*, 1979; Pangani *et al*, 1984; Theppitak *et al*, 2018; Brandão *et al*, 2020). Three classes of lanthanide coordination complexes were synthesized, structurally characterized, and investigated in terms of fluorescence sensing, and magnetic properties namely,  $[\text{Ln}(\text{bzz})(\text{NO}_3)](\text{NO}_3)_2$  (**1<sub>Ln</sub>**; **Ln** = **1<sub>Sm</sub>**, **2<sub>Eu</sub>**, **3<sub>Gd</sub>**, **4<sub>Tb</sub>**, **5<sub>Dy</sub>**),  $[\text{Ln}(\text{bzz})(\text{ben})_3(\text{H}_2\text{O})] \cdot \text{H}_2\text{O}$  (**2<sub>Ln</sub>**; **Ln** = **6<sub>Pr</sub>**, **7<sub>Nd</sub>**, **8<sub>Sm</sub>**, **9<sub>Eu</sub>**, **10<sub>Gd</sub>**, **11<sub>Tb</sub>**, **12<sub>Dy</sub>**, **13<sub>Er</sub>**), and  $[\text{Ln}_3(\text{ben})_3]$  (**3<sub>Ln</sub>**; **Ln** = **14<sub>Eu</sub>**, **15<sub>Gd</sub>**, **16<sub>Tb</sub>**, **17<sub>Dy</sub>**, **18<sub>Er</sub>**, **19<sub>Tm</sub>**, **20<sub>Yb</sub>**, **21<sub>Lu</sub>**). To our understanding, the synthetic coordination polymers **2<sub>Ln</sub>** and **3<sub>Ln</sub>** are the first examples of hydrazide-based ligands used for creating new lanthanide coordination polymers (LnCPs) via hydrothermal *in*

*situ* carboxylate ligand creation. Surprisingly, when the temperature was increased to 400 °C the crystalline samples of the structure of **2<sub>Ln</sub>** transform into the more stable thermodynamic phase **3<sub>Ln</sub>**. The **9<sub>Eu</sub>**, **14<sub>Eu</sub>**, **11<sub>Tb</sub>**, and **16<sub>Tb</sub>**-based CPs exhibit the emission in the visible light region in the solid state, and all LnCPs exhibit good recyclability as specific fluorescent probes for acetone and Co<sup>2+</sup> ions. Furthermore, the temperature-dependent magnetic properties of **10<sub>Gd</sub>**, **15<sub>Gd</sub>**, **12<sub>Dy</sub>**, and **17<sub>Dy</sub>**-based LnCPs indicate characteristic feature antiferromagnetic interactions between adjacent Ln<sup>3+</sup> ions in these compounds.

## 4.2 Experimental section

### 4.2.1 Materials and methods

All starting materials were of reagent-grade quality and obtained without further purification from commercial sources. Elemental (CHN) analysis was measured with a LECO CHNS 932 element analyzer. FTIR spectra were measured on a Perkin-Elmer model Spectrum 100 spectrometer using ATR mode, in the region of 650-4000 cm<sup>-1</sup>. Variable-temperature powder X-ray diffraction (VT-PXRD) measurements were performed on a Bruker D8 ADVANCE X-ray powder diffractometer using Cu-K $\alpha$  ( $\lambda$  = 1.5418 Å) in the temperature between 30 - 800 °C. The luminescence spectra and emission decay curves were reported at room temperature using a Horiba Scientific model FluoroMax-4 spectrofluorometer. A thermogravimetric analyzer (TGA) was carried out by a Netzsch STA 449C thermal analyzer at a heating rate of 10 °C min<sup>-1</sup> in air. X-ray fluorescence spectroscopy (XRF) was collected on a Bruker S6 JAGUAR WDXRF spectrometer under helium. Magnetic susceptibility data were performed using a Quantum Design SQUID magnetometer calibrated against a standard palladium sample. The data were collected in the temperatures region 2 and 300 K and the scan rate of the temperature was fixed at 2.0 K min<sup>-1</sup>. Measurements were taken continuously under an applied field of 5000 Oe.



#### 4.2.2 Synthesis of $[\text{Ln}(\text{bzz})(\text{NO}_3)](\text{NO}_3)_2$ ( $1_{\text{Ln}}$ ; $\text{Ln} = 1_{\text{Sm}}, 2_{\text{Eu}}, 3_{\text{Gd}}, 4_{\text{Tb}}, 5_{\text{Dy}}$ )

The slow evaporation of isopropanol solutions at room temperature produced single crystals of complexes  $1_{\text{Sm}}-5_{\text{Dy}}$ . A mixture of bzz ligand (27.3 mg, 0.2 mmol) and isopropanol (5 ml) was added dropwise to the  $\text{Ln}(\text{NO}_3)_3 \cdot 6\text{H}_2\text{O}$  (0.1 mmol) dissolved in isopropanol (5 ml), stirred at room temperature for 1 h, filtered and remove any precipitate. Then stand the solution for slow evaporation. After that single crystals were obtained from the liquid phase for two weeks ago.

**$[\text{Sm}(\text{bzz})(\text{NO}_3)](\text{NO}_3)_2$  ( $1_{\text{Sm}}$ ).** Light-yellow block crystals were obtained with a yield of 62.7% (59.1 mg) based on  $\text{Sm}(\text{NO}_3)_3 \cdot 6\text{H}_2\text{O}$ . Anal. calc. for  $\text{C}_{28}\text{H}_{32}\text{N}_{12}\text{O}_{16}\text{Sm}$ : C 35.66% H 3.42% N 17.82%. Found: C 35.43% H 3.41% N 17.35%. IR  $\nu/\text{cm}^{-1}$ , s for strong, m medium, w weak: 3285m, 3194m, 3073w, 2974w, 2895w, 1645m, 1564m, 1440m, 1321s, 1270s, 1199s, 1098m, 1025m, 882m, 691m.

**$[\text{Eu}(\text{bzz})(\text{NO}_3)](\text{NO}_3)_2$  ( $2_{\text{Eu}}$ ).** Colorless block crystals were obtained with a yield of 54.2% (51.2) mg based on  $\text{Eu}(\text{NO}_3)_3 \cdot 6\text{H}_2\text{O}$ . Anal. calc. for  $\text{C}_{28}\text{H}_{32}\text{EuN}_{12}\text{O}_{16}$ : C 35.60% H 3.41% N 17.79%. Found: C 35.08% H 3.25% N 17.68%. IR  $\nu/\text{cm}^{-1}$ : 3188m, 2971m, 1631s, 1605s, 1567s, 1490w, 1319m, 1198m, 1184m, 1039w, 947w, 884m, 802m, 681s.

**$[\text{Gd}(\text{bzz})(\text{NO}_3)](\text{NO}_3)_2$  ( $3_{\text{Gd}}$ ).** Colorless block crystals were obtained with a yield of 69.1% (65.6 mg) based on  $\text{Gd}(\text{NO}_3)_3 \cdot 6\text{H}_2\text{O}$ . Anal. calc. for  $\text{C}_{28}\text{H}_{32}\text{GdN}_{12}\text{O}_{16}$ : C 35.40% H 3.40% N 17.69%. Found: C 35.49% H 3.46% N=17.62%. IR  $\nu/\text{cm}^{-1}$ : 3274m, 3202w, 3070w, 2973w, 2890w, 1644m, 1569m, 1546m, 1434m, 1317s, 1197s, 1115s, 1042m, 887m, 717m, 687m.

**$[\text{Tb}(\text{bzz})(\text{NO}_3)](\text{NO}_3)_2$  ( $4_{\text{Tb}}$ ).** Colorless block crystals were obtained with a yield of 71.8% (68.3 mg) based on  $\text{Tb}(\text{NO}_3)_3 \cdot 6\text{H}_2\text{O}$ . Anal. calc. for  $\text{C}_{28}\text{H}_{32}\text{N}_{12}\text{O}_{16}\text{Tb}$ : C 35.34% H 3.39% N 17.66%. Found: C 35.49% H 3.31% N 17.64%. IR  $\nu/\text{cm}^{-1}$ : 3272m, 3074w, 2968w, 1643m, 1603m, 1568m, 1436s, 1328s, 1193s, 1111s, 888m, 717m, 689m.

**$[\text{Dy}(\text{bzz})(\text{NO}_3)](\text{NO}_3)_2$  ( $5_{\text{Dy}}$ ).** Colorless block crystals were obtained with a yield of 65.6% (62.6 mg) based on  $\text{Dy}(\text{NO}_3)_3 \cdot 6\text{H}_2\text{O}$ . Anal. calc. for  $\text{C}_{28}\text{H}_{32}\text{DyN}_{12}\text{O}_{16}$ : C 35.21% H 3.38% N 17.60%. Found: C 35.29% H 3.27% N 17.55%.

IR  $\nu/\text{cm}^{-1}$ : 3268m, 1643m, 1605m, 1567s, 1491w, 1433m, 1319s, 1198m, 1116m, 948w, 887m, 813w, 688m.

#### 4.2.3 Synthesis of $[\text{Ln}(\text{bzz})(\text{ben})_3(\text{H}_2\text{O})]\cdot\text{H}_2\text{O}$ ( $2_{\text{Ln}}$ ; Ln = **6Pr**, **7Nd**, **8Sm**, **9Eu**, **10Gd**, **11Tb**, **12Dy**, **13Er**)

Crystallines of complexes **6Pr**–**13Er** were prepared with a ratio 1 : 2 lanthanide-to-ligand via hydrothermal synthesis at 110 °C for 48 h. Generally, a mixture of  $\text{Ln}(\text{NO}_3)_3\cdot 6\text{H}_2\text{O}$  (0.1 mmol) and bzz (27.3 mg, 0.2 mmol) dissolve in distilled  $\text{H}_2\text{O}$  (4 mL) were sealed in a Teflon lined reactor, stirred at room temperature for 10 min, sealed in stainless steel autoclave (15 ml), following placed in an oven, heated to 110 °C for 48 h. Room temperature was reached for the reaction mixture. Following filtration, the product was washed with distilled water and dried at room temperature.

**$[\text{Pr}(\text{bzz})(\text{ben})_3(\text{H}_2\text{O})]\cdot\text{H}_2\text{O}$  (**6Pr**)**. Green plate crystals were obtained with a yield of 82.3% (55.6 mg) based on  $\text{Pr}(\text{NO}_3)_3\cdot 6\text{H}_2\text{O}$ . Anal. calc. for  $\text{C}_{28}\text{H}_{27}\text{N}_2\text{O}_9\text{Pr}$ : C 64.35% H 5.92% N 4.84%. Found: C 63.69% H 5.76% N 4.39%. IR  $\nu/\text{cm}^{-1}$ : 3461w, 3309w, 3216w, 3057w, 1641m, 1593s, 1530s, 1383s, 1178m, 1068m, 1022m, 876w, 843w, 713s.

**$[\text{Nd}(\text{bzz})(\text{ben})_3(\text{H}_2\text{O})]\cdot\text{H}_2\text{O}$  (**7Nd**)**. Violet plate crystals were obtained with a yield of 77.3% (52.5 mg) based on  $\text{Nd}(\text{NO}_3)_3\cdot 6\text{H}_2\text{O}$ . Anal. calc. for  $\text{C}_{28}\text{H}_{27}\text{N}_2\text{NdO}_9$ : C 49.47% H 4.00% N 4.12%. Found: C 49.40% H 4.14% N 4.02%. IR  $\nu/\text{cm}^{-1}$ : 3452w, 3305w, 3216w, 3051w, 1638w, 1593s, 1529s, 1493m, 1402s, 1174w, 1069w, 1023w, 878w, 843w, 816w, 714s, 687m.

**$[\text{Sm}(\text{bzz})(\text{ben})_3(\text{H}_2\text{O})]\cdot\text{H}_2\text{O}$  (**8Sm**)**. Yellow plate crystals were obtained with a yield of 85.1% (58.3 mg) based on  $\text{Sm}(\text{NO}_3)_3\cdot 6\text{H}_2\text{O}$ . Anal. calc. for  $\text{C}_{28}\text{H}_{27}\text{N}_2\text{O}_9\text{Sm}$ : C 49.03% H 4.08% N 4.08%. Found: C 49.09% H 4.05% N 4.07%. IR ( $\nu/\text{cm}^{-1}$ ): 3461w, 3309w, 3216w, 3059w, 1641m, 1594s, 1538s, 1487m, 1386s, 1340m, 1178m, 1067m, 1023m, 877w, 844w, 818w, 713s.

**$[\text{Eu}(\text{bzz})(\text{ben})_3(\text{H}_2\text{O})]\cdot\text{H}_2\text{O}$  (**9Eu**)**. Colorless plate crystals were obtained with a yield of 89.5% (61.5 mg) based on  $\text{Eu}(\text{NO}_3)_3\cdot 6\text{H}_2\text{O}$ . Anal. calc. for  $\text{C}_{28}\text{H}_{27}\text{EuN}_2\text{O}_9$ : C 48.92% H 3.96% N 4.07%. Found: C 48.89% H 4.00% N 4.01%. IR  $\nu/\text{cm}^{-1}$ : 3465w, 3158w, 3057w, 2890w, 1641m, 1588m, 1557s, 1510s, 1481s, 1398s, 1303m, 1175w, 1068w, 1022w, 931w, 836w, 707s, 671m.

**[Gd(bzz)(ben)<sub>3</sub>(H<sub>2</sub>O)]·H<sub>2</sub>O (10<sub>Gd</sub>).** Colorless plate crystals were obtained with a yield of 80.7% (55.8 mg) based on Gd(NO<sub>3</sub>)<sub>3</sub>·6H<sub>2</sub>O. Anal. calc. for C<sub>28</sub>H<sub>27</sub>GdN<sub>2</sub>O<sub>9</sub>: C 48.54% H 3.93% N 4.04%. Found: C 48.79% H 3.88% N 4.03%. IR  $\nu/\text{cm}^{-1}$ : 3465w, 3314w, 3216w, 3059w, 2093w, 1642m, 1595s, 1539s, 1489m, 1382s, 1342m, 1178m, 1067m, 1023m, 878w, 844w, 820w, 712s.

**[Tb(bzz)(ben)<sub>3</sub>(H<sub>2</sub>O)]·H<sub>2</sub>O (11<sub>Tb</sub>).** Colorless plate crystals were obtained with a yield of 83.3% (57.8 mg) based on Tb(NO<sub>3</sub>)<sub>3</sub>·6H<sub>2</sub>O. Anal. calc. for C<sub>28</sub>H<sub>27</sub>N<sub>2</sub>O<sub>9</sub>Tb: C 48.42% H 3.92% N 4.03%. Found: C 48.39% H 3.75% N 3.99%. IR  $\nu/\text{cm}^{-1}$ : 3465w, 3314w, 3216w, 3059w, 2039w, 1642m, 1594s, 1539s, 1389s, 1342m, 1179m, 1068m, 1023m, 936w, 879w, 845w, 821w, 713s, 673m.

**[Dy(bzz)(ben)<sub>3</sub>(H<sub>2</sub>O)]·H<sub>2</sub>O (12<sub>Dy</sub>).** Colorless plate crystals were obtained with a yield of 80.1% (55.9 mg) based on Dy(NO<sub>3</sub>)<sub>3</sub>·6H<sub>2</sub>O. Anal. calc. for C<sub>28</sub>H<sub>27</sub>DyN<sub>2</sub>O<sub>9</sub>: C 48.18% H 3.90% N 4.01%. Found: C 48.29% H 3.94% N 4.06%. IR  $\nu/\text{cm}^{-1}$ : 3465w, 3309w, 3216w, 3058w, 1775w, 1642m, 1594s, 1538s, 1489m, 1413s, 1389s, 1342m, 1307m, 1178m, 1068m, 1023m, 936w, 879w, 816w, 714s.

**[Er(bzz)(ben)<sub>3</sub>(H<sub>2</sub>O)]·H<sub>2</sub>O (13<sub>Er</sub>).** Orange plate crystals were obtained with a yield of 83.6% (58.7 mg) based on Er(NO<sub>3</sub>)<sub>3</sub>·6H<sub>2</sub>O. Anal. calc. for C<sub>28</sub>H<sub>27</sub>ErN<sub>2</sub>O<sub>9</sub>: C 47.85% H 3.87% N 3.99%. Found: C 47.57% H 3.77% N 3.73%. IR  $\nu/\text{cm}^{-1}$ : 3467w, 3314w, 3211w, 3058w, 2031w, 1643m, 1594s, 1539s, 1489m, 1391s, 1342m, 1179m, 1068m, 1023m, 881w, 846w, 821w, 714s.

#### 4.2.4 Synthesis of [Ln<sub>3</sub>(ben)<sub>9</sub>] (3<sub>Ln</sub>; Ln = 14<sub>Eu</sub>, 15<sub>Gd</sub>, 16<sub>Tb</sub>, 17<sub>Dy</sub>, 18<sub>Er</sub>,

19<sub>Tm</sub>, 20<sub>Yb</sub>, 21<sub>Lu</sub>)

Crystallines of complexes **14<sub>Eu</sub>-21<sub>Lu</sub>** were synthesized via hydrothermal at 140 °C for 24 h using a procedure analogous to **2Ln** above.

**[Eu<sub>3</sub>(ben)<sub>9</sub>] (14<sub>Eu</sub>).** Colorless plate crystals were obtained with a yield of 73.3% (113.2 mg) based on Eu(NO<sub>3</sub>)<sub>3</sub>·6H<sub>2</sub>O. Anal. calc. for C<sub>63</sub>H<sub>45</sub>Eu<sub>3</sub>O<sub>18</sub>: C 48.94% H 2.93%. Found: C 48.90% H 2.96%. IR  $\nu/\text{cm}^{-1}$ : 3340w, 3060w, 2311w, 1973w, 1594m, 1525s, 1407s, 1307m, 1180w, 1070w, 1025w, 935w, 854w, 712s, 683m.

**[Gd<sub>3</sub>(ben)<sub>9</sub>] (15<sub>Gd</sub>).** Colorless plate crystals were obtained with a yield of 67.9% (106.1 mg) based on Gd(NO<sub>3</sub>)<sub>3</sub>·6H<sub>2</sub>O. Anal. calc. for C<sub>63</sub>H<sub>45</sub>Gd<sub>3</sub>O<sub>18</sub>: C

48.45% H 2.90%. Found: C 48.39% H 2.86%. IR  $\nu/\text{cm}^{-1}$ : 3338w, 3063w, 1595m, 1534s, 1412s, 1309w, 1182w, 856w, 730m, 716s, 670m.

**[Tb<sub>3</sub>(ben)<sub>9</sub>] (16<sub>Tb</sub>).** Colorless plate crystals were obtained with a yield of 71.5% (112.1 mg) based on Tb(NO<sub>3</sub>)<sub>3</sub>·6H<sub>2</sub>O. Anal. calc. for C<sub>63</sub>H<sub>45</sub>O<sub>18</sub>Tb<sub>3</sub>: C 48.29% H 2.89%. Found: C 48.23% H 2.81%. IR  $\nu/\text{cm}^{-1}$ : 3395w, 3058w, 2316w, 1592m, 1525s, 1492m, 1415s, 1306m, 1181w, 1069w, 1025w, 935w, 854w, 710s, 684m.

**[Dy<sub>3</sub>(ben)<sub>9</sub>] (17<sub>Dy</sub>).** Colorless plate crystals were obtained with a yield of 77.1% (121.6 mg) based on Dy(NO<sub>3</sub>)<sub>3</sub>·6H<sub>2</sub>O. Anal. calc. for C<sub>63</sub>H<sub>45</sub>Dy<sub>3</sub>O<sub>18</sub>: C 47.96% H 2.88%. Found: C, 47.90%; H, 2.86%. IR  $\nu/\text{cm}^{-1}$ : 3062w, 2311w, 1594m, 1520s, 1493s, 1392s, 1307m, 1177m, 1070w, 1025w, 938w, 861w, 712s, 684m, 668m.

**[Er<sub>3</sub>(ben)<sub>9</sub>] (18<sub>Er</sub>).** Colorless plate crystals were obtained with a yield of 79.8% (126.9 mg) based on Er(NO<sub>3</sub>)<sub>3</sub>·6H<sub>2</sub>O. Anal. calc. for C<sub>63</sub>H<sub>45</sub>Er<sub>3</sub>O<sub>18</sub>: C 47.53% H 2.85%. Found: C, 47.50%; H, 2.81%. IR  $\nu/\text{cm}^{-1}$ : 3060w, 2311w, 1773w, 1593m, 1520s, 1493m, 1402s, 1307m, 1178w, 1069w, 1025w, 936w, 868w, 820w, 713s, 684m, 669m.

**[Tm<sub>3</sub>(ben)<sub>9</sub>] (19<sub>Tm</sub>).** Colorless plate crystals were obtained with a yield of 75.8% (121.1 mg) based on Tm(NO<sub>3</sub>)<sub>3</sub>·6H<sub>2</sub>O. Anal. calc. for C<sub>63</sub>H<sub>45</sub>O<sub>18</sub>Tm<sub>3</sub>: C 47.38% H 2.84%. Found: C, 47.33%; H, 2.77%. IR  $\nu/\text{cm}^{-1}$ : 3314 w, 3059w, 2316w, 1642w, 1595s, 1492m, 1391s, 1305m, 1179m, 1069m, 1024m, 936w, 846w, 713s, 686m.

**[Yb<sub>3</sub>(ben)<sub>9</sub>] (20<sub>Yb</sub>).** Colorless plate crystals were obtained with a yield of 71.7% (115.9) mg based on Yb (NO<sub>3</sub>)<sub>3</sub>·6H<sub>2</sub>O. Anal. calc. for C<sub>63</sub>H<sub>45</sub>O<sub>18</sub>Yb<sub>3</sub>: C 47.02% H 2.82%. Found: C, 47.14%; H, 2.69%. IR  $\nu/\text{cm}^{-1}$ : 3461w, 3314w, 3211w, 3060w, 2316w, 1775w, 1644w, 1595s, 1532s, 1391s, 1344m, 1309m, 1179m, 1068m, 1024m, 846w, 713s.

**[Lu<sub>3</sub>(ben)<sub>9</sub>] (21<sub>Lu</sub>).** Colorless plate crystals were obtained with a yield of 73.3% (118.4 mg) based on Lu(NO<sub>3</sub>)<sub>3</sub>·6H<sub>2</sub>O. Anal. calc. for C<sub>63</sub>H<sub>45</sub>Lu<sub>3</sub>O<sub>18</sub>: C 46.885% H 2.81%. Found: C, 46.80%; H, 2.86%. IR  $\nu/\text{cm}^{-1}$ : 3063w, 2320w, 1593m, 1521s, 1493s, 1308m, 1177m, 1149w, 1070w, 1025w, 938w, 870w, 845w, 712s, 685m, 667m.

#### 4.2.5 X-ray crystallography

Single crystals of all suitable complexes were mounted on MiTeGen micromounts using paratone oil. Data for X-ray diffraction were obtained the data collection using a Bruker D8 Quest Cmos Photon II at temperature of 296(2) K. The information was obtained using scans, as well as Mo-K radiation ( $\lambda = 0.71073 \text{ \AA}$ ). The total number of runs and images was determined using the APEX3 strategy calculation, and unit cell indexing was refined using SAINT (Bruker, 2016). SAINT and SADABS were used to perform data reduction and absorption correction. PLATON was used to verify the symmetry's integrity. (Spek, 2015). The ShelXT method was used to solve the structure. (Sheldrick, 2015). The structure was refined by least squares using ShelXL (Sheldrick, 2008). All non-hydrogen atoms were refined anisotropically in the final refinement cycles. The positions of all carbon-bound hydrogen atoms were determined by calculating using a rigid-model accurate estimate with  $C-H = 0.93 \text{ \AA}$  and  $U_{iso}(H) = 1.2U_{eq}(C)$ . Whereas all N- and O-bound hydrogen atoms were placed and refined in a various-Fourier map with  $N-H = 0.88 \pm 0.01$  and  $OH = 0.84 \pm 0.01$ , respectively. Two nitrate anions and one benzene ring of the bzz ligand are disordered in **1<sub>Ln</sub>** and were refined using the PART instruction with a split over two sites and a total occupancy of 1.0 for each pair of disordered atoms. The positional disorder of the lattice water molecules in **2<sub>Ln</sub>** was improved into two components with a 0.80: 0.20 occupancy ratio. Four highly disordered benzene rings in **3<sub>Ln</sub>** from various ben ligands were split into two fragments with a total occupancy of 1.0. The crystallographic data for **1<sub>Sm</sub>**-**21<sub>Ln</sub>** are reported in Tables 4.1-4.3.

**Table 4.1***Crystal data and structural refinements for 1<sub>Sm</sub>-5<sub>Dy</sub>*

Identification code (CCDC no.)	1 <sub>Sm</sub> (2064160)	2 <sub>Eu</sub> (2064161)	3 <sub>Gd</sub> (2064162)	4 <sub>Tb</sub> (2064163)	5 <sub>Dy</sub> (2064164)
Empirical formula	C <sub>28</sub> H <sub>32</sub> N <sub>12</sub> O <sub>16</sub> Sm	C <sub>28</sub> H <sub>32</sub> EuN <sub>12</sub> O <sub>16</sub>	C <sub>28</sub> H <sub>32</sub> GdN <sub>12</sub> O <sub>16</sub>	C <sub>28</sub> H <sub>32</sub> N <sub>12</sub> O <sub>16</sub> Tb	C <sub>28</sub> H <sub>32</sub> DyN <sub>12</sub> O <sub>16</sub>
Formula weight	943.00	944.61	949.90	951.57	955.15
Temperature (K)	296	296	296	296	296
Crystal system	Monoclinic	Monoclinic	Monoclinic	Monoclinic	Monoclinic
Space group	<i>C2/c</i>	<i>C2/c</i>	<i>C2/c</i>	<i>C2/c</i>	<i>C2/c</i>
<i>a</i> (Å)	24.726(8)	24.7339(8)	24.6998(8)	24.6726(9)	24.6473(7)
<i>b</i> (Å)	15.346(5)	15.3481(6)	15.3676(5)	15.3731(5)	15.3972(5)
<i>c</i> (Å)	10.498(3)	10.4654(4)	10.4550(4)	10.4434(4)	10.4290(3)
$\beta$ (°)	99.982(10)	100.1570(10)	100.1530(10)	100.1700(10)	100.2710(10)
<i>V</i> (Å <sup>3</sup> )	3923(2)	3910.6(2)	3906.3(2)	3898.9(2)	3894.4(2)
<i>Z</i>	4	4	4	4	4
$\rho_{\text{calcd}}$ (g cm <sup>-3</sup> )	1.597	1.604	1.615	1.621	1.629
GOF on <i>F</i> <sup>2</sup>	1.069	1.051	1.115	1.072	1.124
<i>R</i> <sub>1</sub> , <i>wR</i> <sub>2</sub> [ <i>I</i> > 2 $\sigma$ ( <i>I</i> )]	0.0389, 0.0895	0.0460, 0.0985	0.0337, 0.0812	0.0440, 0.1085	0.0336, 0.0799
<i>R</i> <sub>1</sub> , <i>wR</i> <sub>2</sub> [all data]	0.0594, 0.1018	0.0910, 0.1274	0.0479, 0.0939	0.0569, 0.1233	0.0435, 0.0925

**Table 4.2***Crystal data and structural refinements for 6Pr-13Er*

Identification code (CCDC no.)	<b>6Pr</b> (2064165)	<b>7Nd</b> (2064166)	<b>8Sm</b> (2064167)	<b>9Eu</b> (2064168)
Empirical formula	C <sub>28</sub> H <sub>27</sub> N <sub>2</sub> O <sub>9</sub> Pr	C <sub>28</sub> H <sub>27</sub> N <sub>2</sub> NdO <sub>9</sub>	C <sub>28</sub> H <sub>27</sub> N <sub>2</sub> O <sub>9</sub> Sm	C <sub>28</sub> H <sub>27</sub> EuN <sub>2</sub> O <sub>9</sub>
Formula weight	676.42	679.75	685.86	687.47
Temperature (K)	296	296	296	296
Crystal system,	Monoclinic	Monoclinic	Monoclinic	Monoclinic
Space group	<i>P</i> 2 <sub>1</sub> / <i>c</i>	<i>P</i> 2 <sub>1</sub> / <i>c</i>	<i>P</i> 2 <sub>1</sub> / <i>c</i>	<i>P</i> 2 <sub>1</sub> / <i>c</i>
<i>a</i> (Å)	14.5239(7)	14.5092(4)	14.496(3)	14.4680(5)
<i>b</i> (Å)	19.8515(10)	19.8107(6)	19.771(4)	19.7315(6)
<i>c</i> (Å)	9.9728(4)	9.9678(3)	9.9597(19)	9.9544(3)
$\beta$ (°)	91.725(2)	91.7130(10)	91.561(7)	91.5680(10)
<i>V</i> (Å <sup>3</sup> )	2874.1(2)	2863.84(15)	2853.4(10)	2840.67(16)
<i>Z</i>	4	4	4	4
$\rho_{\text{calcd}}$ (g cm <sup>-3</sup> )	1.563	1.577	1.597	1.607
GOF on <i>F</i> <sup>2</sup>	1.034	1.034	1.041	1.044
<i>R</i> <sub>1</sub> , <i>wR</i> <sub>2</sub> [ <i>I</i> > 2σ( <i>I</i> )]	0.0211, 0.0468	0.0296, 0.0488	0.0270, 0.0512	0.0245, 0.0485
<i>R</i> <sub>1</sub> , <i>wR</i> <sub>2</sub> [all data]	0.0303, 0.0500	0.0509, 0.0536	0.0409, 0.0554	0.0346, 0.0516
Identification code (CCDC no.)	<b>10Gd</b> (2064169)	<b>11Tb</b> (2064170)	<b>12Dy</b> (2064171)	<b>13Er</b> (2064172)
Empirical formula	C <sub>28</sub> H <sub>27</sub> GdN <sub>2</sub> O <sub>9</sub>	C <sub>28</sub> H <sub>27</sub> N <sub>2</sub> O <sub>9</sub> Tb	C <sub>28</sub> H <sub>27</sub> DyN <sub>2</sub> O <sub>9</sub>	C <sub>28</sub> H <sub>27</sub> ErN <sub>2</sub> O <sub>9</sub>
Formula weight	692.76	694.43	698.01	702.77
Temperature (K)	296	296	296	296
Crystal system,	Monoclinic	Monoclinic	Monoclinic	Monoclinic
Space group	<i>P</i> 2 <sub>1</sub> / <i>c</i>	<i>P</i> 2 <sub>1</sub> / <i>c</i>	<i>P</i> 2 <sub>1</sub> / <i>c</i>	<i>P</i> 2 <sub>1</sub> / <i>c</i>
<i>a</i> (Å)	14.4470(6)	14.4340(5)	14.4572(5)	14.3923(8)
<i>b</i> (Å)	19.6992(9)	19.7062(7)	19.7227(7)	19.6216(11)
<i>c</i> (Å)	9.9464(3)	9.9308(3)	9.9440(3)	9.8933(5)
$\beta$ (°)	91.5220(10)	91.4340(10)	91.4680(10)	91.287(2)
<i>V</i> (Å <sup>3</sup> )	2829.69(19)	2823.82(16)	2834.45(16)	2793.2(3)
<i>Z</i>	4	4	4	4
$\rho_{\text{calcd}}$ (g cm <sup>-3</sup> )	1.626	1.633	1.636	1.671
GOF on <i>F</i> <sup>2</sup>	1.062	1.047	1.077	1.136
<i>R</i> <sub>1</sub> , <i>wR</i> <sub>2</sub> [ <i>I</i> > 2σ( <i>I</i> )]	0.0247, 0.0442	0.0262, 0.0472	0.0240, 0.0552	0.0349, 0.0768
<i>R</i> <sub>1</sub> , <i>wR</i> <sub>2</sub> [all data]	0.0392, 0.0478	0.0422, 0.0515	0.0328, 0.0591	0.0492, 0.0811

**Table 4.3***Crystal data and structural refinements for 14<sub>Eu</sub>-21<sub>Lu</sub>*

Identification code (CCDC no.)	<b>14<sub>Eu</sub></b> (2064173)	<b>15<sub>Gd</sub></b> (2064174)	<b>16<sub>Tb</sub></b> (2064175)	<b>17<sub>Dy</sub></b> (2064176)
Empirical formula	C <sub>63</sub> H <sub>45</sub> Eu <sub>3</sub> O <sub>18</sub>	C <sub>63</sub> H <sub>45</sub> Gd <sub>3</sub> O <sub>18</sub>	C <sub>63</sub> H <sub>45</sub> O <sub>18</sub> Tb <sub>3</sub>	C <sub>63</sub> H <sub>45</sub> Dy <sub>3</sub> O <sub>18</sub>
Formula weight	1545.87	1561.74	1566.75	1577.49
Temperature (K)	296	296	296	296
Crystal system	Monoclinic	Monoclinic	Monoclinic	Monoclinic
Space group	<i>P</i> 2 <sub>1</sub> / <i>n</i>	<i>P</i> 2 <sub>1</sub> / <i>n</i>	<i>P</i> 2 <sub>1</sub> / <i>n</i>	<i>P</i> 2 <sub>1</sub> / <i>n</i>
<i>a</i> (Å)	11.4654(4)	11.4601(3)	11.4419(4)	11.4293(6)
<i>b</i> (Å)	22.6148(8)	22.5734(4)	22.5595(7)	22.5089(10)
<i>c</i> (Å)	22.7507(8)	22.7365(5)	22.7629(8)	22.7805(11)
$\beta$ (°)	95.350(2)	95.3270(10)	95.3380(10)	95.250(2)
<i>V</i> (Å <sup>3</sup> )	5873.3(4)	5856.4(2)	5850.2(3)	5835.9(5)
<i>Z</i>	4	4	4	4
$\rho_{\text{calcd}}$ (g cm <sup>-3</sup> )	1.748	1.771	1.779	1.795
GOF on <i>F</i> <sup>2</sup>	1.040	1.062	1.031	1.054
<i>R</i> <sub>1</sub> , <i>wR</i> <sub>2</sub> [ <i>I</i> > 2σ( <i>I</i> )]	0.0297, 0.0529	0.0245, 0.0410	0.0294, 0.0485	0.0189, 0.0390
<i>R</i> <sub>1</sub> , <i>wR</i> <sub>2</sub> [all data]	0.0492, 0.0584	0.0365, 0.0446	0.0534, 0.0542	0.0249, 0.0410
Identification code (CCDC no.)	<b>18<sub>Er</sub></b> (2064177)	<b>19<sub>Tm</sub></b> (2064178)	<b>20<sub>Yb</sub></b> (2064179)	<b>21<sub>Lu</sub></b> (2064180)
Empirical formula	C <sub>63</sub> H <sub>45</sub> Er <sub>3</sub> O <sub>18</sub>	C <sub>63</sub> H <sub>45</sub> O <sub>18</sub> Tm <sub>3</sub>	C <sub>21</sub> H <sub>15</sub> O <sub>6</sub> Yb	C <sub>63</sub> H <sub>45</sub> Lu <sub>3</sub> O <sub>18</sub>
Formula weight	1591.77	1596.78	536.37	1614.90
Temperature (K)	296	296	296	296
Crystal system	Monoclinic	Monoclinic	Monoclinic	Monoclinic
Space group	<i>P</i> 2 <sub>1</sub> / <i>n</i>	<i>P</i> 2 <sub>1</sub> / <i>n</i>	<i>P</i> 2 <sub>1</sub> / <i>n</i>	<i>P</i> 2 <sub>1</sub> / <i>n</i>
<i>a</i> (Å)	11.3816(4)	11.3218(8)	11.2721(3)	11.2439(14)
<i>b</i> (Å)	22.4859(8)	22.5530(15)	22.5893(7)	22.591(2)
<i>c</i> (Å)	22.8587(7)	22.9222(18)	23.0294(6)	23.111(3)
$\beta$ (°)	95.3050(10)	95.884(3)	96.1110(10)	96.311(5)
<i>V</i> (Å <sup>3</sup> )	5825.1(3)	5822.1(7)	5830.6(3)	5834.9(12)
<i>Z</i>	4	4	4	4
$\rho_{\text{calcd}}$ (g cm <sup>-3</sup> )	1.815	1.822	1.833	1.838
GOF on <i>F</i> <sup>2</sup>	1.038	1.040	1.030	1.124
<i>R</i> <sub>1</sub> , <i>wR</i> <sub>2</sub> [ <i>I</i> > 2σ( <i>I</i> )]	0.0279, 0.0468	0.0288, 0.0467	0.0287, 0.0495	0.0256, 0.0504
<i>R</i> <sub>1</sub> , <i>wR</i> <sub>2</sub> [all data]	0.0491, 0.0517	0.0500, 0.0536	0.0458, 0.0551	0.0370, 0.0572



## 4.3 Results and discussion

### 4.3.1 Synthesis

The condition of the bzz ligand with hydrated  $\text{Ln}(\text{NO}_3)_3$  under different synthetic conditions yielded different products. There are three types with all of twenty-one lanthanide coordination polymers, as shown in Figure 4.1. The formation of the products has already shown the critical roles of solvents, reaction temperatures, and synthetic methods in understanding the structure of coordination polymers. The single crystal structure determination of the discrete complexes  $\mathbf{1}_{\text{Sm}}\text{-}\mathbf{5}_{\text{Dy}}$  in series  $\mathbf{1}_{\text{Ln}}$ . The complexes were crystallized by a slow evaporation method in isopropanol at room temperature. Complexes in series  $\mathbf{1}_{\text{Ln}}$  are moisture-sensitive and can solidify after 10 hours in the air. Additionally, the structure of the polymeric complexes in the series  $\mathbf{2}_{\text{Ln}}$   $\mathbf{6}_{\text{Pr}}\text{-}\mathbf{13}_{\text{Er}}$  and  $\mathbf{3}_{\text{Ln}}$   $\mathbf{14}_{\text{Eu}}\text{-}\mathbf{21}_{\text{Lu}}$  can be effectively handled by carefully choosing the reaction temperature under hydrothermal methods. The initially used bzz ligand was partially transformed into the ben ligand by *in situ* hydrolysis when the reactions were carried out at 110 °C. The cooperation of the ligands bzz and ben leads to the generation of stable products that take the form of polymeric species  $\mathbf{2}_{\text{Ln}}$ . Lastly, when the reaction temperature was raised to 145 °C. The complete hydrolysis of bzz into ben has resulted in the structures of the series  $\mathbf{3}_{\text{Ln}}$ .

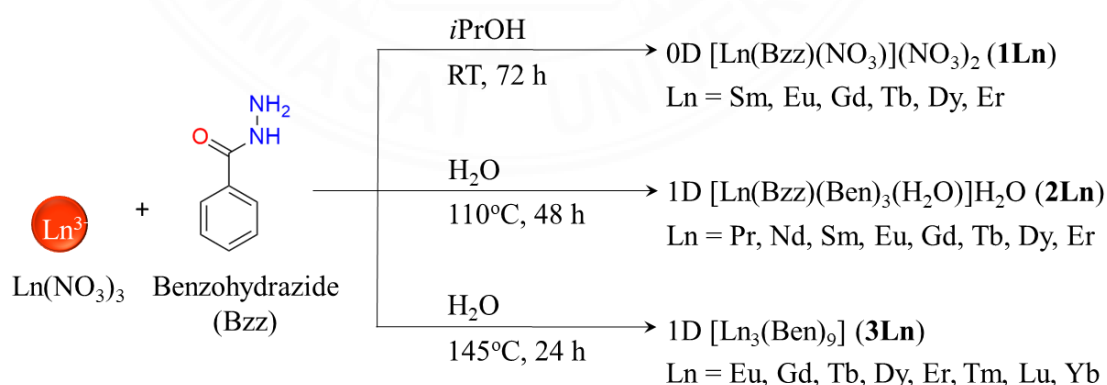
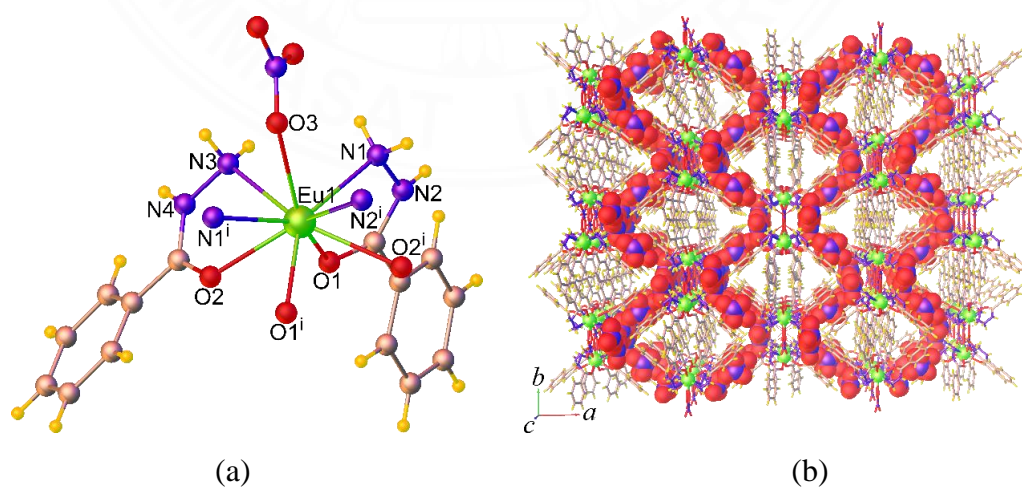


Figure 4.1 Synthetic routes for  $\mathbf{1}_{\text{Ln}}$ ,  $\mathbf{2}_{\text{Ln}}$ , and  $\mathbf{3}_{\text{Ln}}$ .

### 4.3.2 Structural description

#### Crystal structure of $1_{Ln}$

In the single crystal X-ray structural analysis at room temperature, complexes  $1_{Sm}$ - $5_{Dy}$  are isostructural. They crystallize in the monoclinic system with the space group  $C2/c$ . As a result,  $2_{Eu}$  is given as an example for a more detailed description. As shown in Figure 4.2a, the asymmetric unit of  $2_{Eu}$  consists of one  $Eu^{3+}$  ion on a two-fold rotation axis, two bzz ligands, one coordinated  $NO_3^-$  anion, and two isolated  $NO_3^-$  anions. The metal center is coordinated with the hydrazide group of bzz ligand by a  $\mu_2$ - $\kappa^1:\kappa^1$  bidentate chelating coordination mode (Zinner *et al*, 1979; Pangani *et al*, 1984; Theppitak *et al*, 2018; Brandão *et al*, 2020). The  $Eu^{3+}$  ion is nine-coordinated by four N atoms and four O atoms of four different bzz ligands, and one O atom of the coordinated  $NO_3^-$  anion. The coordination geometry of the  $Eu^{3+}$  ion is a distorted tricapped trigonal-prismatic geometry. The Eu–N bond lengths (2.601(7) and 2.630(6) Å) are tiny bit longer than the Eu–O bond lengths (2.380(4)-2.522(8) Å). The bond angles around the central  $Eu^{3+}$  are in the region of 58.8(2) to 145.5(2)°. The Ln–N/O bond lengths for  $1_{Ln}$  are possibly a bit lower from  $1_{Sm}$  to  $5_{Dy}$  as shown in Table 4.4, which is consistent with the lanthanide contraction (Seitz *et al*, 2007; Aguilà *et al*, 2013; Ferru *et al*, 2016; Cotton *et al*, 2017; Gao *et al*, 2017). Complex  $2_{Eu}$  shows the crystal packing showed along the  $c$  axis in Figure 4.2b.



**Figure 4.2** (a) Coordination environment of the  $Eu^{3+}$  ion and (b) perspective view of the crystal packing of  $2_{Eu}$  along the  $c$  axis. Symmetry code: (i)  $1-x, y, 3/2-z$ .

**Table 4.4***Selected bond lengths (Å) and bond angles (°) for  $1_{Sm}$ - $5_{Dy}$* 

	<b>1<sub>Sm</sub></b>	<b>2<sub>Eu</sub></b>	<b>3<sub>Gd</sub></b>	<b>4<sub>Tb</sub></b>	<b>5<sub>Dy</sub></b>
Ln1–O1	2.395(3)	2.380(4)	2.369(3)	2.355(4)	2.343(3)
Ln1–O2	2.420(3)	2.409(4)	2.404(2)	2.392(3)	2.381(3)
Ln1–O3	2.542(7)	2.522(8)	2.508(5)	2.509(7)	2.497(5)
Ln1–N1	2.620(5)	2.601(7)	2.592(4)	2.574(6)	2.559(5)
Ln1–N3	2.644(4)	2.630(6)	2.615(3)	2.595(5)	2.585(4)
O1–Ln1–O1 <sup>i</sup>	103.42(16)	102.78(19)	102.77(12)	102.76(18)	102.63(14)
O1–Ln1–O2	74.46(11)	74.41(14)	74.19(9)	74.10(13)	73.91(10)
O1–Ln1–O2 <sup>i</sup>	71.80(11)	71.43(13)	71.48(9)	71.44(13)	71.35(10)
O1–Ln1–O3	113.12(15)	113.55(19)	113.85(12)	113.98(17)	114.16(13)
O1 <sup>i</sup> –Ln1–O3	143.45(15)	143.66(19)	143.36(12)	143.24(17)	143.18(13)
O1–Ln1–N1 <sup>i</sup>	145.64(14)	145.57(17)	145.34(11)	145.13(16)	145.19(13)
O1–Ln1–N1	63.28(15)	63.91(19)	64.00(12)	64.54(18)	64.73(14)
O1–Ln1–N3 <sup>i</sup>	132.94(12)	132.90(15)	132.98(9)	133.39(14)	133.45(10)
O1–Ln1–N3	75.15(14)	75.43(17)	75.60(11)	75.51(16)	75.70(12)
O2 <sup>i</sup> –Ln1–O2	124.17(16)	123.9(2)	123.59(13)	123.34(19)	122.96(15)
O2–Ln1–O3	118.43(16)	118.7(2)	118.85(13)	118.84(19)	119.09(14)
O2 <sup>i</sup> –Ln1–O3	115.31(17)	115.4(2)	115.56(13)	115.83(19)	115.98(15)
O2–Ln1–N1 <sup>i</sup>	71.28(15)	71.24(18)	71.22(11)	71.07(17)	71.30(13)
O2–Ln1–N1	127.22(16)	127.7(2)	127.80(13)	128.42(19)	128.44(15)
O2–Ln1–N3 <sup>i</sup>	141.63(13)	141.46(17)	141.72(11)	141.46(16)	141.59(12)
O2–Ln1–N3	62.42(11)	62.70(14)	62.80(9)	63.24(13)	63.46(10)
O3–Ln1–N1 <sup>i</sup>	85.95(19)	85.5(2)	85.31(15)	84.8(2)	84.56(17)
O3–Ln1–N1	59.02(18)	58.8(2)	59.10(14)	59.1(2)	58.97(16)
O3–Ln1–N3	61.76(16)	61.8(2)	61.83(13)	61.53(19)	61.49(15)
O3–Ln1–N3 <sup>i</sup>	79.13(17)	79.0(2)	78.54(13)	78.45(19)	78.15(15)
N1–Ln1–N1 <sup>i</sup>	144.7(2)	144.1(3)	144.14(19)	143.5(3)	143.2(2)
N1–Ln1–N3	76.82(16)	76.9(2)	77.19(12)	77.24(19)	77.18(15)
N1–Ln1–N3 <sup>i</sup>	91.14(18)	90.8(2)	90.47(14)	90.1(2)	89.97(17)
N3–Ln1–N3 <sup>i</sup>	139.90(19)	139.8(2)	139.40(15)	139.0(2)	138.70(17)

Symmetry codes: (i)  $-x + 1, y, -z + 3/2$ .

The structures contain extensive intermolecular interactions that are hydrogen bonding and  $\pi$ - $\pi$  stacking interactions. These are in charge of stabilizing and packing of the structure. Figure 4.3a illustrates two adjacent [Eu(bzz)(NO<sub>3</sub>)] butterfly-like complexes that form centrosymmetric dimeric entities via N-H $\cdots$ O hydrogen bonds related to the amine NH<sub>2</sub> group of the bzz ligands and the coordinated NO<sub>3</sub> groups ( $d[\text{N}\cdots\text{O}] = 2.883(11)\text{--}2.945(10)$  Å). The dimers are linked through the use of N-H $\cdots$ O hydrogen bonds between the bzz nitrogen atoms and the isolated NO<sub>3</sub><sup>-</sup> oxygen atoms ( $d[\text{N}\cdots\text{O}] = 2.893(19)\text{--}3.02(3)$  Å), and resulting in a 3D supramolecular structure. Besides,  $\pi$ - $\pi$  stacking interactions on face-to-face (*ff*) between the benzene rings of bzz ligands show  $Cg\cdots Cg$  distances = 3.677(5) and 3.904(4) Å in the packing as Figure 4.3b.

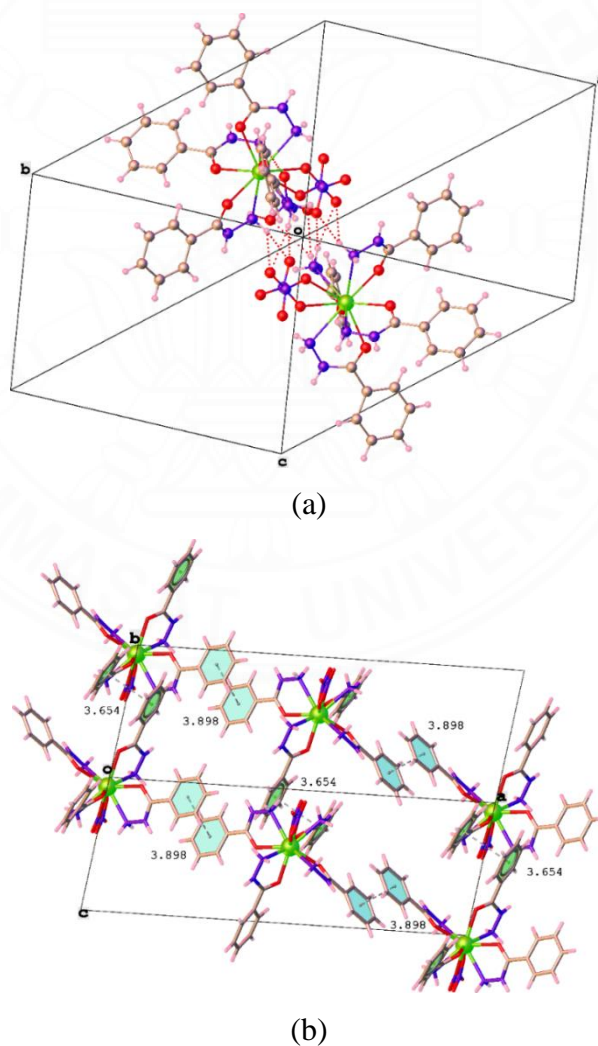


Figure 4.3 Partial packing diagram of  $2_{\text{Eu}}$ , showing (a) N-H $\cdots$ O hydrogen bonds and (b)  $\pi$ - $\pi$  interactions (dashed lines).

### Crystal structure of $2_{Ln}$ .

In series  $2_{Ln}$ , complexes  $6_{Pr}$ – $13_{Er}$  are isostructural structures. They are crystallized in the monoclinic system with the space group  $P2_1/c$ . As an illustration, the crystal structure of **9** is described in detail. The asymmetric unit of  $9_{Eu}$  includes one  $Eu^{3+}$  ion, one bzz ligand, three ben ligands, one coordinated water molecule, and one lattice water molecule, as shown in Figure 4.4a. The  $Eu^{3+}$  ion in  $9_{Eu}$  is eight-coordinated with trigonal-dodecahedron geometry, to be encompassed by one N atom and one O atom of the bzz ligand, five O atoms from five different ben ligands, and one O atom from the coordinated water molecule. The Eu–N bond length in  $9_{Eu}$  is 2.6207(16) Å, whereas the Eu–O bond lengths range from 2.2992(13) to 2.5175(15) Å. The bond angles around the central  $Eu^{3+}$  ion are between 61.53(4) and 146.26(5)°. Like  $1_{Ln}$ , the Ln–N/O bond lengths in  $2_{Ln}$ , as shown in Table 4.5, decrease along with increasing lanthanide atomic numbers from 6 - 13, because of the effect of lanthanide contraction (Seitz *et al*, 2007; Aguilà *et al*, 2013; Ferru *et al*, 2016; Cotton *et al*, 2017; Gao *et al*, 2017).

The coordination mode of complex  $9_{Eu}$  shows a  $\mu_2$ - $\kappa^1$ : $\kappa^2$  bidentate chelation of the bzz ligand, while the ben ligand has two kinds of coordination fashions *viz.* the  $\mu_2$ - $\kappa^1$ : $\kappa^2$  bidentate chelating and  $\kappa^1$  monodentate that depart an uncoordinated carboxylate group. The  $Eu^{3+}$  ion is fastened by a bidentate chelating bzz ligand and a monodentate ben ligand. In addition, the bidentate ben ligands bridge two symmetry-related  $Eu^{3+}$  ions via the carboxylate group into a 1D chain-like structure running parallel to the crystallographic *a* axis as shown in Figure 4.4b. The Eu···Eu distance is 4.9816(2) Å. There are classical O–H···O ( $d[O\cdots O] = 2.638(2)$ – $3.117(4)$  Å) and N–H···O ( $d[N\cdots O] = 2.817(14)$ – $3.122(2)$  Å) hydrogen bonds engaging the amine group and water molecules as the donors and the acyl and carboxylate groups as acceptors in Figure 4.5a, which aids in the spatial stabilization of the 1D chain. The lattice water molecules are situated between the chains along the *a* axis and act as both hydrogen bond donors and acceptors capable of engaging noncovalently with the amine groups. The coordinated water molecules include the acyl groups of neighboring chains. Consequently, a 2D wrinkled layer is created. The shortest interlayer distance between the  $Eu^{3+}$  centers is 10.824(2) Å. Additionally, edge-to-face (*ef*) N–H··· $\pi$  interaction of the hydrogen atom of amine and the aromatic centroid (Cg) of the ben molecule

**Table 4.5***Selected bond lengths (Å) and bond angles (°) for 6Pr-13Er*

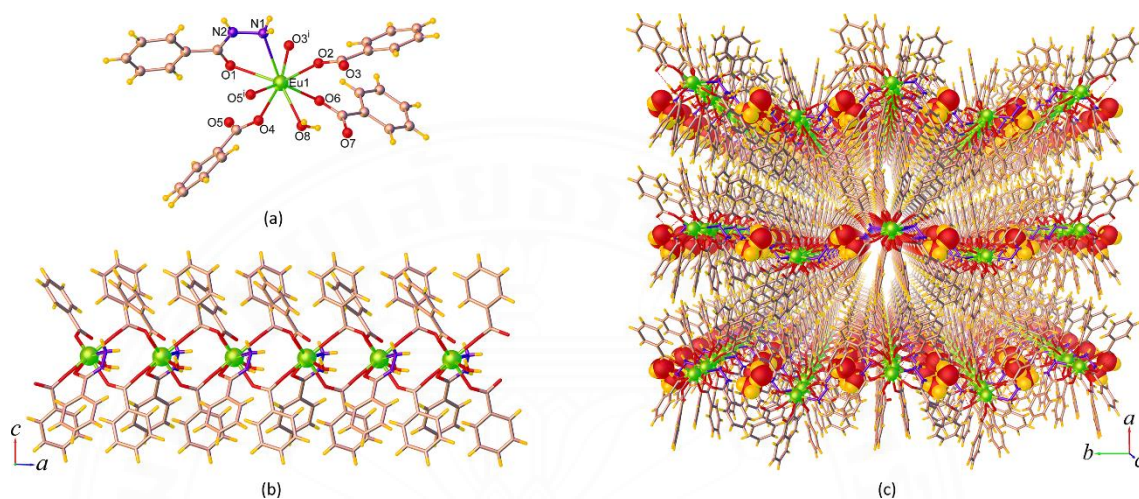
	6Pr	7Nd	8Sm	9Eu	10Gd	11Tb	12Dy	13Er
Ln1–O1	2.5567(14)	2.5355(16)	2.511(2)	2.4965(13)	2.481(2)	2.470(2)	2.4857(18)	2.440(4)
Ln1–O2	2.3781(16)	2.3607(17)	2.326(2)	2.3124(13)	2.298(2)	2.279(2)	2.2974(19)	2.250(4)
Ln1–O3 <sup>i</sup>	2.4395(15)	2.4227(17)	2.396(2)	2.3825(13)	2.366(2)	2.352(2)	2.3629(18)	2.311(4)
Ln1–O4	2.3531(15)	2.3406(17)	2.312(2)	2.2992(13)	2.288(2)	2.269(2)	2.2837(18)	2.233(4)
Ln1–O5 <sup>ii</sup>	2.4203(16)	2.4088(17)	2.382(2)	2.3682(13)	2.354(2)	2.339(2)	2.3508(19)	2.303(4)
Ln1–O6	2.4085(15)	2.3987(16)	2.381(2)	2.3717(13)	2.362(2)	2.354(2)	2.3604(18)	2.326(4)
Ln1–O8	2.5775(17)	2.5600(19)	2.531(3)	2.5175(15)	2.501(2)	2.490(2)	2.499(2)	2.446(4)
Ln1–N1	2.6887(17)	2.670(2)	2.638(3)	2.6207(16)	2.609(3)	2.592(2)	2.606(2)	2.554(4)
O1–Ln1–O8	136.43(6)	136.11(7)	135.52(9)	135.18(5)	135.00(9)	134.59(9)	134.84(7)	133.79(15)
O1–Ln1–N1	60.09(5)	60.52(6)	61.23(8)	61.53(4)	61.80(7)	62.12(8)	61.82(6)	62.99(13)
O2–Ln1–O1	131.71(5)	132.12(6)	132.63(8)	132.92(5)	133.21(7)	133.38(8)	133.14(7)	134.10(13)
O2–Ln1–O3 <sup>i</sup>	86.11(6)	86.39(6)	86.54(9)	86.96(5)	87.09(8)	87.38(8)	87.17(7)	87.83(14)
O2–Ln1–O5 <sup>ii</sup>	96.49(6)	96.55(6)	96.70(8)	96.62(5)	96.65(8)	96.60(8)	96.66(7)	96.76(14)
O2–Ln1–O6	82.93(6)	82.73(6)	82.12(8)	82.05(5)	81.93(8)	81.75(8)	81.84(7)	81.22(14)
O2–Ln1–O8	74.82(6)	75.05(7)	75.74(9)	75.88(5)	76.06(8)	76.38(9)	76.23(7)	76.96(15)
O2–Ln1–N1	71.64(5)	71.62(6)	71.44(8)	71.43(5)	71.45(8)	71.30(8)	71.36(7)	71.14(14)
O3 <sup>i</sup> –Ln1–O1	77.50(5)	77.37(6)	77.28(8)	77.22(5)	77.20(8)	77.10(8)	77.15(7)	77.03(13)
O3 <sup>i</sup> –Ln1–O8	145.33(6)	145.62(7)	146.04(9)	146.26(5)	146.32(9)	146.66(9)	146.48(7)	147.08(15)
O3 <sup>i</sup> –Ln1–N1	70.65(5)	70.95(6)	71.32(8)	71.60(5)	71.70(8)	72.04(8)	71.73(7)	72.10(14)
O4–Ln1–O1	74.78(5)	74.68(6)	74.49(8)	74.32(5)	74.12(8)	73.90(8)	74.17(7)	73.39(13)
O4–Ln1–O2	152.90(6)	152.69(7)	152.56(9)	152.49(5)	152.44(8)	152.54(8)	152.47(7)	152.39(15)
O4–Ln1–O3 <sup>i</sup>	108.56(5)	107.95(6)	106.91(8)	106.08(5)	105.76(8)	105.02(8)	105.58(7)	103.96(14)
O4–Ln1–O5 <sup>ii</sup>	86.28(6)	86.69(6)	87.60(8)	88.06(5)	88.31(8)	88.68(8)	88.33(7)	89.33(13)
O4–Ln1–O6	78.72(6)	78.51(6)	78.40(8)	78.17(5)	78.11(8)	78.12(8)	78.14(7)	78.08(14)
O4–Ln1–O8	80.71(6)	80.54(7)	80.26(9)	80.30(5)	80.19(8)	80.21(9)	80.11(7)	79.95(14)
O4–Ln1–N1	134.19(6)	134.55(6)	135.16(8)	135.36(5)	135.45(8)	135.58(8)	135.53(7)	136.07(14)
O5 <sup>ii</sup> –Ln1–O1	71.89(5)	72.08(6)	72.26(8)	72.42(5)	72.45(7)	72.61(7)	72.50(7)	72.56(13)
O5 <sup>ii</sup> –Ln1–O3 <sup>i</sup>	140.99(5)	141.13(6)	141.23(8)	141.49(5)	141.46(8)	141.67(8)	141.58(7)	141.61(14)
O5 <sup>ii</sup> –Ln1–O8	71.07(6)	70.85(7)	70.65(9)	70.37(5)	70.46(8)	70.10(9)	70.25(7)	70.05(14)
O5 <sup>ii</sup> –Ln1–N1	73.34(6)	73.33(6)	73.22(8)	73.33(5)	73.27(8)	73.28(8)	73.42(7)	73.49(14)
O6–Ln1–O1	134.39(5)	134.03(5)	133.75(7)	133.53(4)	133.35(7)	133.30(7)	133.48(6)	133.14(12)
O6–Ln1–O3 <sup>i</sup>	76.69(5)	76.33(6)	75.71(8)	75.39(5)	75.26(8)	75.04(8)	75.27(6)	74.16(14)
O6–Ln1–O5 <sup>ii</sup>	142.31(6)	142.54(6)	143.06(8)	143.12(5)	143.28(8)	143.29(8)	143.15(7)	143.62(14)
O6–Ln1–O8	72.49(6)	72.86(6)	73.35(9)	73.64(5)	73.66(8)	73.95(8)	73.71(7)	74.16(14)
O6–Ln1–N1	139.42(6)	139.15(7)	138.43(9)	138.21(5)	138.08(9)	137.88(8)	137.98(7)	137.11(15)
O8–Ln1–N1	127.01(6)	126.95(6)	127.01(9)	127.03(5)	127.18(8)	127.06(8)	127.20(7)	127.44(14)

Symmetry codes: (i)  $x, -y + 3/2, z - 1/2$ ; (ii)  $x, -y + 3/2, z + 1/2$ .

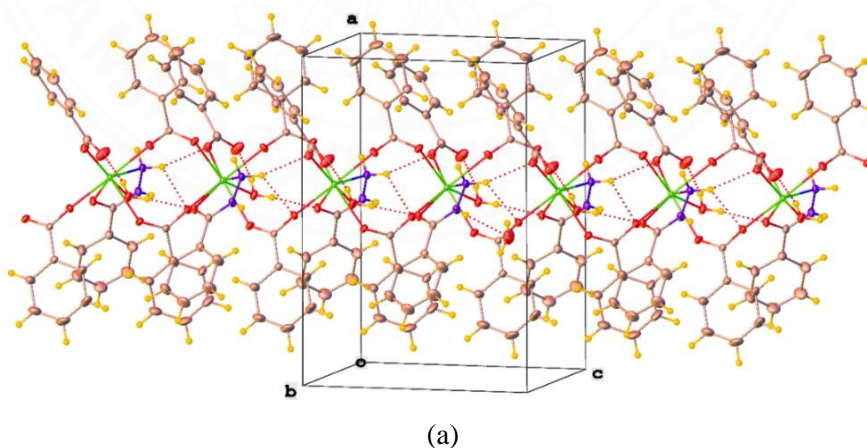
(H $\cdots$ Cg = 3.410(4) Å) shows the additional reinforcement of this layer structure. The 2D layers are stacked together via *ef* C–H $\cdots$  $\pi$  interactions (C $\cdots$ Cg = 3.193(4) Å) as



shown in Figure 4.5b, which contain between the bzz molecule's hydrogen atom and the aromatic ben molecule, resulting in a 3D supramolecular structure, Figure 4.4c. It is worth noting that in **9<sub>Eu</sub>** there are no aromatic  $\pi$ - $\pi$  interactions between the aromatic rings of the ligands.



**Figure 4.4** (a) Coordination environment of  $\text{Eu}^{3+}$  ion, (b) the 1D chain along the  $a$  axis, and (c) perspective view of the packing in **9<sub>Eu</sub>** along the  $c$  axis. Symmetry code: (i)  $x, 3/2 - y, z - 1/2$ .



**Figure 4.5** Partial packing diagram of **9<sub>Eu</sub>**, (a) O-H...O and N-H...O hydrogen bonds and (b) C-H... $\pi$  interactions (dashed lines).

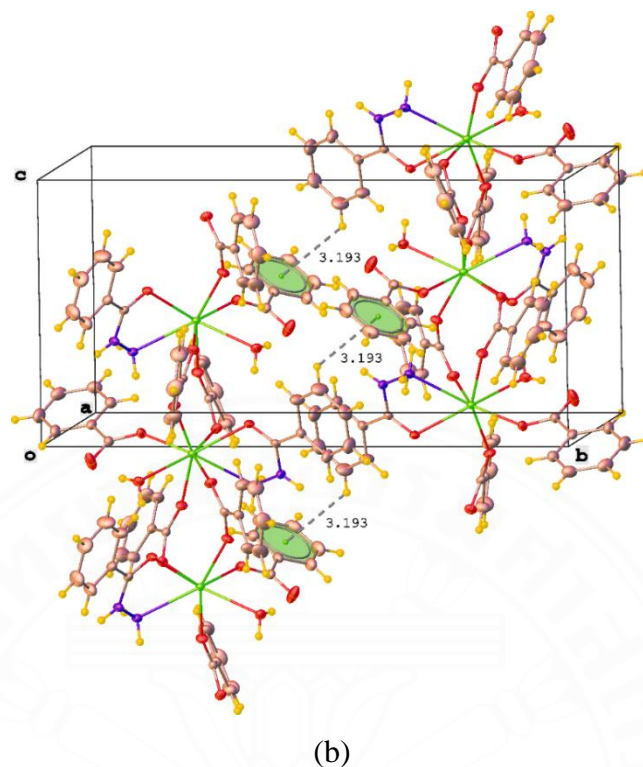


Figure 4.5 (Continued).

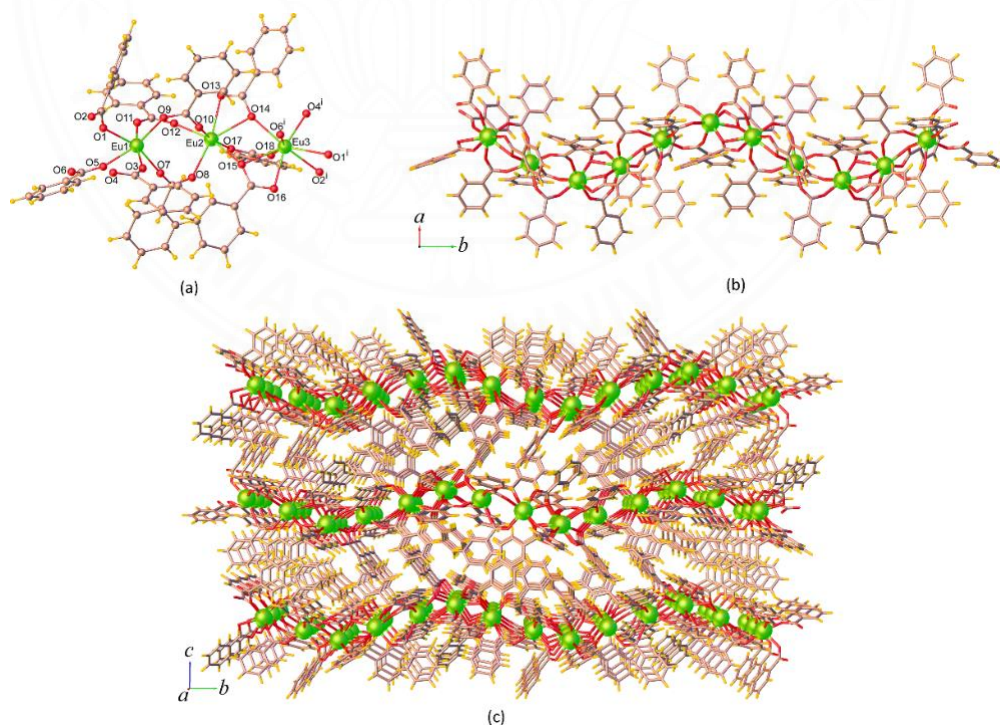
### Crystal structure of **3Ln**.

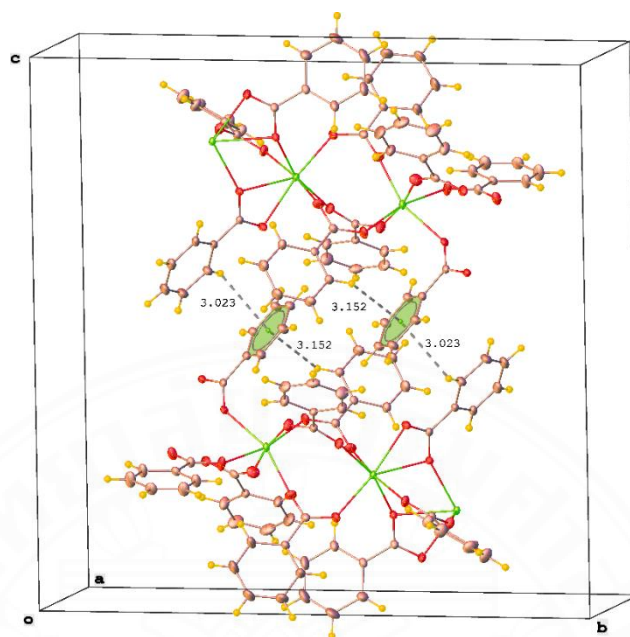
In the **3Ln** series, complexes **14Eu-21Lu** are isostructural. They crystallize in the monoclinic system with the space group  $P2_1/n$ . As a result, the structure of **14Eu** is described in detail as an example. The asymmetric unit of **14Eu** is made up of three crystallographically independent  $\text{Eu}^{3+}$  ions and nine ben ligands without guest molecules in the structure. Noticeably, the coordination numbers of  $\text{Eu}^{3+}$  ions in **14Eu** range from 6-8. As shown in Figure 4.6a, the central Eu1 atom is six-coordinated in a distorted octahedral geometry determined by six O-carboxylate from six different ben ligands. The Eu2 is seven-coordinated with a distorted pentagonal bipyramid geometry formed by seven O-carboxylate from six different ben ligands. Eventually, the Eu3 is eight-coordinated in a distorted dodecahedron geometry surrounded by eight O-carboxylate from six different ben ligands. The Eu–O bond lengths are in the region of 2.246(3)–2.657(3) Å. The O–Eu–O bond angles region 51.94(8) - 170.73(12)°. Comparable to complexes in series **1Ln** and **2Ln**, the average Ln–O bond lengths of **3Ln** (Table 4.6) decrease from **14Eu** to **21Lu** as a result of the



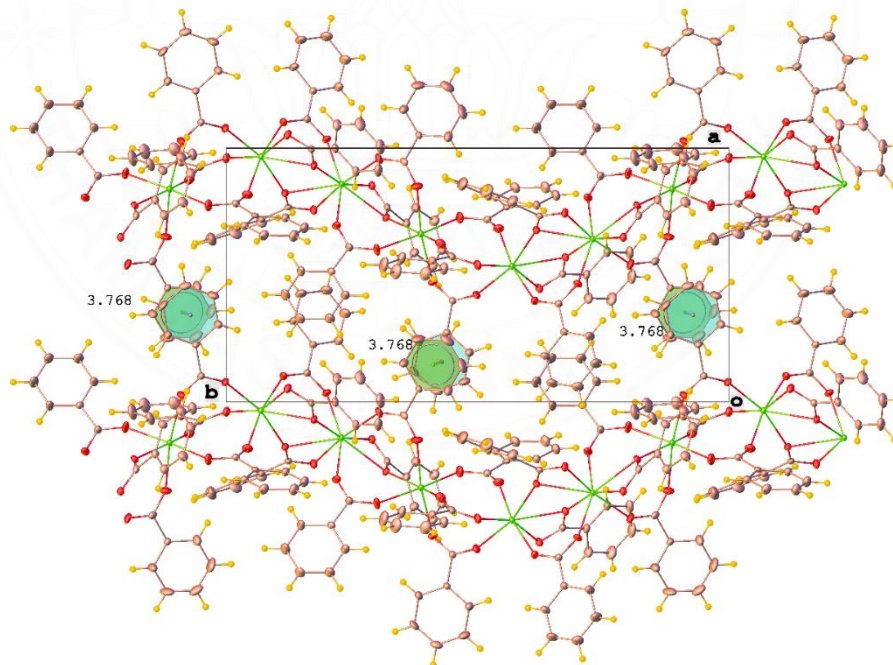
lanthanide contraction effect (Seitz *et al*, 2007; Aguilà *et al*, 2013; Ferru *et al*, 2016; Cotton *et al*, 2017; Gao *et al*, 2017).

The ben ligands in **14**<sub>Eu</sub> connect two different types of coordination modes, the  $\mu_2$ - $\kappa^1$ : $\kappa^1$  chelating bidentate and  $\mu_3$ - $\kappa^1$ : $\kappa^2$  bridging-chelating tridentate. As shown in Figure. 4.6b, these ben ligands are linked to neighboring Eu<sup>3+</sup> ions to form a 1D ribbon chain along the *b* axis. The Eu...Eu distances in the ribbon chains of **14**<sub>Eu</sub> are 4.5549(3) Å of Eu1...Eu2, 4.0139(3) Å of Eu2...Eu3, and 4.3537(3) Å of Eu1...Eu3. These values are all shorter than the Eu...Eu separations found in the chains of **9**<sub>Eu</sub> described above. The chains are built-up by C–H... $\pi$  3.023(5) Å interactions as shown in Figure. 4.7a, and are stacked along the *a* axis by face-to-face (ff)  $\pi$ – $\pi$  interactions Cg...Cg 3.768(4) Å as shown in Figure. 4.7b, showing the formation of a 2D sheet. Besides, stabilization of the structure is achieved by other C–H... $\pi$  3.127(4) Å and  $\pi$ – $\pi$  interactions Cg...Cg 4.175(4) Å, which link the sheets along the *c* axis to form a supramolecular 3D network as shown in Figure. 4.6c. The intersheet Eu...Eu separation in **14**<sub>Eu</sub> is 11.103(4) Å.





(a)



(b)

Figure 4.7 Partial packing diagram of  $14_{Eu}$ , showing (a) C-H... $\pi$  and (b)  $\pi$ - $\pi$  interactions.

**Table 4.6***Selected bond lengths (Å) and bond angles (°) for 14Eu-21Lu*

	<b>14Eu</b>	<b>15Gd</b>	<b>16Tb</b>	<b>17Dy</b>	<b>18Er</b>	<b>19Tm</b>	<b>20Yb</b>	<b>21Lu</b>
Ln1–O1	2.388(3)	2.370(2)	2.349(2)	2.338(2)	2.273(3)	2.298(7)	2.236(10)	2.204(14)
Ln1–O3	2.246(3)	2.23 (3)	2.225(3)	2.209(2)	2.182(3)	2.167(2)	2.152(3)	2.144(3)
Ln1–O5	2.261(3)	2.250(2)	2.239(2)	2.229(2)	2.210(3)	2.200(2)	2.199(3)	2.189(3)
Ln1–O7	2.254(3)	2.232(3)	2.223(3)	2.216(2)	2.193(3)	2.176(2)	2.171(3)	2.165(3)
Ln1–O9	2.305(3)	2.291(2)	2.279(2)	2.266(2)	2.241(3)	2.226(2)	2.213(3)	2.208(3)
Ln1–O11	2.287(3)	2.278(2)	2.262(3)	2.247(2)	2.222(3)	2.207(2)	2.191(3)	2.180(3)
Ln2–O8	2.341(3)	2.329(2)	2.312(2)	2.300(2)	2.271(2)	2.254(2)	2.239(2)	2.231(3)
Ln2–O10	2.280(3)	2.269(2)	2.250(2)	2.240(2)	2.213(3)	2.195(2)	2.184(2)	2.172(3)
Ln2–O12	2.303(2)	2.290(2)	2.277(2)	2.270(2)	2.244(2)	2.231(2)	2.223(2)	2.213(3)
Ln2–O13	2.449(3)	2.440(2)	2.426(2)	2.417(2)	2.391(2)	2.375(2)	2.366(2)	2.356(3)
Ln2–O14	2.527(2)	2.514(2)	2.498(2)	2.4866(19)	2.468(2)	2.4642(19)	2.459(2)	2.452(2)
Ln2–O15	2.378(2)	2.359(2)	2.346(2)	2.3380(19)	2.315(2)	2.306(2)	2.297(2)	2.293(3)
Ln2–O17	2.301(3)	2.295(2)	2.279(2)	2.268(2)	2.245(2)	2.231(2)	2.219(2)	2.210(3)
Ln3–O1 <sup>ii</sup>	2.657(3)	2.659(2)	2.684(3)	2.689(2)	2.882(4)	2.834(13)	3.029(19)	2.170(3)
Ln3–O2 <sup>ii</sup>	2.438(3)	2.428(2)	2.407(2)	2.392(2)	2.331(3)	2.400(9)	2.368(15)	2.239(6)
Ln3–O4 <sup>ii</sup>	2.302(3)	2.291(2)	2.276(2)	2.267(2)	2.241(3)	2.229(2)	2.222(2)	2.215(3)
Ln3–O6 <sup>ii</sup>	2.290(3)	2.284(2)	2.263(2)	2.249(2)	2.214(3)	2.190(2)	2.172(2)	2.158(3)
Ln3–O14	2.403(2)	2.392(2)	2.377(2)	2.3655(19)	2.331(2)	2.310(2)	2.297(2)	2.284(3)
Ln3–O15	2.569(2)	2.555(2)	2.544(2)	2.5312(19)	2.512(2)	2.496(2)	2.492(2)	2.482(2)
Ln3–O16	2.443(3)	2.432(2)	2.412(3)	2.401(2)	2.372(3)	2.361(2)	2.349(3)	2.341(3)
Ln3–O18	2.308(3)	2.297(2)	2.283(2)	2.2713(19)	2.240(2)	2.225(2)	2.212(2)	2.204(2)
O3–Ln1–O1	83.81(11)	84.13(10)	83.62(10)	83.77(9)	84.95(14)	94.9(3)	94.1(2)	92.2(6)
O3–Ln1–O5	97.21(13)	97.57(12)	97.06(12)	97.30(10)	96.36(12)	94.37(10)	94.1(2)	93.32(13)
O3–Ln1–O9	85.32(13)	85.32(11)	85.68(11)	85.87(10)	85.97(12)	86.12(10)	86.52(11)	86.45(13)
O3–Ln1–O11	170.73(12)	170.24(10)	170.37(11)	170.48(9)	171.51(12)	172.89(10)	173.94(11)	174.51(13)
O5–Ln1–O1	77.25(10)	77.40(9)	77.69(9)	77.99(8)	78.93(11)	78.1(2)	79.3(4)	96.1(6)
O5–Ln1–O9	166.58(12)	167.18(10)	168.35(10)	168.78(9)	169.57(11)	171.01(10)	171.83(11)	172.58(13)
O5–Ln1–O11	89.80(12)	89.91(11)	90.27(11)	89.96(10)	90.42(12)	91.47(11)	91.58(12)	91.29(14)
O7–Ln1–O1	161.32(11)	161.41(9)	161.47(10)	161.54(8)	163.80(12)	160.5(3)	162.8(5)	169.51(15)
O7–Ln1–O5	87.37(11)	87.38(10)	87.26(10)	87.12(8)	87.27(10)	87.30(9)	87.33(10)	87.18(12)
O7–Ln1–O9	105.94(11)	105.27(10)	104.20(10)	103.81(8)	102.99(10)	101.68(9)	100.83(10)	100.24(12)
O7–Ln1–O11	86.53(12)	86.67(10)	86.50(11)	86.80(9)	87.00(12)	86.47(10)	86.52(12)	86.70(14)
O9–Ln1–O1	89.97(11)	90.53(9)	91.42(9)	91.72(8)	91.18(11)	93.3(2)	92.7(4)	90.24(15)
O11–Ln1–O1	103.73(10)	103.71(9)	104.13(10)	103.85(8)	101.43(13)	106.6(3)	104.5(5)	93.29(17)
O11–Ln1–O9	89.26(12)	88.76(11)	88.38(11)	88.17(9)	88.28(12)	88.73(11)	89.03(12)	89.36(14)
O8–Ln2–O13	156.08(10)	156.02(8)	155.91(9)	155.68(7)	155.75(9)	156.01(8)	155.91(9)	155.89(10)
O8–Ln2–O14	146.02(9)	146.49(8)	146.82(8)	146.94(7)	147.02(9)	147.21(7)	147.63(8)	147.87(9)
O8–Ln2–O15	82.34(9)	82.55(8)	82.54(8)	82.59(7)	82.44(9)	82.49(7)	82.62(9)	82.59(10)
O10–Ln2–O8	105.19(11)	104.62(9)	104.08(9)	103.86(8)	103.28(10)	103.02(9)	102.61(10)	102.29(11)
O10–Ln2–O12	87.51(11)	87.60(9)	87.56(10)	87.86(8)	88.87(10)	89.55(9)	90.34(10)	91.23(11)
O10–Ln2–O13	88.00(10)	88.16(9)	88.14(9)	88.37(8)	88.36(10)	87.93(9)	87.95(10)	88.03(11)

**Table 4.6** (*Continued*)

	<b>14Eu</b>	<b>15Gd</b>	<b>16Tb</b>	<b>17Dy</b>	<b>18Er</b>	<b>19Tm</b>	<b>20Yb</b>	<b>21Lu</b>
O10–Ln2–O14	88.05(10)	87.92(9)	87.66(9)	87.56(7)	87.08(9)	86.37(8)	85.78(9)	85.51(10)
O10–Ln2–O15	87.23(10)	86.99(9)	86.85(9)	86.49(8)	86.16(9)	86.20(8)	86.13(9)	86.14(10)
O10–Ln2–O17	168.98(11)	169.14(9)	168.72(9)	168.67(8)	168.50(10)	168.10(8)	168.09(9)	168.06(10)
O12–Ln2–O8	83.71(10)	83.25(9)	82.85(9)	82.60(8)	82.23(10)	81.87(8)	81.47(9)	81.23(11)
O12–Ln2–O13	76.91(9)	77.01(8)	76.93(9)	76.86(7)	76.74(9)	76.87(8)	76.83(9)	76.77(10)
O12–Ln2–O14	128.77(9)	128.92(8)	129.21(8)	129.37(7)	129.79(9)	130.11(8)	130.21(9)	130.21(10)
O12–Ln2–O15	163.24(9)	163.00(8)	162.58(8)	162.39(7)	162.34(9)	162.43(8)	162.52(9)	162.66(10)
O13–Ln2–O14	51.94(8)	52.00(7)	52.39(8)	52.63(6)	53.14(8)	53.32(7)	53.46(8)	53.50(9)
O15–Ln2–O13	118.77(8)	118.89(7)	119.33(8)	119.58(7)	119.98(9)	119.93(7)	120.06(8)	120.20(9)
O15–Ln2–O14	66.91(8)	66.96(7)	67.00(8)	67.02(6)	66.89(8)	66.65(7)	66.63(8)	66.71(9)
O17–Ln2–O8	82.48(11)	82.88(9)	83.35(9)	83.44(8)	84.07(10)	84.54(8)	85.00(9)	85.34(11)
O17–Ln2–O12	101.37(10)	101.24(9)	101.94(9)	101.82(8)	101.00(10)	100.72(9)	99.94(10)	99.08(11)
O17–Ln2–O13	87.69(10)	87.71(9)	88.12(9)	88.12(8)	88.19(10)	88.57(9)	88.55(10)	88.49(11)
O17–Ln2–O14	81.31(9)	81.62(8)	81.64(8)	81.75(7)	82.08(9)	66.65(7)	82.99(8)	83.23(9)
O17–Ln2–O15	85.96(9)	86.22(8)	85.71(9)	85.88(7)	86.07(9)	85.70(8)	85.78(9)	85.76(10)
O2 <sup>ii</sup> –Ln3–O1 <sup>ii</sup>	50.50(9)	50.66(8)	50.48(8)	50.38(7)	47.63(11)	37.5(3)	35.6(3)	53.50(9)
O2 <sup>ii</sup> –Ln3–O15	123.13(9)	123.41(8)	123.73(8)	124.04(7)	125.69(9)	127.4(2)	128.5(2)	128.5(2)
O2 <sup>ii</sup> –Ln3–O16	74.93(9)	75.02(8)	75.14(9)	75.15(8)	75.05(10)	74.3(2)	75.1(2)	75.1(2)
O4 <sup>ii</sup> –Ln3–O1 <sup>ii</sup>	81.14(10)	80.99(8)	80.84(9)	80.73(7)	80.61(9)	78.40(17)	78.6(3)	96.7(8)
O4 <sup>ii</sup> –Ln3–O2 <sup>ii</sup>	85.78(10)	85.67(9)	85.43(9)	85.13(8)	84.62(10)	82.6(3)	82.1(4)	84.5(2)
O4 <sup>ii</sup> –Ln3–O14	80.89(9)	80.78(8)	80.70(8)	80.68(7)	80.78(9)	80.67(8)	80.74(9)	80.48(10)
O4 <sup>ii</sup> –Ln3–O15	145.83(9)	145.69(8)	145.53(8)	145.62(7)	145.76(9)	145.77(7)	145.71(9)	145.59(10)
O4 <sup>ii</sup> –Ln3–O16	160.71(10)	160.68(9)	160.57(9)	160.27(8)	159.64(9)	158.92(8)	158.33(9)	157.94(11)
O4 <sup>ii</sup> –Ln3–O18	87.64(12)	87.76(10)	87.69(10)	87.76(9)	87.56(11)	87.05(9)	84.6(2)	86.13(11)
O6 <sup>ii</sup> –Ln3–O1 <sup>ii</sup>	73.85(9)	73.67(8)	73.12(8)	72.74(7)	69.77(10)	67.19(15)	64.9(2)	96.2(8)
O6 <sup>ii</sup> –Ln3–O2 <sup>ii</sup>	122.11(10)	122.06(9)	121.37(9)	120.97(8)	115.48(12)	113.5(3)	109.0(4)	99.0(2)
O6 <sup>ii</sup> –Ln3–O4 <sup>ii</sup>	101.93(12)	101.97(10)	101.93(10)	101.86(9)	101.16(11)	100.26(9)	99.93(10)	100.01(11)
O6 <sup>ii</sup> –Ln3–O14	77.20(10)	77.36(9)	77.71(9)	77.97(8)	79.46(10)	81.16(9)	82.40(10)	83.29(11)
O6 <sup>ii</sup> –Ln3–O15	79.00(10)	78.91(8)	79.44(9)	79.59(7)	81.08(9)	83.04(8)	84.55(9)	85.45(10)
O6 <sup>ii</sup> –Ln3–O16	88.47(11)	88.13(10)	88.19(10)	88.11(9)	88.71(11)	90.27(10)	91.22(11)	91.61(12)
O6 <sup>ii</sup> –Ln3–O18	155.00(10)	155.07(9)	155.81(9)	156.12(8)	159.00(10)	162.58(8)	165.04(10)	166.57(11)
O14–Ln3–O1 <sup>ii</sup>	141.70(8)	141.48(7)	141.15(8)	140.98(7)	139.88(8)	137.76(14)	137.1(2)	165.0(2)
O14–Ln3–O2 <sup>ii</sup>	158.68(9)	158.50(8)	158.61(9)	158.54(8)	161.00(11)	159.5(3)	160.9(4)	159.0(11)
O14–Ln3–O15	65.87(8)	65.81(7)	65.79(7)	65.89(6)	65.92(8)	66.07(7)	66.07(8)	66.34(9)
O14–Ln3–O16	117.57(8)	117.81(8)	117.97(8)	118.35(7)	118.82(9)	119.25(7)	119.41(9)	119.76(9)
O15–Ln3–O1 <sup>ii</sup>	130.27(8)	130.44(7)	130.80(8)	130.75(6)	130.39(8)	132.23(17)	132.1(3)	134.6(11)
O16–Ln3–O1 <sup>ii</sup>	86.33(8)	86.24(8)	86.42(8)	86.16(7)	86.30(9)	89.15(16)	89.6(2)	81.2(11)
O16–Ln3–O15	51.75(8)	52.05(7)	52.24(8)	52.53(7)	52.94(8)	53.20(7)	53.34(8)	53.42(9)
O18–Ln3–O1 <sup>ii</sup>	130.87(9)	130.97(8)	130.77(8)	130.82(7)	130.93(9)	130.10(15)	129.9(2)	96.7(8)
O18–Ln3–O2 <sup>ii</sup>	81.21(10)	81.14(9)	81.13(9)	81.24(8)	84.11(11)	82.9(2)	85.1(4)	93.4(2)
O18–Ln3–O14	81.68(10)	81.72(8)	82.11(9)	82.19(7)	83.20(9)	84.50(8)	85.38(9)	85.99(10)
O18–Ln3–O15	80.25(9)	80.25(8)	80.21(8)	80.27(7)	81.08(9)	82.13(7)	82.62(9)	82.84(9)
O18–Ln3–O16	89.56(10)	89.76(9)	89.62(10)	89.76(8)	89.34(11)	88.14(9)	87.29(10)	86.69(12)

Symmetry codes: (i)  $-x + 3/2, y + 1/2, -z + 3/2$ ; (ii)  $-x + 3/2, y - 1/2, -z + 3/2$ .

### 4.3.3 Infrared spectra

The infrared spectra of the complexes were recorded in the region 650-4000  $\text{cm}^{-1}$ . The complexes in each series have practically identical IR spectra, highlighting their isomorphous natures as shown in Figure 4.8. The presence of a hydrazine group is demonstrated by the absorption band reported at around 3100  $\text{cm}^{-1}$  for series **1<sub>Ln</sub>** (**1<sub>Sm</sub>**-**5<sub>Dy</sub>**) and **2<sub>Ln</sub>** (**6<sub>Pr</sub>**-**13<sub>Er</sub>**). While the predicted strong characteristic absorption for the symmetric stretching vibrations of carboxylate groups in series **2<sub>Ln</sub>** (**6<sub>Pr</sub>**-**13<sub>Er</sub>**) and **3<sub>Ln</sub>** (**14<sub>Eu</sub>**-**21<sub>Lu</sub>**) is observed in the region of 1360-1438 and 1530-1640  $\text{cm}^{-1}$ , respectively. Furthermore, the absorption in the range of 739-1148  $\text{cm}^{-1}$  demonstrates the presence of coordinated and isolated nitrate groups in the structures of **1<sub>Ln</sub>** (**1-5**), whereas the broad bands between 3474 and 3266  $\text{cm}^{-1}$  indicate the presence of coordinated and lattice water molecules in the series **2<sub>Ln</sub>** CPs (**6<sub>Pr</sub>**-**13<sub>Er</sub>**).

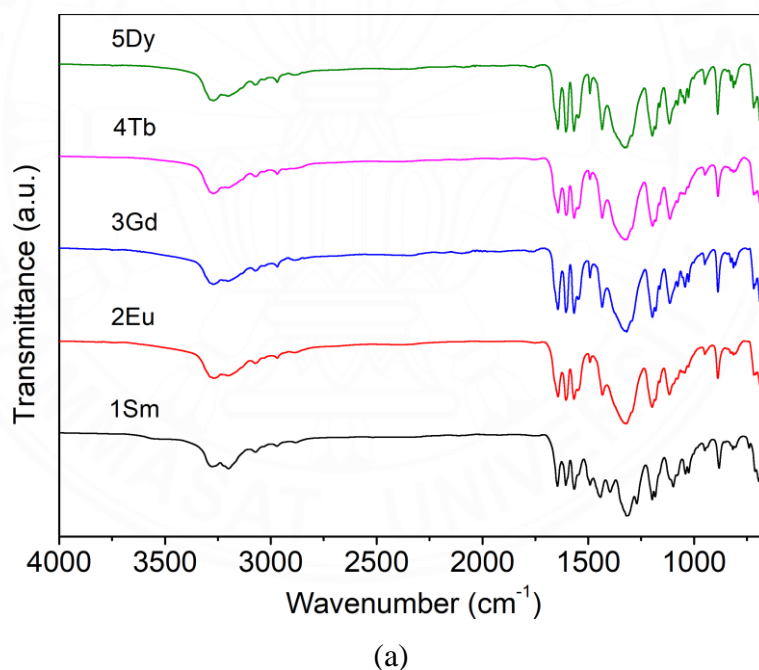
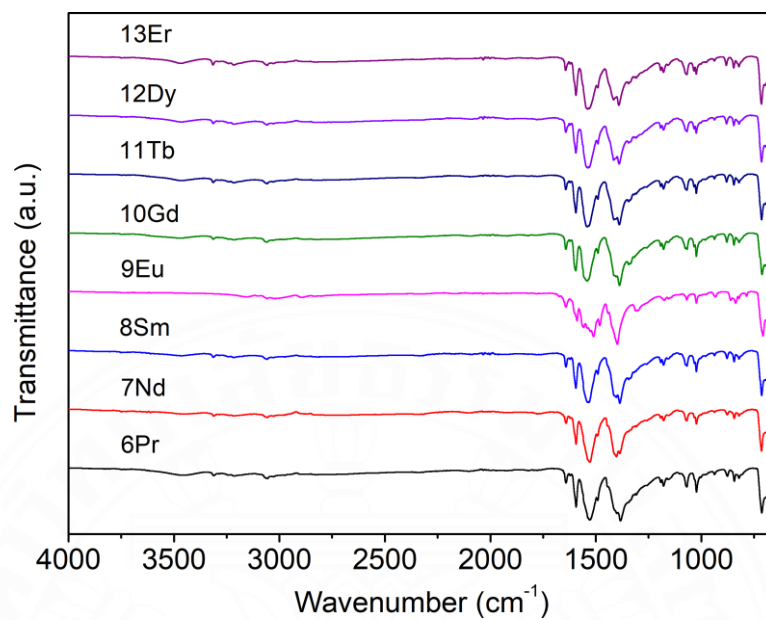
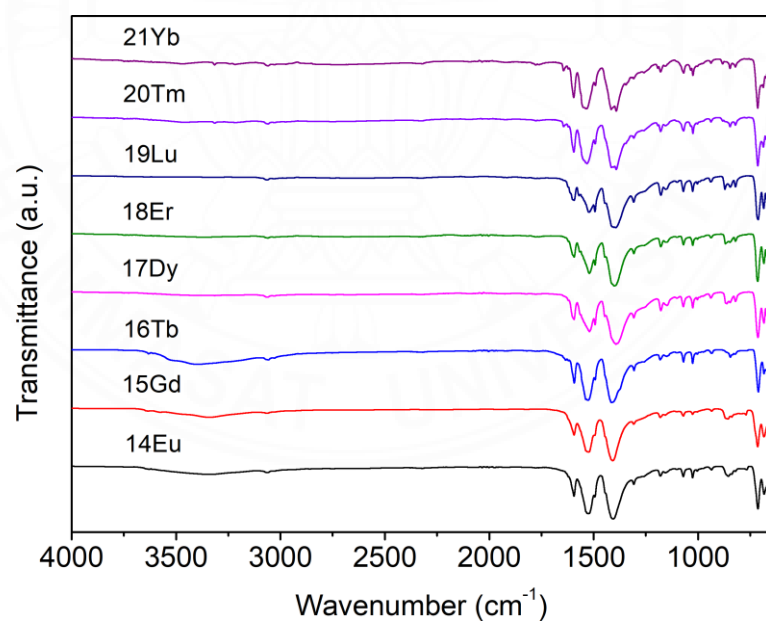


Figure 4.8 IR spectra of each series (a) **1<sub>Ln</sub>** (**1<sub>Sm</sub>**-**5<sub>Dy</sub>**), (b) **2<sub>Ln</sub>** (**6<sub>Pr</sub>**-**13<sub>Er</sub>**), and (c) **3<sub>Ln</sub>** (**14<sub>Eu</sub>**-**21<sub>Lu</sub>**).



(b)



(c)

*Figure 4.8 (Continued).*



#### 4.3.4 Powder X-ray diffraction

PXRD analysis was used to confirm the purity of crystalline powders of all complexes at room temperature. The main peaks displayed in the measured patterns match with the XRD patterns simulated from single-crystal data, confirming the relatively high phase purity of the synthesized products. Some differences in intensity and peak positions may be attributed to the preferred orientation and stacking models of the crystalline powder products. In each series, the PXRD patterns of complexes are comparable because there are isostructural complexes as shown in Figure 4.9. Surprisingly, all of the polymeric complexes in series **2<sub>Ln</sub>** (**6<sub>Pr</sub>**-**13<sub>Er</sub>**) and **3<sub>Ln</sub>** (**14<sub>Eu</sub>**-**21<sub>Lu</sub>**) are extremely stable in solid state after long-term exposure to air for more than ten months as shown in Figure 4.10. The PXRD patterns of the representative examples **9<sub>Eu</sub>**, **11<sub>Tb</sub>**, **14<sub>Eu</sub>**, and **16<sub>Tb</sub>** are insoluble in water and various organic solvents, implying the extremely high stability of the synthesized products that can be used for industrial, as shown in Figure 4.11.

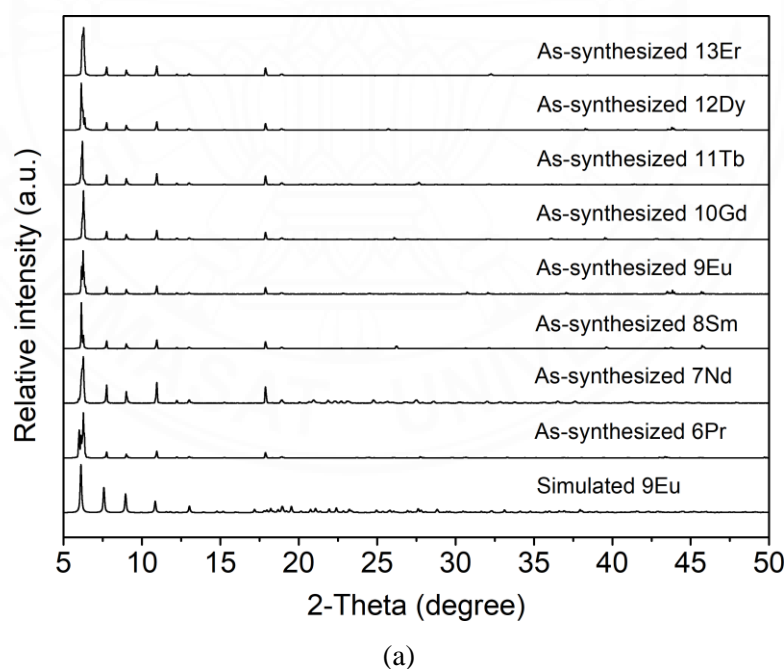


Figure 4.9 Comparison of the simulated and experimental PXRD patterns of the as synthesized complexes (a) **6<sub>Pr</sub>**-**13<sub>Er</sub>** and (b) **14<sub>Eu</sub>**-**21<sub>Lu</sub>**.

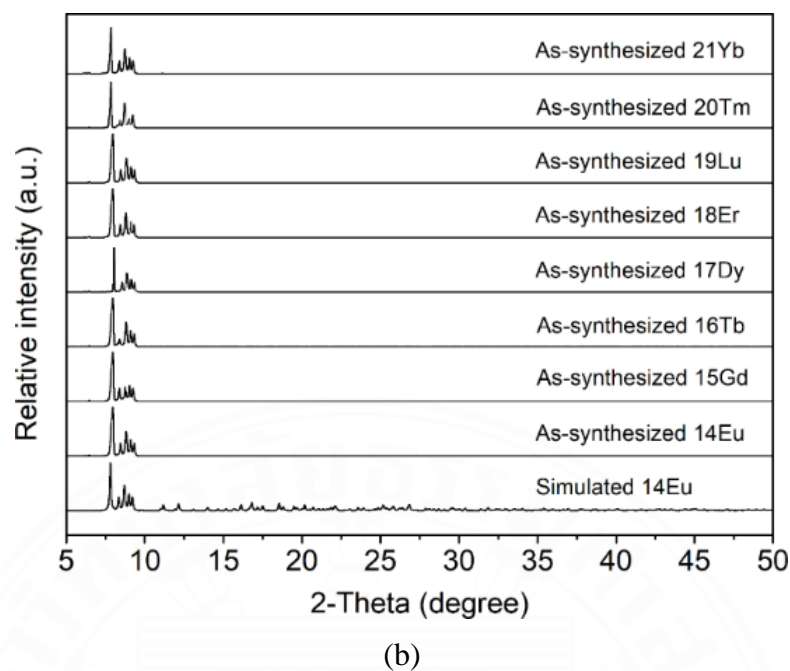


Figure 4.9 (Continued).

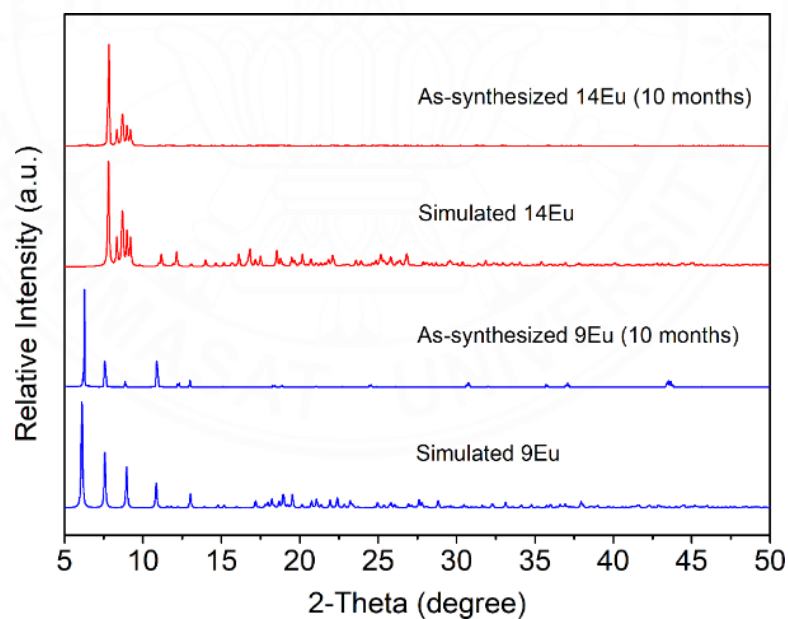
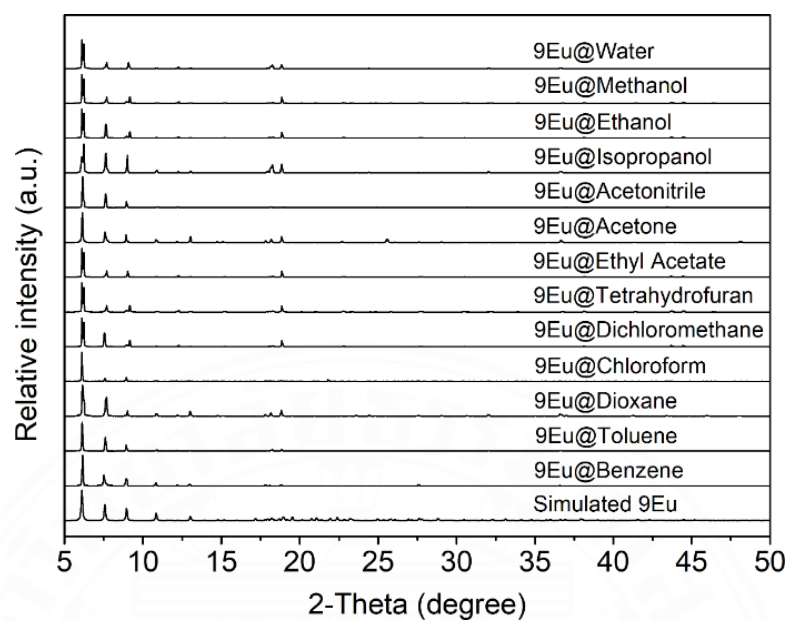
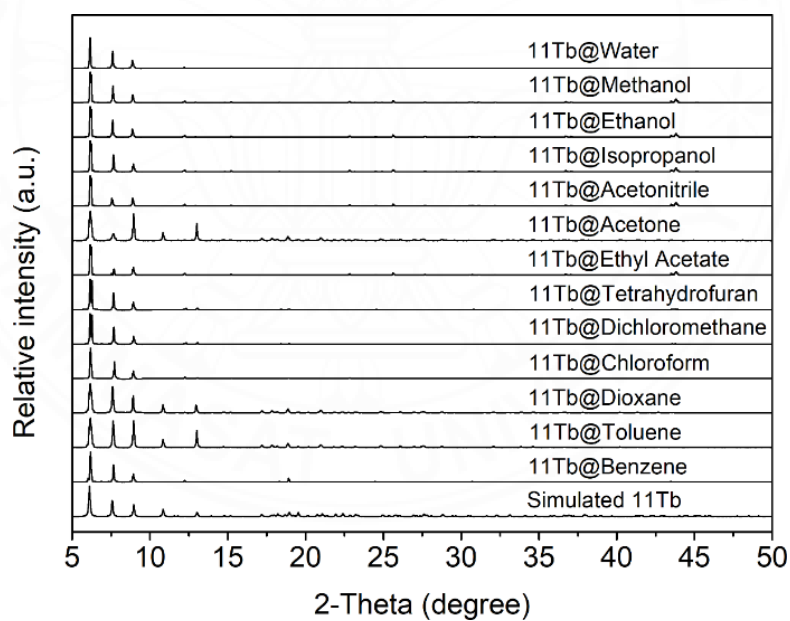


Figure 4.10 Comparison of the experimental PXRD patterns of the representative complexes **9<sub>Eu</sub>** (series **2Ln**) and **14<sub>Eu</sub>** (series **3Ln**) after exposure to air for ten months with the simulated diffraction patterns based on the single crystal X-ray structure determinations.



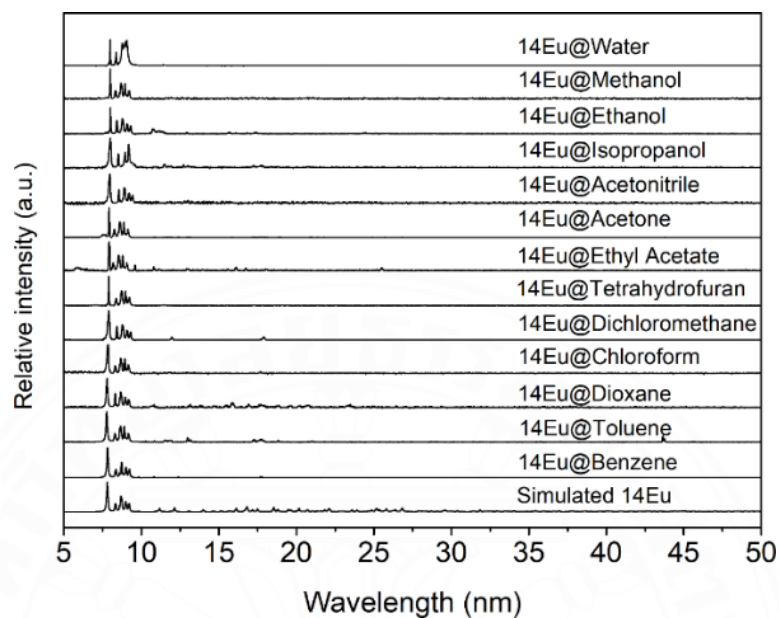


(a)

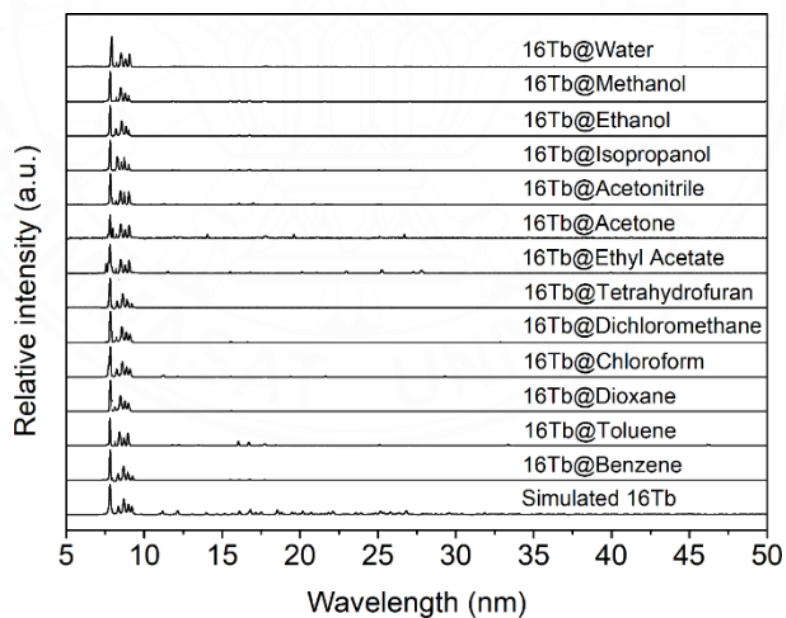


(b)

Figure 4.11 The PXRD patterns of the representative example (a) **9Eu**, (b) **11Tb** (c,) **14Eu**, and (d) **16Tb** after immersing in various organic solvents for 24 h.



(c)



(d)

Figure 4.11 (Continued).

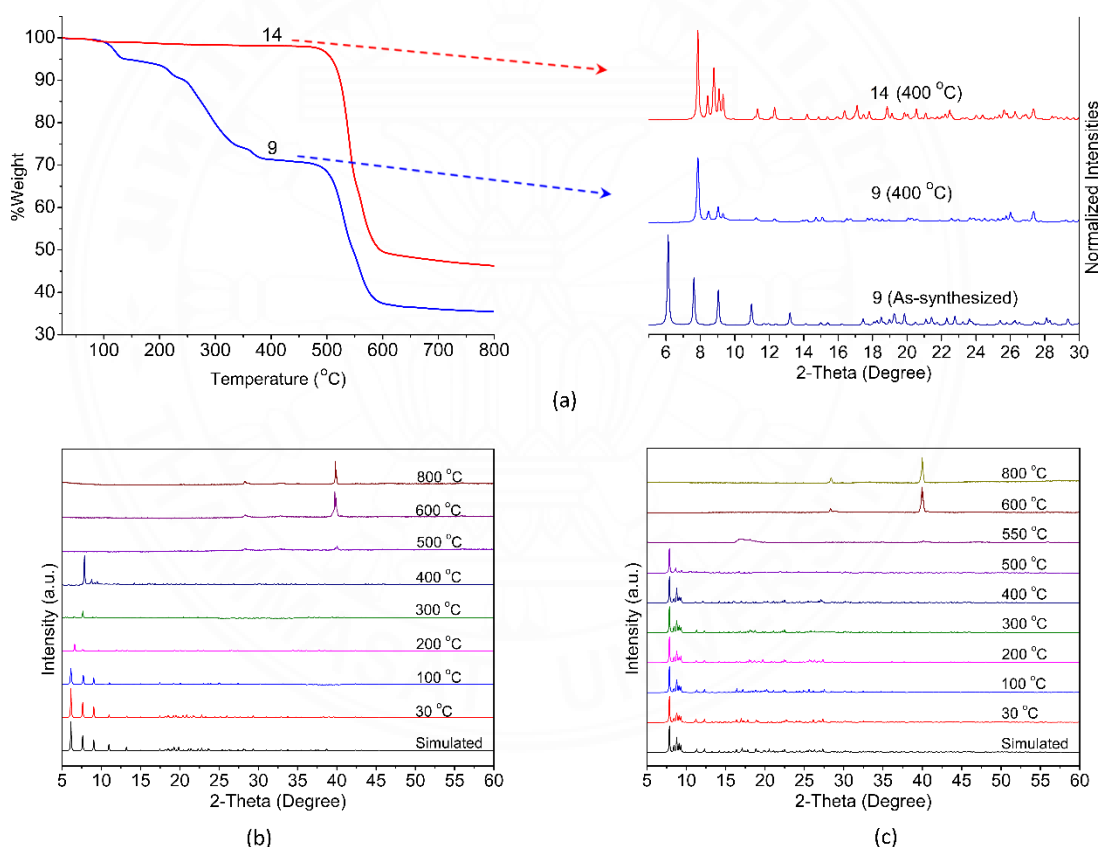
### 4.3.5 Thermogravimetric analysis

Thermal stability was investigated using thermogravimetric analysis (TGA) and *in situ* VT-PXRD. Although the complexes are classified into three classes, the complexes in series **1<sub>Ln</sub>** (**1<sub>Sm</sub>**-**5<sub>Dy</sub>**) were not stable when bared to air. Hence, the Eu-based CPs **9<sub>Eu</sub>** and **14<sub>Eu</sub>** are chosen as representative examples. In the case of complex **9<sub>Eu</sub>**, the loss weight curve occurs in three steps. The first step shows a weight loss of 5.3% between 90 and 160 °C (calcd 5.2%) which is one lattice of water and one coordinated water molecule. The second weight loss occurs in the 200-355 °C range of 21.6% is the loss of one bzz ligand (calcd 19.8%) and ends at 415 °C, after that the structure decomposes, as shown in Figure 4.12a.

The solid-state structures of **9<sub>Eu</sub>** and **14<sub>Eu</sub>** were determined by their VT-XRD diffraction patterns. Three different phases of **9<sub>Eu</sub>** can be identified from the patterns as shown in Figure 4.12b. At 30 to 100 °C, the pattern is identical to the as-synthesized crystal structure. At 200 to 300 °C, the pattern was transformed and found in the 6.48-7.85 of the  $2\theta$  range, indicating that some structural deformation has happened as a result of the loss of the water molecules and the bzz ligands. Eventually, when we raised the temperature to 400 °C peaks at  $2\theta = 7.91, 8.64, 8.95,$  and  $9.46^\circ$  were observed, inferring that the formation of a new phase has occurred. At 500 °C, the crystal structure of **9<sub>Eu</sub>** decomposed and became amorphous. After increasing the temperature to 800 °C, new peaks appeared at  $2\theta = 28.30, 32.80,$  and  $55.85^\circ$ , which may be attributed to solid-state reactivity. This pattern is comparable with the  $\text{Eu}_2\text{O}_3$  pattern (PDF: 00-034-0392).

In the case of complex **14<sub>Eu</sub>**, the TGA curve demonstrates no mass loss up to 500 °C. After that, the ben ligands decompose, the structure collapses, and provides the final  $\text{Eu}_2\text{O}_3$  residue. When compared with the PXRD patterns it showed that no phase transition occurs, and the structure remains intact up to 500 °C as shown in Figure 4.12c. This result is consistent with the TGA results described above. The distinguished thermal stability could be related to the diverse coordination environments of the lanthanide metal centers, as a result, the aromatic backbones of the ligands become more rigid. This data will lead to a better appreciation of intermolecular interactions between their ligands.

As a result of these findings, In the solid state, crystal **9<sub>Eu</sub>** undergoes complete transformation to crystal **14<sub>Eu</sub>** thus the as-synthesized complex of **9<sub>Eu</sub>** is heated at 400 °C in air. Material prepared in this way exhibits identical PXRD patterns and the shape of the TGA curves after removing the water molecules and bzz ligands clearly demonstrate this as shown in Figure. 4.12a. It appears to mean that heating the crystalline samples **2<sub>Ln</sub>** in the air at 400 °C completely transformed the structure into **3<sub>Ln</sub>**. The PXRD patterns of **2<sub>Ln</sub>** and **3<sub>Ln</sub>** collected at 400 °C confirm with a good fit in the main peak positions finding indicated that series **3<sub>Ln</sub>** complexes are more thermodynamically stable than series **2<sub>Ln</sub>** complexes.



**Figure 4.12** (a) TGA plots (left) and PXRD patterns (right) at 400 °C for **9<sub>Eu</sub>** and **14<sub>Eu</sub>**. VT-PXRD patterns for (b) **9<sub>Eu</sub>** and (c) **14<sub>Eu</sub>**.

Furthermore, the utter lack of the vibrations band at 3000-3200  $\text{cm}^{-1}$  in the IR spectra confirms the absence of the hydrazine group. as shown in Figure. 4.13 (Gulaczyk *et al*, 2003; Brahmayya *et al*, 2015).

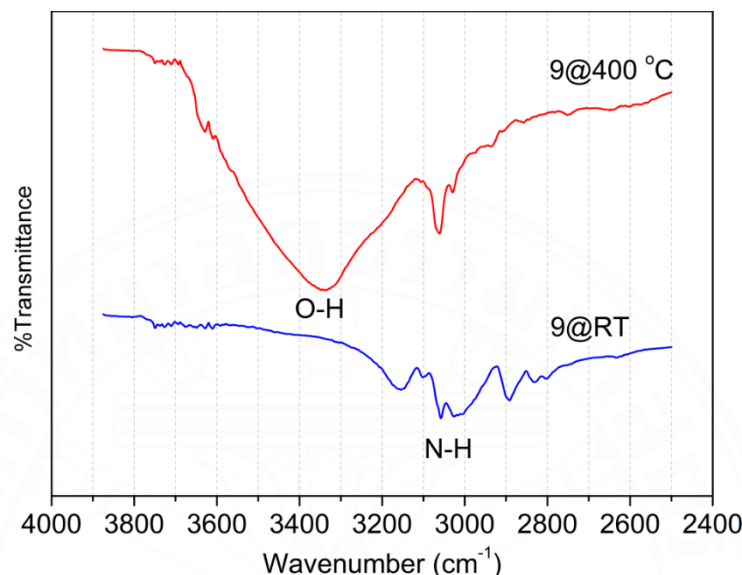


Figure 4.13 IR spectra of **9<sub>Eu</sub>** at room temperature (blue line) and 400 °C (red line).

#### 4.3.6 Solid-state photoluminescence properties

The images of crystals of complexes **2<sub>Eu</sub>**, **9<sub>Eu</sub>**, **14<sub>Eu</sub>** and **4<sub>Tb</sub>**, **11<sub>Tb</sub>**, and **16<sub>Tb</sub>** obtained using an optical microscope under UV light at a short wavelength (254 nm) are illustrated in Figure. 4.14. Eu- and Tb-based complexes often display unique photoluminescence that usually provides red and green light emissions, respectively. Therefore, the solid-state photoluminescence properties and lifetime decay were studied at room temperature. The ligands were firstly investigated in the solid state. The emission spectra of the free ligands revealed two broad emissions at 417 and 437 nm ( $\lambda_{\text{ex}} = 290$  nm) for the bzz and 333 and 450 nm ( $\lambda_{\text{ex}} = 290$  nm) for the ben, which are attributable to  $\pi \rightarrow \pi^*$  and/or  $n \rightarrow \pi^*$  transitions of the molecules as shown in Figure. 4.15. Then under excitation at 290 nm, the Eu-based complexes **2<sub>Eu</sub>**, **9<sub>Eu</sub>**, and **14<sub>Eu</sub>** display four distinct emission bands for f-f transitions of the  $\text{Eu}^{3+}$  ion, which correspond to the  $^5\text{D}_0 \rightarrow ^7\text{F}_J$  ( $J = 1-4$ ) transitions, as shown in Figure 4.16. (Parker *et al*, 1996; Wang *et al*, 2014). The peak intensity at 614, 617, and 615 for **2<sub>Eu</sub>**, **9<sub>Eu</sub>**, and **14<sub>Eu</sub>**,

respectively, is strongest, indicating that  $^5D_0 \rightarrow ^7F_2$  transition is hypersensitive to the coordination environment of the  $Eu^{3+}$  ion, and shows a red luminescence of the complexes. Absolutely, in these complexes, the intensity of the electric dipole transitions is much higher than that of the magnetic dipole transitions ( $^5D_0 \rightarrow ^7F_1$ ), implying that the  $Eu^{3+}$  ion occupies a low-symmetry coordination site without an inversion center (Klink *et al*, 2000; Borisova *et al*, 2014; Smith *et al*, 2016). This is consistent with the findings of the previously mentioned X-ray structural analyses. When excited at 300 nm, the emission spectra of Tb-based complexes **4Tb**, **11Tb**, and **16Tb** exhibit four emission bands, which can be attributed to the  $^5D_4 \rightarrow ^7F_J$  ( $J = 6-3$ ) transitions of the  $Tb^{3+}$  ions (Aime *et al*, 1998; Li *et al*, 2016). The extremely narrow emission bands from the  $^5D_4 \rightarrow ^7F_5$  transition are present at 544, 545, and 542 nm for **4Tb**, **11Tb**, and **16Tb**, respectively. As a result, green luminescence is emitted. It should be mentioned that the absence of ligand-centered emission bands around 380-450 nm in all luminescence spectra of these complexes proved that  $Eu^{3+}$  and  $Tb^{3+}$  centers can be successfully sensitized by the ligands. For **2Eu**, **4Tb**, **9Eu**, **11Tb**, **14Eu**, and **16Tb** the decay lifetimes ( $\tau$ ) are 0.18, 0.57, 0.40, 1.01, 2.27, and 1.43 ms, respectively as shown in Table 4.7 and Figure. 4.17.

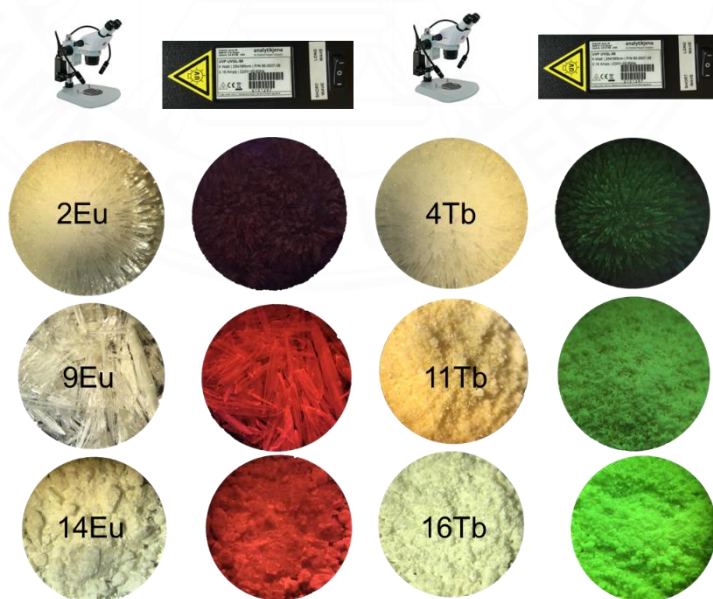


Figure 4.14 (left) Optical microscopy images and (right) irradiated under UV light of complexes **2Eu**, **9Eu**, **14Eu**, **4Tb**, **11Tb**, and **16Tb**.

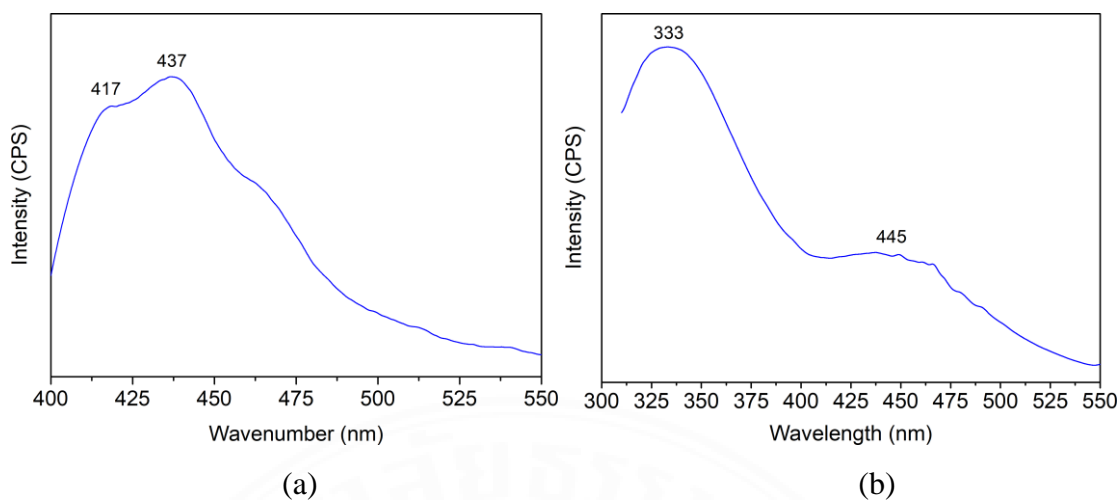


Figure 4.15 The solid-state PL emission spectra of the free ligands (a) Bzz and (b) Ben when excited at 290 nm.

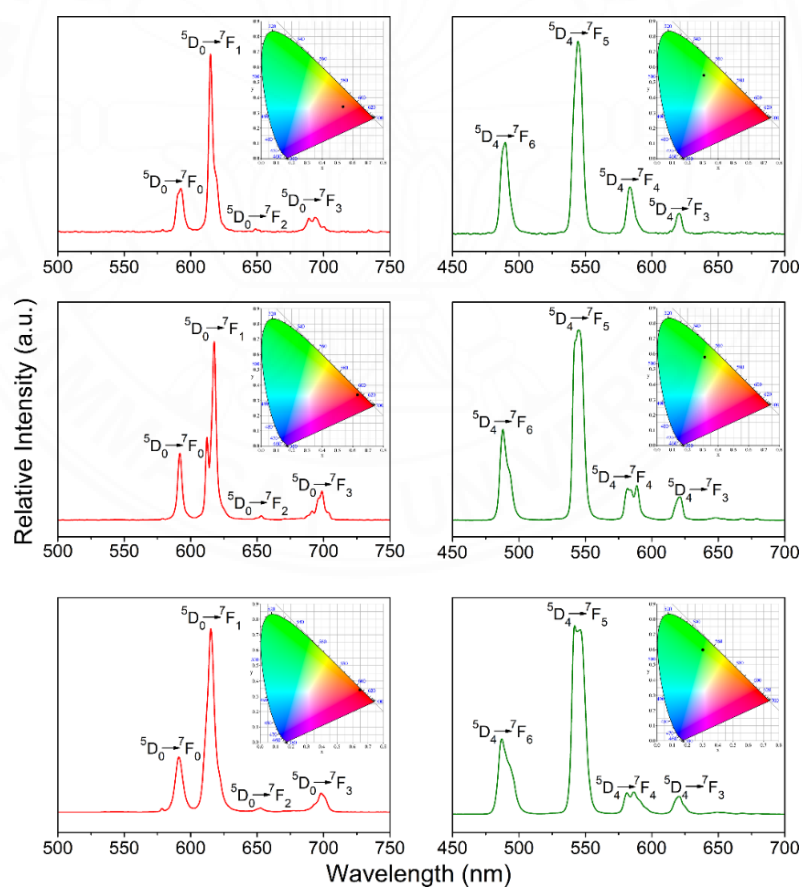


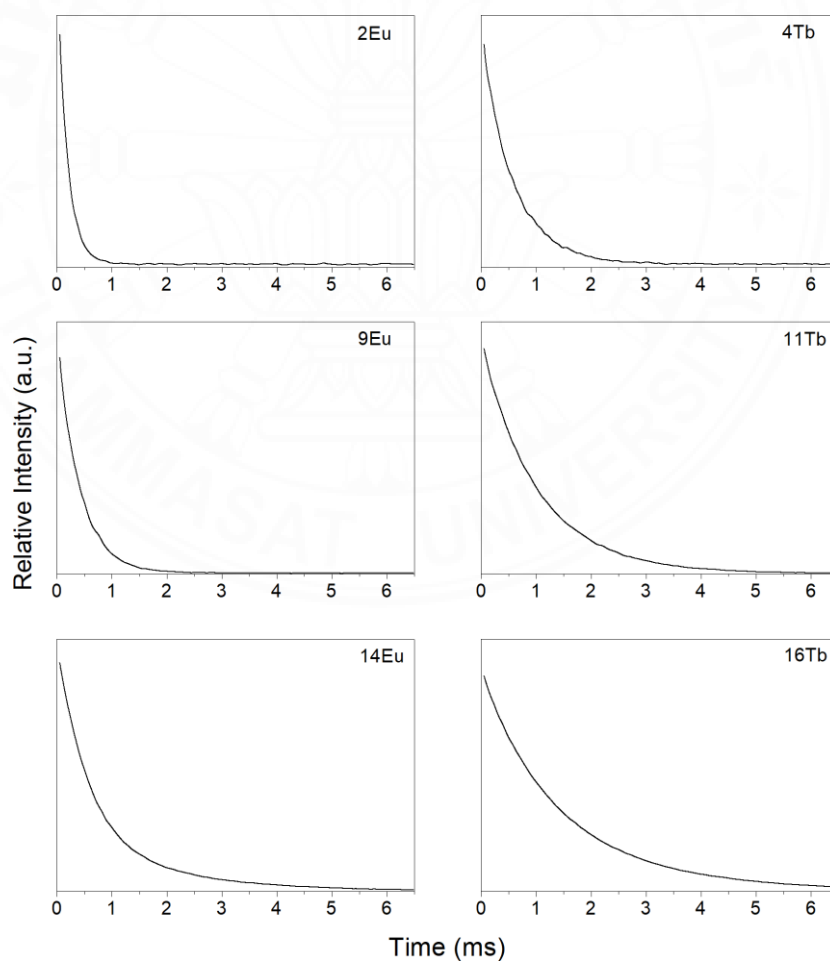
Figure 4.16 Emission spectra and (insert) CIE coordinates of (a) **2**<sub>Eu</sub>, (b) **4**<sub>Tb</sub>, (c) **9**<sub>Eu</sub>, (d) **11**<sub>Tb</sub>, (e) **14**<sub>Eu</sub>, and (f) **16**<sub>Tb</sub>.

**Table 4.7**

*Emission bands, luminescent lifetimes ( $\tau$ ), and CIE color coordinates of the Eu- and Tb-based CPs*

	$\lambda_{\text{ex}}$ (nm)	$\lambda_{\text{em}}$ (nm)	$\tau$ ( $\mu\text{s}$ )	CIE Coordinate
<b>2<sub>Eu</sub></b>	290	592, 614, 649, 693	0.18	(0.55, 0.34)
<b>9<sub>Eu</sub></b>	290	591, 617, 654, 699	0.40	(0.64, 0.34)
<b>14<sub>Eu</sub></b>	290	591, 615, 653, 698	2.27	(0.65, 0.35)
<b>4<sub>Tb</sub></b>	300	489, 544, 584, 620	0.57	(0.31, 0.55)
<b>11<sub>Tb</sub></b>	300	488, 544, 589, 621	1.01	(0.31, 0.59)
<b>16<sub>Tb</sub></b>	300	487, 542, 586, 620	1.43	(0.29, 0.60)

CIE1931 color space chromaticity diagram



*Figure 4.17* Luminescence decay ( $\tau$ ) curves for **2<sub>Eu</sub>**, **4<sub>Tb</sub>**, **9<sub>Eu</sub>**, **11<sub>Tb</sub>**, **14<sub>Eu</sub>**, and **16<sub>Tb</sub>**.



### 4.3.7 Photoluminescent sensing properties

Based on the intense red and green luminescence emissions, as well as the chemical stability of the Eu- and Tb-based LnCPs, their utility as chemical sensors for molecules and ions was probed. To determine the potential of complexes **9<sub>Eu</sub>**, **11<sub>Tb</sub>**, **14<sub>Eu</sub>**, and **16<sub>Tb</sub>** for sensing small organic molecules. The crystalline samples (3 mg) were immersed in various solvents (3 mL), such as acetone, acetonitrile (MeCN), benzene, dioxane, chloroform (CHCl<sub>3</sub>), dichloromethane (DCM), *N,N*-dimethyl formamide (DMF), Dimethyl sulfoxide (DMSO), toluene, Tetrahydrofuran (THF), methanol (MeOH), ethanol (EtOH), isopropanol (iPrOH), ethyl acetate (EtOAc), and distilled water (H<sub>2</sub>O), and subsequently ultrasonicated for 10 min, among all the suspensions. These complexes display distinct solvent-dependent luminescence intensities as shown in Figure 4.18, and the luminescence is quenched by acetone. The competitive energy absorption may be responsible for the quenching by acetone molecules (Kreno *et al*, 2012; Reddy *et al*, 2013; Meyer *et al*, 2014; Liang *et al*, 2015; Mahata *et al*, 2017; Lustig *et al*, 2017; Li *et al*, 2020; Huangfu *et al*, 2021).

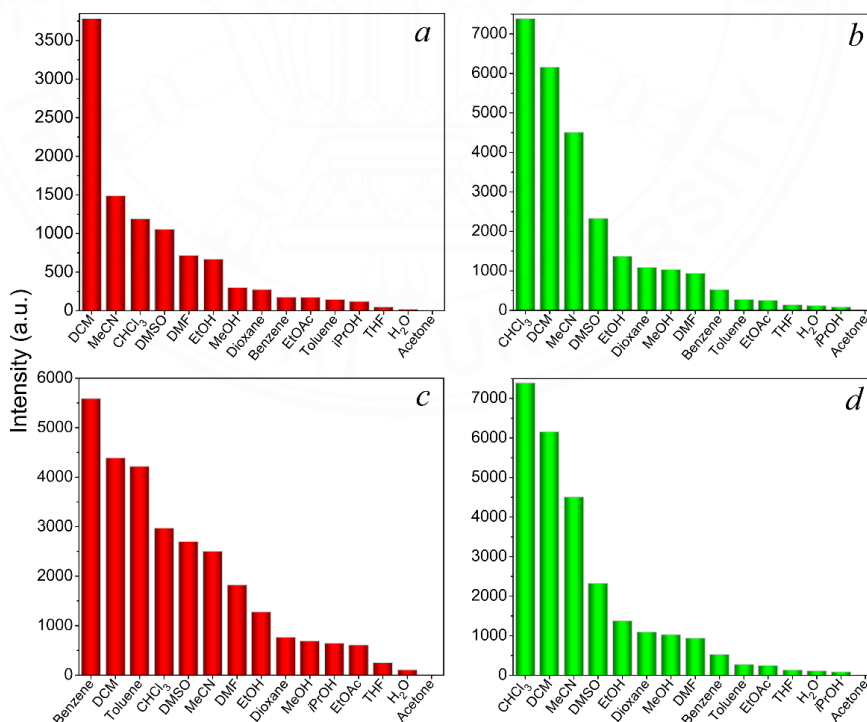


Figure 4.18 Emission intensities in different organic solvents for (a) **9<sub>Eu</sub>**, (b) **11<sub>Tb</sub>**, (c) **14<sub>Eu</sub>**, and (d) **16<sub>Tb</sub>**.

This was demonstrated by the analysis of an overlap of the absorption band of acetone compared with the excitation spectra of complexes **9<sub>Eu</sub>**, **11<sub>Tb</sub>**, **14<sub>Eu</sub>**, and **16<sub>Tb</sub>** in the UV-Visible spectra as shown in Figure. 4.19. Besides, the PXRD patterns of the samples after sensing tests are similar to the original samples as shown in Figure. 4.20, indicating that the basic 1D chain CPs have not changed. This also demonstrates that the luminescence quenching by acetone was not caused by the collapse of the structure.

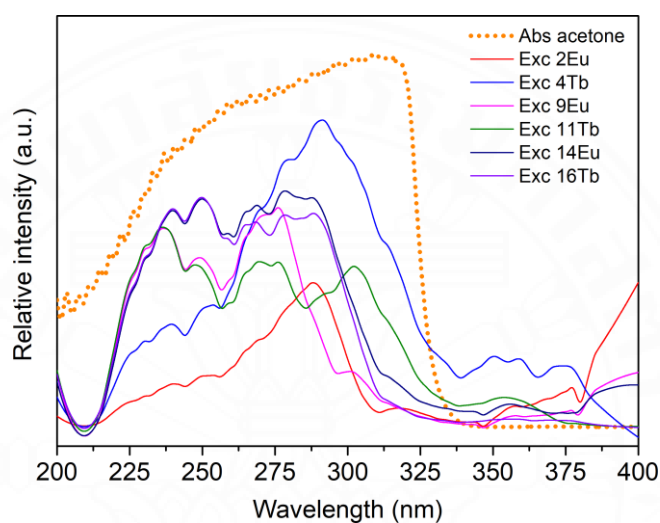


Figure 4.19 UV-Vis spectra of acetone and excitation spectra of **2<sub>Eu</sub>**, **4<sub>Tb</sub>**, **9<sub>Eu</sub>**, **11<sub>Tb</sub>**, **14<sub>Eu</sub>**, and **16<sub>Tb</sub>**.

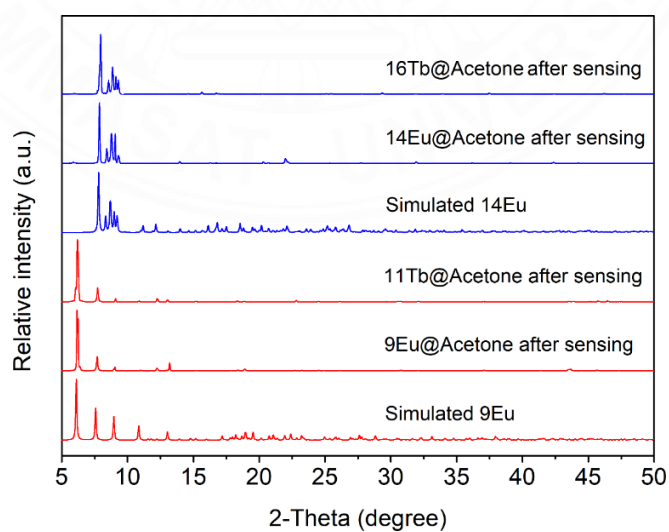


Figure 4.20 PXRD patterns of **9<sub>Eu</sub>**, **11<sub>Tb</sub>**, **14<sub>Eu</sub>**, and **16<sub>Tb</sub>**: simulated and after sensing of acetone.

When considering the chemical stability and excellent luminescence properties of the complexes in DCM and MeCN solvents. Thus, additional investigation of their trace detection abilities amounts of metal ions was conducted in MeCN solutions. The crystalline samples (3 mg) of complexes **9**<sub>Eu</sub>, **11**<sub>Tb</sub>, **14**<sub>Eu</sub>, and **16**<sub>Tb</sub> were ground and immersed in individual MeCN solutions of M<sup>x+</sup> ions (3 mL) with a concentration of  $5 \times 10^{-4}$  M (M = K<sup>+</sup>, Na<sup>+</sup>, Ag<sup>+</sup>, Ca<sup>2+</sup>, Cd<sup>2+</sup>, Co<sup>2+</sup>, Cu<sup>2+</sup>, Fe<sup>2+</sup>, Hg<sup>2+</sup>, Mn<sup>2+</sup>, Ni<sup>2+</sup>, Zn<sup>2+</sup>, Al<sup>3+</sup>, Co<sup>3+</sup>, Cr<sup>3+</sup>, and Fe<sup>3+</sup>). The luminescence properties of the suspensions, M<sup>x+</sup>@**9**<sub>Eu</sub>, M<sup>x+</sup>@**11**<sub>Tb</sub>, M<sup>x+</sup>@**14**<sub>Eu</sub>, and M<sup>x+</sup>@**16**<sub>Tb</sub> were studied as shown in Figure. 4.21, their emission intensity increases of the MeCN solutions were observed comparing with the blank MeCN suspension which emissions are strongly quenched by the Co<sup>2+</sup> ion as shown in Figure. 4.22. The luminescence intensity of the suspension can be seen and displays slightly adjusted with the addition of Co<sup>3+</sup> ions. This is available to guide which **9**<sub>Eu</sub>, **14**<sub>Eu</sub>, **11**<sub>Tb</sub>, and **16**<sub>Tb</sub>-based CPs could be as luminescent probes for selective sensing of Co<sup>2+</sup> ions in Co<sup>2+</sup>/Co<sup>3+</sup> solution mixtures. There is the potential for use in environmental, pharmaceutical, and biological systems (Baldwin *et al*, 2004; Han *et al*, 2014; Ke *et al*, 2018).

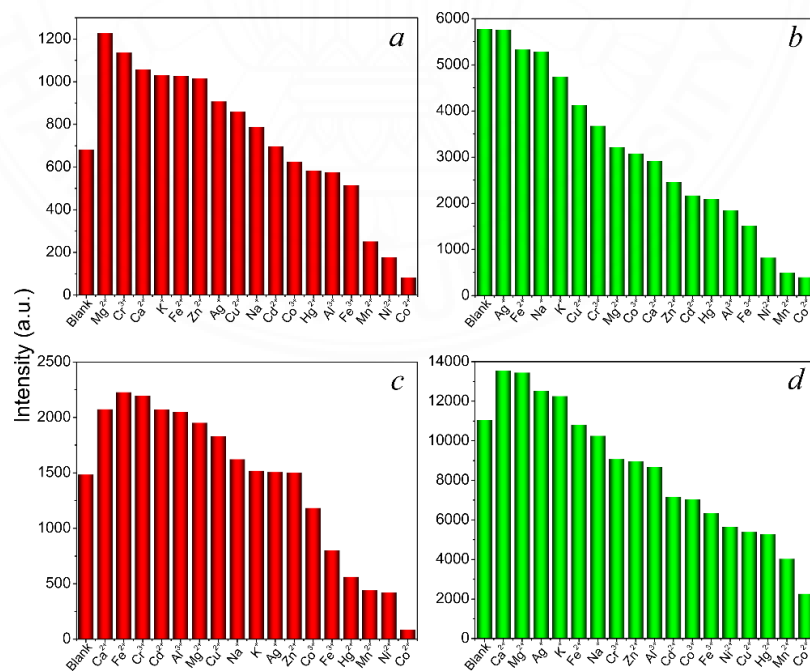


Figure 4.21 Emission intensities for (a) **9**<sub>Eu</sub>, (b) **11**<sub>Tb</sub>, (c) **14**<sub>Eu</sub>, and (d) **16**<sub>Tb</sub> in MeCN solutions of different metal ions.

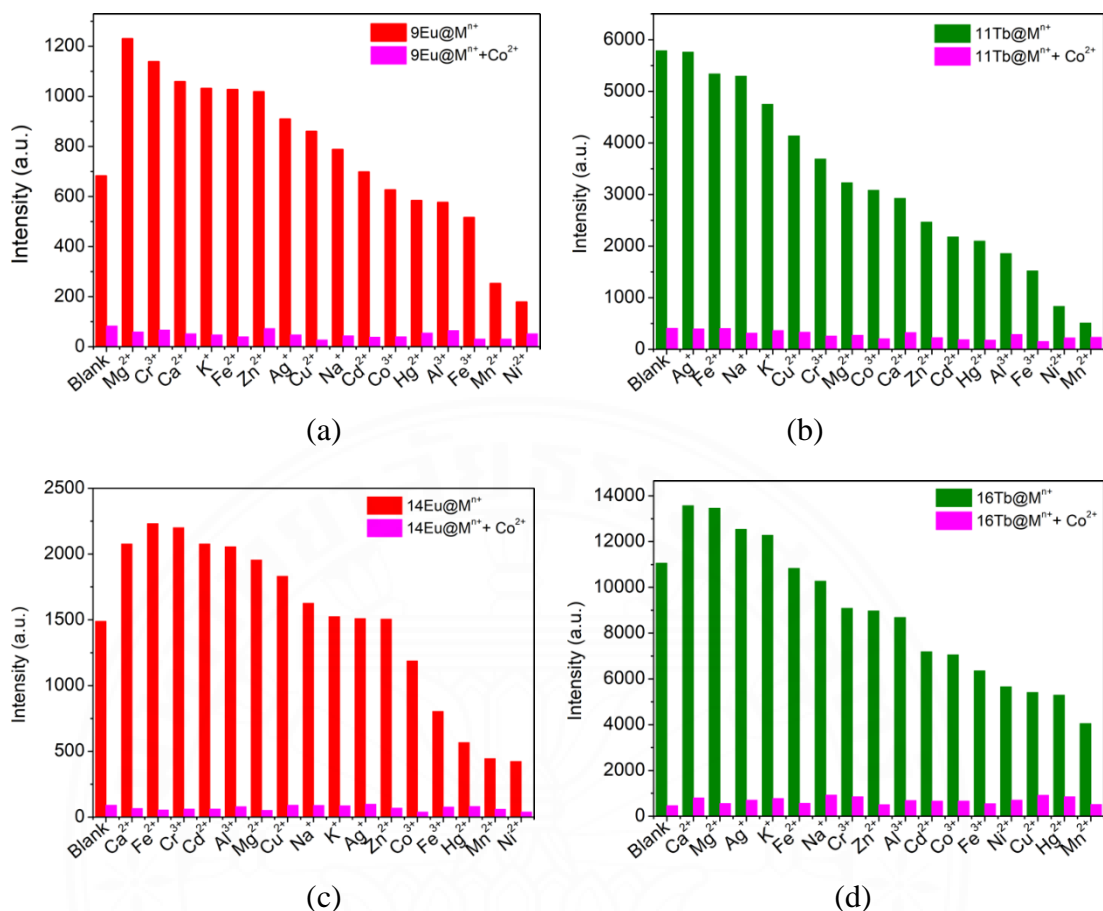


Figure 4.22 Relative luminescence intensities of (a) **9Eu**, (b) **11Tb**, (c) **14Eu**, and (d) **16Tb** dispersed in the solutions of individual metal ions and the quenched luminescence intensities after the addition of solutions of  $\text{Co}^{2+}$  in acetonitrile.

The relationship curve of the quenching effect ( $I_0/I$ ) and  $\text{Co}^{2+}$  can be well fitted by the Stern–Volmer equation,  $I_0/I = 1 + K_{SV} \times [M]$  (Rose *et al.*, 2005) ( $I_0$  and  $I$  are the luminescence intensities of the suspension of **9Eu**, **14Eu**, **11Tb**, and **16Tb** before and after the addition of  $\text{Co}^{2+}$ , respectively;  $K_{SV}$  is the quenching constant, and  $[M]$  is the molar concentration of  $\text{Co}^{2+}$ ). So, the detection limit of  $\text{Co}^{2+}$  can check by Stern–Volmer equations and established from the luminescence data according to the  $3\sigma/k$  ( $\sigma$  = standard error;  $k$  = slope). These  $K_{SV}$  values for  $\text{Co}^{2+}$  were found to be  $1.29 \times 10^4$ ,  $1.02 \times 10^4$ ,  $8.9 \times 10^3$ , and  $8.2 \times 10^3 \text{ M}^{-1}$  for complexes **9Eu**, **11Tb**, **14Eu**, and **16Tb**, respectively. Following the IUPAC recommendation for determining the limit of

detection (LOD) at a signal-to-noise ratio (S/N) of 3 ( $\text{LOD} = 3\sigma_{\text{blank}}/K_{\text{sv}}$ ), (Xu et al, 2011; Zhang et al, 2014; Qi et al, 2017) the LOD values for  $\text{Co}^{2+}$  in complexes **9<sub>Eu</sub>**, **11<sub>Tb</sub>**, **14<sub>Eu</sub>**, and **16<sub>Tb</sub>** were approximated 20.1, 12.7, 6.1, and 6.5  $\mu\text{M}$ , respectively as shown in Figure. 4.23. This result indicates that the S-V plots are nearly linear thus the mechanism of  $\text{Co}^{2+}$  ion luminescence quenching was related to the dynamic quenching process (Zhou *et al*, 2013).

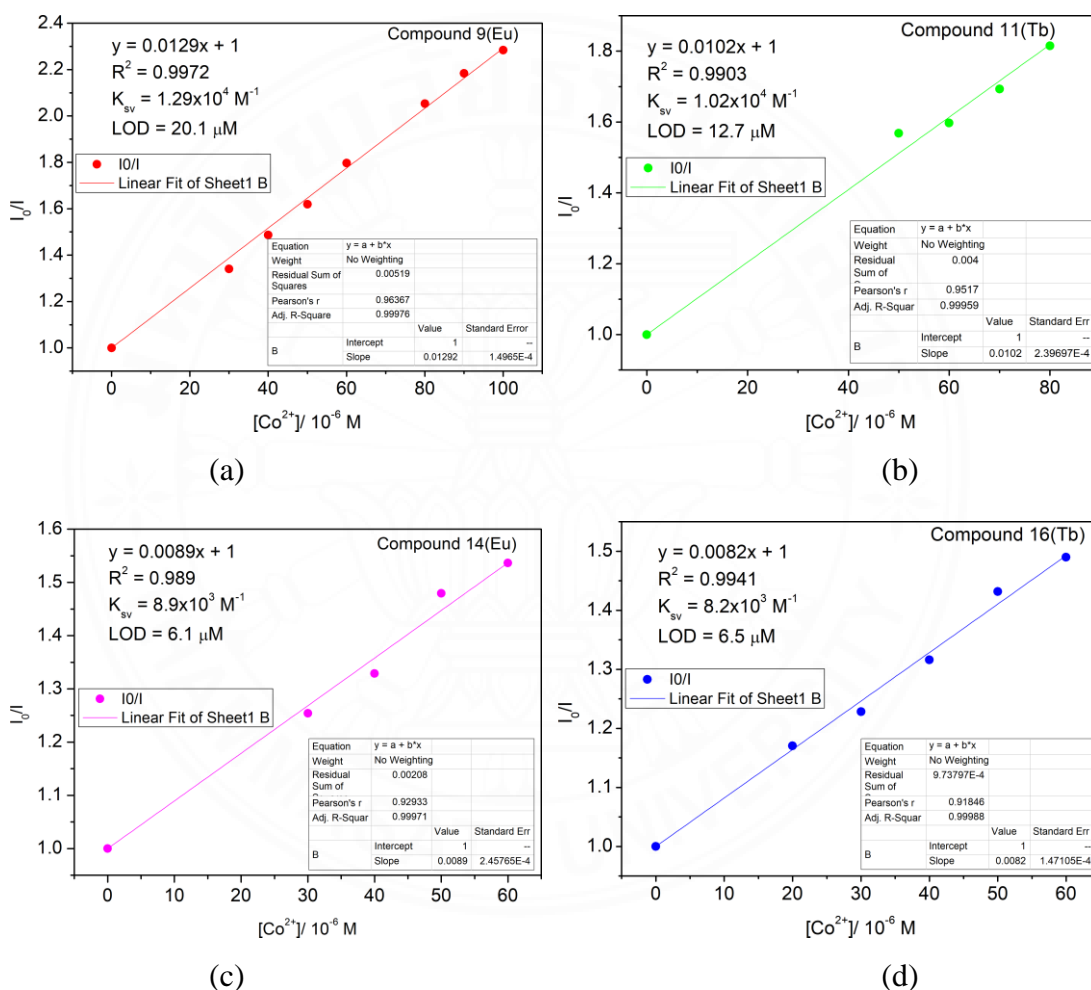


Figure 4.23 Plots of  $I_0/I$  versus the concentration of  $\text{Co}^{2+}$  ions plotted according to the Stern–Volmer equation as well as the linear fitting results for (a) **9<sub>Eu</sub>**, (b) **11<sub>Tb</sub>**, (c) **14<sub>Eu</sub>**, and (d) **16<sub>Tb</sub>**.

The mechanism of luminescence quenching by  $\text{Co}^{2+}$  ions was investigated. The sample's PXRD patterns after sensing  $\text{Co}^{2+}$  ions were collected and

contrasted with the as-synthesized patterns as shown in Figure. 4.24. This suggests that the quenching of luminescence is not caused by the collapse of the structure. In addition, the UV-Vis absorption spectra of metal ions in MeCN solutions were measured. The UV-Vis absorption spectrum of the  $\text{Co}^{2+}$  solution at 250-400 nm mainly originates from the d-d transition and was discovered a wide overlap with the excitation spectra of **9**<sub>Eu</sub>, **11**<sub>Tb</sub>, **14**<sub>Eu</sub>, and **16**<sub>Tb</sub>. Whereas  $\text{Ni}^{2+}$  and  $\text{Mn}^{2+}$  have a slight spectrum overlap with other metals in MeCN solutions as shown in Figure. 4.25. Then excited at 290 nm (**9**<sub>Eu</sub>, **14**<sub>Eu</sub>) or 300 nm (**11**<sub>Tb</sub>, **16**<sub>Tb</sub>), the lanthanide CPs and analytes compete for the energy of excitation and absorption. This could explain the quenching phenomenon (Kreno *et al*, 2012; Reddy *et al*, 2013; Meyer *et al*, 2014; Liang *et al*, 2015; Mahata *et al*, 2017; Lustig *et al*, 2017; Li *et al*, 2020; Huangfu *et al*, 2021). Furthermore, the sensing properties of **9**<sub>Eu</sub> and **11**<sub>Tb</sub> for anions were investigated by recording their emissive spectra of MeCN solutions containing potassium salts at a concentration of  $5.0 \times 10^{-4}$  M as shown in Figure. 4.26. The results demonstrate that anionic analytes do not affect the luminescence intensity.

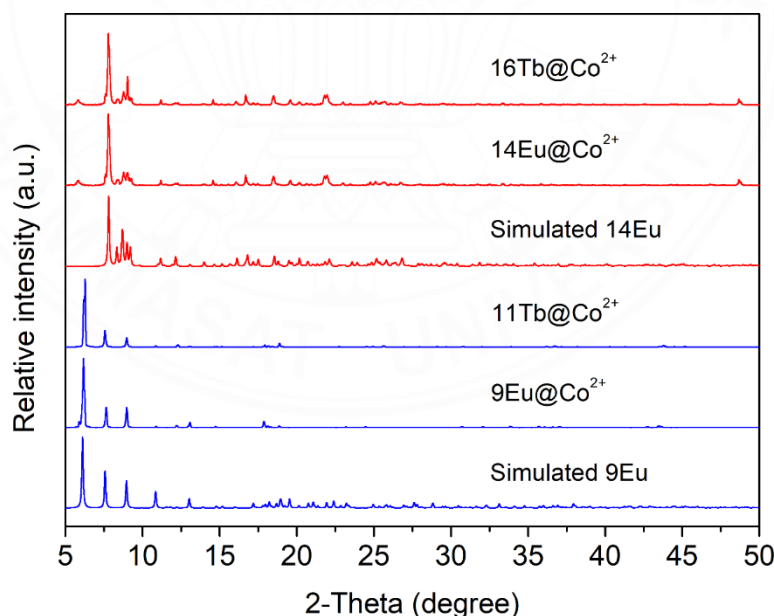
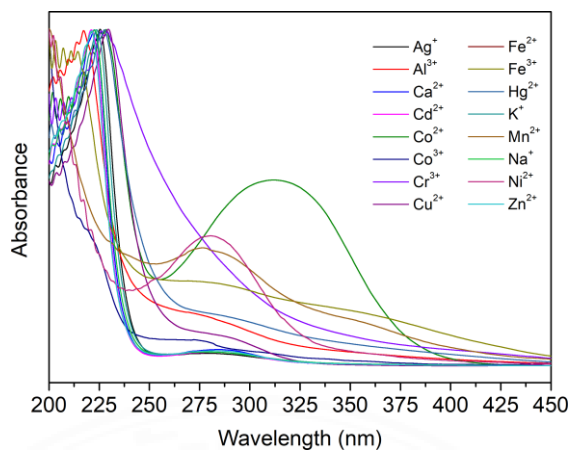
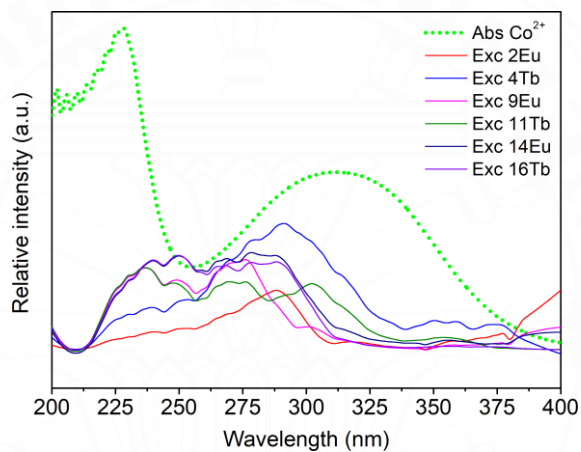


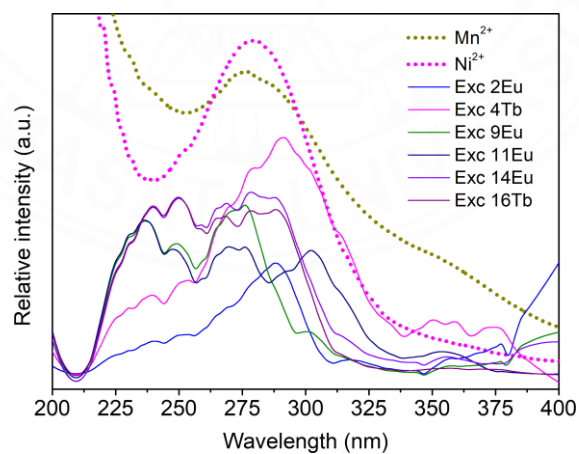
Figure 4.24 PXRD patterns of **9**<sub>Eu</sub>, **11**<sub>Tb</sub>, **14**<sub>Eu</sub>, and **16**<sub>Tb</sub>: simulated and after sensing of  $\text{Co}^{2+}$  ions.



(a)



(b)



(c)

Figure 4.25 (a) UV-Vis absorption spectra for metal ions in acetonitrile solutions. (b) UV-Vis spectra of  $\text{Co}^{2+}$  and excitation spectra of **2Eu**, **4Tb**, **9Eu**, **11Tb**, **14Eu**, and **16Tb**. (c) UV-Vis spectra of  $\text{Mn}^{2+}$  and  $\text{Ni}^{2+}$  and excitation spectra of **2Eu**, **4Tb**, **9Eu**, **11Tb**, **14Eu**, and **16Tb**.

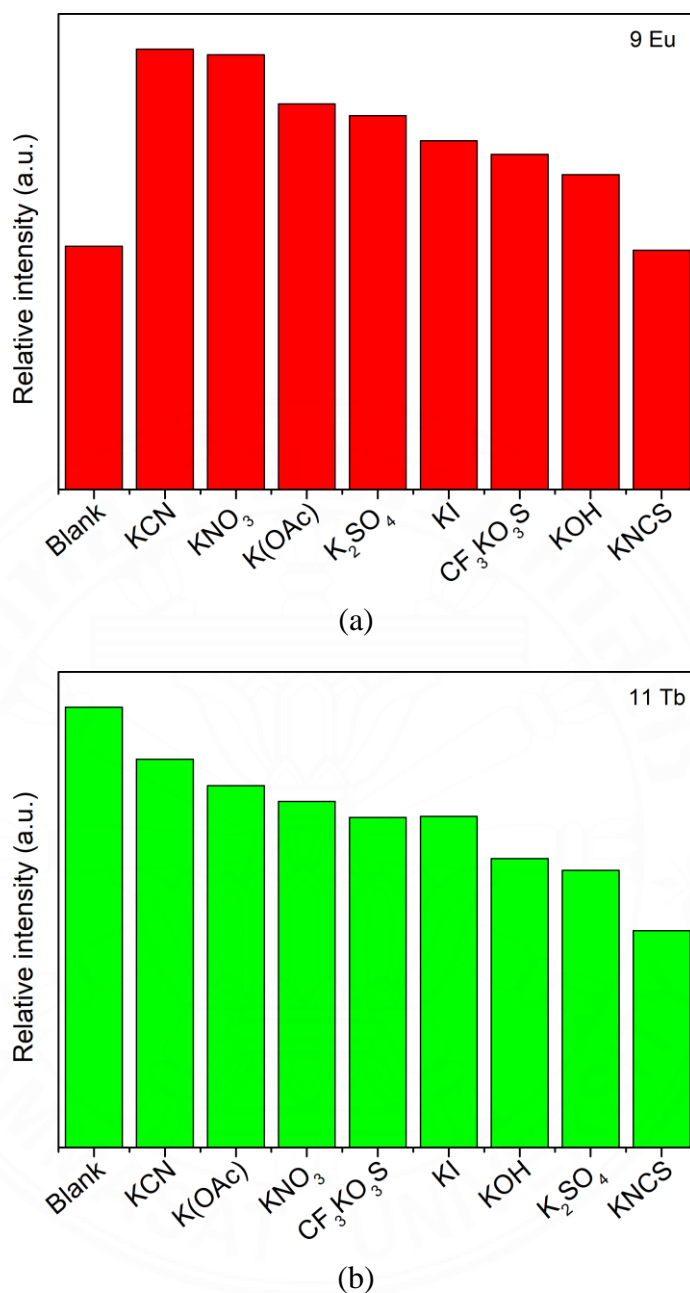


Figure 4.26 Emission intensities of the representative complexes (a) **9Eu** and (b) **11Tb** in acetonitrile solutions possessing potassium salts at  $5.0 \times 10^{-4}$  M.

Moreover, experimental studies were carried out to test the sensing results following recycling to investigate the recyclability and stability of **9Eu**, **11Tb**, **14Eu**, and **16Tb** for the luminescent sensing detection of Co<sup>2+</sup> ions. For this reason, the solid samples that were recovered after Co<sup>2+</sup> sensing were centrifuged from the solution



and washed ten times with MeCN. The emission intensities of the recovered solids were measured and compared. The luminescence intensities for three recycles are nearly identical to the previous emission intensities of the as-synthesized compounds as shown in Figure 4.27. Notably, the PXRD patterns of the obtained samples after three cycles are nearly identical to the original one as shown in Figure 4.28, inferring also that materials retain their crystal structure and crystallinity following these experiments. It means that complexes **9<sub>Eu</sub>**, **11<sub>Tb</sub>**, **14<sub>Eu</sub>**, and **16<sub>Tb</sub>** are compostable luminescent probes for  $\text{Co}^{2+}$  ions because these materials can be recycled at least three times without deterioration in performance. Following the detection of  $\text{Co}^{2+}$ , the recovered solid samples were subjected to XRF analysis. The presence of only the Eu or Tb signals in the XRF profiles as shown in Figure 4.29, which means the  $\text{Co}^{2+}$  ion was not incorporated in the crystal structures, is revealed by the results. This finding supports the conclusion that the binding interactions between the  $\text{Co}^{2+}$  analyte and the luminescent LnCP species in MeCN solution are relatively weak.

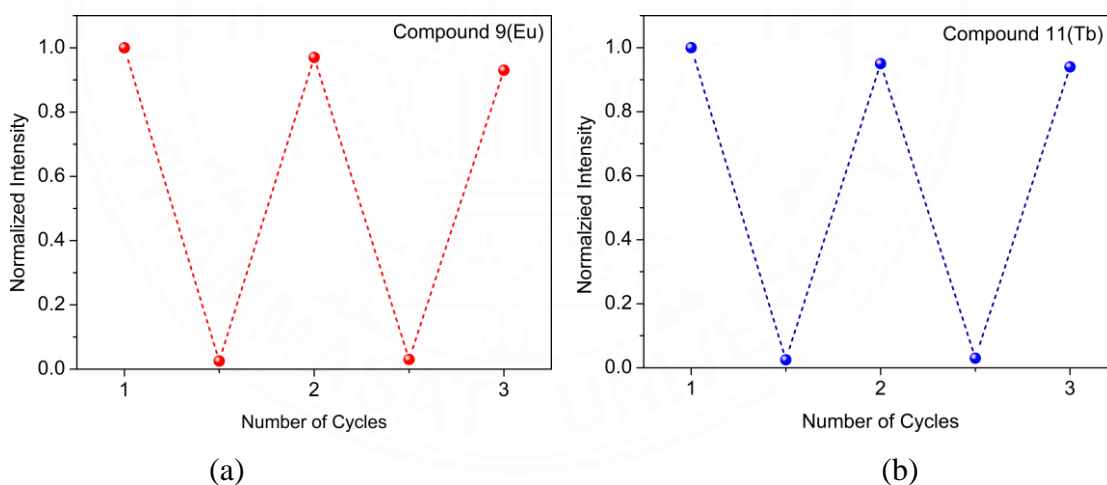


Figure 4.27 The quenching and recyclability test of (a) **9<sub>Eu</sub>**, (b) **11<sub>Tb</sub>**, (c) **14<sub>Eu</sub>**, and (d) **16<sub>Tb</sub>**, the upper dots represent the initial luminescence intensity and the lower dots represent the intensity upon addition of  $5 \times 10^{-4}$  M of the acetonitrile solution of  $\text{Co}^{2+}$ .

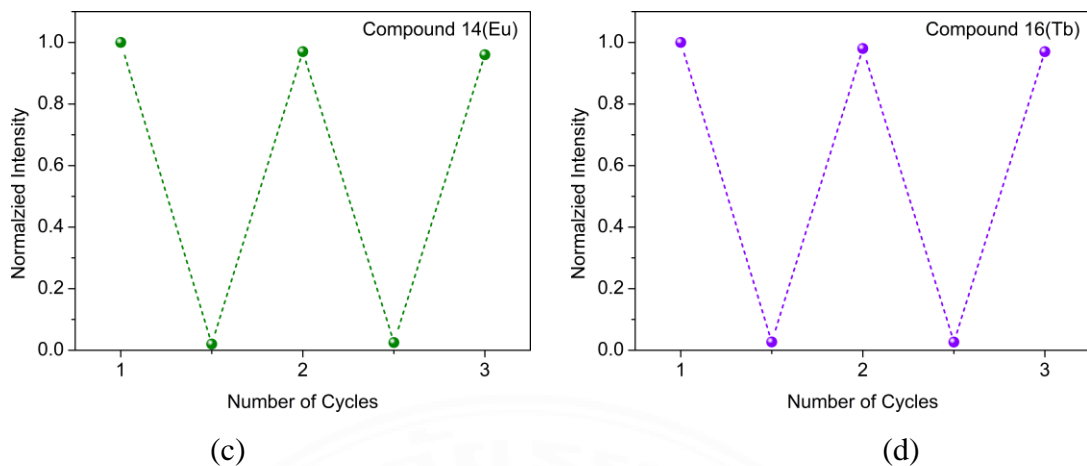


Figure 4.27 (Continued).

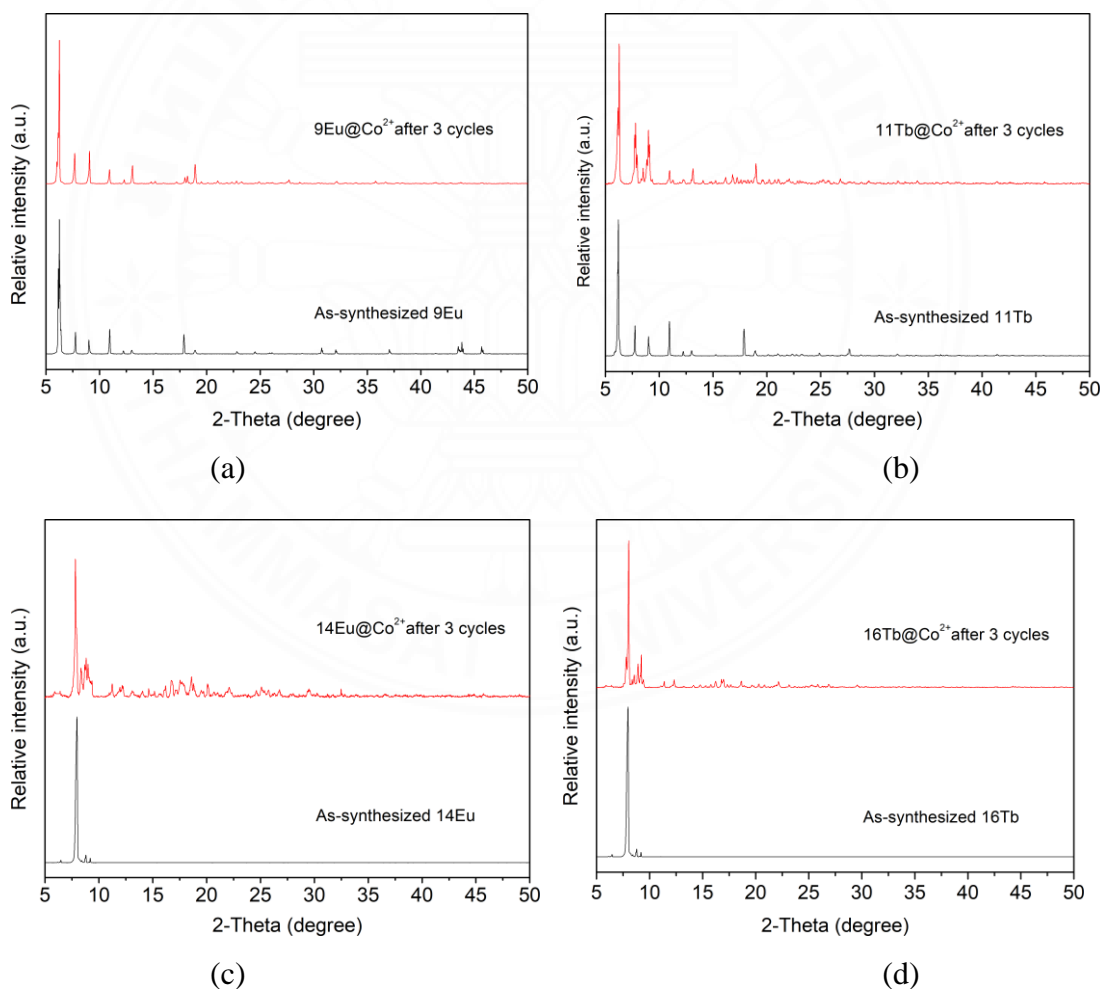


Figure 4.28 PXRD patterns of (a) **9<sub>Eu</sub>**, (b) **11<sub>Tb</sub>**, (c) **14<sub>Eu</sub>**, and (d) **16<sub>Tb</sub>** before and after three cycles of sensing tests.

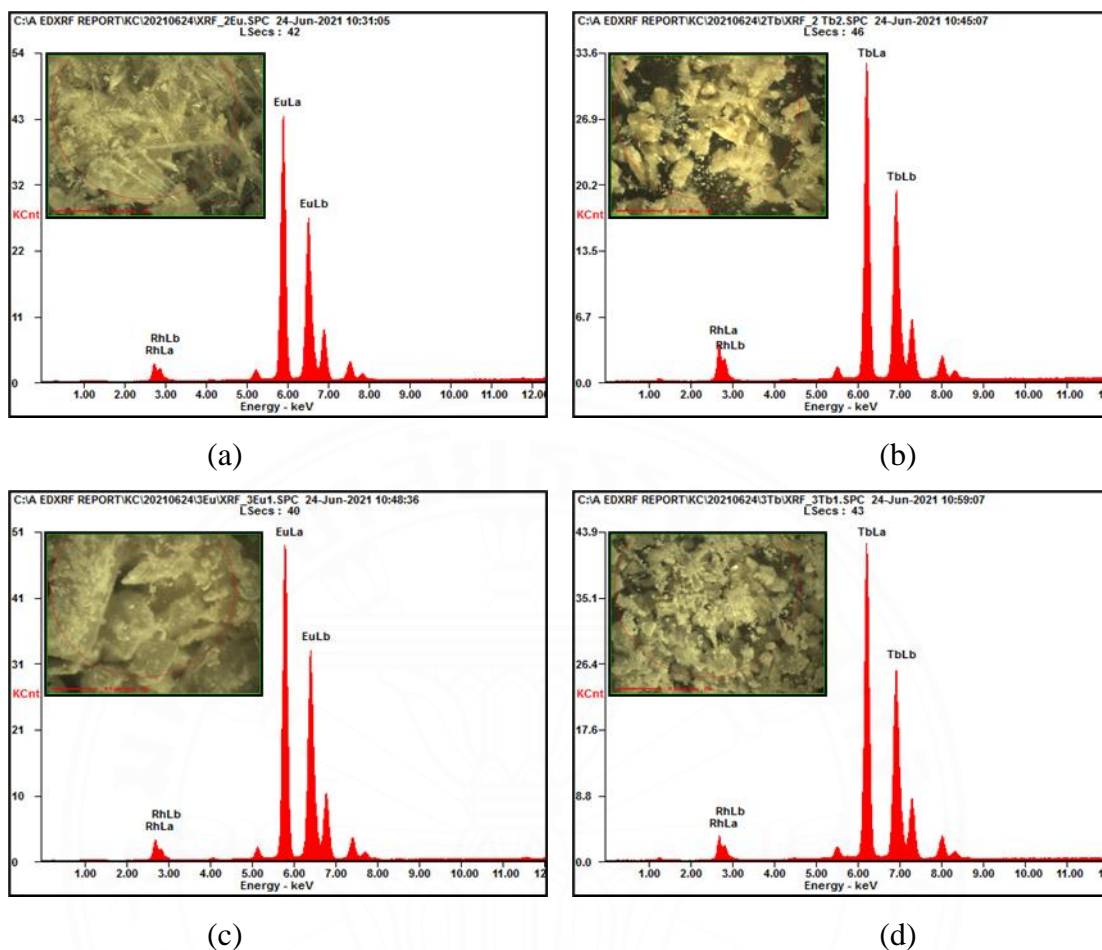


Figure 4.29 XRF spectra of (a) **9**<sub>Eu</sub>, (b) **11**<sub>Tb</sub>, (c) **14**<sub>Eu</sub>, and (d) **16**<sub>Tb</sub> after sensing tests.

#### 4.3.8 Magnetic properties

Magnetic properties of complexes **10**<sub>Gd</sub>, **12**<sub>Dy</sub>, **15**<sub>Gd</sub>, and **17**<sub>Dy</sub> were studied in order to understand potential magnetic interactions. Magnetic susceptibilities of Gd- and Dy-based CPs were measured at different temperatures between the region of 2–300 K with an applied magnetic field of 5000 Oe. As shown in Figure 4.30, the experimental  $\chi_m T$  product as a function of the temperature ( $\chi_m$  is the magnetic susceptibility per mole of  $\text{Ln}^{3+}$  ion) is presented. Complexes **10**<sub>Gd</sub> and **12**<sub>Dy</sub>, the  $\chi_m T$  values at 300 K are 7.92 and 14.10  $\text{cm}^3 \text{K mol}^{-1}$ , respectively. For one magnetically isolated  $\text{Ln}^{3+}$  ion, there are nearly theoretical values (7.88 (**10**<sub>Gd</sub>) and 14.17 (**12**<sub>Dy</sub>)  $\text{cm}^3 \text{K mol}^{-1}$ ). ( $\text{Gd}^{3+}$ ,  $^8\text{S}_{7/2}$ ,  $g = 2$ ;  $\text{Dy}^{3+}$ ,  $^6\text{H}_{15/2}$ ,  $g = 4/3$ ) (Hatscher *et al*, 2003; Caneschi *et al*, 2004; Cañadillas *et al*, 2010; Das *et al*, 2014; Chen *et al*, 2016; Akhtar *et al*, 2017).

While the  $\chi_m T$  values of 23.57 and 41.65  $\text{cm}^3 \text{K mol}^{-1}$  at 300 K are also nearly the values expected (23.64 (**15Gd**) and 42.51 (**17Dy**)  $\text{cm}^3 \text{K mol}^{-1}$ ) for three isolated  $\text{Ln}^{3+}$  ions. The  $\chi_m T$  values of complexes **10Gd**, **12Dy**, **15Gd**, and **17Dy** gradually decrease with decreasing temperature down to 6.79, 8.20, 21.97, and 31.90  $\text{cm}^3 \text{K mol}^{-1}$  at 2 K, respectively. Such magnetic behaviors in the thermal depopulation of the Stark sublevels and weak antiferromagnetic interactions between the  $\text{Ln}^{3+}$  centers are related to the Gd- and Dy-CPs (Zhao *et al*, 2013; Hutchings *et al*, 2014; Wang *et al*, 2020).

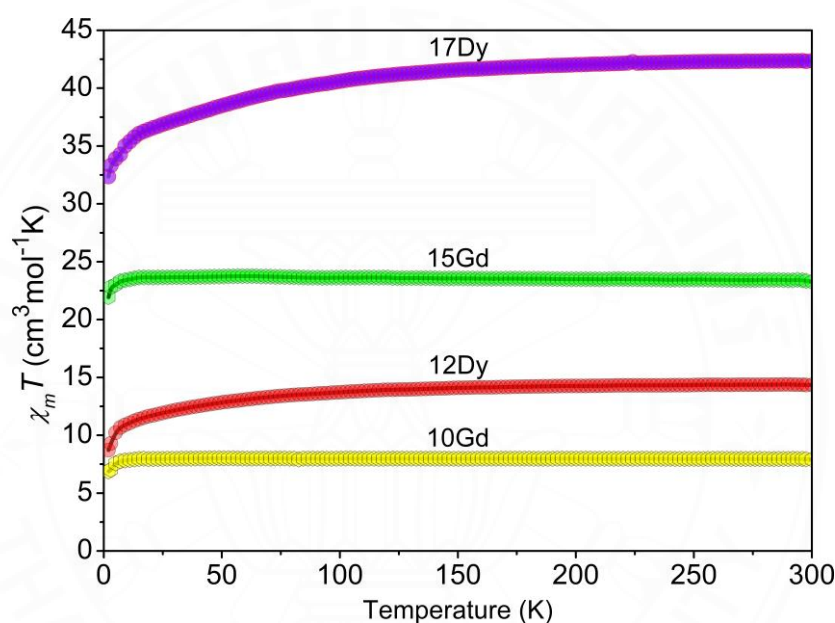


Figure 4.30 Plots of  $\chi_m T$  as a function of temperature for the **10Gd**, **15Gd**, **12Dy**, and **17Dy** containing complexes under a 1000 Oe field.

#### 4.4 Conclusion

Twenty-one lanthanide coordination complexes were successfully synthesized as single crystal samples based on the reaction between the bzz ligand with  $\text{Ln(III)}$  nitrate salts under different reaction conditions. In this research, the hydrothermal *in situ* formation of the ben ligand via bzz molecule hydrolysis has a significant impact on the development of thermodynamically stable lanthanide-based CPs **2Ln** and **3Ln**. These CPs are still stable in the air for long periods (up to ten months). And all the while, discrete mononuclear complexes **1Ln** enclosing only

chelated bzz ligands become unstable after 6 hours in the air. Interestingly, when heating the crystalline samples in the air at 400 °C **2Ln** structures are transformed into the thermodynamically more stable phase **3Ln**. Particularly, in the **3Ln** series, the structure of **14Eu** has good thermal stability up to 500 °C. Furthermore, the solid-state photoluminescence properties of the Eu- and Tb-based CPs show that the ligands bzz and ben give good sensitization of the Eu<sup>3+</sup> and Tb<sup>3+</sup> luminescence through the ligand-to-lanthanide energy transfer process. The **9Eu**, **14Eu**, **11Tb**, **16Tb** based CPs not only emit red and green intense luminescence with long lifetimes at the microsecond scale but also show function as luminescent sensors for acetone and Co<sup>2+</sup> ions via an energy competition mechanism with high recyclability. Moreover, temperature-dependent magnetic susceptibility data indicate that **10Gd**, **15Gd**, **12Dy**, and **17Dy** display antiferromagnetic coupling between the corresponding Ln<sup>3+</sup> ions. This research reveals, for the first time, that *in situ* hydrolyses of hydrazide-based organic ligands can occur in lanthanide-based CPs with 1D chain structures, as well as their intriguing thermal, luminescence, and magnetic properties. Additionally, the investigation will focus on the development of novel functional lanthanide-based CPs with the bzz derivatives by utilizing *in situ* hydrolysis of hydrothermally to generate carboxylate-based ligands from the hydrazide group, and such investigations are currently underway.

#### 4.5 References

- Aguilà, D., Barrios, L. A., Velasco, V., Arnedo, L., Aliaga-Alcalde, N., Menelaou, M., ... & Aromí, G. (2013). Lanthanide contraction within a series of asymmetric dinuclear [Ln<sub>2</sub>] complexes. *Chemistry—A European Journal*, 19(19), 5881-5891.
- Aime, S., Botta, M., Dickins, R. S., Maupin, C. L., Parker, D., Riehl, J. P., & Williams, J. G. (1998). Synthesis, NMR, relaxometry and circularly polarised luminescence studies of macrocyclic monoamidetriss (phosphinate) complexes bearing a remote chiral centre. *Journal of the Chemical Society, Dalton Transactions*, (6), 881-892.

- Akhtar, M. N., Chen, Y. C., AlDamen, M. A., & Tong, M. L. (2017). 3D oxalato-bridged lanthanide (III) MOFs with magnetocaloric, magnetic and photoluminescence properties. *Dalton Transactions*, 46(1), 116-124.
- Baldwin, E. L., Byl, J. A. W., & Osheroff, N. (2004). Cobalt enhances DNA cleavage mediated by human topoisomerase II $\alpha$  in vitro and in cultured cells. *Biochemistry*, 43(3), 728-735.
- Bernot, K., Daiguebonne, C., Calvez, G., Suffren, Y., & Guillou, O. (2021). A journey in lanthanide coordination chemistry: from evaporable dimers to magnetic materials and luminescent devices. *Accounts of Chemical Research*, 54(2), 427-440.
- Borisova, N. E., Kostin, A. A., Eroshkina, E. A., Reshetova, M. D., Lyssenko, K. A., Spodine, E. N., & Puntus, L. N. (2014). Lanthanide Complexes with Tetradentate N, N', O, O'-Dipyridyl-Based Ligands: Structure, Stability, and Photophysical Properties. *European Journal of Inorganic Chemistry*, 2014(13), 2219-2229.
- Brahmayya, M., Dai, S. A., & Suen, S. Y. (2015). Synthesis of 5-substituted-3 H-[1, 3, 4]-oxadiazol-2-one derivatives: a carbon dioxide route (CDR). *RSC Advances*, 5(80), 65351-65357.
- Brandão, S. G., Ribeiro, M. A., Perrella, R. V., de Sousa Filho, P. C., & Luz, P. P. (2020). Substituent effects on novel lanthanide (III) hydrazides complexes. *Journal of Rare Earths*, 38(6), 642-648.
- Bruker, *APEX3, SAINT and SADABS*, Bruker AXS Inc., Madison, Wisconsin, USA, 2016
- Cañadillas-Delgado, L., Martín, T., Fabelo, O., Pasán, J., Delgado, F. S., Lloret, F., ... & Ruiz-Pérez, C. (2010). The Construction of Open GdIII Metal–Organic Frameworks Based on Methanetriacetic Acid: New Objects with an Old Ligand. *Chemistry—A European Journal*, 16(13), 4037-4047.
- Caneschi, A., Dei, A., Gatteschi, D., Poussereau, S., & Sorace, L. (2004). Antiferromagnetic coupling between rare earth ions and semiquinones in a series of 1: 1 complexes. *Dalton Transactions*, (7), 1048-1055.
- Chainok, K., Ponjan, N., Theppitak, C., Khemthong, P., Kiellar, F., Dungkaew, W., ... & Batten, S. R. (2018). Temperature-dependent 3D structures of lanthanide

- coordination polymers based on dicarboxylate mixed ligands. *CrystEngComm*, 20(46), 7446-7457.
- Chen, X. M., & Tong, M. L. (2007). Solvothermal in situ metal/ligand reactions: a new bridge between coordination chemistry and organic synthetic chemistry. *Accounts of chemical research*, 40(2), 162-170.
- Chen, B., Wang, L., Xiao, Y., Fronczek, F. R., Xue, M., Cui, Y., & Qian, G. (2009). A luminescent metal–organic framework with Lewis basic pyridyl sites for the sensing of metal ions. *Angewandte Chemie*, 121(3), 508-511.
- Chen, B., Xiang, S., & Qian, G. (2010). Metal– organic frameworks with functional pores for recognition of small molecules. *Accounts of chemical research*, 43(8), 1115-1124.
- Chen, Y. C., Liu, J. L., Ungur, L., Liu, J., Li, Q. W., Wang, L. F., ... & Tong, M. L. (2016). Symmetry-supported magnetic blocking at 20 K in pentagonal bipyramidal Dy (III) single-ion magnets. *Journal of the American Chemical Society*, 138(8), 2829-2837.
- Cotton, S. A., & Raithby, P. R. (2017). Systematics and surprises in lanthanide coordination chemistry. *Coord. Chem. Rev.*, 340, 220-231.
- Cui, Y., Zhang, J., He, H., & Qian, G. (2018). Photonic functional metal–organic frameworks. *Chemical Society Reviews*, 47(15), 5740-5785.
- da Rosa, P. P. F., Kitagawa, Y., & Hasegawa, Y. (2020). Luminescent lanthanide complex with seven-coordination geometry. *Coordination Chemistry Reviews*, 406, 213153.
- Das, S., Dey, A., Biswas, S., Colacio, E., & Chandrasekhar, V. (2014). Hydroxide-free cubane-shaped tetranuclear [Ln<sub>4</sub>] complexes. *Inorganic Chemistry*, 53(7), 3417-3426.
- Debatin, F., Thomas, A., Kelling, A., Hedin, N., Bacsik, Z., Senkovska, I., ... & Holdt, H. J. (2010). In Situ Synthesis of an Imidazolate-4-amide-5-imidate Ligand and Formation of a Microporous Zinc–Organic Framework with H<sub>2</sub>-and CO<sub>2</sub>-Storage Ability. *Angewandte Chemie*, 122(7), 1280-1284.
- Dolomanov, O. V., Bourhis, L. J., Gildea, R. J., Howard, J. A. K. & Puschmann, H. (2009). *J. Appl. Cryst.* 42, 339-341.



- Eliseeva, S. V., & Bünzli, J. C. G. (2010). Lanthanide luminescence for functional materials and bio-sciences. *Chemical Society Reviews*, 39(1), 189-227.
- Fan, T., Xia, T., Zhang, Q., Cui, Y., Yang, Y., & Qian, G. (2018). A porous and luminescent metal-organic framework containing triazine group for sensing and imaging of  $\text{Zn}^{2+}$ . *Microporous and Mesoporous Materials*, 266, 1-6.
- Feng, L., Pang, J., She, P., Li, J. L., Qin, J. S., Du, D. Y., & Zhou, H. C. (2020). Metal-organic frameworks based on group 3 and 4 metals. *Advanced Materials*, 32(44), 2004414.
- Feng, L., Wang, H. S., Xu, H. L., Huang, W. T., Zeng, T. Y., Cheng, Q. R., ... & Zhou, H. (2019). A water stable layered Tb (III) polycarboxylate with high proton conductivity over  $10^{-2} \text{ S cm}^{-1}$  in a wide temperature range. *Chemical Communications*, 55(12), 1762-1765.
- Ferru, G., Reinhart, B., Bera, M. K., Olvera de la Cruz, M., Qiao, B., & Ellis, R. J. (2016). The lanthanide contraction beyond coordination chemistry. *Chemistry—A European Journal*, 22(20), 6899-6904.
- Gao, H. Y., Peng, W. L., Meng, P. P., Feng, X. F., Li, J. Q., Wu, H. Q., ... & Luo, F. (2017). Lanthanide separation using size-selective crystallization of Ln-MOFs. *Chemical Communications*, 53(42), 5737-5739.
- Gulaczyk, I., Kręglewski, M., & Valentin, A. (2003). The N–N stretching band of hydrazine. *Journal of Molecular Spectroscopy*, 220(1), 132-136.
- Han, Y. H., Tian, C. B., & Du, S. W. (2014). An unusual chiral 3D inorganic connectivity featuring a {Pb 18} wheel: rapid and highly selective and sensitive sensing of Co (ii). *Dalton Transactions*, 43(30), 11461-11464.
- Hatscher, S. T., & Urland, W. (2003). Unexpected Appearance of Molecular Ferromagnetism in the Ordinary Acetate  $[\{\text{Gd}(\text{OAc}_3 (\text{H}_2\text{O})_2)_2\} \cdot 4\text{H}_2\text{O}]$ . *Angewandte Chemie International Edition*, 42(25), 2862-2864.
- Huangfu, M., Wang, M., Lin, C., Wang, J., & Wu, P. (2021). Luminescent metal-organic frameworks as chemical sensors based on “mechanism–response”: A review. *Dalton Transactions*, 50(10), 3429-3449.
- Hutchings, A. J., Habib, F., Holmberg, R. J., Korobkov, I., & Murugesu, M. (2014). Structural rearrangement through lanthanide contraction in dinuclear complexes. *Inorganic Chemistry*, 53(4), 2102-2112.



- Jiang, H., Jia, J., Shkurenko, A., Chen, Z., Adil, K., Belmabkhout, Y., ... & Eddaoudi, M. (2018). Enriching the reticular chemistry repertoire: merged nets approach for the rational design of intricate mixed-linker metal–organic framework platforms. *Journal of the American Chemical Society*, 140(28), 8858-8867.
- Ke, B., Ma, L., Kang, T., He, W., Gou, X., Gong, D., ... & Li, M. (2018). In vivo bioluminescence imaging of cobalt accumulation in a mouse model. *Analytical chemistry*, 90(8), 4946-4950.
- Klink, S. I., Grave, L., Reinhoudt, D. N., van Veggel, F. C., Werts, M. H., Geurts, F. A., & Hofstraat, J. W. (2000). A systematic study of the photophysical processes in polydentate triphenylene-functionalized  $\text{Eu}^{3+}$ ,  $\text{Tb}^{3+}$ ,  $\text{Nd}^{3+}$ ,  $\text{Yb}^{3+}$ , and  $\text{Er}^{3+}$  complexes. *The Journal of Physical Chemistry A*, 104(23), 5457-5468.
- Kreno, L. E., Leong, K., Farha, O. K., Allendorf, M., Van Duyne, R. P., & Hupp, J. T. (2012). Metal–organic framework materials as chemical sensors. *Chemical reviews*, 112(2), 1105-1125.
- Kumar, M., Li, L. Q., Zaręba, J. K., Tashi, L., Sahoo, S. C., Nyk, M., ... & Sheikh, H. N. (2020). Lanthanide contraction in action: structural variations in 13 lanthanide (III) thiophene-2, 5-dicarboxylate coordination polymers ( $\text{Ln} = \text{La} - \text{Lu}$ , except  $\text{Pm}$  and  $\text{Tm}$ ) featuring magnetocaloric effect, slow magnetic relaxation, and luminescence-lifetime-based thermometry. *Crystal Growth & Design*, 20(10), 6430-6452.
- Li, H., Liu, Y., Zheng, R., Chen, L., Zhao, J. W., & Yang, G. Y. (2016). Trigonal pyramidal  $\{\text{AsO}_2(\text{OH})\}$  bridging tetranuclear rare-earth encapsulated polyoxotungstate aggregates. *Inorganic Chemistry*, 55(8), 3881-3893.
- Li, H. Y., Zhao, S. N., Zang, S. Q., & Li, J. (2020). Functional metal–organic frameworks as effective sensors of gases and volatile compounds. *Chemical Society Reviews*, 49(17), 6364-6401.
- Liang, Y. T., Yang, G. P., Liu, B., Yan, Y. T., Xi, Z. P., & Wang, Y. Y. (2015). Four super water-stable lanthanide–organic frameworks with active uncoordinated carboxylic and pyridyl groups for selective luminescence sensing of  $\text{Fe}^{3+}$ . *Dalton Transactions*, 44(29), 13325-13330.

- Liu, B., Qiu, Y. C., Peng, G., & Deng, H. (2010). In situ solvothermal syntheses of a heteronuclear copper (I)-alkaline metallic tetrazole-based coordination polymer. *CrystEngComm*, 12(1), 270-276.
- Liu, Y. F., Hu, J. H., Lee, W. T., Yang, X. K., & Chen, J. D. (2020). Structural Transformations of Cobalt (II) Coordination Polymers Constructed from N, N'-Di-3-pyridyladipoamide and Tetracarboxylic Acids: Disentanglement upon Water Coordination. *Crystal Growth & Design*, 20(11), 7211-7218.
- Lustig, W. P., Mukherjee, S., Rudd, N. D., Desai, A. V., Li, J., & Ghosh, S. K. (2017). Metal-organic frameworks: functional luminescent and photonic materials for sensing applications. *Chemical Society Reviews*, 46(11), 3242-3285.
- Mahata, P., Mondal, S. K., Singha, D. K., & Majee, P. (2017). Luminescent rare-earth-based MOFs as optical sensors. *Dalton Transactions*, 46(2), 301-328.
- Meyer, L. V., Schönfeld, F., & Müller-Buschbaum, K. (2014). Lanthanide based tuning of luminescence in MOFs and dense frameworks—from mono-and multimetal systems to sensors and films. *Chemical Communications*, 50(60), 8093-8108.
- Muldoon, P. F., Collet, G., Eliseeva, S. V., Luo, T. Y., Petoud, S., & Rosi, N. L. (2020). Ship-in-a-bottle preparation of long wavelength molecular antennae in lanthanide metal-organic frameworks for biological imaging. *Journal of the American Chemical Society*, 142(19), 8776-8781.
- Qi, X., Jin, Y., Li, N., Wang, Z., Wang, K., & Zhang, Q. (2017). A luminescent heterometallic metal-organic framework for the naked-eye discrimination of nitroaromatic explosives. *Chemical Communications*, 53(74), 10318-10321.
- Pangani, V. S., Machhoshvili, R. I., Agre, V. M., Trunov, V. K., & Shchelokov, R. N. (1984). Coordination compounds of lanthanides with acetylhydrazine. *Inorganica Chimica Acta*, 94(1-3), 79.
- Parker, D., & Williams, J. G. (1996). Getting excited about lanthanide complexation chemistry. *Journal of the Chemical Society, Dalton Transactions*, (18), 3613-3628.
- Phadungsak, N., Kielar, F., Dungkaew, W., Sukwattanasinitt, M., Zhou, Y., & Chainok, K. (2019). A new luminescent anionic metal-organic framework based on heterometallic zinc (II)-barium (II) for selective detection of Fe<sup>3+</sup> and Cu<sup>2+</sup> ions

- in aqueous solution. *Acta Crystallographica Section C: Structural Chemistry*, 75(10), 1372-1380.
- Ponjan, N., Kielar, F., Dungkaew, W., Kongpatpanich, K., Zenno, H., Hayami, S., ... & Chainok, K. (2020). Self-assembly of three-dimensional oxalate-bridged alkali (I)–lanthanide (III) heterometal–organic frameworks. *CrystEngComm*, 22(29), 4833-4841.
- Reddy, M. L. P., & Sivakumar, S. (2013). Lanthanide benzoates: a versatile building block for the construction of efficient light emitting materials. *Dalton Transactions*, 42(8), 2663-2678.
- Rose, A., Zhu, Z., Madigan, C. F., Swager, T. M., & Bulović, V. (2005). Sensitivity gains in chemosensing by lasing action in organic polymers. *Nature*, 434(7035), 876-879.
- Sairenji, S., Akine, S., & Nabeshima, T. (2016). Lanthanide contraction for helicity fine-tuning and helix-winding control of single-helical metal complexes. *Dalton Transactions*, 45(38), 14902-14906.
- Seitz, M., Oliver, A. G., & Raymond, K. N. (2007). The lanthanide contraction revisited. *Journal of the American Chemical Society*, 129(36), 11153-11160.
- Sheldrick, G. M. (2015). SHELXT–Integrated space-group and crystal-structure determination. *Acta Crystallographica Section A: Foundations and Advances*, 71(1), 3-8.
- Sheldrick, G. M. (2008). *Acta Cryst.* A64, 112-122.
- Smith, J. A., Singh-Wilmot, M. A., Carter, K. P., Cahill, C. L., Lough, A. J., & Knee, C. S. (2016). Eight rare earth metal organic frameworks and coordination polymers from 2-nitroterephthalate: syntheses, structures, solid-state luminescence and an unprecedented topology. *New Journal of Chemistry*, 40(9), 7338-7349.
- Spek, A. L. (2015). PLATON SQUEEZE: a tool for the calculation of the disordered solvent contribution to the calculated structure factors. *Acta Crystallographica Section C: Structural Chemistry*, 71(1), 9-18.
- Theppitak, C., Kielar, F., & Chainok, K. (2018). Crystal structure of diaquatrakis (benzohydrazide- $\kappa^2$ N,O)(isophthalato- $\kappa$ O) samarium (III) nitrate. *Acta*

- Crystallographica Section E: Crystallographic Communications*, 74(12), 1691-1694.
- Wang, W. M., Huai, L., Wang, X. W., Jiang, K. J., Shen, H. Y., Gao, H. L., ... & Cui, J. Z. (2020). Structures, magnetic refrigeration and single molecule-magnet behavior of five rhombus-shaped tetranuclear Ln (III)-based clusters. *New Journal of Chemistry*, 44(25), 10266-10274.
- Wang, X., Zhai, Q. G., Li, S. N., Jiang, Y. C., & Hu, M. C. (2014). Synthesis, crystal structures, and solid-state luminescent properties of diverse Ln–Pyridine-3, 5-Dicarboxylate coordination polymers modulated by the ancillary ligand. *Crystal growth & design*, 14(1), 177-188.
- Xu, H., Liu, F., Cui, Y., Chen, B., & Qian, G. (2011). A luminescent nanoscale metal–organic framework for sensing of nitroaromatic explosives. *Chemical Communications*, 47(11), 3153-3155.
- Xu, H., Cao, C. S., Kang, X. M., & Zhao, B. (2016). Lanthanide-based metal–organic frameworks as luminescent probes. *Dalton transactions*, 45(45), 18003-18017.
- Zhang, J., Zheng, B., Zhao, T., Li, G., Huo, Q., & Liu, Y. (2014). Topological diversities and luminescent properties of lanthanide metal–organic frameworks based on a tetracarboxylate ligand. *Crystal growth & design*, 14(5), 2394-2400.
- Zhang, X., Vieru, V., Feng, X., Liu, J. L., Zhang, Z., Na, B., ... & Long, J. R. (2015). Influence of Guest Exchange on the Magnetization Dynamics of Dilanthanide Single-Molecule-Magnet Nodes within a Metal–Organic Framework. *Angewandte Chemie International Edition*, 54(34), 9861-9865.
- Zhao, L., Wu, J., Ke, H., & Tang, J. (2013). Three dinuclear lanthanide (iii) compounds of a polydentate Schiff base ligand: Slow magnetic relaxation behaviour of the Dy III derivative. *CrystEngComm*, 15(26), 5301-5306.
- Zheng, Z., Lu, H., Wang, Y., Bao, H., Li, Z. J., Xiao, G. P., ... & Wang, J. Q. (2020). Tuning of the network dimensionality and photoluminescent properties in homo-and heteroleptic lanthanide coordination polymers. *Inorganic Chemistry*, 60(3), 1359-1366.
- Zhou, X. H., Li, L., Li, H. H., Li, A., Yang, T., & Huang, W. (2013). A flexible Eu (III)-based metal–organic framework: turn-off luminescent sensor for the detection of Fe (III) and picric acid. *Dalton Transactions*, 42(34), 12403-12409.

- Zhu, Q., Sheng, T., Tan, C., Hu, S., Fu, R., & Wu, X. (2011). Formation of Zn (II) and Cd (II) coordination polymers assembled by triazine-based polycarboxylate and in-situ-generated pyridine-4-thiolate or dipyridylsulfide ligands: observation of an unusual luminescence thermochromism. *Inorganic Chemistry*, 50(16), 7618-7624.
- Zinner, L. B., Crotty, D. E., Anderson, T. J., & Glick, M. D. (1979). Synthesis and structure of complexes of lanthanide nitrates and isonicotinic acid hydrazide,  $\text{Ln}(\text{NO}_3)_3 \cdot 3 \text{INH} \cdot 3\text{H}_2\text{O}$ . *Inorganic Chemistry*, 18(7), 2045-2048.



## CHAPTER 5

### SELF-ASSEMBLY OF LANTHANIDE COORDINATION POLYMERS VIA IN SITU-GENERATED BENZHYDRAZIDE LIGANDS

#### 5.1 Introduction

Coordination polymers are a type of crystalline hybrid materials between organic-inorganic composed of coordination bonds that link metal ions or clusters and organic bridges (Batten *et al*, 2009). These hybrid solid materials have fascinating structures of variable dimensionality, which permit applications in areas of adsorption, luminescence, catalysis, and magnetism (Gorai *et al*, 2021; He *et al*, 2015; Kuwamura *et al*, 2021; Roy *et al*, 2014). Lanthanide-based coordination polymers (LnCPs) also gained considerable interest in recent decades because of their distinct optical and electronic properties, including such high luminescence efficiency, long lifetimes, and narrow bandwidths, which allow for useful applications in sensors, illumination, and comprehensive optics (Cui *et al*, 2012). LnCPs are more difficult to rationally design and synthesize than transition metal-based coordination polymers because  $\text{Ln}^{3+}$  ions frequently exhibit increased coordination numbers (typically from 6 - 12) and versatile coordination geometries. Furthermore, the various parameters of the synthesis reactions, including reactant ratio, solvent, reaction temperature, and pH can affect the nucleation and crystal growth of the final products (Ju *et al*, 2020; Han *et al*, 2015; Wu *et al*, 2020; Klongdee *et al*, 2017). As a consequence, further research into the effect of synthetic parameters on the crystal growth and self-assembly of LnCPs is required. This is generally recognized that  $\text{Ln}^{3+}$  ions have a strong affinity for hard donor atoms and favor to be bound to them. The organic ligands containing oxygen and/or nitrogen, specifically benzene and pyridine carboxylates, have been popularly for created in the creation of new lanthanide-based luminescent materials. These ligands can exhibit an array of coordination modes for the central  $\text{Ln}^{3+}$  ions. They can also be used as illumination antennas to efficiently sensitize  $\text{Ln}^{3+}$  ions and increase their emission intensity (Chen *et al*, 2009; Lin *et al*, 2016; Li *et al*, 2020).

Hydro/solvothermal reactions with *in situ* ligand synthesis have been established as one of the most viable strategies for the development of novel coordination polymers (Zhang, 2005). For example, a diversity of fascinating structural topologies of tetrazole-based polymeric complexes have been designed and synthesized by *in situ* [2 + 3] cycloaddition reaction of nitriles and an azide in the inclusion of metal salts under hydrothermal conditions (Xiong *et al*, 2002; Tang *et al*, 2015). Furthermore, this method can be applied to a wide range of carboxylate-based coordination polymers obtained from the hydrolysis of ester or cyano groups in water. (Fishburn *et al*, 2020; Kong *et al*, 2021).

We are researching the synthesis of novel crystalline coordination polymers in order to better understand their structure-property relationships. (Chainok *et al*, 2018; Phadungsak *et al*, 2019; Ponjan *et al*, 2020). In this research, we aim to investigate the possibility of synthesizing novel LnCPs with benzhydrazide (bzz) as a ligand. We present two new LnCPs, [Sm<sub>2</sub>(bzz)(ben)<sub>6</sub>(H<sub>2</sub>O)<sub>3</sub>] · 0.5H<sub>2</sub>O (**22<sub>Sm</sub>**) and 3D [Eu(bbz)(ben)<sub>3</sub>] (**2Eu**), derived by *in situ* synthesis of *N'*-benzoylbenzohydrazide (bbz) and benzoate (ben) ligands of bzz and lanthanide nitrate salts by hydrothermal reactions. Single crystal X-ray diffraction analysis has clearly demonstrated *in situ* ligand formation. High-pressure CO<sub>2</sub> adsorption of the activated sample **22<sub>Sm</sub>** was studied in the pressure region up to 50 bars at 298 K. Furthermore, the solid-state photoluminescence and lifetime decay behavior of **23<sub>Eu</sub>** was investigated.

## 5.2 Experimental section

### 5.2.1 Materials and methods

All starting materials, i.e., Sm(NO<sub>3</sub>)<sub>3</sub>·6H<sub>2</sub>O, Eu(NO<sub>3</sub>)<sub>3</sub>·6H<sub>2</sub>O, and benzhydrazide (bzz) were of reagent-grade quality, and obtained without further purification from commercial sources. A LECO CHNS 932 elemental analyzer was used to determine elemental (C, H, N) analysis. FT-IR spectra were reported on a PerkinElmer model Spectrum 100 spectrometer using ATR mode, in the range of 650–4000 cm<sup>-1</sup>. PXRD measurements were collected on a Bruker D8 ADVANCE X-ray powder diffractometer using Cu-Kα (λ = 1.5418 Å). TGA thermograms were obtained



in N<sub>2</sub> atmosphere on a TGA 55 TA instrument. The measurement was carried out from room temperature to 650 °C at a heating rate of 10 °C min<sup>-1</sup>. A Quantachrome iSorb HP1 analyzer was used to measure CO<sub>2</sub> adsorption isotherms in the pressure range of 0.1-50 bar at 298 K. The adsorption measurements were performed using ultrapure (99.995%) CO<sub>2</sub> gas. At room temperature, the PL spectra and emission decay curves were obtained with a Horiba Scientific model FluoroMax-4 spectrofluorometer.

### 5.2.2 Synthesis of [Sm<sub>2</sub>(bzz)(ben)<sub>6</sub>(H<sub>2</sub>O)<sub>3</sub>]·H<sub>2</sub>O (**22<sub>Sm</sub>**)

A mixture of Sm(NO<sub>3</sub>)<sub>3</sub>·6H<sub>2</sub>O (44.7 mg, 0.1 mmol) and bzz (27.3 mg, 0.2 mmol) in distilled H<sub>2</sub>O (4 mL) was sealed in a Teflon-lined autoclave (15 mL) heated to 130 °C for 96 h. After that slowly cooled to ambient temperature, The crystalline product was filtered, rinsed with distilled water, and dried in ambient air. The crystal was obtained in the form of light-yellow needle-like crystals with a yield of 84% 37.5 mg based on Sm(NO<sub>3</sub>)<sub>3</sub>·6H<sub>2</sub>O. Anal. calc. for C<sub>49</sub>H<sub>46</sub>N<sub>2</sub>O<sub>17</sub>Sm<sub>2</sub>: C 47.63% H 3.75% N 2.27%. Found: C 47.54% H 3.49% N 2.56%. FT-IR ATR, ν/cm<sup>-1</sup>, s for strong, m for medium, w for weak: 3430w, 3058w, 1593m, 1532s, 1492m, 1403s, 1307w, 1180s, 1070w, 1025w, 845w, 712s, 684m.

### 5.2.3 Synthesis of [Eu(bbz)(ben)<sub>3</sub>] (**23<sub>Eu</sub>**)

The protocol was identical to that of **22<sub>Sm</sub>**, except that Sm(NO<sub>3</sub>)<sub>3</sub>·6H<sub>2</sub>O was replaced by Eu(NO<sub>3</sub>)<sub>3</sub>·6H<sub>2</sub>O (44.9 mg, 0.1 mmol). The crystal was obtained as light-yellow block-shaped crystals with a yield of 47% 21.1 mg based on Eu(NO<sub>3</sub>)<sub>3</sub>·6H<sub>2</sub>O. Anal. calc. for C<sub>35</sub>H<sub>27</sub>EuN<sub>2</sub>O<sub>8</sub>: C 35.66% H 3.42% N 17.82%. Found: C 35.43% H 3.41% N 17.35%. FT-IR ATR, ν/cm<sup>-1</sup>: 3155w, 3055w, 3002w, 2896w, 1643m, 1587m, 1504s, 1477s, 1398s, 1305m, 1173w, 1066w, 1020w, 921w, 834w, 695m.

### 5.2.4 X-ray crystallography

The single crystal X-ray diffraction measurements for compounds **22<sub>Sm</sub>** and **23<sub>Eu</sub>** were mounted on MiTeGen micromounts using paratone oil (Hampton Research). Diffraction measurements were taken with a Bruker D8 QUEST CMOS PHOTON II at T = 296(2) K. Data were collected using ω and φ scans and as well as Mo-K radiation (λ = 0.71073 Å). The all number of runs and images was determined using the APEX3 strategy calculation, and unit cell indexing was refined using SAINT



(APEX3, SAINT and SADABS, 2021). SAINT was used for data reduction, and SADABS was used for absorption correction. PLATON was used to verify the symmetry's integrity. (Spek, 2015). The ShelXT structure solution program was used to solve the structure, which used a combination of Patterson and dual-space recycling methods. (Sheldrick, 2015). ShelXL was used to refine the structure using least squares (Sheldrick, 2015) using the OLEX2 (Dolomanov, 2009) interface. All non-H atoms were refined anisotropically in the final refinement cycles. All C-bound H atoms were determined by calculating and refined using a riding-model approximation with C-H = 0.93 Å and  $U_{iso}(H) = 1.2 U_{eq}(C)$ , while all N- and O-bound H atoms were located in a difference Fourier map and refined with N-H = 0.86–0.89 Å and O-H =  $0.84 \pm 0.01$  Å, respectively. The positional disorder in the lattice water molecule in **22<sub>Sm</sub>** was refined as two contributions, with a 0.80:0.20 occupancy ratio. The benzene rings of the ligands in **22<sub>Sm</sub>** and **23<sub>Eu</sub>** were obtained to be disordered over two 50% occupancy sites. Table 5.1 reported the crystallographic parameters, data collection, and refinements for all complexes.

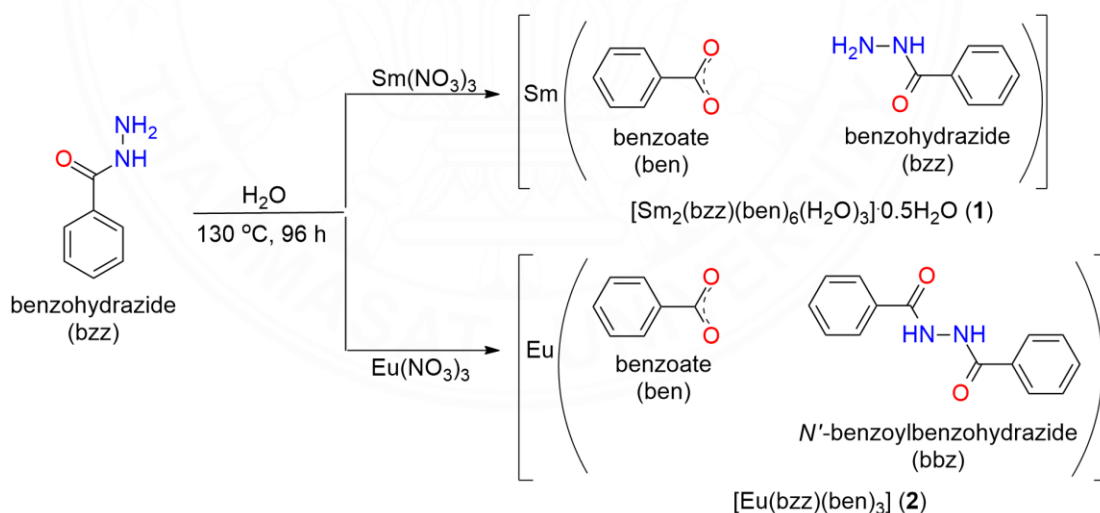


Figure 5.1 Synthetic routes for compounds **22<sub>Sm</sub>** and **23<sub>Eu</sub>**.

**Table 5.1***Crystal data and structure refinement for 22<sub>Sm</sub> and 23<sub>Eu</sub>.*

Identification code (CCDC no.)	22 <sub>Sm</sub> (2083033)	23 <sub>Eu</sub> (2083034)
Empirical formula	C <sub>49</sub> H <sub>46</sub> N <sub>2</sub> O <sub>17</sub> Sm <sub>2</sub>	C <sub>35</sub> H <sub>27</sub> EuN <sub>2</sub> O <sub>8</sub>
Formula weight	1235.58	755.54
Crystal system	Triclinic	Orthorhombic
Space group	<i>P</i> -1	<i>Pnna</i>
<i>a</i> (Å)	10.1273(11)	19.1656(5)
<i>b</i> (Å)	15.0479(16)	19.3314(5)
<i>c</i> (Å)	16.9178(17)	17.7307(5)
$\alpha$ (°)	97.949(3)	90
$\beta$ (°)	105.451(3)	90
$\gamma$ (°)	91.345(3)	90
<i>V</i> (Å <sup>3</sup> )	2456.2(4)	6569.2(3)
<i>Z</i>	2	8
<i>D</i> <sub>calc</sub> (g cm <sup>-3</sup> )	1.671	1.528
$\mu$ (mm <sup>-1</sup> )	2.441	1.960
Crystal size (mm <sup>3</sup> )	0.23 × 0.11 × 0.10	0.23 × 0.11 × 0.10
Diffractometer	Bruker D8 QUEST CMOS	Bruker D8 QUEST CMOS
Radiation	MoK $\alpha$ ( $\lambda$ = 0.71073 Å)	MoK $\alpha$ ( $\lambda$ = 0.71073 Å)
Absorption correction	Multi-scan	Multi-scan
$\theta$ range for data collection	3.1–26.4°	3.0–30.4°
Data completeness	99.8 ( $\theta_{\max}$ = 26.4°)	99.9 ( $\theta_{\max}$ = 30.4°)
Index ranges	–12 ≤ <i>h</i> ≤ 12 –18 ≤ <i>k</i> ≤ 17 –21 ≤ <i>l</i> ≤ 21	–25 ≤ <i>h</i> ≤ 24 –26 ≤ <i>k</i> ≤ 23 –23 ≤ <i>l</i> ≤ 23
Reflections collected	59514	86697
Independent reflections	10102	8483
Observed reflections	8345	6515
<i>R</i> <sub>int</sub> , <i>R</i> <sub>sigma</sub>	0.0261, 0.0175	0.0354, 0.0207
Number of restraints	555	710
Number of parameters	823	643
Goodness-of-fit on <i>F</i> <sup>2</sup>	1.046	1.046
<i>R</i> <sub>1</sub> , <i>wR</i> <sub>2</sub> [ <i>I</i> ≥ 2σ( <i>I</i> )]	0.0195, 0.0421	0.0339, 0.0779
<i>R</i> <sub>1</sub> , <i>wR</i> <sub>2</sub> [all data]	0.0287, 0.0457	0.0523, 0.0872
$\Delta\rho_{\max}$ , $\Delta\rho_{\min}$ (e Å <sup>-3</sup> )	0.83, –0.41	1.97, –0.37

## 5.3 Results and discussion

### 5.3.1 Synthesis

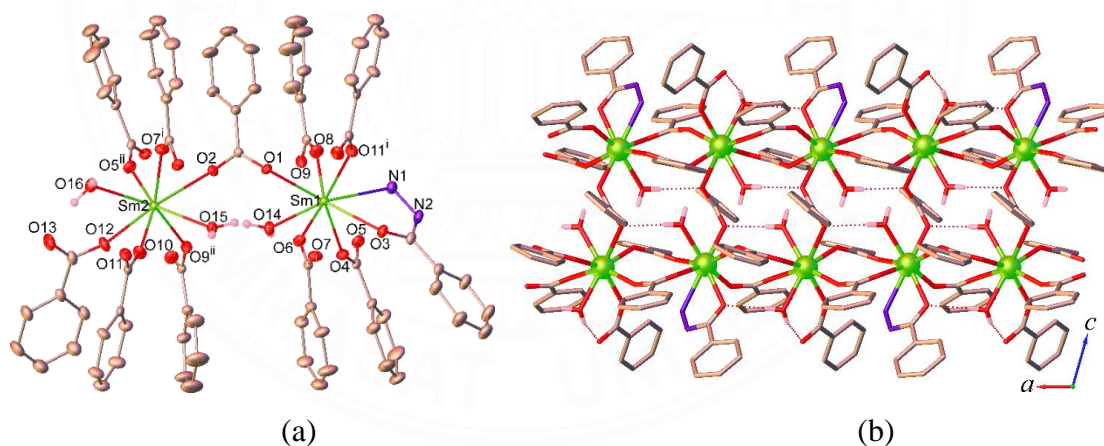
Compounds **22<sub>Sm</sub>** and **23<sub>Eu</sub>** were produced under identical conditions by hydrothermal synthesis of  $\text{Ln}(\text{NO}_3)_3 \cdot 6\text{H}_2\text{O}$  and bzz in a ratio of 1:2 over 96 *in situ* hours at 130 °C, as illustrated in Figure 5.1. The bzz precursor transformation produced the new bbz and ben ligands by acting as bridging and/or chelating ligands for  $\text{Ln}^{3+}$  ions via N and O sites, these new ligands can encourage the formation of different polymeric structures, including a 1D chain and a 3D framework for **22<sub>Sm</sub>** and **23<sub>Eu</sub>**, respectively. It should be pointed out that the bzz precursor was completely transformed into the ben ligand through the breakage of C-N bonds when the hydrothermal reactions were conducted at temperatures above 140 °C (Theppitak *et al.*, 2021).

### 5.3.2 Structural description

The details of selected bond lengths and bond angles for **22<sub>Sm</sub>** are listed in Table 5.2. Compound **22<sub>Sm</sub>** has a 1D chain structure and crystallizes in the triclinic system with *P*-1 space group. The asymmetric unit of **22<sub>Sm</sub>** contains two crystallographically independent  $\text{Sm}^{3+}$  ions, one bzz ligand, six ben ligands, three coordinated water molecules, and one disordered lattice water molecule with occupancy factors of 0.50. Both  $\text{Sm}^{3+}$  ions in **22<sub>Sm</sub>** take on comparable eight-coordinate geometries as shown in Figure 5.2a. Sm1 is coordinated by five O atoms from different ben ligands, one O atom and one N atom from a bzz ligand, and one O atom from a coordinated water molecule. While Sm2 is coordinated by six oxygen atoms from different ben ligands and two O atoms from coordinated water molecules. The coordination polyhedra around the  $\text{Ln}^{3+}$  metal centers can be best characterized as distorted trigonal dodecahedral geometries. The Sm-O/N bond lengths in **22<sub>Sm</sub>** are in the region 2.3088(16)-2.6290(19), which is typical for these compounds (Xu *et al.*, 2019).

In these compounds, the bzz ligand only exhibits a bidentate-chelating  $\eta^2$  mode to bind one  $\text{Ln}^{3+}$  ion through use of hydrazide oxygen and nitrogen sites, whereas the ben ligands exhibit both monodentate  $\eta^2$  (O4-O12) and bidentate-bridging  $\mu_2$  (O1, O2) modes. Two neighboring  $\text{Ln}^{3+}$  ions are bridged by carboxylate oxygen atoms of the ben ligands in a  $\mu_2$  fashion to form a 1D single chain running

parallel to  $a$  axis as shown in Figure 5.2b. The Ln...Ln separations via the  $\mu_2$ -ben ligands in **22<sub>Sm</sub>** are 5.0195(4) and 5.1423(4) Å. These chains are cross-linked along the  $c$  axis by the ben carboxylate oxygen (O1, O2) atoms, resulting in the formation of a 1D double chain. The Sm...Sm separation between the single chains via the  $\mu_2$ -ben ligands is 5.9773(4). These 1D double chains have been stabilized by extensive O-H...O and O-H...N hydrogen bonds among coordinated water and amine NH<sub>2</sub> donors and carboxylate acceptors, as well as C-H... $\pi$  arene edge-to-face interactions. Moreover, the double chains are linked together by O-H...O and O-H...N hydrogen bonds involving lattice water molecules. There are terminal carboxylate oxygen atoms and amine NH groups, as well as additional N-H... $\pi$  interactions between bzz molecules. Consequently, a 2D sheet is formed that propagates along the  $b$  axis. The ultimate 3D supramolecular architecture is the result of the stacking of the 2D sheets along the  $c$  axis and through van der Waals interactions. Table 5.3 shows the geometrical details of hydrogen bonds for **22<sub>Sm</sub>**.



**Figure 5.2** (a) Coordination environment of the Sm<sup>3+</sup> ion in **22<sub>Sm</sub>**. (b) 1D chain of **22<sub>Sm</sub>**. (c) 3D packing of **22<sub>Sm</sub>** and yellow colored space is the void space.

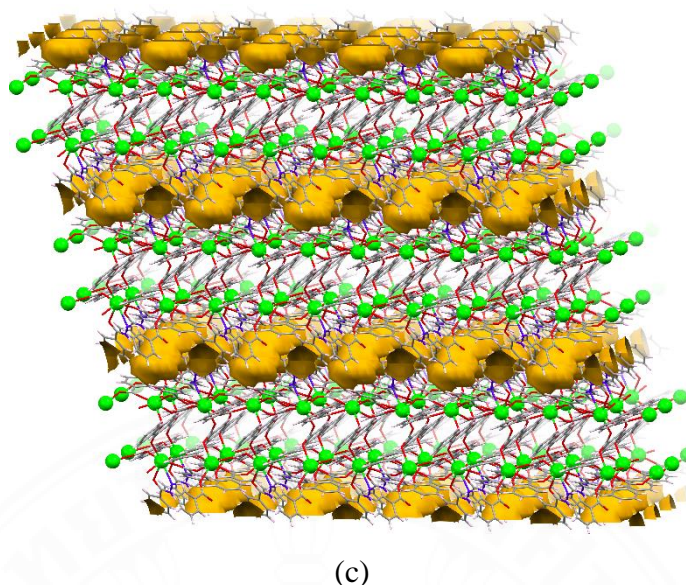


Figure 5.2 (Continued).

Besides, it is clear from the crystal structure of **22<sub>sm</sub>** that the lattice and the coordinated water molecules occupy the intralayer space and also the free space between the layers. The PLATON program (Spek, 2015) was used to perform void analysis. After removing the water molecules, the simulated solvent-accessible void space of **22<sub>sm</sub>** is approximated to be 5.9% ( $146. \text{\AA}^3$ ) of the crystal volume using a probe molecule radius of  $1.4 \text{\AA}$  and a grid interval of  $0.2 \text{\AA}$ . Figure 5.2c represents the potential void space of **22<sub>sm</sub>** calculated in mercury program (Macrae *et al*, 2020) using a probe radius of  $1.2 \text{\AA}$ .

**Table 5.2***Selected bond lengths (Å) and bond angles (°) for 22<sub>Sm</sub>*

<b>22<sub>Sm</sub></b>			
Sm1–O6	2.3088 (16)	Sm2–O7 <sup>i</sup>	2.3714 (17)
Sm1–O8	2.3278 (17)	Sm2–O9 <sup>ii</sup>	2.3386 (16)
Sm1–O11 <sup>i</sup>	2.3498 (17)	Sm2–O10	2.3551 (18)
Sm1–O14	2.4631 (18)	Sm2–O12	2.4332 (17)
Sm1–N1	2.6290 (19)	Sm2–O15	2.4840 (17)
Sm2–O2	2.5470 (16)	Sm2–O16	2.5279 (19)
Sm2–O5 <sup>ii</sup>	2.3220 (17)	Sm2–O7 <sup>i</sup>	2.3714 (17)
		Sm2–O9 <sup>ii</sup>	2.3386 (16)
O1–Sm1–O3	134.69 (5)	O5 <sup>ii</sup> –Sm2–O2	75.99 (6)
O1–Sm1–O14	73.60 (6)	O5 <sup>ii</sup> –Sm2–O7 <sup>i</sup>	88.07 (6)
O1–Sm1–N1	142.44 (6)	O5 <sup>ii</sup> –Sm2–O9 <sup>ii</sup>	94.32 (7)
O3–Sm1–N1	61.49 (6)	O5 <sup>ii</sup> –Sm2–O10	145.19 (7)
O4–Sm1–O1	140.85 (6)	O5 <sup>ii</sup> –Sm2–O12	74.96 (7)
O4–Sm1–O3	71.95 (6)	O5 <sup>ii</sup> –Sm2–O15	147.53 (6)
O4–Sm1–O14	68.20 (6)	O5 <sup>ii</sup> –Sm2–O16	79.19 (7)
O4–Sm1–N1	70.74 (6)	O7 <sup>i</sup> –Sm2–O2	73.38 (6)
O6–Sm1–O1	73.28 (6)	O7 <sup>i</sup> –Sm2–O12	140.62 (7)
O6–Sm1–O3	75.98 (6)	O7 <sup>i</sup> –Sm2–O15	83.89 (7)
O6–Sm1–O4	92.31 (6)	O7 <sup>i</sup> –Sm2–O16	69.04 (7)
O6–Sm1–O8	150.16 (7)	O9 <sup>ii</sup> –Sm2–O2	71.63 (6)
O6–Sm1–O11 <sup>i</sup>	102.37 (7)	O9 <sup>ii</sup> –Sm2–O7 <sup>i</sup>	143.17 (6)
O6–Sm1–O14	81.09 (7)	O9 <sup>ii</sup> –Sm2–O10	96.63 (7)
O6–Sm1–N1	137.15 (6)	O9 <sup>ii</sup> –Sm2–O12	74.56 (6)
O8–Sm1–O1	78.38 (6)	O9 <sup>ii</sup> –Sm2–O15	74.56 (7)
O8–Sm1–O3	132.59 (6)	O9 <sup>ii</sup> –Sm2–O16	147.44 (7)
O8–Sm1–O4	104.13 (7)	O10–Sm2–O2	138.79 (6)
O8–Sm1–O11 <sup>i</sup>	80.73 (7)	O10–Sm2–O7 <sup>i</sup>	102.14 (7)
O8–Sm1–O14	82.18 (7)	O10–Sm2–O12	76.33 (7)
O8–Sm1–N1	72.50 (7)	O10–Sm2–O15	67.24 (7)
O11 <sup>i</sup> –Sm1–O1	78.80 (6)	O10–Sm2–O16	73.87 (7)
O11 <sup>i</sup> –Sm1–O3	76.22 (6)	O12–Sm2–O2	132.94 (5)
O11 <sup>i</sup> –Sm1–O4	140.35 (6)	O12–Sm2–O15	128.23 (7)
O11 <sup>i</sup> –Sm1–O14	149.91 (7)	O12–Sm2–O16	72.94 (7)
O11 <sup>i</sup> –Sm1–N1	73.61 (7)	O15–Sm2–O2	71.56 (6)
O14–Sm1–O3	132.66 (6)	O15–Sm2–O16	125.97 (7)
O14–Sm1–N1	123.84 (6)	O16–Sm2–O2	135.19 (6)

Symmetry codes: (i)  $-x, -y+I, -z+I$ ; (ii)  $-x+I, -y+I, -z+I$ .

**Table 5.3***Hydrogen-bond geometry (Å, °) for 22<sub>Sm</sub>*

D–H···A	D–H	H···A	D···A	D∠H···A
O14–H14A···O2	0.74(3)	2.41(3)	2.945(3)	130(3)
O14–H14A···O9i	0.74(3)	2.29(3)	2.974(3)	155(3)
O14–H14B···O2i	0.79(3)	2.20(3)	2.974(2)	167(3)
O15–H15A···O1ii	0.83(3)	2.11(3)	2.925(2)	164(3)
O15–H15B···O1	0.73(3)	2.39(3)	2.959(2)	136(3)
O15–H15B···O6	0.73(3)	2.42(3)	3.079(2)	151(3)
O16–H16A···O13	0.84(4)	1.81(4)	2.634(3)	168(4)
O16–H16B···O3ii	0.78(3)	2.19(4)	2.972(3)	178(4)
O17–H17B···O13iii	0.85	2.32	2.936(6)	160
O17A–H17C···O13i	0.85	2.32	3.051(5)	143
O17A–H17D···O16iii	0.85	2.32	3.147(5)	162
N1–H1A···O12i	0.89	2.24	3.100(3)	163
N2–H2···O17	0.86	2.06	2.753(5)	138
N2–H2···O17A	0.86	2.16	2.946(5)	153
C14–H14···O17	0.93	2.32	3.176(7)	153

Symmetry codes: (i)  $-x+1, -y+1, -z+1$ ; (ii)  $-x, -y+1, -z+1$ ; (iii)  $x, y, z-1$ .

For **23<sub>Eu</sub>**, the C–N bond is formed during the hydrothermal *in situ* synthesis of the new bbz ligand. This ligand is flexible and can link two Eu<sup>3+</sup> centers via oxygen sites, which facilitates the development of a high-dimensional coordination framework. Compound **23<sub>Eu</sub>** crystallizes in the orthorhombic system with *Pnna*, and the asymmetric unit is made up of one Eu<sup>3+</sup> ion, three ben ligands, and half of two bbz ligands, all of that are arranged on an inversion center. The Eu<sup>3+</sup> ion is eight-coordinated with six oxygen atoms from five different ben ligands and two oxygen atoms from two bbz ligands, as shown in Figure 5.3, using a distorted square antiprismatic geometry. The lengths of the Eu–O bonds range from 2.277(2) to 2.559(2), as shown in Table 5.4, which are significant compared to other observed (EuO<sub>8</sub>) compounds (Simler *et al*, 2019).



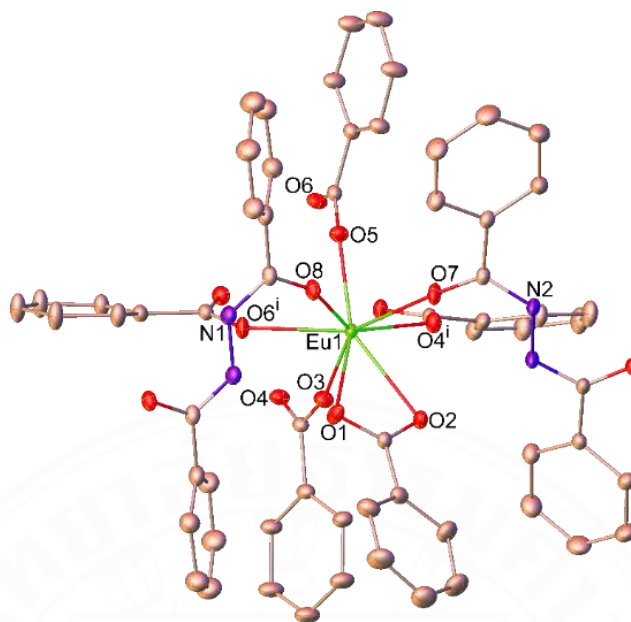
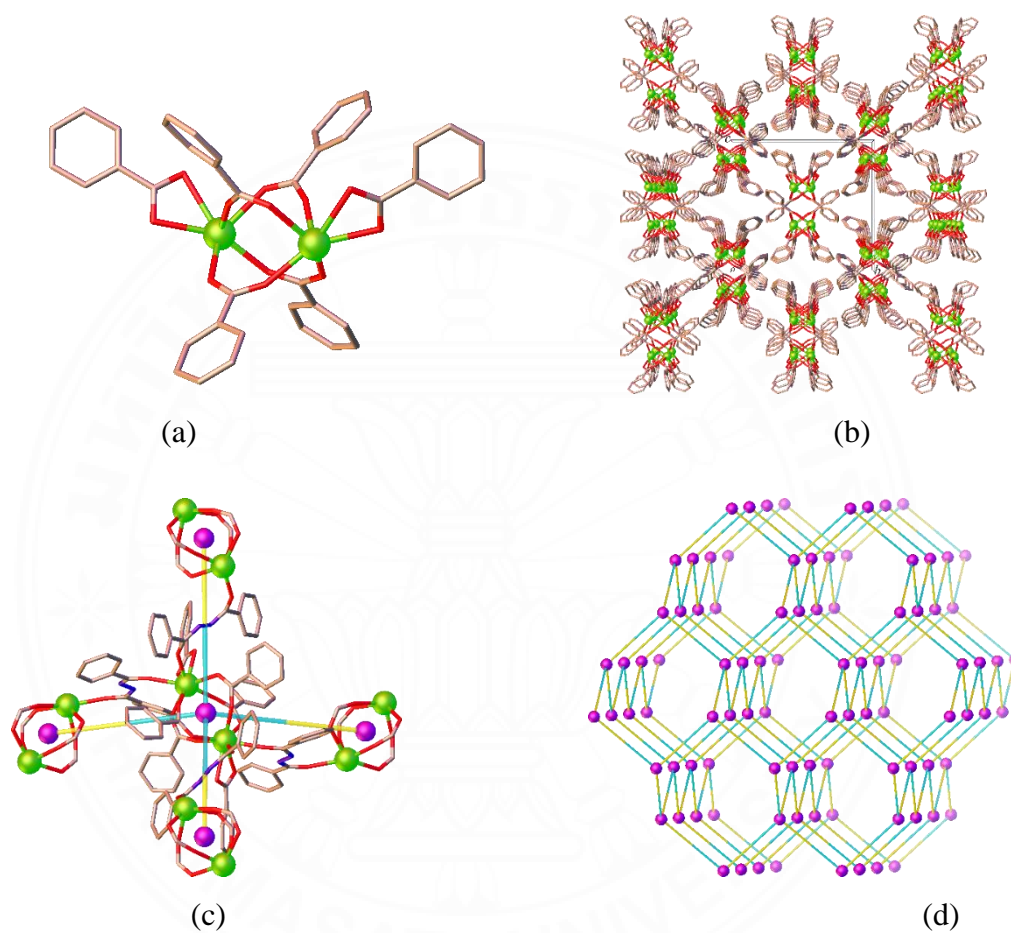


Figure 5.3 Coordination environment of **2Eu**.

In conversely to **22Sm**, the ben ligand in **23Eu** has two coordination modes: bidentate-chelating  $\eta^2$  mode (O1, O2) and bidentate-bridging  $\mu_2$  mode (O3–O6). As illustrated in Figure 5.4a, two symmetry-related  $\text{Eu}^{3+}$  ions are connected by four 2-bridging carboxylate groups from four different ben ligands to form a dinuclear  $[\text{Eu}_2(\text{ben})_6]$  secondary building unit (SBU) that is the midpoint of the SBU lies on a twofold rotation axis. The  $\text{Eu}\cdots\text{Eu}$  division throughout the dinuclear SBU is 4.2842(4) Å. As can be seen in Figure 5.4b, such SBUs are connected in a  $\mu_2$ -bridging coordination mode via bbz ligands (not shown), resulting in form of a 3D channel. The  $\text{Eu}\cdots\text{Eu}$  distances through the bbz ligands are 8.1379(4) and 8.2993(4) Å. Moreover, the network is now even better supported by  $\text{N-H}\cdots\text{O}$  and  $\text{C-H}\cdots\text{O}$  hydrogen bonds formed between the carboxylate oxygen atoms and the hydrazine NH groups or the phenyl proton of the ligands. Furthermore, there are also weak  $\text{C-H}\cdots\pi$  interactions between the phenyl rings of the bzz and ben ligands as shown in Figure 5.5 and Table 5.5. The dimer  $[\text{Eu}_2(\text{ben})_6]$  SBU and the bbz ligand can be recognised as 4- and 2-connected nodes, respectively as shown in Figure 5.4c. As illustrated in Figure 5.4d, the network structure of **23Eu** can be optimized to a 4-connected ( $6^6$ ) **dia** net.





*Figure 5.4* Views of (a) SBU of  $[\text{Eu}_2(\text{ben})_6]$ , (b) the packing of SBUs, (c) the optimized 4-connected node of the SBUs and 2-connected of the ligand, and (d) the 4-connected  $(6^6)$  dia of  $23\text{Eu}$ .

**Table 5.4***Selected bond lengths (Å) and bond angles (°) for 23Eu.*

	<b>23Eu</b>
Eu1–O1	2.475 (3)
Eu1–O2	2.559 (2)
Eu1–O3	2.277 (2)
Eu1–O4 <sup>i</sup>	2.405 (2)
Eu1–O5	2.297 (2)
Eu1–O6 <sup>i</sup>	2.423 (2)
Eu1–O7	2.391 (2)
Eu1–O8	2.436 (2)
O1–Eu1–O2	51.12 (7)
O3–Eu1–O1	84.85 (10)
O3–Eu1–O2	77.77 (9)
O3–Eu1–O4 <sup>i</sup>	78.97 (9)
O3–Eu1–O5	112.25 (9)
O3–Eu1–O6 <sup>i</sup>	75.26 (10)
O3–Eu1–O7	143.73 (9)
O3–Eu1–O8	138.82 (9)
O4 <sup>i</sup> –Eu1–O1	125.54 (8)
O4 <sup>i</sup> –Eu1–O2	74.62 (8)
O4 <sup>i</sup> –Eu1–O6 <sup>i</sup>	138.84 (8)
O4 <sup>i</sup> –Eu1–O8	142.20 (8)
O5–Eu1–O1	153.21 (9)
O5–Eu1–O2	149.75 (8)
O5–Eu1–O4 <sup>i</sup>	79.38 (9)
O5–Eu1–O6 <sup>i</sup>	81.37 (9)
O5–Eu1–O7	86.29 (9)
O5–Eu1–O8	82.76 (9)
O6 <sup>i</sup> –Eu1–O1	83.53 (8)
O6 <sup>i</sup> –Eu1–O2	128.70 (8)
O6 <sup>i</sup> –Eu1–O8	69.27 (8)
O7–Eu1–O1	91.37 (10)
O7–Eu1–O2	72.02 (8)
O7–Eu1–O4 <sup>i</sup>	74.10 (9)
O7–Eu1–O6 <sup>i</sup>	140.21 (8)
O7–Eu1–O8	71.73 (8)
O8–Eu1–O1	71.22 (9)
O8–Eu1–O2	108.93 (9)

Symmetry codes: (i)  $-x+3/2, -y+1, z$ ; (ii)  $-x+1, -y+1, -z+1$ ; (iii)  $x, -y+1/2, -z+1/2$ .

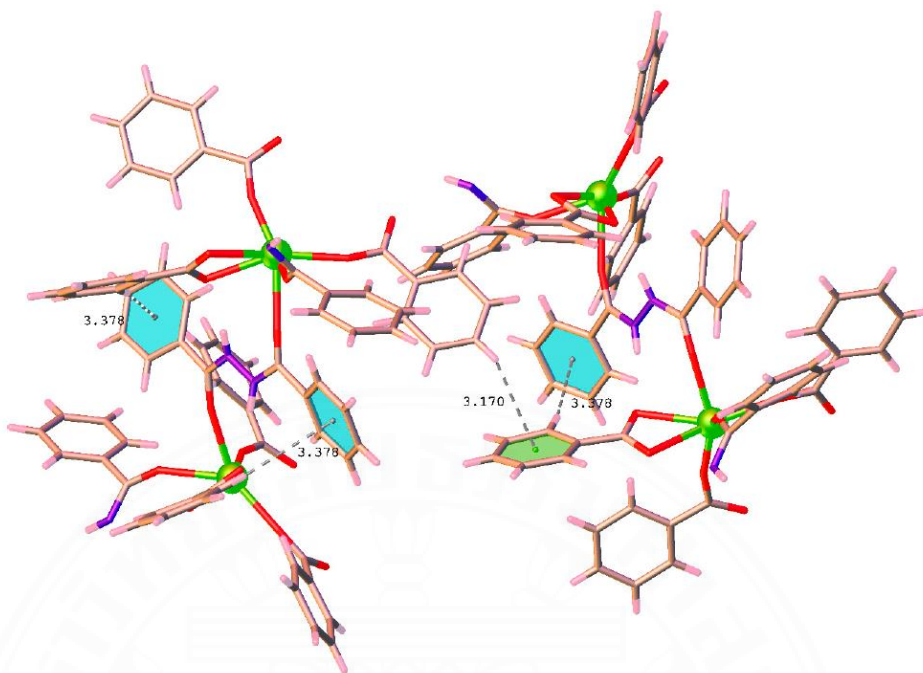


Figure 5.5 C–H⋯ $\pi$  interactions for compound **23<sub>Eu</sub>**.

Table 5.5

*C–H⋯ $\pi$  interactions (Å, °) for **23<sub>Eu</sub>***

[D–H⋯ring]	d[X⋯Cg]	d[X⋯Plane]	[D–X–Cg]	Symmetry Code
C7–H7⋯Cg2	3.378(19)	3.127(3)	164.6(8)	+x, 1/2–y, 1/2–z
C19–H19⋯Cg1	3.170(7)	2.916(10)	125.4(7)	–1/2+x, 1/2–y, –1/2+z

### 5.3.3 Infrared spectra

The infrared spectra of compounds **22<sub>Sm</sub>** and **23<sub>Eu</sub>** exhibit the absorption bands in Figure 5.6. The peaks of each group are similar in ranges 4000–650  $\text{cm}^{-1}$ . They are observed as asymmetric and symmetric. The bands around 1600 and 1400  $\text{cm}^{-1}$  in the IR spectra indicate the stretching vibrations of the carboxylate groups, guiding the ben ligand's presence in their crystalline structure. For the absorption bands in the range 3126–3067  $\text{cm}^{-1}$  demonstrate the presence of N–H stretching vibrations of the hydrazine or hydrazide groups of the ligands. Compound **22<sub>Sm</sub>** shows the strong and broad absorption bands in the range 3600–3400  $\text{cm}^{-1}$  that are identified as the

characteristic absorption bands of O-H stretching of water molecules, contributing to hydrogen bonding. All features of the FT-IR spectra of both compounds are consistent with the crystal structure when findings from single crystal X-ray diffraction analysis.

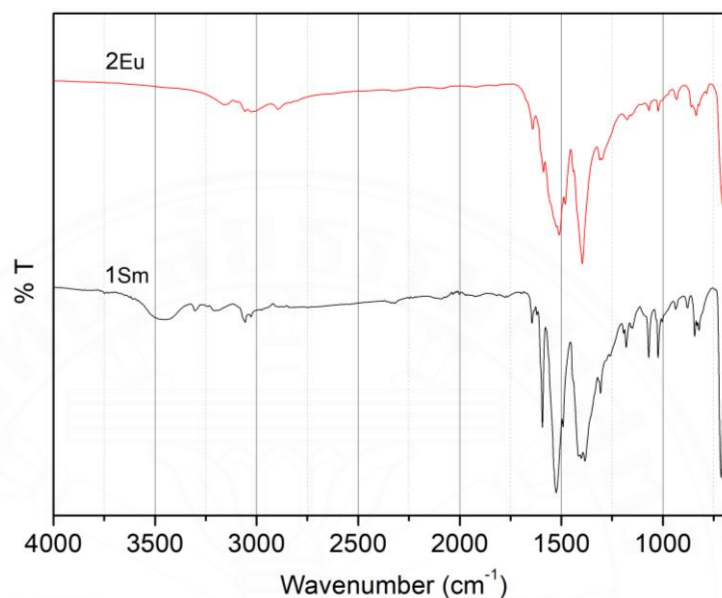


Figure 5.6 FTIR spectra for compounds **22<sub>Sm</sub>** and **23<sub>Eu</sub>**.

### 5.3.4 Powder X-ray diffraction

PXRD analysis studies the phase purities and phase transitions of **22<sub>Sm</sub>** and **23<sub>Eu</sub>**. The crystallographic data allow the simulated PXRD patterns and the experimental PXRD patterns derived from the as-synthesized samples. The as-synthesized samples of **22<sub>Sm</sub>** and **23<sub>Eu</sub>** are characterized. As shown in Figure 5.7, the PXRD patterns are almost consistent with the simulated spectra, demonstrating the high phase purity of the compounds.

Compound **23<sub>Eu</sub>** was observed by variable temperature PXRD. Besides **23<sub>Eu</sub>** shows the meaningful adjustments in the PXRD patterns when compared to the as-synthesized sample, as illustrated in Figure 5.8. These might be explained by structural modification brought on by the absence of the bbz ligands during raise the temperature, that results show of a new phase. The four distinct phases that can be identified in the VT- PXRD patterns are clearly visible. As can be observed, when the sample is heated to 300 °C, the first phase (identified as the as-synthesized **23<sub>Eu</sub>**) can

change into a second phase. Certainly, this second phase's PXRD pattern displays crystallinity with defined boundaries and the major characteristic peaks of the experimental data are very related to those of the  $[\text{Eu}_3(\text{ben})_9]$  (Simler *et al*, 2019) observed 1D polymeric structure of the europium-benzoate compound. Up to 400 °C, this phase II was stable, but at 500 °C, it underwent phase changes and became an amorphous state in phase III. Particularly, new peaks were seen after temperatures rising from 600-800 °C, indicating the production of a new phase in phase IV. This may be the consequence of the 1D chain frameworks being pyrolyzed in the air. In the patterns, there are new sharp diffraction peaks at  $2\theta = 7.23, 19.88, 28.32, 32.79$ , and  $47.01$ , which is reliable with the pattern of  $\text{Eu}_2\text{O}_3$  (PDF: 00-034-0392). Consequently, it's possible to imply from the previously mentioned characteristic in which the 3D diamond network of **23**<sub>Eu</sub> can transform into the 1D chain structure of  $[\text{Eu}_3(\text{ben})_9]$  via crystalline-to-crystalline transformation, instead of the sample being heated to 300 °C.

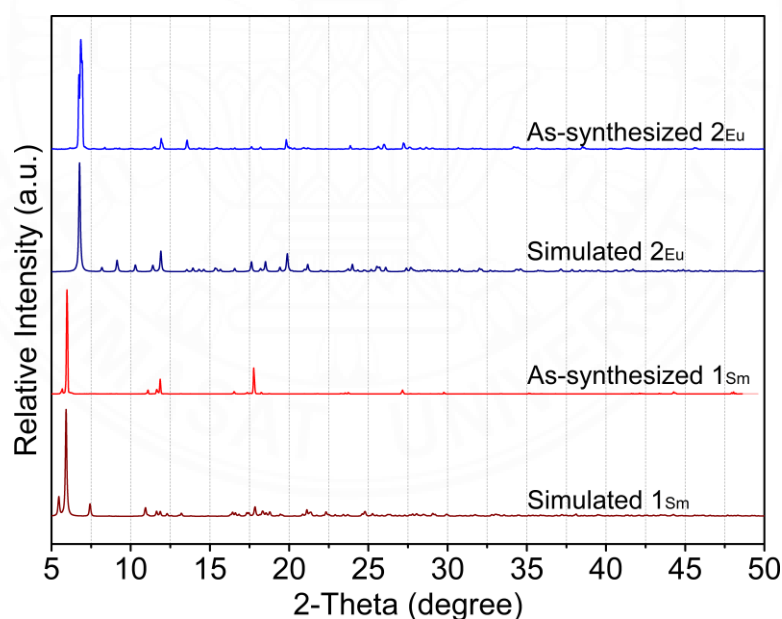


Figure 5.7 PXRD pattern for compounds **22**<sub>Sm</sub> and **23**<sub>Eu</sub>.

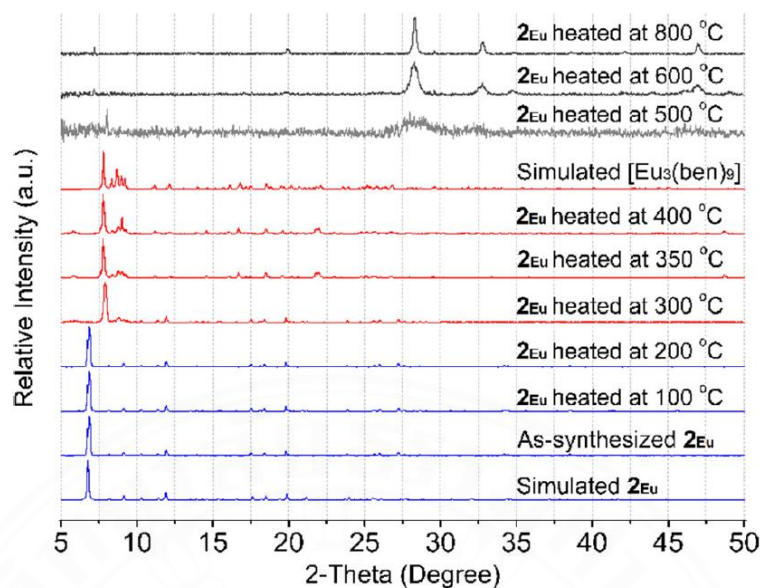


Figure 5.8 Variable temperature PXRD patterns of **23**<sub>Eu</sub>.

### 5.3.5 Thermogravimetric analysis

The thermal stabilities of **22**<sub>Sm</sub> and **23**<sub>Eu</sub> were also investigated using TGA from room temperature to 650 °C in a N<sub>2</sub> atmosphere. The TGA curves of **22**<sub>Sm</sub> and **2Eu** were observed as shown in Figure 5.9. Compound **22**<sub>Sm</sub> at the first step lost one coordinated water molecule (5.3%) from room temperature upon heating around 50-115 °C, which was consistent with the calculated value (5.1%). After the loss of guest water molecules, the second weight loss of 11.6% from 150 to 350 °C corresponds to the bzz ligands (cal 11.5%). From 425 °C, the compound began to decompose organic ligands. On further heating, the framework gradually decomposed. For compound **23**<sub>Eu</sub>, the first weight loss of 30.9% in the region 225-365 °C indicated the loss of bbz ligands (cal 31.8%). The removal of ben ligands with the collapse of the skeleton into unidentified products caused the second weight loss of 38.7% from 470 to 560 °C. It is noteworthy that the heated sample of **23**<sub>Eu</sub> retained structural integrity, then TGA experiment's initial weight loss step.

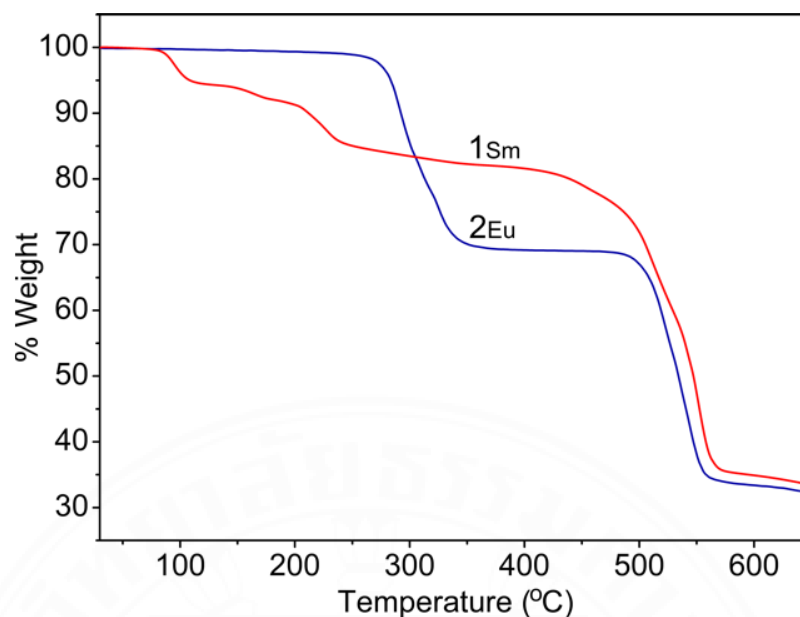


Figure 5.9 TGA curves for compounds **22<sub>Sm</sub>** and **23<sub>Eu</sub>**.

### 5.3.6 High pressure CO<sub>2</sub> adsorption

As described previous section, The structure of compound **22<sub>Sm</sub>** is a 1D polymeric double chain with a small void space to accommodate water molecules. On the contrary, compound **23<sub>Eu</sub>** displays a **dia** topology with a closely packed network structure. Contemplating the CO<sub>2</sub> adsorption isotherms for **22<sub>Sm</sub>** at 298 K in the high pressure up to 50 bar using a high-pressure volumetric gas adsorption analyzer to investigate the relationship between structure and adsorption capacity. As shown in Figure 5.10, the amount of crystal sample **22<sub>Sm</sub>** (about 50 mg) was activated at 110 °C (1°C/min) under a vacuum (2.25 mTorr) for 24 h. Compound **22<sub>Sm</sub>** exhibits a type III isotherm according to the IUPAC classification (Sing *et al*, 1985), which implies a weak adsorbent-adsorbate interaction, as can be seen in Figure 5.11. In fact, the activated sample was absorbed with low CO<sub>2</sub> adsorption uptake at low pressure (1-10 bar). It is not exactly a surprise because its structure contains a small void space. With rising gas pressure, the amount of adsorbed CO<sub>2</sub> in **22<sub>Sm</sub>** gradually increased that could be related to pore expansion, differences in the crystal structure, and specific interactions between the sorbent **22<sub>Sm</sub>** and the CO<sub>2</sub> sorbate. Obviously, the maximum CO<sub>2</sub> adsorption value of **22<sub>Sm</sub>** achieved an incredibly high volumetric uptake capacity of 376.7 cm<sup>3</sup> g<sup>-1</sup> (42.5 wt%) at 49.8 bar without saturation. Significantly, **22<sub>Sm</sub>** exhibits reversible CO<sub>2</sub>



desorption preceded with a small hysteresis. This observation most likely results from the interaction between the adsorbent and adsorbate, and demonstrates that means the adsorption does not achieve equilibrium within the measurement pressure limit of 50 bars.

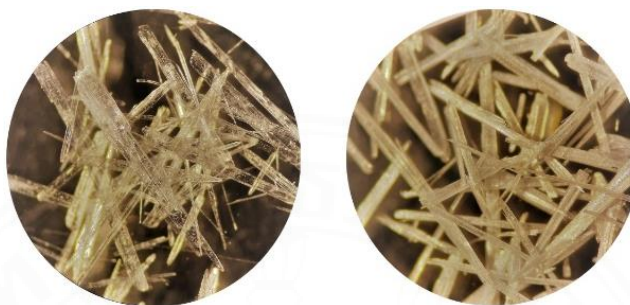


Figure 5.10 Single crystal of **22<sub>Sm</sub>**, (left) as-synthesized and (right) after measuring CO<sub>2</sub> adsorption.

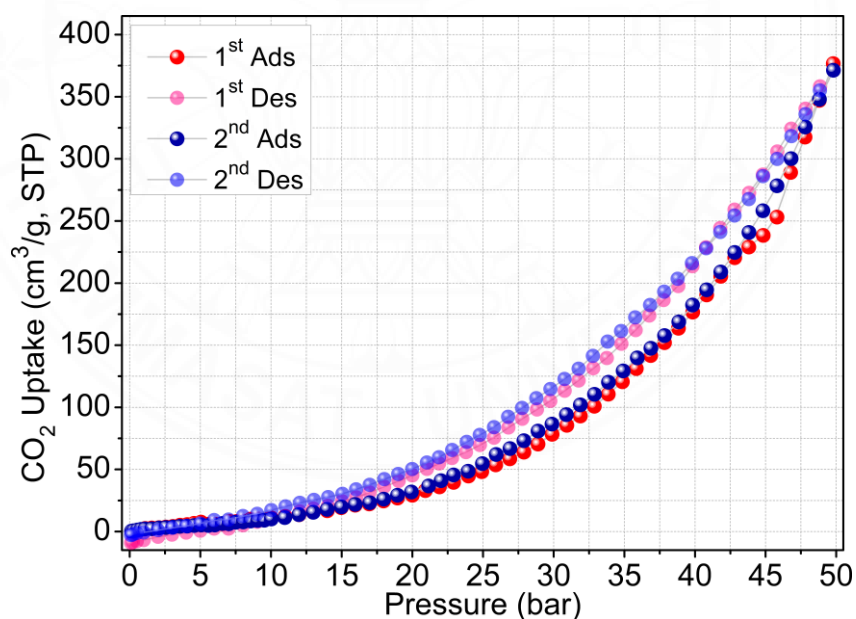


Figure 5.11 The high-pressure CO<sub>2</sub> adsorption for **22<sub>Sm</sub>**.

Additionally, the repeatability of CO<sub>2</sub> sorption of **22<sub>Sm</sub>** was investigated. The results revealed that **22<sub>Sm</sub>** can be utilized repeatedly for at least two successive cycles without significantly losing adsorption capacity. Furthermore, the



PXRD findings in Figure 5.12 demonstrate that the crystallinity of **22<sub>Sm</sub>** can be preserved even after two cycles of sorption. Nevertheless, the primary diffraction peak at  $2\theta \approx 5.93^\circ$  was significantly moved to a higher angle at  $2\theta \approx 6.69^\circ$ , and the peaks at  $2\theta \approx 11.03^\circ$ ,  $11.88^\circ$ , and  $17.73^\circ$  disappeared, inferring systemic reform upon solvent molecules are entirely removed. Unfortunately, due to poor diffraction, we were unable to identify the crystal structure of the desolvated **22<sub>Sm</sub>**.

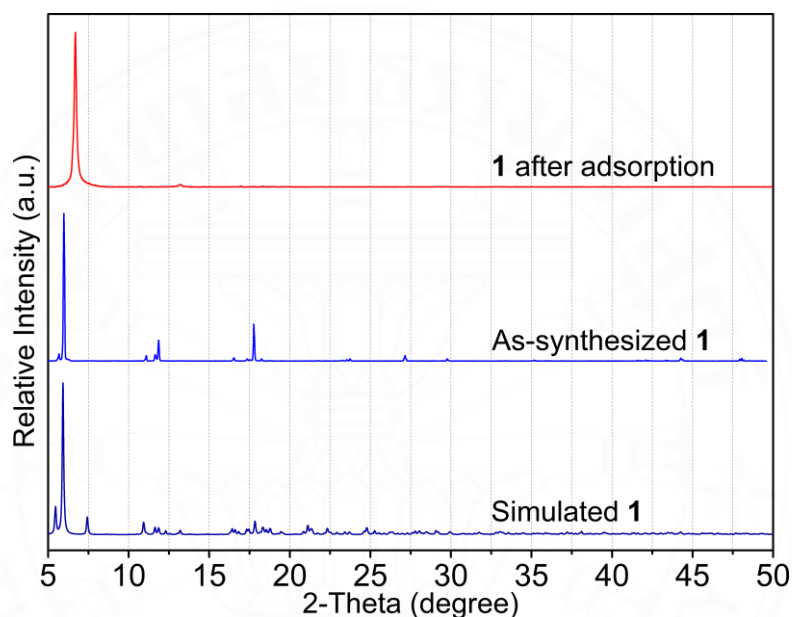


Figure 5.12 PXRD pattern before and after the CO<sub>2</sub> adsorption for **22<sub>Sm</sub>**.

### 5.3.7 Solid-state photoluminescence properties

The solid-state photoluminescence and lifetime decay of **23<sub>Eu</sub>** were recorded at RT. Compound **23<sub>Eu</sub>** emits red light under UV light irradiation, which is visible radiation to the naked eyes. Upon excitation at 297 nm as shown in Figure 5.13, the characteristics emission of Eu<sup>3+</sup> display four distinct emission bands for f-f transitions at 592, 612, 620, 652, and 702 nm as shown in Figure 5.14, which correspond to the  $^5D_0 \rightarrow ^7F_J$  ( $J = 1-4$ ) transitions, respectively. The 1931 CIE chromaticity diagram of **23<sub>Eu</sub>** shows coordinates (0.650, 0.337) that can be responds to the bright red emission. The luminescence decay times was also measured as shown in Figure 5.15. The decay time is 1.2 ms for  $^5D_0 \rightarrow ^7F_2$  of Eu<sup>3+</sup> in **23<sub>Eu</sub>**. Thus, it should be

noted that there are no emission bands of **23**<sub>Eu</sub> upon excitation at different wavelengths from 254 to 420 nm with UV light.

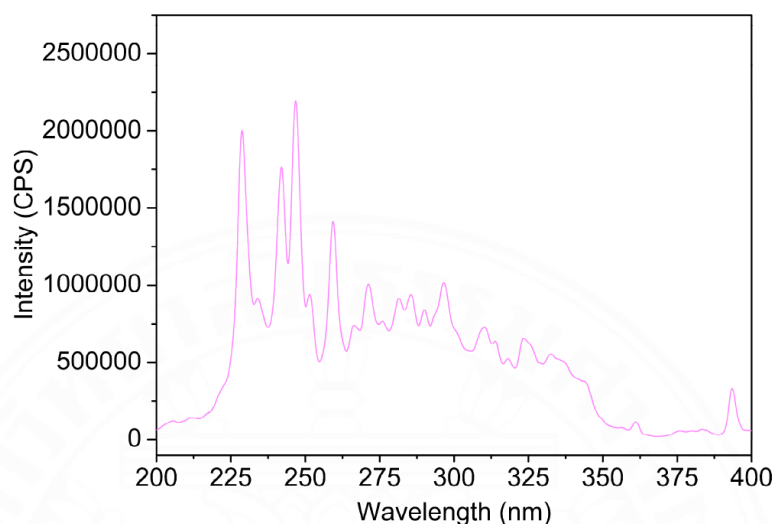


Figure 5.13 Solid state excitation of **23**<sub>Eu</sub> at  $\lambda_{em} = 615$  nm.

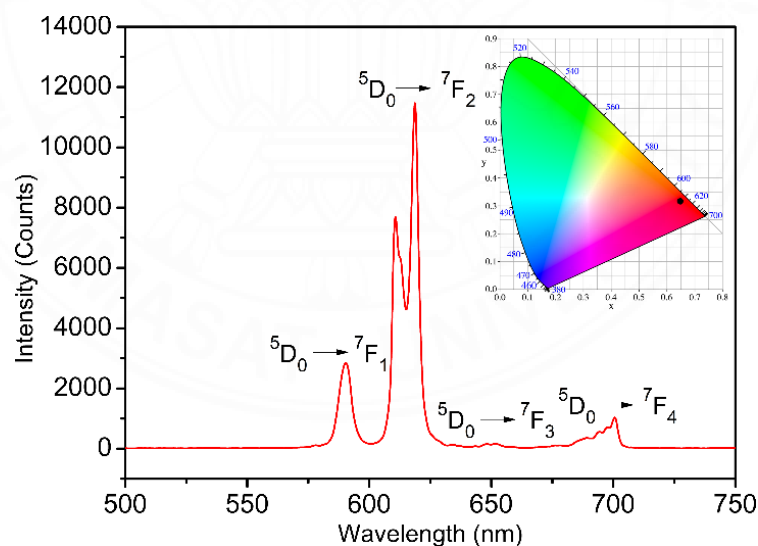


Figure 5.14 Solid state emission spectrum of **23**<sub>Eu</sub> at  $\lambda_{ex} = 297$  nm. Insert: the 1931 CIE chromaticity diagram showing the emission of **23**<sub>Eu</sub>.

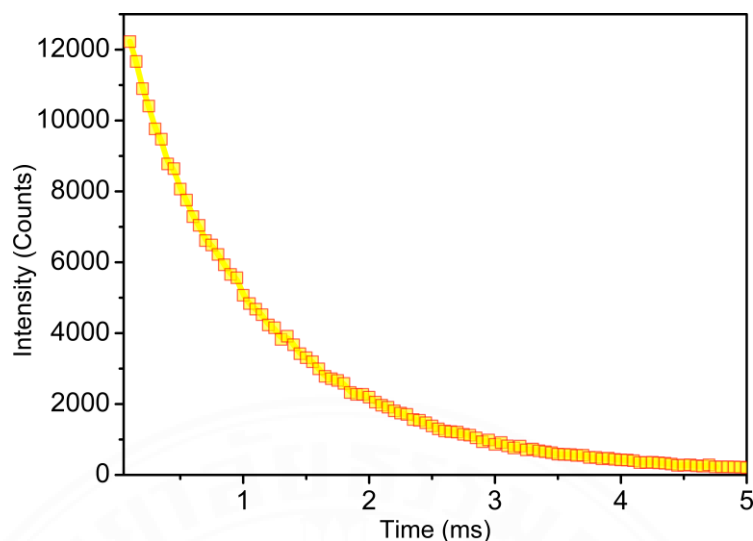


Figure 5.15 A decay lifetime of **23**<sub>Eu</sub>.

## 5.4 Conclusion

In this work, two new lanthanide coordination polymers based on *in situ* generated benzhydrazide (bzz) ligands have been synthesized by hydrothermal reactions and structurally characterized. The involvement of the ben and bbz ligands formed during the transformation of bzz ligand is critical in the formation of structural differences between the network structures of compounds **22**<sub>Sm</sub> and **23**<sub>Eu</sub>. Compound **22**<sub>Sm</sub> crystallizes in the triclinic system with  $P\bar{1}$  and displays a 1D double chain. Compound **23**<sub>Eu</sub> crystallizes in the orthorhombic  $Pnna$  and shows a 3-dimensional network with a 4-connected ( $6^6$ ) **dia** topology. Furthermore, compound **22**<sub>Sm</sub> shows uptake of high-pressure CO<sub>2</sub> adsorption of 376.7 cm<sup>3</sup> g<sup>-1</sup> (42.5 wt%) under a pressure of 49.8 bar at 298 K with good recyclability. Whereas compound **23**<sub>Eu</sub> demonstrates a typical red emission in the solid state at room temperature with the decay lifetime of 1.2 ms.

## 5.5 References

Batten, S. R., Neville, S. M., & Turner, D. R. (2009). *Coordination Polymers: Design, Analysis and Application*. (1 ed.) RSC Publishing.

- Foo, M. L., Matsuda, R., & Kitagawa, S. (2014). Functional hybrid porous coordination polymers. *Chemistry of materials*, 26(1), 310-322.
- Gorai, T., Schmitt, W., & Gunnlaugsson, T. (2021). Highlights of the development and application of luminescent lanthanide based coordination polymers, MOFs and functional nanomaterials. *Dalton Transactions*, 50(3), 770-784.
- He, C., Liu, D., & Lin, W. (2015). Nanomedicine applications of hybrid nanomaterials built from metal–ligand coordination bonds: nanoscale metal–organic frameworks and nanoscale coordination polymers. *Chemical reviews*, 115(19), 11079-11108.
- Kuwamura, N., & Konno, T. (2021). Heterometallic coordination polymers as heterogeneous electrocatalysts. *Inorganic Chemistry Frontiers*, 8(10), 2634-2649.
- Roy, S., Chakraborty, A., & Maji, T. K. (2014). Lanthanide–organic frameworks for gas storage and as magneto-luminescent materials. *Coordination Chemistry Reviews*, 273, 139-164.
- Cui, Y., Yue, Y., Qian, G., & Chen, B. (2012). Luminescent functional metal–organic frameworks. *Chemical reviews*, 112(2), 1126-1162.
- Ju, H., Habata, Y., & Lee, S. S. (2020). Temperature-Dependent Supramolecular Isomeric Zn (II)-Metal–Organic Frameworks and Their Guest Exchange. *Crystal growth & design*, 20(7), 4640-4648.
- Han, M. L., Bai, L., Tang, P., Wu, X. Q., Wu, Y. P., Zhao, J., ... & Wang, Y. Y. (2015). Biphenyl-2, 4, 6, 3', 5'-pentacarboxylic acid as a tecton for six new Co (II) coordination polymers: pH and N-donor ligand-dependent assemblies, structure diversities and magnetic properties. *Dalton Transactions*, 44(33), 14673-14685.
- Wu, Z. L., Gu, A. L., Gao, N., Cui, H. Y., Wang, W. M., & Cui, J. Z. (2020). Solvent-dependent assembly and magnetic relaxation behaviors of [Cu<sub>4</sub>I<sub>3</sub>] cluster-based lanthanide MOFs: Acting as efficient catalysts for carbon dioxide conversion with propargylic alcohols. *Inorganic Chemistry*, 59(20), 15111-15119.
- Klongdee, F., Boonmak, J., & Youngme, S. (2017). Anion-dependent self-assembly of copper coordination polymers based on pyrazole-3, 5-dicarboxylate and 1, 2-di (4-pyridyl) ethylene. *Dalton Transactions*, 46(14), 4806-4815.

- Chen, B., Wang, L., Xiao, Y., Fronczek, F. R., Xue, M., Cui, Y., & Qian, G. (2009). A luminescent metal–organic framework with Lewis basic pyridyl sites for the sensing of metal ions. *Angewandte Chemie*, 121(3), 508-511.
- Lin, X. M., Niu, J. L., Wen, P. X., Pang, Y., Hu, L., & Cai, Y. P. (2016). A polyhedral metal–organic framework based on supramolecular building blocks: catalysis and luminescent sensing of solvent molecules. *Crystal Growth & Design*, 16(8), 4705-4710.
- Li, Q., Qian, J., Zhou, J., Du, L., & Zhao, Q. (2020). Highly chemically and thermally stable lanthanide coordination polymers for luminescent probes and white light emitting diodes. *CrystEngComm*, 22(15), 2667-2674.
- Zhang, X. M. (2005). Hydro (solvo) thermal in situ ligand syntheses. *Coordination chemistry reviews*, 249(11-12), 1201-1219.
- Xiong, R. G., Xue, X., Zhao, H., You, X. Z., Abrahams, B. F., & Xue, Z. (2002). Novel, acentric metal–organic coordination polymers from hydrothermal reactions involving in situ ligand synthesis. *Angewandte Chemie*, 114(20), 3954-3957.
- Tang, Y. Z., Xiong, J. B., Gao, J. X., Tan, Y. H., Xu, Q., & Wen, H. R. (2015). Spontaneous resolution, asymmetric catalysis, and fluorescence properties of  $\Delta$ - and  $\Lambda$ -[Cu(Tzmp)]<sub>n</sub> enantiomers from in situ [2+3] cycloaddition synthesis. *Inorganic Chemistry*, 54(11), 5462-5466.
- Fishburn, M. G., Skelton, D. R., Telfer, S. G., Wagner, P., & Richardson, C. (2020). Second-order programming the synthesis of metal–organic frameworks. *Chemical Communications*, 56(82), 12355-12358.
- Kong, X. J., He, T., Zhou, J., Zhao, C., Li, T. C., Wu, X. Q., ... & Li, J. R. (2021). In Situ Porphyrin Substitution in a Zr (IV)-MOF for Stability Enhancement and Photocatalytic CO<sub>2</sub> Reduction. *Small*, 17(22), 2005357.
- Chainok, K., Ponjan, N., Theppitak, C., Khemthong, P., Kielar, F., Dungkaew, W., ... & Batten, S. R. (2018). Temperature-dependent 3D structures of lanthanide coordination polymers based on dicarboxylate mixed ligands. *CrystEngComm*, 20(46), 7446-7457.
- Phadungsak, N., Kielar, F., Dungkaew, W., Sukwattanasinitt, M., Zhou, Y., & Chainok, K. (2019). A new luminescent anionic metal–organic framework based on heterometallic zinc (II)–barium (II) for selective detection of Fe<sup>3+</sup> and Cu<sup>2+</sup>

- ions in aqueous solution. *Acta Crystallographica Section C: Structural Chemistry*, 75(10), 1372-1380.
- Ponjan, N., Kielar, F., Dungkaew, W., Kongpatpanich, K., Zenno, H., Hayami, S., ... & Chainok, K. (2020). Self-assembly of three-dimensional oxalate-bridged alkali (I)–lanthanide (III) heterometal–organic frameworks. *CrystEngComm*, 22(29), 4833-4841.
- Theppitak, C., Kielar, F., Dungkaew, W., Sukwattanasinitt, M., Kangkaew, L., Sahasithiwat, S., ... & Chainok, K. (2021). The coordination chemistry of benzhydrazide with lanthanide (III) ions: Hydrothermal in situ ligand formation, structures, magnetic and photoluminescence sensing properties. *RSC advances*, 11(40), 24709-24721.
- Nijem, N., Canepa, P., Kaipa, U., Tan, K., Roodenko, K., Tekarli, S., ... & Chabal, Y. J. (2013). Water cluster confinement and methane adsorption in the hydrophobic cavities of a fluorinated metal–organic framework. *Journal of the American Chemical Society*, 135(34), 12615-12626.
- Xu, Y. Y., Chen, P., Gao, T., Li, H. F., & Yan, P. F. (2019). White-light emission based on a single component Sm (III) complex and enhanced optical properties by doping methods. *CrystEngComm*, 21(6), 964-970.
- Spek, A. L. (2015). PLATON SQUEEZE: a tool for the calculation of the disordered solvent contribution to the calculated structure factors. *Acta Crystallographica Section C: Structural Chemistry*, 71(1), 9-18.
- Macrae, C. F., Sovago, I., Cottrell, S. J., Galek, P. T., McCabe, P., Pidcock, E., ... & Wood, P. A. (2020). Mercury 4.0: From visualization to analysis, design and prediction. *Journal of applied crystallography*, 53(1), 226-235.
- Simler, T., Feuerstein, T. J., Yadav, R., Gamer, M. T., & Roesky, P. W. (2019). Access to divalent lanthanide NHC complexes by redox-transmetallation from silver and CO<sub>2</sub> insertion reactions. *Chemical Communications*, 55(2), 222-225.
- Sing, K. S. (1985). Reporting physisorption data for gas/solid systems with special reference to the determination of surface area and porosity (Recommendations 1984). *Pure and applied chemistry*, 57(4), 603-619.

- Da Silva, C. M., Ellena, J., & Frem, R. C. G. (2020). Chemical transformation of a luminescent two-dimensional Eu (III) coordination polymer in the aqueous phase. *New Journal of Chemistry*, 44(24), 10146-10152.
- Guo, L. R., Tang, X. L., Ju, Z. H., Zhang, K. M., Jiang, H. E., & Liu, W. S. (2013). Lanthanide metal–organic frameworks constructed by asymmetric 2-nitrobiphenyl-4, 4'-dicarboxylate ligand: syntheses, structures, luminescence and magnetic investigations. *CrystEngComm*, 15(44), 9020-9031.
- APEX3, SAINT and SADABS; Bruker AXS Inc.: Madison, WI, USA, 2016. Available online: <https://www.bruker-support.com> (accessed on 21 July 2021).
- Sheldrick, G. M. (2015). SHELXT—Integrated space-group and crystal-structure determination. *Acta Crystallographica Section A: Foundations and Advances*, 71(1), 3-8.
- Sheldrick, G. M. (2015). Crystal structure refinement with SHELXL. *Acta Crystallographica Section C: Structural Chemistry*, 71(1), 3-8.
- Dolomanov, O. V., Bourhis, L. J., Gildea, R. J., Howard, J. A., & Puschmann, H. (2009). OLEX2: a complete structure solution, refinement and analysis program. *Journal of applied crystallography*, 42(2), 339-341.



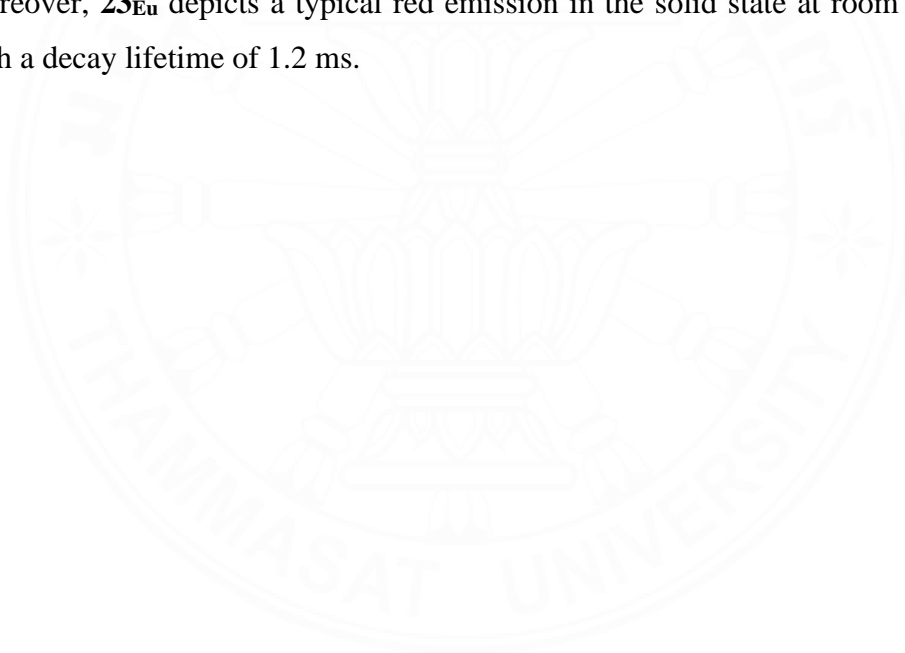
## CHAPTER 6

### CONCLUSIONS AND RECOMMENDATIONS

In summary, twenty-three novel lanthanide coordination polymers (Ln-CPs) have been synthesized. Ln-CPs have been synthesized using hydrazide-based ligands and their crystal structures were investigated using X-ray crystallography. Under solvothermal conditions, the hydrazide groups of ligands could be easily hydrolyzed to carboxylic groups through the *in situ* ligand transformation reaction. Interestingly, this process can be controlled carefully by choosing the reaction temperatures and selecting the solvent types. Reactions of benzhydrazide (bzz) and Ln(III) nitrate in alcoholic solution at room temperature afforded a series of discrete mononuclear compounds  $[\text{Ln}(\text{bzz})(\text{NO}_3)](\text{NO}_3)_2$  (**1<sub>Ln</sub>** = **1<sub>Sm</sub>**, **2<sub>Eu</sub>**, **3<sub>Gd</sub>**, **4<sub>Tb</sub>**, **5<sub>Dy</sub>**), and ligand transformation has not occurred. The isomorphous compounds crystallize in the centrosymmetric monoclinic space group *C2/c*. The Ln(III) cation is nine-coordinated by bonded to N and O atoms from four chelating hydrazide ligands and one O from nitrate groups. Using the hydrothermal method, a series of 1D polymer chains with mixed chelating bzz and bridging ben (benzoate) ligands of compounds  $[\text{Ln}(\text{bzz})(\text{ben})_3(\text{H}_2\text{O})] \cdot \text{H}_2\text{O}$  (**2<sub>Ln</sub>** = **6<sub>Pr</sub>**, **7<sub>Nd</sub>**, **8<sub>Sm</sub>**, **9<sub>Eu</sub>**, **10<sub>Gd</sub>**, **11<sub>Tb</sub>**, **12<sub>Dy</sub>**, **13<sub>Er</sub>**) have been successfully synthesized at 110 °C, in which some of the bzz ligands in situ generated ben ligands. The isomorphous compounds crystallize in monoclinic space group *P2<sub>1</sub>/c*. The Ln(III) atom is eight-coordinated with one oxygen and one nitrogen atom from a chelating bzz ligand, five oxygen atoms from five individual  $\mu_2$ -ben ligands, and one water molecule. Raising the hydrothermal temperature to 140 °C, the bzz in situ completely generated all ben ligands allowing for the formation of 1D chain structure of compounds  $[\text{Ln}_3(\text{ben})_3]$  (**3<sub>Ln</sub>** = **14<sub>Eu</sub>**, **15<sub>Gd</sub>**, **16<sub>Tb</sub>**, **17<sub>Dy</sub>**, **18<sub>Er</sub>**, **19<sub>Tm</sub>**, **20<sub>Yb</sub>**, **21<sub>Lu</sub>**). The isomorphous compounds crystallize in monoclinic space group *P2<sub>1</sub>/n*. The independent Ln(III) atom displays various coordination numbers ranging from six-eight coordinated. Noted that attempts to synthesize the compounds by the direct reactions of lanthanide nitrate with benzoic acid under the same hydrothermal condition were unsuccessful. The structures show good thermal stability. Both Eu-CPs and Tb-CPs display good sensitization in the solid-state photoluminescence properties, and they can

be used as sensor for acetone and  $\text{Co}^{2+}$  ion with good recyclability. Additionally, the temperature-dependent magnetic properties of Gd-CPs and Dy-CPs exhibit antiferromagnetic.

Furthermore, two novel Ln-CPs,  $[\text{Sm}_2(\text{bzz})(\text{ben})_6(\text{H}_2\text{O})_3] \cdot 0.5\text{H}_2\text{O}$  (**22<sub>Sm</sub>**) and  $[\text{Eu}(\text{bbz})(\text{ben})_3]$  (**23<sub>Eu</sub>**) were synthesized under hydrothermal conditions. The hydrazide groups of ligands could be hydrolyzed to carboxylic groups that are the *in situ* generated benzoate (ben) and *N'*-benzoylbenzohydrazide (bbz) ligands. **22<sub>Sm</sub>** crystallize in triclinic space group *P*-1. **23<sub>Eu</sub>** crystallizes in the orthorhombic *Pnna* and shows a 3D network with a 4-connected ( $6^6$ ) **dia** topology. High-pressure  $\text{CO}_2$  sorption studies on activated of **22<sub>Sm</sub>** show that maximum uptake increases to extremely high values of  $376.7 \text{ cm}^3 \text{ g}^{-1}$  (42.5 wt%) at 50 bars at 298 K with good recycling and reuse. Moreover, **23<sub>Eu</sub>** depicts a typical red emission in the solid state at room temperature with a decay lifetime of 1.2 ms.



The seal of Thammasat University is a large, faint, circular watermark in the background. It features a central emblem with a lotus flower and a crown, surrounded by the university's name in Thai and English.

## APPENDIX

## HYDROGEN BOND

Hydrogen bond geometry (Å, °) for **1<sub>Ln</sub>**

Complexes	[D—H...A]	d[D—H]	d[H...A]	d[D...A]	∠[D—H...A]
<b>1<sub>Sm</sub></b>	N1—H1A...O5 <sup>i</sup>	0.89 (1)	2.07 (3)	2.901 (9)	156 (5)
	N1—H1B...O7A <sup>ii</sup>	0.89 (1)	2.07 (3)	2.90 (2)	154 (6)
	N2—H2...O8A <sup>iii</sup>	0.86 (1)	2.48 (6)	3.05 (3)	125 (5)
	N3—H3A...O8 <sup>iv</sup>	0.89 (1)	2.00 (2)	2.88 (2)	174 (5)
	N3—H3B...O5 <sup>i</sup>	0.89 (1)	2.13 (3)	2.961 (8)	155 (5)
	N4—H4...O6	0.86 (1)	2.21 (3)	2.953 (15)	145 (5)
	N4—H4...O6A	0.86 (1)	2.06 (2)	2.884 (14)	161 (5)
<b>2<sub>Eu</sub></b>	N1—H1A...O5 <sup>i</sup>	0.89 (1)	2.07 (3)	2.883 (11)	152 (6)
	N1—H1B...O7A <sup>ii</sup>	0.89 (1)	2.06 (4)	2.89 (3)	155 (7)
	N2—H2...O8A <sup>iii</sup>	0.86 (1)	2.39 (8)	3.02 (3)	130 (9)
	N3—H3A...O8 <sup>iv</sup>	0.89 (1)	2.01 (2)	2.893 (19)	174 (5)
	N3—H3B...O5 <sup>i</sup>	0.89 (1)	2.13 (4)	2.945 (10)	152 (7)
	N4—H4...O6	0.86 (1)	2.19 (4)	2.931 (13)	145 (6)
	N4—H4...O6A	0.86 (1)	2.07 (3)	2.89 (2)	159 (7)
<b>3<sub>Gd</sub></b>	N1—H1A...O5 <sup>i</sup>	0.89 (1)	2.07 (2)	2.891 (7)	153 (5)
	N1—H1B...O7A <sup>ii</sup>	0.89 (1)	2.08 (3)	2.904 (18)	153 (5)
	N2—H2...O8A <sup>iii</sup>	0.86 (1)	2.60 (5)	3.20 (2)	128 (5)
	N3—H3A...O8 <sup>iv</sup>	0.89 (1)	2.07 (2)	2.96 (2)	174 (4)
	N3—H3B...O5 <sup>i</sup>	0.89 (1)	2.13 (2)	2.957 (6)	155 (4)
	N4—H4...O6	0.86 (1)	2.25 (3)	2.966 (15)	141 (4)
	N4—H4...O6A	0.86 (1)	2.08 (2)	2.880 (10)	157 (4)
<b>4<sub>Tb</sub></b>	N1—H1A...O5 <sup>i</sup>	0.89 (1)	2.02 (3)	2.890 (10)	164 (8)
	N1—H1B...O7A <sup>ii</sup>	0.89 (1)	2.07 (4)	2.91 (2)	157 (8)
	N2—H2...O8A <sup>iii</sup>	0.86 (1)	2.57 (6)	3.16 (3)	128 (5)
	N3—H3A...O8 <sup>iv</sup>	0.89 (1)	2.01 (3)	2.90 (3)	172 (6)
	N3—H3B...O5 <sup>i</sup>	0.89 (1)	2.15 (3)	2.959 (9)	152 (6)
	N4—H4...O6	0.86 (1)	2.23 (4)	2.968 (18)	144 (5)
	N4—H4...O6A	0.86 (1)	2.04 (3)	2.862 (14)	159 (5)
<b>5<sub>Dy</sub></b>	N1—H1A...O5 <sup>i</sup>	0.89 (1)	2.08 (3)	2.888 (8)	152 (6)
	N1—H1B...O7A <sup>ii</sup>	0.89 (1)	2.10 (3)	2.933 (19)	155 (5)
	N2—H2...O8A <sup>iii</sup>	0.85 (1)	2.44 (4)	3.028 (19)	127 (4)
	N3—H3A...O8 <sup>iv</sup>	0.89 (1)	2.00 (3)	2.88 (2)	170 (5)
	N3—H3B...O5 <sup>i</sup>	0.89 (1)	2.14 (3)	2.953 (7)	151 (5)
	N4—H4...O6	0.86 (1)	2.27 (4)	2.963 (15)	138 (5)
	N4—H4...O6A	0.86 (1)	2.07 (3)	2.874 (12)	155 (5)

Symmetry codes: (i)  $x, -y+1, z-1/2$ ; (ii)  $-x+1, -y+1, -z+1$ ; (iii)  $-x+1, y, -z+1/2$ ; (iv)  $x, -y+1, z+1/2$ .

Hydrogen bond geometry (Å,°) for **2<sub>Ln</sub>**

Complexes	[D—H...A]	d[D—H]	d[H...A]	d[D...A]	∠[D—H...A]
<b>6<sub>Pr</sub></b>	O8—H8A...O7	0.84 (1)	1.83 (1)	2.658 (3)	168 (3)
	O8—H8B...O1 <sup>i</sup>	0.84 (1)	2.09 (1)	2.922 (2)	178 (3)
	O9A—H9AA...O7 <sup>ii</sup>	0.85	2.30	3.026 (12)	144
	O9A—H9AB...O9A <sup>iii</sup>	0.85	2.35	2.90 (2)	123
	O9B—H9BA...O8 <sup>ii</sup>	0.85	2.16	2.990 (3)	165
	O9B—H9BB...O7 <sup>i</sup>	0.85	2.38	3.117 (4)	146
	N1—H1A...O4 <sup>i</sup>	0.89	2.56	3.086 (2)	119
	N1—H1A...O6 <sup>i</sup>	0.89	2.25	3.108 (2)	161
	N2—H2...O9A	0.86	2.14	2.821 (12)	135
	N2—H2...O9B	0.86	2.10	2.879 (3)	151
<b>7<sub>Na</sub></b>	O8—H8A...O7	0.84 (1)	1.82 (1)	2.650 (3)	167 (3)
	O8—H8B...O1 <sup>i</sup>	0.83 (1)	2.10 (1)	2.928 (3)	172 (3)
	O9A—H9AA...O7 <sup>ii</sup>	0.85	2.32	3.027 (15)	141
	O9A—H9AB...O9A <sup>iii</sup>	0.85	2.26	2.91 (3)	133
	O9B—H9BA...O8 <sup>ii</sup>	0.85	2.20	2.998 (4)	155
	O9B—H9BB...O7 <sup>i</sup>	0.85	2.33	3.115 (4)	154
	N1—H1A...O4 <sup>i</sup>	0.89	2.54	3.077 (3)	120
	N1—H1A...O6 <sup>i</sup>	0.89	2.26	3.109 (3)	160
	N2—H2...O9A	0.86	2.14	2.812 (15)	135
	N2—H2...O9B	0.86	2.09	2.881 (3)	152
<b>8<sub>Sm</sub></b>	O8—H8A...O7	0.84 (1)	1.82 (1)	2.646 (4)	168 (4)
	O8—H8B...O1 <sup>i</sup>	0.83 (1)	2.11 (1)	2.941 (4)	172 (5)
	O9A—H9AA...O7 <sup>ii</sup>	0.85	2.54	3.05 (3)	120
	O9A—H9AB...O9A <sup>iii</sup>	0.85	2.29	2.90 (5)	130
	O9B—H9BA...O8 <sup>ii</sup>	0.85	2.23	3.005 (5)	152
	O9B—H9BB...O7 <sup>i</sup>	0.85	2.32	3.123 (6)	157
	N1—H1A...O4 <sup>i</sup>	0.89	2.53	3.078 (4)	121
	N1—H1A...O6 <sup>i</sup>	0.89	2.27	3.118 (4)	160
	N2—H2...O9A	0.86	2.16	2.82 (2)	133
	N2—H2...O9B	0.86	2.09	2.888 (4)	153
<b>9<sub>Eu</sub></b>	O8—H8A...O7	0.84 (1)	1.81 (1)	2.638 (2)	167 (3)
	O8—H8B...O1 <sup>i</sup>	0.83 (1)	2.12 (1)	2.9471 (19)	174 (3)
	O9A—H9AA...O7 <sup>ii</sup>	0.85	2.31	3.062 (15)	147
	O9A—H9AB...O9A <sup>iii</sup>	0.85	2.34	2.87 (3)	121
	O9B—H9BA...O8 <sup>ii</sup>	0.85	2.23	3.009 (3)	153
	O9B—H9BB...O7 <sup>i</sup>	0.85	2.33	3.117 (4)	154
	N1—H1A...O4 <sup>i</sup>	0.89	2.51	3.069 (2)	121
	N1—H1A...O6 <sup>i</sup>	0.89	2.27	3.122 (2)	161
	N2—H2...O9A	0.86	2.16	2.817 (14)	133
	N2—H2...O9B	0.86	2.09	2.882 (3)	153

Complexes	[D—H...A]	d[D—H]	d[H...A]	d[D...A]	$\angle$ [D—H...A]
<b>10<sub>Gd</sub></b>	O8—H8A...O7	0.84 (1)	1.81 (2)	2.628 (4)	164 (4)
	O8—H8B...O1 <sup>i</sup>	0.84 (1)	2.13 (1)	2.956 (3)	172 (4)
	O9A—H9AA...O7 <sup>ii</sup>	0.85	2.49	3.07 (2)	126
	O9A—H9AB...O9A <sup>iii</sup>	0.85	2.18	2.89 (4)	142
	O9B—H9BA...O8 <sup>ii</sup>	0.85	2.21	3.014 (4)	158
	O9B—H9BB...O7 <sup>i</sup>	0.85	2.36	3.114 (5)	148
	N1—H1A...O4 <sup>i</sup>	0.89	2.51	3.067 (3)	121
	N1—H1A...O6 <sup>i</sup>	0.89	2.27	3.125 (3)	160
	N2—H2...O9A	0.86	2.14	2.79 (2)	133
	N2—H2...O9B	0.86	2.09	2.886 (4)	153
<b>11<sub>Tb</sub></b>	O8—H8A...O7	0.84 (1)	1.80 (2)	2.621 (4)	164 (4)
	O8—H8B...O1 <sup>i</sup>	0.84 (1)	2.13 (2)	2.955 (3)	168 (5)
	O9A—H9AA...O7 <sup>ii</sup>	0.85	2.37	3.09 (2)	142
	O9A—H9AB...O9A <sup>iii</sup>	0.85	2.13	2.86 (5)	144
	O9B—H9BA...O8 <sup>ii</sup>	0.85	2.23	3.022 (4)	156
	O9B—H9BB...O7 <sup>i</sup>	0.85	2.35	3.130 (5)	153
	N1—H1A...O4 <sup>i</sup>	0.89	2.50	3.060 (3)	122
	N1—H1A...O6 <sup>i</sup>	0.89	2.27	3.125 (3)	161
	N2—H2...O9A	0.86	2.13	2.80 (2)	134
	N2—H2...O9B	0.86	2.10	2.895 (4)	154
<b>12<sub>Dy</sub></b>	O8—H8A...O7	0.83 (1)	1.83 (2)	2.633 (3)	163 (3)
	O8—H8B...O1 <sup>i</sup>	0.83 (1)	2.13 (1)	2.957 (3)	177 (3)
	O9A—H9AA...O7 <sup>ii</sup>	0.85	2.35	3.06 (2)	143
	O9A—H9AB...O9A <sup>iii</sup>	0.85	2.37	2.89 (4)	120
	O9B—H9BA...O8 <sup>ii</sup>	0.85	2.27	3.021 (4)	148
	O9B—H9BB...O7 <sup>i</sup>	0.85	2.32	3.112 (5)	156
	N1—H1A...O4 <sup>i</sup>	0.89	2.51	3.068 (3)	121
	N1—H1A...O6 <sup>i</sup>	0.89	2.27	3.128 (3)	161
	N2—H2...O9A	0.86	2.15	2.80 (2)	133
	N2—H2...O9B	0.86	2.09	2.887 (4)	154
<b>13<sub>Er</sub></b>	O8—H8A...O7	0.84 (1)	1.79 (2)	2.606 (7)	163 (7)
	O8—H8B...O1 <sup>i</sup>	0.84 (1)	2.16 (2)	2.966 (5)	162 (6)
	O9A—H9AA...O9A <sup>ii</sup>	0.85	2.12	2.81 (11)	138
	O9A—H9AB...O7 <sup>iii</sup>	0.84	2.55	3.00 (6)	114
	O9B—H9BA...O8 <sup>iii</sup>	0.84	2.28	3.050 (8)	152
	O9B—H9BB...O7 <sup>i</sup>	0.84	2.32	3.100 (9)	154
	N1—H1A...O4 <sup>i</sup>	0.89	2.48	3.055 (6)	122
	N1—H1A...O6 <sup>i</sup>	0.89	2.28	3.136 (6)	161
	N2—H2...O9A	0.86	2.15	2.81 (5)	134
	N2—H2...O9B	0.86	2.08	2.878 (7)	154

Symmetry codes (i)  $x, -y+3/2, z+1/2$ ; (ii)  $-x+1, y+1/2, -z+3/2$ ; (iii)  $-x+1, -y+2, -z+2$ .

Hydrogen bond geometry (Å,°) for **22<sub>Sm</sub>**

Complexes	[D—H...A]	d[D—H]	d[H...A]	d[D...A]	∠[D—H...A]
<b>22<sub>Sm</sub></b>	O14—H14A...O2	0.74 (3)	2.41 (3)	2.945 (3)	130 (3)
	O14—H14A...O9 <sup>i</sup>	0.74 (3)	2.29 (3)	2.974 (3)	155 (3)
	O14—H14B...O2 <sup>i</sup>	0.79 (3)	2.20 (3)	2.974 (2)	167 (3)
	O15—H15A...O1 <sup>ii</sup>	0.83 (3)	2.11 (3)	2.925 (2)	164 (3)
	O15—H15B...O1	0.73 (3)	2.39 (3)	2.959 (2)	136 (3)
	O15—H15B...O6	0.73 (3)	2.42 (3)	3.079 (2)	151 (3)
	O16—H16A...O13	0.84 (4)	1.81 (4)	2.634 (3)	168 (4)
	O16—H16B...O3 <sup>ii</sup>	0.78 (3)	2.19 (4)	2.972 (3)	178 (4)
	O17—H17B...O13 <sup>iii</sup>	1.00	1.97	2.936 (6)	160
	O17A—H17C...O13 <sup>i</sup>	0.85	2.32	3.051 (5)	143
	O17A—H17D...O16 <sup>iii</sup>	0.85	2.32	3.147 (5)	162
	N1—H1A...O12 <sup>i</sup>	0.89	2.24	3.100 (3)	163
	N2—H2...O17	0.86	2.06	2.753 (5)	138
	N2—H2...O17A	0.86	2.16	2.946 (5)	153
	C14—H14...O17	0.93	2.32	3.176 (7)	153

Symmetry codes (i)  $-x+1, -y+1, -z+1$ ; (ii)  $-x, -y+1, -z+1$ ; (iii)  $x, y, z-1$ .

Hydrogen bond geometry (Å,°) for **23<sub>Eu</sub>**

Complexes	[D—H...A]	d[D—H]	d[H...A]	d[D...A]	∠[D—H...A]
<b>23<sub>Eu</sub></b>	N1—H1...O1 <sup>i</sup>	0.87 (1)	1.89 (1)	2.755 (4)	178 (4)
	N2—H2...O2 <sup>ii</sup>	0.86 (1)	1.98 (1)	2.832 (4)	173 (4)
	C28—H28...O2 <sup>ii</sup>	0.93	2.58	3.156 (4)	120

Symmetry codes (i)  $-x+1, -y+1, -z+1$ ; (ii)  $x, -y+1/2, -z+1/2$ .

## BIOGRAPHY

Name	Chatphorn Theppitak
Educational Attainment	2022: Ph.D. in Chemistry, Thammasat University, Thailand 2016: M.Sc. in Chemistry, Naresuan University, Thailand 2012: B.Sc. in Chemistry, Naresuan University, Thailand
Scholarship	2018: STEM (Science, Technology Engineering, and Mathematics) (SCA-CO-2561-6014-TH) from National Science and Technology Development Agency 2020: Graduate Development Scholarship 2020, National Research Council of Thailand (Contact No. 15/2563) 2021: TINT to University
Relevant Experience	2017: Research Assistant: Assoc. Prof. Dr. Kittipong Chainok 2018: Teaching assistant in the chemistry laboratory at the Faculty of Science and Technology, Thammasat University 2018: Research Assistant with PTTEP in the projects “Carbon dioxide removal adsorbent by MOF” and “Mercury removal adsorbent by MOF” 2022: Research Assistant with EGAT in the projects “Development of Porous Metal-Organic Frameworks for Gas Adsorption”



## Publications

- Theppitak, C.**, Laksee, S., & Chainok, K. (2022). Crystal structure and Hirshfeld surface analysis of tris (acetohydrazide- $\kappa^2N, O$ )(nitrato- $\kappa O$ )(nitrato- $\kappa^2O, O'$ ) terbium (III) nitrate. *Acta Crystallographica Section E: Crystallographic Communications*, 78(4).
- Theppitak, C.**, Kielar, F., Dungkaew, W., Sukwattanasinitt, M., Kangkaew, L., Sahasithiwat, S., ... & Chainok, K. (2021). The coordination chemistry of benzhydrazide with lanthanide (III) ions: Hydrothermal in situ ligand formation, structures, magnetic and photoluminescence sensing properties. *RSC advances*, 11(40), 24709-24721.
- Theppitak, C.**, Jiajaroen, S., Chongboriboon, N., Chanthee, S., Kielar, F., Dungkaew, W., ... & Chainok, K. (2021). Self-Assembly of 1D Double-Chain and 3D Diamondoid Networks of Lanthanide Coordination Polymers through In Situ-Generated Ligands: High-Pressure CO<sub>2</sub> Adsorption and Photoluminescence Properties. *Molecules*, 26(15), 4428.
- Chainok, K., Jittirattanakun, S., **Theppitak, C.**, Jiajaroen, S., Puangsing, P., Saphu, W., ... & Sukwattanasinitt, M. (2021). Coordination-driven self-assembly of a series of dinuclear M<sub>2</sub>L<sub>2</sub> mesocates with a bis-bidentate pyridylimine ligand. *Dalton Transactions*, 50(22), 7736-7743.
- Jittirattanakun, S., **Theppitak, C.**, Wannarit, N., Rotsut, B., & Chainok, K. (2020). Crystal structures and Hirshfeld surface analysis of trans-bis (thiocyanato- $\kappa N$ ) bis {2,4,6-trimethyl-*N*-[(pyridin-2-yl) methylidene] aniline- $\kappa^2N, N'$ } manganese (II) and trans-bis (thiocyanato- $\kappa N$ ) bis {2,4,6-trimethyl-*N*-[(pyridin-2-yl) methylidene] aniline- $\kappa^2N, N'$ } nickel (II). *Acta Crystallographica Section E: Crystallographic Communications*, 76(2), 288-293.
- Samakun, K., **Theppitak, C.**, Jiajaroen, S., Dungkaew, W., Piromchat, T., & Chainok, K. (2019). Synthesis and characterization of a new copper(II) coordination polymer with mixed ligands of tetrabromoterephthalic acid and imidazole. *JCST*, 9, 131–139.

- Khotchasanthong, K., Jittirattanakun, S., Jiajaroen, S., **Theppitak, C.**, & Chainok, K. (2019). Crystal structure and Hirshfeld surface analysis of 2, 5-dibromoterephthalic acid ethylene glycol monosolvate. *Acta Crystallographica Section E: Crystallographic Communications*, 75(8), 1228-1231.
- Dungkaew, W., Jiajaroen, S., **Theppitak, C.**, Sertphon, D., & Chainok, K. (2019). Copper (II) adsorption property of 1D coordination polymer  $[\text{Cu}_2(\text{H}_2\text{O})(\text{bipy})_2(\text{tp})_2](\text{bipy} = 2, 2'\text{-bipyridine}, \text{tp} = \text{terephthalate})$  after acid treatment. *JCST*, 9(1), 29-39.
- Chainok, K., Ponjan, N., **Theppitak, C.**, Khemthong, P., Kielar, F., Dungkaew, W., ... & Batten, S. R. (2018). Temperature-dependent 3D structures of lanthanide coordination polymers based on dicarboxylate mixed ligands. *CrystEngComm*, 20(46), 7446-7457.
- Theppitak, C.**, Kielar, F., & Chainok, K. (2018). Crystal structure of diaquatris (benzohydrazide- $\kappa^2\text{N}$ ,  $O$ )(isophthalato- $\kappa O$ ) samarium (III) nitrate. *Acta Crystallographica Section E: Crystallographic Communications*, 74(12), 1691-1694.
- Theppitak, C.**, & Chainok, K. (2015). Crystal structure of  $\text{CdSO}_4 \cdot (\text{H}_2\text{O})$ : a redetermination. *Acta Crystallographica Section E: Crystallographic Communications*, 71(10), i8-i9.
- Theppitak, C.**, & Chainok, K. (2015). Crystal structure of poly [(2, 2'-bipyridine- $\kappa^2\text{N}$ ,  $N'$ ) tetra- $\mu^2$ -cyanido- $\kappa^4\text{C}$ :  $\text{N}$ ;  $\kappa^4\text{N}$ :  $\text{C}$ -manganese (II) disilver (I)]. *Acta Crystallographica Section E: Crystallographic Communications*, 71(10), m179-m180.
- Theppitak, C.** (2015). Supramolecular interaction in copper (II) complexes containing schiff base ligands Phailyn Khemthong<sup>1</sup>, Chatphorn Theppitak<sup>1</sup>, Filip Kielar<sup>1</sup> and Kittipong Chainok<sup>2</sup>. วารสาร วิทยาศาสตร์ และ เทคโนโลยี หัวเฉียวเฉลิมพระเกียรติ ISSN 2651-2483 (Online)(TCI Tier 2), 1(1), 33-41.
- Theppitak, C.**, Meesangkaew, M., Chanthee, S., Sriprang, N., & Chainok, K. (2014). Crystal structure of (pyridin-2-ylmethylidene)(triphenylmethyl) amine. *Acta*

*Crystallographica Section E: Structure Reports Online*, 70(10), o1094-o1095.

Boonlue, S., **Theppitak, C.**, & Chainok, K. (2012). Tetraaqua (2, 2'-bipyridine- $\kappa^2N$ ,  $N'$ ) nickel (II) sulfate. *Acta Crystallographica Section E: Structure Reports Online*, 68(7), m908-m908.

